Optimization of Endwall Film-Cooling in Axial Turbines

by

Mitra Thomas

University College



A thesis submitted for the degree of Doctor of Philosophy

April 2014

Department of Engineering Science

Parks Road, Oxford, OX1 3PJ

Abstract

Considerable reductions in gas turbine weight and fuel consumption can be achieved by operating at a higher turbine entry temperature. The move to lean combustors with flatter outlet temperature profiles will increase temperatures on the turbine endwalls. This work will study methods to improve endwall film cooling, to allow these advances.

Turbine secondary flows are caused by a deficit in near-wall momentum. These flow features redistribute near-wall flows and make it difficult to film-cool endwalls. In this work, endwall film cooling was studied by CFD and validated by experimental measurements in a linear cascade. This study will add to the growing body of evidence that injection of high momentum coolant into the upstream boundary layer can suppress secondary flows by increasing near-wall momentum. The reduction of secondary flows allows for effective cooling of the endwall. It is also noted that excess near-wall momentum is undesirable. This leads to upwash on the vane, driving coolant away from the endwall.

A passive-scalar tracking method has been devised to isolate the contribution of individual film cooling holes to cooling effectiveness. This method was used to systematically optimize endwall cooling systems. Designs are presented which use half the coolant mass flow compared to a baseline design, while maintaining similar cooling effectiveness levels on the critical trailing endwall. By studying the effect of coolant injection on vane inlet total pressure profile, secondary flows were suppressed and upwash on the vane was reduced.

The methods and insight obtained from this study were applied to a high pressure nozzle guide vane endwall from a current engine. The optimized cooling system developed offers significant improvement over the baseline.

Acknowledgements

Many thanks are owed to Prof. Thomas Povey for a very enjoyable DPhil. I thank Prof. Povey for being Colonel Trautman to Rambo, training me to write better, present better, and engineer better. Prof. Povey has set standards of technical skill and leadership that I hope to emulate in my career.

To Dr. David Gillespie for useful feedback on my work. To a very skilled Dave O'Dell, Dominic Harris, Gerald Walker, Hal Surtell and many others who made a behemoth test facility come together in record time. You are better engineers than I will ever be. Many thanks are due to the UK/European taxpayer for paying (among other dues) their 'pasty' taxes. It is my hope that the PhD you've partly funded will lead to cleaner skies and cheaper tickets to Ibiza someday. To Rolls-Royce for co-funding my PhD. I thank you for the “trust”, and hope I have "delivered excellence". To Prof. Peter Ireland for many conversations on life, compressibility and the pursuit of metal effectiveness.

My thanks to Fred and Wilma (chaffinches) who chose to raise young outside my window last year. And the two magpies who have chosen to nest right outside my window this year. You have been endlessly entertaining. If you must know, your birdfeed cost me around 10 pounds a year.

I am grateful to Dr. Chris Long (Uni of Sussex), Dr. Nick Atkins (Cambridge), Prof. Luca d'Agostino, Prof. Fabrizio Paganucci, Prof. Luigi Lazzeri (Uni. of Pisa), Prof. M. Ramakrishna, Prof. H. S. N. Murthy, Prof. S. C. Rajan (IIT-Madras) who bravely recommended me for Masters and PhD study. I hope I have not let you down.

My thanks to the many who have risen up the Inner Circle of Trust Ladder (ICOTL 1-5). To Ben, designated confidante, who has slipped from ICOTL 4.0 to 3.5 for concealing a belly dancing past. To Lana Al-Shami (ICOTL 3.5) who is a contender for Best supporting act. To the Best Newcomer 2014, Kathryn (ICOTL 2) for positive feedback on my Angry Bird hat.

To Lisa, mein Zuckerbird, for being personal sunshine.

And to my parents for their unwavering support and encouragement.

Contents

Abstract ..... **i**

Acknowledgements ..... **i**

Contents ..... **ii**

Nomenclature ..... **vi**

Tables and Figures ..... **viii**

1 BACKGROUND **1**

1.1 Gas turbine performance 1

1.2 Progress in combustor technology 4

1.3 Film cooling 4

1.4 Endwall cooling requirements 8

1.5 Research objective 8

1.6 Classical turbine secondary flow picture 9

1.7 Secondary flow reduction methods 12

1.8 Effect of combustor on vane secondary flows 13

1.9 Effect of endwall coolant injection on secondary flows 16

1.10 Contribution of this study 19

2 EXPERIMENTAL AND COMPUTATIONAL METHODS **20**

2.1 Super Scale Platform Cooling Facility (SSPCF) 20

2.1.1 Flow conditioning 23

2.1.2 Instrumentation 24

2.1.3 Vanes 25
2.1.4 Combustor simulator 28
2.1.5 Test section 32
2.1.6 Coolant feed 33
2.1.7 IR thermography 35
2.1.8 Cascade periodicity 39
2.2 CFD models 41
2.3 Turbulence modelling theory 46
3 PHYSICS OF ENDWALL FLOWS 48
3.1 Planar Cascade Study 48
3.1.1 Low coolant flow rate 49
3.1.2 Effect of inlet boundary layer 51
3.1.3 Mitigation of secondary flows at higher coolant flow rates 52
3.1.4 Effect of hole inclination angle 56
3.1.5 Effect of inlet turbulence level 62
3.1.6 Effect of coolant injection on vane pressure field 64
3.2 Experimental validation 66
3.2.1 Planar cascade vs. SSPCF cascade geometry 66
3.2.2 Casing: CFD and experimental validation 67
3.2.3 Hub: results and discussion 75
3.3 Further observations 78

3.3.1 Effect of combustor simulator 78
3.3.2 Effect of vane potential field 80
3.3.3 Effect of low coolant mass flux ratio 82
3.3.4 Effect of endwall contraction 83
3.3.5 Effect of reducing cooling hole diameters 84
3.4 Conclusions 85
3.5 Engine conditions vs. SSPCF conditions 86
3.6 Usefulness of conclusions in engine design 90
4 OPTIMIZATION OF ENDWALL FILM COOLING SYSTEMS 92
4.1 Optimization goals 92
4.2 Passive-scalar tracking method 93
4.2.1 Theory 93
4.2.2 Implementation in FLUENT and validation 96
4.3 Application to cooling system optimization 98
4.3.1 Compensating for cross-passage flow 98
4.3.2 Improving cooling of the trailing endwall 104
4.3.3 Reducing coolant consumption 110
4.4 Summary 117
5 OPTIMIZATION OF AN ENGINE HP NGV ENDWALL COOLING SYSTEM 118
5.1 Uncooled NGV 121
5.2 Baseline RIDN/RODN cooling system 123

5.3 Design of optimized cooling system 124

5.4 Robustness to combustor outlet profile 130

5.5 Summary 132

6 CONCLUSIONS 133

6.1 Interaction of endwall coolant with vane secondary flows 133

6.2 Validation of CFD results with experiment 134

6.3 Improved design philosophy and methods for endwall film cooling systems 134

6.4 Application to engine development program 134

7 SUGGESTIONS FOR FURTHER RESEARCH 135

7.1.1 Experimental studies 135

7.1.2 CFD studies 136

REFERENCES 138

Appendix 145

A. Measurement uncertainty estimates 145

B. CFD optimization loop 155

C. CO_2 coolant injection system 159

D. Passive scalar tracking method: correction for specific heat variation 161

E. Combustor momentum flux ratio matching 163

Nomenclature

Abbreviations:

BC	Boundary Condition
CFD	Computational Fluid Dynamics
DAQ	Data Acquisition
IR	Infrared
LE	Leading Edge
NGV	Nozzle Guide Vane
PR	Pressure Ratio
PS	Pressure Side
RIDN	Rear Inner Discharge Nozzle (hub double row cooling system)
RODN	Rear Outer Discharge Nozzle (casing double row cooling system)
RQL	Rich-burn Quick-quench Lean-burn
SS	Suction Side
SSPCF	Super Scale Platform Cooling Facility
TE	Trailing Edge
TR	Temperature Ratio

Symbols:

A	Area
α	Hole inclination
BR	Blowing ratio
C_{ax}	Axial chord length
C_D	Discharge coefficient
c_p	Specific heat
C_P	Pressure coefficient
D	Hole diameter
DR	Density ratio
ε	Turbulence dissipation rate
η_{eff}	Adiabatic effectiveness

I	Momentum flux ratio
k	Turbulence kinetic energy
M	Mach number
υ_T	Eddy viscosity
P	Pressure
$\hat{P}$	Non-dimensional total pressure, $(P_0 - P_{out})/(P_{0,in} - P_{out})$
ϕ_i	concentration of scalar 'i'
Re	Reynolds number
S	Vane span
ψ	Non-dimensional total temperature
T	Temperature
Γ	Scalar diffusivity
Tu	Turbulence intensity
u	Velocity
V	Vane pitch

Subscripts:

0	Stagnation conditions
3	compressor outlet conditions
4	combustor outlet conditions
∞	Freestream conditions
aw	Adiabatic wall conditions
c	Coolant conditions
f	Film coolant conditions
j	Jet conditions
m	Mixed conditions
max	Maximum
min	Minimum
r	Recovery conditions
w	Wall conditions

Tables and Figures

Table 2-1: SSPCF flow conditions 21

Table 2-2: Coolant mass flow metering 35

Table 2-3: CFD boundary conditions 42

Table 4-1: Summary of optimization studies 117

Table 5-1: Engine geometry and flow boundary conditions 120

Figure 1-1: Gas turbine performance (based on analytical expressions from Hill and Peterson (1992) 2

Figure 1-2: NGV cooling system (adapted from The Jet Engine, 1996) 3

Figure 1-3: Kidney vortices in jet core and horseshoe vortex around cooling jet (adapted from Haas et. al., 1991) 7

Figure 1-4: Classical secondary flow model 10

Figure 1-5: (a) Cross-passage flow mechanism; (b) Velocity vectors on vane stagnation plane (adapted from Simpson, 2001) 11

Figure 1-6: Design of an endwall cooling system accounting for classical secondary flows (adapted from Friedrichs, 1997b) 12

Figure 1-7: Velocity measurements downstream of combustor dilution holes (adapted from Barringer et. al., 2002) 15

Figure 1-8: (a) Streamlines at vane stagnation plane (from Takeishi, 2013); (b) Endwall η_{eff} plots from Benton et. al. 2005 18

Figure 2-1: SSPCF schematic 22

Figure 2-2: IR thermograph of mesh heater outlet 24

Figure 2-3: Engine and SSPCF vane geometries 25

Figure 2-4: (a) Vane surface pressure tap locations; (b) C_P distribution 27

Figure 2-5: Vane geometric throat location 28
Figure 2-6: Combustor simulator schematic 30
Figure 2-7: SSPCF test section 32
Figure 2-8: RIDN/RODN cooling system: geometrical details at SSPCF scale 33
Figure 2-9: Critical-flow venturi nozzle (Throat diameter = 9 mm) 34
Figure 2-10: IR calibration procedure 36
Figure 2-11: IR camera views 37
Figure 2-12: Test section viewed from vane outlet 39
Figure 2-13: Tailboard angle setting 40
Figure 2-14: CFD model 42
Figure 2-15: Mesh independence study 44
Figure 2-16: Endwall mesh resolution 45
Figure 3-1: Planar cascade geometry: (a) Vane cross-section; (b) CFD domain 48
Figure 3-2: η_{eff} contours (CFD) for $\dot{m}_c/\dot{m}_\infty = 1\%$: (a) Plan view; (b) Isometric view 49
Figure 3-3: (a) Surface streamlines coloured by η_{eff}; (b) Freestream and coolant streamlines 50
Figure 3-4: (a) $1/7^{th}$ power law velocity profile; η_{eff} contours with: (b) Constant inlet velocity; (c) Power-law velocity profile 51
Figure 3-5: Effect of coolant injection on secondary flows 52
Figure 3-6: Total pressure profile: (a) Averaging plane location; (b) Pitchwise averaged total pressure profiles 53
Figure 3-7: Oilflow streamlines on vane surface 54
Figure 3-8: Coolant streamlines 56
Figure 3-9: Effect of hole inclination ($\dot{m}_c/\dot{m}_\infty$ = 2%) 57
Figure 3-10: Effect of hole inclination: pitchwise averaged $\hat{P}$ plots 58

Figure 3-11: Effect of hole inclination ($\dot{m}_c/\dot{m}_\infty$ = 3%, 6%) 59

Figure 3-12: Oilflow visualization: $\dot{m}_c/\dot{m}_\infty$ = 3% 60

Figure 3-13: Oilflow visualization: $\dot{m}_c/\dot{m}_\infty$ = 6% 61

Figure 3-14: Effect of turbulence intensity: η_{eff} contours 63

Figure 3-15: Effect of turbulence intensity: vane inlet total pressure profiles 64

Figure 3-16: Effect of coolant injection on vane pressure field 65

Figure 3-17: Vane pressure field at 10% span: Baseline vs. Low inclination ($\dot{m}_c/\dot{m}_\infty$ = 6%) 66

Figure 3-18: Solid model of SSPCF cascade and cooling system..... 67

Figure 3-19: Experimentally measured η_{eff} on casing: (a) Cascade front view, (b) Cascade rear view; (c) CFD η_{eff} map on casing 68

Figure 3-20: $\dot{m}_c/\dot{m}_\infty$ = 1%: (a) CFD predicted η_{eff}; (b) Oilflow streamlines (CFD) coloured by η_{eff}; (c) LE flow structure; Experimentally measured η_{eff} on: (d) Leading endwall, (e) Trailing endwall..... 70

Figure 3-21: $\dot{m}_c/\dot{m}_\infty$ = 4%: (a) CFD predicted η_{eff}; (b) Oilflow streamlines (CFD) coloured by η_{eff}; (c) LE flow structure; Experimentally measured η_{eff} on: (d) Leading endwall, (e) Trailing endwall..... 70

Figure 3-22: $\dot{m}_c/\dot{m}_\infty$ = 9%: (a) CFD predicted η_{eff}; (b) Oilflow streamlines (CFD) coloured by η_{eff}; (c) LE flow structure; Experimentally measured η_{eff} on: (d) Leading endwall, (e) Trailing endwall..... 70

Figure 3-23: (a) Location of vane inlet plane; (b) $\hat{P}$ profiles at vane inlet plane 71

Figure 3-24: Upwash and downwash on vane: (a) Near-wall streamlines in SSPCF, $\dot{m}_c/\dot{m}_\infty$ = 4%; (b) Surface streamlines on planar cascade vane, $\dot{m}_c/\dot{m}_\infty$ = 6% 72

Figure 3-25: η_{eff} data for $\dot{m}_c/\dot{m}_\infty$ = 1%: (a) CFD predicted, (b) Experimentally measured; η_{eff} data for $\dot{m}_c/\dot{m}_\infty$ = 4%: (a) CFD predicted, (b) Experimentally measured 73

Figure 3-26: CFD predictions for $\dot{m}_c/\dot{m}_\infty$ = 9% 74

Figure 3-27: Comparison of η_{eff} at vane outlet line 75

Figure 3-28: Experimentally measured η_{eff} maps on the hub endwall 76

Figure 3-29: Effect of combustor simulator 79

Figure 3-30: Effect of vane potential field for $\dot{m}_c/\dot{m}_\infty$ = 4% 81

Figure 3-31: Effect of coolant injection at low mass flux ratio 83

Figure 3-32: Effect of contouring: total pressure profile 83

Figure 3-33: Effect of reducing diameters: (a) Total pressure profiles; Oilflow streamlines for: (b) RODN baseline, $\dot{m}_c/\dot{m}_\infty$ = 4%; (c) RODN: $D/4$ ($P_{0,c}$ matched) 85

Figure 3-34: Mismatches in C_P at engine realistic conditions 87

Figure 4-1: Control volume analysis for scalar concentration 94

Figure 4-2: Passive-scalar tracking method implementation 97

Figure 4-3: Passive-scalar tracking method: validation 97

Figure 4-4: Scalar tracking method applied to RIDN SSPCF model 99

Figure 4-5: Hole diameter distribution 101

Figure 4-6: Optimization using scalar tracking method 103

Figure 4-7: Hub cooling system optimization 105

Figure 4-8: Config2 design 107

Figure 4-9: Passage hole placement for minimal aerodynamic loss 108

Figure 4-10: Config3 design 109

Figure 4-11: Optimization procedure: Config4 design 111

Figure 4-12: Optimization of Config4 design using scalar tracking method 113

Figure 4-13: Config5 design 115

Figure 4-14: Coolant upwash on vane 116
Figure 5-1: (a) Vane pair solid model; CFD model: (b) Front view, (c) Side view 119
Figure 5-2: Inlet turbulence profiles 121
Figure 5-3: (a) Inlet ψ profile; (b) Contours of ψ on vane pair 122
Figure 5-4: Contours of ψ on: (a) Uncooled casing endwall; (b) Uncooled hub endwall 123
Figure 5-5: Contours of ψ with baseline cooling system: (a) Casing; (b) Hub 124
Figure 5-6: Placing cooling holes on the endwall: design principles 125
Figure 5-7: Contours of ψ on casing (open passage) with: (a) Baseline (RODN) cooling system, (b) Optimized cooling system; (c) Comparison of ψ at vane outlet line 126
Figure 5-8: Contours of ψ on hub (open passage) with: (a) Baseline (RIDN) cooling system, (b) Optimized cooling system; (c) Comparison of ψ at vane outlet line 127
Figure 5-9: Circumferentially averaged temperatures at the vane outlet 128
Figure 5-10: Cooling of the closed passage casing 128
Figure 5-11: Reduced-flow design: ψ contours on (a) casing, (b) hub; comparison on ψ on vane outlet line on (c) casing, (d) hub 130
Figure 5-12: Effect of clocking combustor outlet profile 131
Figure 7-1: Converging hole geometry 136
Figure A-1: Thermocouple bias estimate 149
Figure A-2: IR calibration curves and uncertainties caused by curve fit 151
Figure A-3: Thermocouple bias estimate $\Delta(T_\infty - T_c)$ 152
Figure A-4: Definitions of terms P_{dil}, A_{th}, u_{out},u_j, $u_{c,out}$ 153
Figure B-1: SSPCF and engine CFD template domains 155
Figure B-2: Meshing automation problems using single passage and two passage CFD domains 156
Figure B-3: Untrimmed film cooling hole geometries 157

Figure B-4: Hole inlet patch surfaces 158

Figure C-1: CO_2 coolant injection system schematic 160

Figure D-1: Control volume analysis for scalar concentration 161

Figure E-1: Definitions of terms P_{dil}, A_{th}, u_{out},u_j, $u_{c,out}$ 163

1 BACKGROUND

1.1 Gas turbine performance

The gas turbine industry is a competitive one, with few players. Barriers to entry are high because of the investment required to develop advanced technology. Manufacturers maintain a competitive advantage by improving the performance of their product through research and development.

The gas turbine compresses a stream of air to high pressures, adds heat to the stream in a combustor and expands it through a turbine and a nozzle, generating shaft power or thrust. Two performance parameters of particular interest to operators are the thermal efficiency ($\eta_{th} = \dot{W}/\dot{Q}$) and the specific power ($\dot{W}/\dot{m}$). The thermal efficiency is the ratio of useful work ($\dot{W}$) obtained, to heat supplied in the combustor ($\dot{Q}$). Higher thermal efficiency results in lower fuel consumption for stationary gas turbines, and higher range and payload in aircraft applications. Higher specific power results in an engine of reduced size and weight. This is particularly attractive in aircraft applications.

Thermal efficiency and specific power are strongly dependent on two variables: the compressor pressure ratio (PR) and the combustor temperature ratio (TR). Also, inefficiencies in individual components can degrade performance. Isentropic efficiencies are used to benchmark compressor and turbine performance. Isentropic efficiency, η_{is}, compares power consumption/output at isentropic and non-ideal conditions. The power output of a gas turbine is the difference of two large quantities: the turbine power output and the compressor power consumption. A small decrease in efficiency of either the turbine or the compressor results in a large percentage drop in gas turbine output.

Figure 1-1 shows the effect of PR and TR for a compressor η_{is} of 0.90 and turbine η_{is} of 0.95. Increasing PR results in improved η_{th}, until the higher compressor work required degrades efficiency (Figure 1-1 (a)). Achieving higher compressor PR while maintaining high η_{is} is the object of active research programs (Biollo and Benini, 2013).

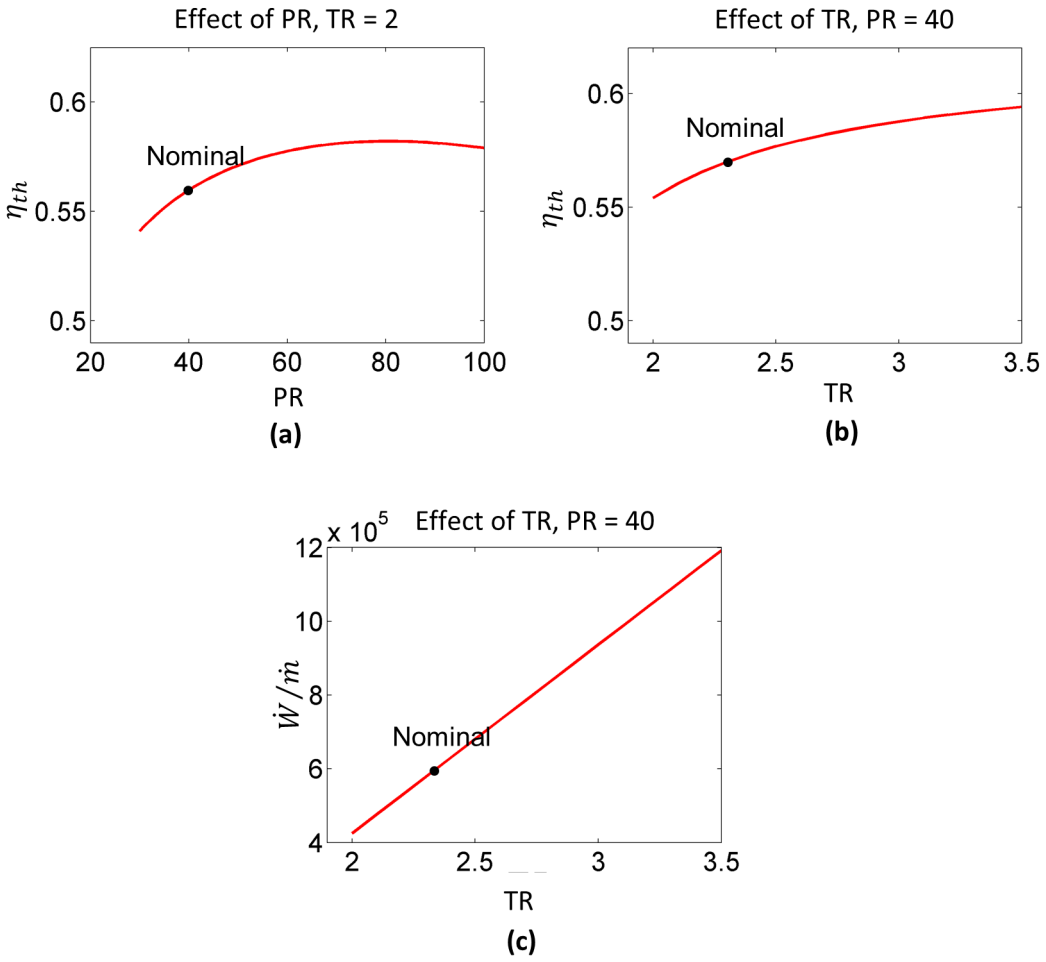


Figure 1-1: Gas turbine performance (based on analytical expressions from Hill and Peterson (1992)

Increasing TR results in improved η_{th} (Figure 1-1 (b)) and significant improvements in $\dot{W}/\dot{m}$ (Figure 1-1 (c)). The high pressure turbine expands combustor gases through a stationary nozzle guide vane (NGV) and a turbine rotor. Higher TR exposes the turbine to higher turbine entry temperatures (TET). The use of super-alloy materials, single crystal casting and thermal barrier coatings have allowed considerable increases in permissible TET.

However, high pressure turbine components are run at temperatures well above the melting point of their materials (The Jet Engine, 1996). This is made possible by cooling components using air from the compressor.

Figure 1-2 shows a schematic for an NGV cooling system. Heat is removed from the metal walls by passing cooling air through passages inside the component. This is called internal convective cooling. Heat transfer is enhanced by the use of ribs and pin fins (Han et. al., 2013). The coolant is then released through holes and slots to form a protective film over the blade. This is called external film cooling.

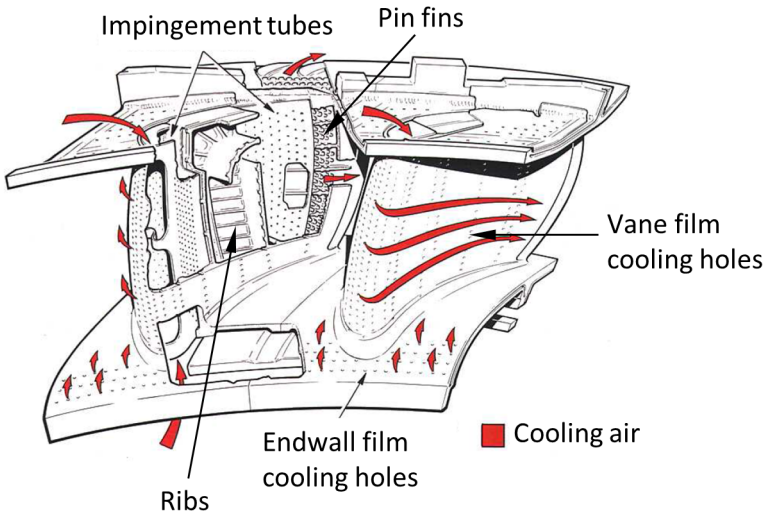


Figure 1-2: NGV cooling system (adapted from The Jet Engine, 1996)

The design of cooling systems needs to be conservative, yet accurate. The life of critical hot path components can be halved by a 30 K increase in TET (Han et. al., 2013). However, reduced consumption of coolant is desirable. As will be described in Section 4.3.2, the injection of coolant, particularly into high Mach number streams, is associated with high aerodynamic losses.

The turbine rotor is exposed to a lower relative stagnation temperature than the NGV because of rotation. However, the thermal design of the rotor is more conservative, since damage can result in release of the turbine rotor from the engine.

1.2 Progress in combustor technology

While higher TETs are desired, combustion at higher temperatures results in the formation of NOx (Lefebvre, 1999). NOx are a family of pollutants that result in smog and acid rain. There is significant regulatory pressure to reduce NOx emissions (Nitrogen Oxides, 1999). Current combustor designs use a Rich-burn Quick-quench Lean-burn (RQL) architecture. This reduces NOx production by burning fuel at rich conditions, quenching rapidly using dilution jets, and then completing combustion at lean conditions. The turbine rotor root and tip are critical regions: the root suffers high centrifugal stresses, while the tip experiences high heat transfer rates (Bunker, 2001). Dilution flow is used to tailor combustor outlet temperature profiles, to ensure low temperatures at the root and tip.

To achieve further reduction in NOx emissions, future engines are likely to use a lean pre-mixed combustor architecture (Bender, 2006). These combustors maintain lean burn throughout, with most of the combustor flow introduced through the central swirlers. Dilution jets are not used. Lean burn combustors thus have more uniform outlet temperature profiles. Temperatures at the endwalls will be significantly higher than with RQL combustors.

1.3 Film cooling

Film cooling involves releasing coolant to form a protective film over a surface. The wall temperature, T_w, needs to be predicted accurately for component life estimation. The rate of heat transfer to a wall is expressed as:

$$q_0 = h_0(T_w - T_d), \tag{1-1}$$

where T_d is a suitably chosen driving temperature and h_0 is a heat transfer coefficient. The driving temperature for a flat plate placed in a flow is the gas recovery temperature, T_r:

$$T_r = T_\infty + r\frac{u_\infty^2}{2c_p}, \qquad r = \mathrm{Pr}^{1/3}, \text{ for turbulent flow} \tag{1-2}$$

where T_∞ is the freestream static temperature, u_∞ is the freestream velocity, Pr is the Prandtl number, and c_p is the specific heat capacity. The recovery factor, $r = \mathrm{Pr}^{1/3}$, is around 0.9 at typical hot gas path temperatures. The simplification $T_r \approx T_0$, will be adopted to simplify analysis in several parts of this work (Section 4.2, Section 5.1). T_r is around 30 K less than the total temperature, T_0 $\left(= T_\infty + \frac{u_\infty^2}{2c_p}\right)$, at M = 1. The difference between T_r and T_0 will need to be adjusted before use in thermal design calculations.

The film cooling problem involves three temperatures: T_r, T_w and T_c, the temperature of the coolant stream. Jones (1991) showed that heat transfer to a film cooled wall can be expressed as:

$$q_f = h_f(T_{aw} - T_w), \tag{1-3}$$

where h_f is the heat transfer coefficient with film cooling present and T_{aw} is the temperature of an adiabatic wall with the same film cooling flow.

The net heat transfer rate reduction (Δq) quantifies the benefit of film cooling:

$$\Delta q = 1 - \frac{q_f}{q_0} = 1 - \frac{h_f(T_{aw} - T_w)}{h_0(T_\infty - T_w)} = 1 - \frac{h_f}{h_0}\left(1 - \frac{\eta_{eff}}{\phi}\right), \tag{1-4}$$

where adiabatic effectiveness, η_{eff}, and metal effectiveness ϕ are:

$$\eta_{eff} = \frac{T_\infty - T_{aw}}{T_\infty - T_c}, \phi = \frac{T_\infty - T_w}{T_\infty - T_c} \tag{1-5}$$

The values of h_f are generally higher than h_0 because of increased turbulence and mixing caused by coolant injection. Values of h_f/h_0 are typically obtained using an

experimental setup with isothermal film cooling jets ($T_c = T_\infty$) and uniform wall heat flux boundary condition set by a resistive heater. Wall temperature is measured to obtain heat transfer coefficient. (Bogard, 2006). Ammari et. al. (1990) and Saumweber and Schulz (2004) measured h_f/h_0 on cooled walls. At low blowing ratios, h_f/h_0 returns to unity 30 hole diameters downstream of injection. The disruption to the boundary layer caused by high blowing rates results in heat transfer augmentation far downstream. However values of h_f/h_0 are less than 1.25 for distances greater than 30 hole diameters.

Values of η_{eff} are typically obtained by measuring temperatures on a low-conductivity wall, with cooled or heated film flow.

η_{eff} and h_f/h_0 are governed by the following non-dimensional variables:

$$DR = \frac{\rho_c}{\rho_\infty}, VR = \frac{u_c}{u_\infty}, BR = \frac{\rho_c u_c}{\rho_\infty u_\infty}, I = \frac{\rho_c u_c^2}{\rho_\infty u_\infty^2}, \kappa = \frac{{c_p}_c}{{c_p}_\infty} \tag{1-6}$$

where ρ, u, c_p are density, velocity and specific heat, and subscripts c and ∞ refer to coolant and freestream conditions.

Flow from a cooling hole can either stay attached to the downstream surface, or lift-off and reattach, or lift-off completely. Sinha et. al. (1991) showed that the momentum flux ratio (I) determines jet lift-off. Lift-off is more likely at higher momentum flux ratio. For attached jets, the blowing ratio (BR) serves as a local mass flux ratio and determines the concentration of coolant at the wall. Velocity ratio (VR) determines the shear at the cooling jet/mainstream interface. The shear results in turbulence generation and mixing of cooling jets. At engine conditions, a density ratio (DR) of around 2 results from the difference in coolant and freestream temperatures ($T_c \sim 900$ K and $T_\infty \sim 1800$ K). Since most experiments in literature are conducted with $T_c/T_\infty \approx 1$, DR is matched by using a foreign gas of

different density as coolant. Specific heat (c_p) varies with temperature: $\kappa = c_{p_c}/c_{p_\infty} = 0.9$ for $T_c \sim 900$ K and $T_\infty \sim 1800$ K.

For the same coolant consumption, continuous slots provide better cooling performance than discrete cooling holes. At high momentum flux ratios, jets emerging from cooling holes can lift-off from the metal surface, leaving downstream regions unprotected. Kidney vortices form in the jet core and horseshoe vortices can form around the periphery of the jets (Haas et. al., 1991, see Figure 1-3). These vortices enhance mixing with the freestream leading to more rapid decay of η_{eff}. Also, jets emerging from cooling holes are exposed to a greater freestream area, leading to greater mixing. Oke et. al. (2000) compared the cooling performance of a double row of film cooling holes with the cooling performance of a continuous slot. The coolant mass flux was kept constant in both cases. η_{eff} values are 20%-30% higher downstream of the slot. Despite its benefits, slot cooling is generally not possible in turbine applications because of mechanical limitations. However, a double-row of cooling holes approximates a slot when hole rows are sufficiently close to each other (Saumweber and Schulz, 2004).

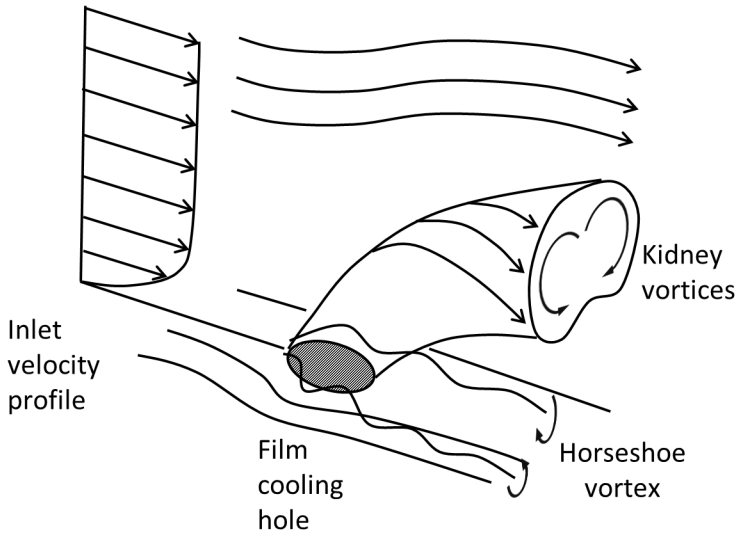


Figure 1-3: Kidney vortices in jet core and horseshoe vortex around cooling jet (adapted from Haas et. al., 1991)

Harrison and Bogard (2008) performed CFD simulations to compare predictions of heat transfer made using Equation (1-3), $q_f = h_f(T_{aw} - T_w)$, with predictions made using a fully coupled conjugate heat-transfer CFD simulation. A fixed coolant side heat transfer rate was assumed in both cases. To match the experimental procedure commonly used in literature, the quantities in Equation (1-3) were predicted using two CFD simulations: one using adiabatic wall BCs to predict T_{aw}, and another with constant heat flux wall BCs to predict h_f. The wall temperature T_w was predicted using a solid conduction simulation, using q_f as the external heat transfer boundary condition. The authors show that using T_{aw} as a driving temperature generally predicts q_f accurately, except in regions of jet lift-off. In these regions, q_f may be inaccurate by up to 300% when compared with the fully-coupled conjugate heat transfer simulation. However, the wall temperature T_w is predicted to within 10% accuracy. The authors also comment on the underlying assumption that thermal boundary layer thickness is much smaller than cooling jet thickness; this is generally true in gas turbine flows. The use of T_{aw} as a driving temperature is thus justified.

1.4 Endwall cooling requirements

The trailing endwall experiences high heat transfer rates. This is because of high Mach numbers and thin boundary layers in the region. This is shown in measurements by Nicklas (2001). The vane wake is of particular concern: high turbulence levels and mixing occurs in this region. The trailing endwall is difficult to cool: cooling films released upstream decay in effectiveness before they reach the rear; injecting coolant locally results in high aerodynamic losses because of high freestream M.

1.5 Research objective

This work will study means for improving film cooling of the NGV and turbine rotor endwalls. These improvements will permit future engines to run at a higher TET and use lean

combustors. In particular, the focus will be on cooling the rear vane endwall because of high heat transfer rates in this region. Also, lowering endwall temperatures here will result in cooler rotor endwalls downstream. Endwall film cooling will need to be improved without incurring large aerodynamic penalties caused by coolant injection.

1.6 Classical turbine secondary flow picture

Flow through a turbine vane is generally well behaved because of strong acceleration and a favourable pressure gradient. However, the near-wall region has been described by several authors as dominated by secondary flows. Smoke and oil flow visualization has been used to identify secondary flow features in linear cascade studies. Such studies are the basis of secondary flow models proposed by Langston (1977), Sieverding and Van den Bosch (1985), Sharma and Butler (1987), Wang and Olson (1997).

Figure 1-4 summarizes important features of the models. The endwall boundary layer separates upstream of a vane cascade. This is shown to roll-up into vortex systems of varying complexity. In common with all models are the following features:

- *Horseshoe vortex system*: this is formed upstream of the vanes and is composed of a pressure side and a suction side leg. The two legs interact in the downstream passage to form the passage vortex.
- *Boundary layer separation*: A fresh boundary layer is formed downstream of the horseshoe vortex lift-off line.
- *Cross passage flow*: The cross-passage pressure gradient, acting from the vane PS to SS, drives the low-velocity flow in the boundary layer further towards the SS.

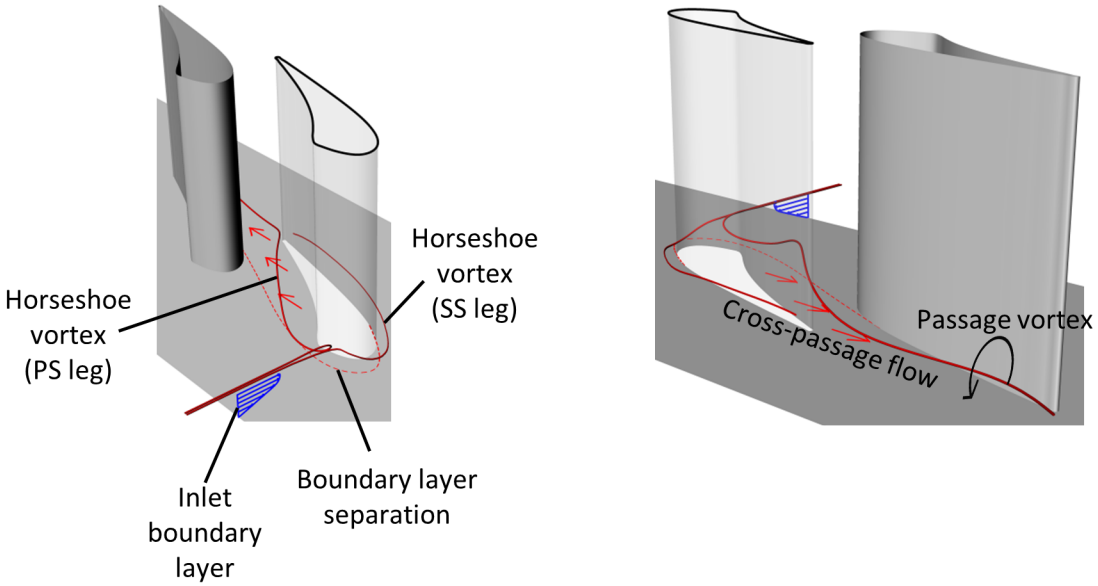


Figure 1-4: Classical secondary flow model

Hawthorne (1951) attributed the formation of secondary flows to the spanwise gradient of vane inlet total pressure. The total pressure gradient is converted to a static pressure gradient when flow stagnates upstream of the vane. This pressure gradient imparts a vortex motion to the flow.

Lakshminarayana (1996) described the formation of cross-passage flows near the endwall. In Figure 1-5 (a), flow streamline A lies outside the boundary layer while B is near the endwall. Static pressure is roughly constant through the thickness of a boundary layer (Schlichting and Gersten, 2000). Thus streamline A and B are subjected to the same cross-passage pressure gradient. The radial equilibrium equation is given below:

$$\frac{\partial p}{\partial n} = \rho_A \frac{V_A^2}{R_A} = \rho_B \frac{V_B^2}{R_B} \tag{1-7}$$

Since $V_A > V_B$, this implies $R_A > R_B$. i.e. streamline B has a smaller radius of curvature. This drives near-wall flow further towards the SS, resulting in a cross-passage flow.

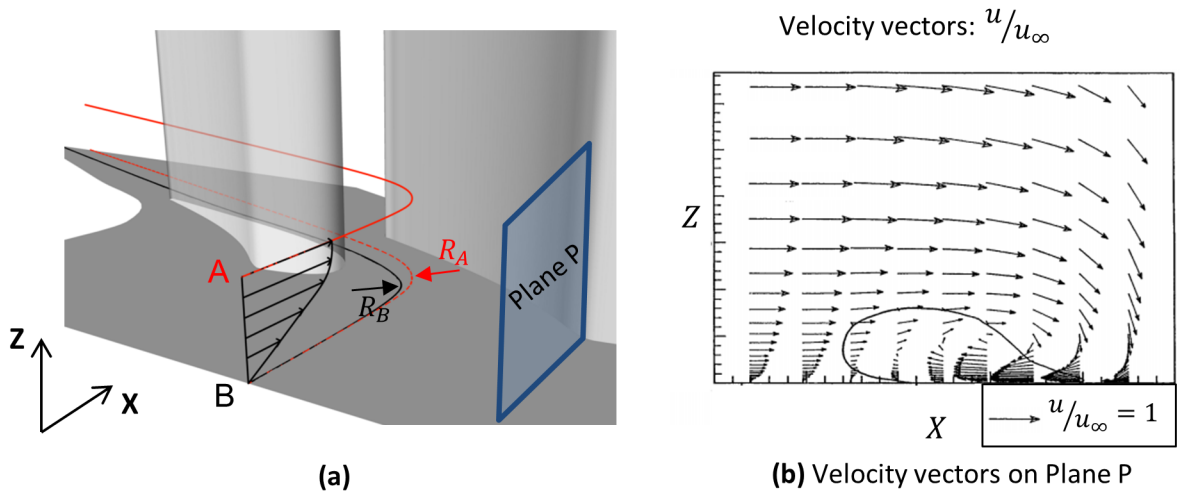
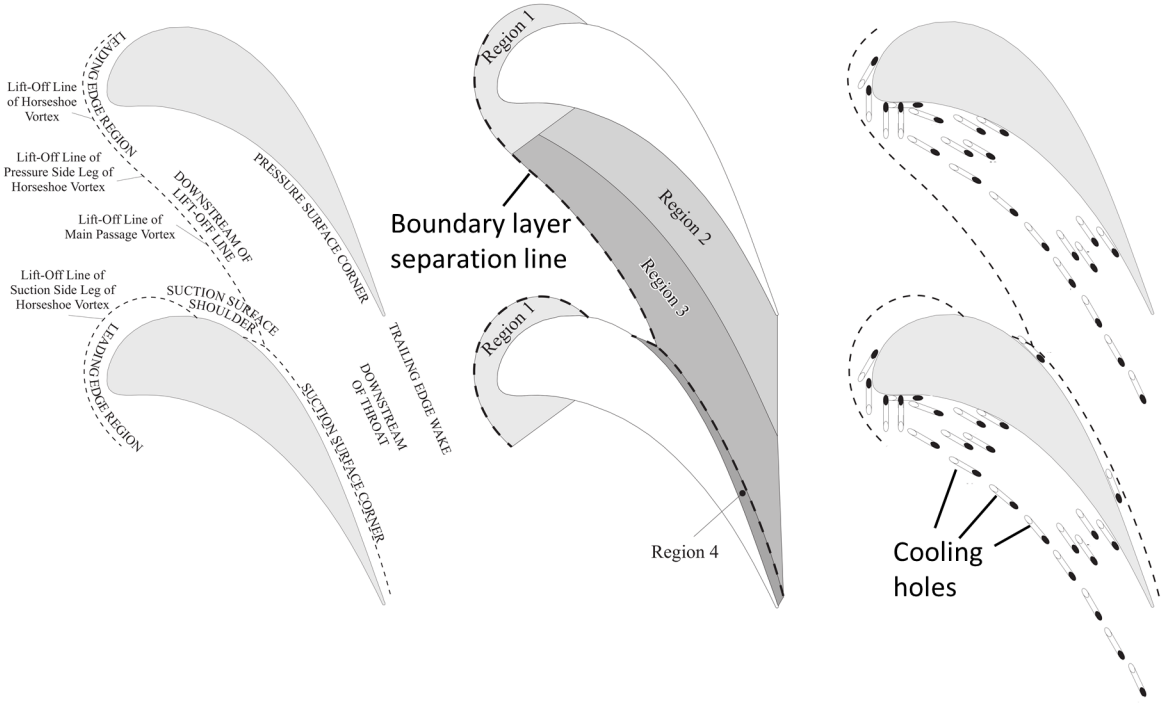


Figure 1-5: (a) Cross-passage flow mechanism; (b) Velocity vectors on vane stagnation plane (adapted from Simpson, 2001)

Simpson (2001) reviewed 'junction flows' that occur at the intersection of cylinders and walls. Junction flows are a model for wing-body interaction in airplanes and submarines, river-bridge pier flows, and, indeed, turbomachinery endwall flows. Figure 1-5 (b) shows normalized velocity vectors on the stagnation plane of a vane. The approaching boundary layer is decelerated by the adverse pressure gradient imposed by the vane. The boundary layer separates upstream and then rolls-up to form the horseshoe vortex.

These secondary flow features have been recognized as significant in the near-wall flow; models based on these have informed the design of endwall cooling systems. An early study by Graziani et. al. (1980) showed how the formation of a fresh boundary layer downstream of the horseshoe vortex lift-off line results in high heat transfer rates. Friedrichs et. al. (1999) noted that film coolant released on the endwall upstream of the lift-off line is swept into the freestream by the horseshoe vortex. They identify potential regions of high heat transfer (Figure 1-6 (a)), divide the endwall into different regions affected by secondary flows (Figure 1-6 (b)), and distribute cooling holes according to local need (Figure 1-6 (c)).



(a) Endwall boundary layer separation line and potential regions of high heat transfer

(b) Endwall divided into regions affected by secondary flows

(c) Cooling hole pattern

Figure 1-6: Design of an endwall cooling system accounting for classical secondary flows (adapted from Friedrichs, 1997b)

Secondary flows are also considered detrimental to turbine performance. They have been shown to contribute up to 30% of the aerodynamic losses in a cascade (Sharma and Butler, 1987, Denton, 1993).

1.7 Secondary flow reduction methods

Various methods have been proposed to reduce secondary flows.

A contraction of the endwall is known to be beneficial. Boletis (1985) compared traverse measurements on two annular cascades, one with cylindrical endwalls and another with an axisymmetric contraction on one endwall. The vane aerodynamic loading in the latter case was shifted rearwards. This reduced cross-passage flows. The contraction introduces a pressure gradient that drives flow radially outward. This counteracts the radial pressure

gradient introduced by turning of the flow by the vane. The net effect is to reduce radial migration of the boundary layer. The reduced secondary flows in the passage resulted in lower aerodynamic losses. Barigozzi et. al. (2010) showed that an axisymmetric contraction can reduce aerodynamic losses significantly. Flow acceleration leads to a thinner boundary layer on the converging endwall.

Praisner et. al. (2007) demonstrated the application of non-axisymmetric contouring to the endwalls of high-lift LP turbines. The optimization goal was to reduce total pressure losses. A convex curvature on the endwall PS locally accelerates the flow, reducing static pressure. A concave curvature on the endwall SS locally decelerates the flow, increasing static pressure. Measurements by Knezevici et. al. (2010) showed reduced cross-passage flows and reduced aerodynamic losses for such a contoured endwall. Lynch et. al. (2011) demonstrated that the tendency for film coolant to be swept from the endwall PS to SS by secondary flows is reduced on endwalls contoured in this manner.

The use of fillets at the vane-endwall junction is known to reduce secondary flows. Devenport et. al. (1992) showed that the use of a well-designed fillet can eliminate endwall boundary layer separation. Static pressure measurements on the endwall and fillet show a considerable reduction in the adverse pressure gradient. This reduction prevents boundary layer separation. Zess and Thole (2002) described a vane fillet design that eliminated the leading edge horseshoe vortex and significantly reduced passage secondary flows. The incoming boundary layer was shown to accelerate as it travels over the fillet, decreasing secondary flow formation.

1.8 Effect of combustor on vane secondary flows

Classical secondary flow models were considered an accurate picture of turbine flows in reviews by Sieverding (1985), Chyu (2001), Langston (2001). The models were proposed

on the basis of smoke and oil-flow visualization in linear cascades, with low freestream turbulence intensities. Of particular importance is the turbulent boundary layer inlet condition in all cases. Recent studies question if this inlet condition is an accurate description of engine flows.

The freestream turbulence levels at the outlet of RQL combustors are high. This is because of vigorous mixing of dilution jets (Cha et. al., 2012). Barringer et. al. (2002) measured flow downstream of an engine realistic combustor simulator incorporating dilution and liner flow. High turbulence levels (Tu) of 15% – 18% were observed, with turbulence length scale on the order of the dilution hole diameter. The total pressure profile at the vane inlet plane did not resemble a turbulent boundary layer. In the near-wall region, peaks in velocity were observed downstream of combustor liner coolant injection (see Figure 1-7). These peaks corresponded to the location of coolant jets from different hole rows. Dilution jets increased total pressure in the core of the combustor.

Weaker secondary flows have been reported at high freestream Tu (Thole et. al., 2002, Narzary et. al., 2009). This is because of enhanced momentum transport from the freestream which results in boundary layers with higher momentum.

Freestream turbulence affects film cooling effectiveness significantly. High freestream Tu results in increased mixing, which causes accelerated decay of cooling films (Mayhew et. al., 2003). Saumweber et. al. (2003) showed that the impact of turbulence length scale on η_{eff} is small in comparison to the effect of Tu.

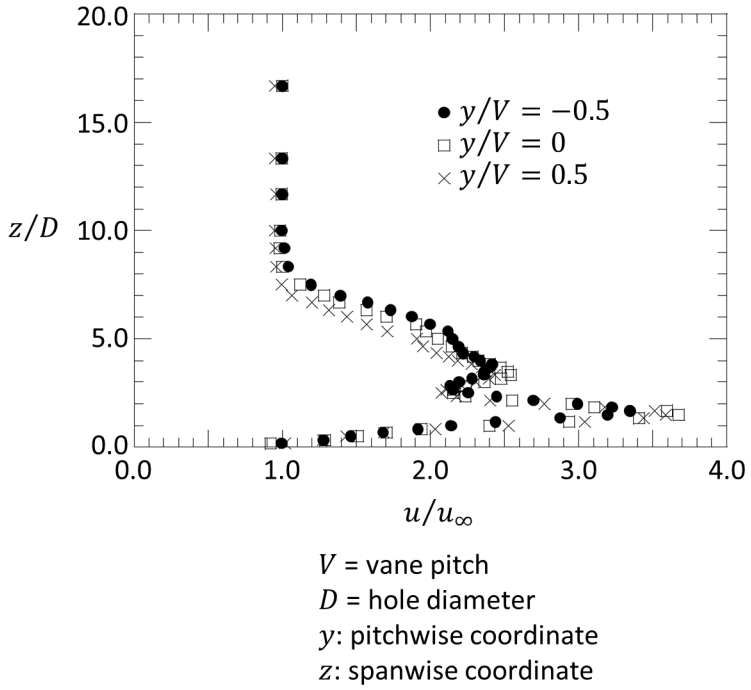


Figure 1-7: Velocity measurements downstream of combustor dilution holes (adapted from Barringer et. al., 2002)

Colban et. al. (2003a and 2003b) studied the influence of these combustor representative inlet conditions on flow in a vane cascade. New secondary flow patterns were seen to result from the peak in total pressure introduced by combustor liner flow injection. However, a backward facing step at the interface of combustor and cascade resulted in low total pressure near the endwall. Thus, secondary flow patterns similar to the classical picture were observed at the endwall.

Hermanson and Thole (2000b) highlighted the importance of the vane inlet total pressure profile in determining secondary flows. CFD studies were conducted with various inlet boundary conditions. A thinner inlet boundary layer was shown to result in reduced secondary flows. Secondary flows were absent with a constant inlet total pressure profile. Considering uniform inlet velocity and an inlet temperature profile with a peak at midspan, secondary flow vortices were observed with a sense of rotation inverted from the classical horseshoe vortex. In this case, the total pressure profile is inverted, with higher total pressure at the endwall.

1.9 Effect of endwall coolant injection on secondary flows

Injecting high momentum flow into the boundary layer is known to suppress separation. The boundary layer is energized by the injection of momentum and is able to resist an adverse pressure gradient better.

Sieverding (1981) measured flows in a vane passage with multiple cooling hole rows at compressible Mach numbers (M = 0.6, 0.8). On injection of coolant, reduced cross-passage flows and a diminished passage vortex were observed. Granser and Schulenberg (1990) performed oil flow visualization on two endwalls, one without film cooling and another with an upstream slot. At high slot momentum flux ratios, the horseshoe vortex separation line moved closer to the leading edge. Cross-passage flows were also reduced. Biesinger and Gregory-Smith (1993) studied the effect of a slot blowing upstream of a vane passage. The slot was partially inclined in the pitchwise direction. While the authors attribute reduction in secondary flows to pitchwise blowing, it is likely that the axial component of injection has a more significant effect. Friedrichs (1997b) studied flow in a low-speed linear cascade with coolant injected from multiple rows on the endwall. Secondary flows were reduced when coolant was injected at high momentum flux ratio from holes upstream of the lift-off line. Coolant injection downstream of the lift-off line did not have this beneficial effect.

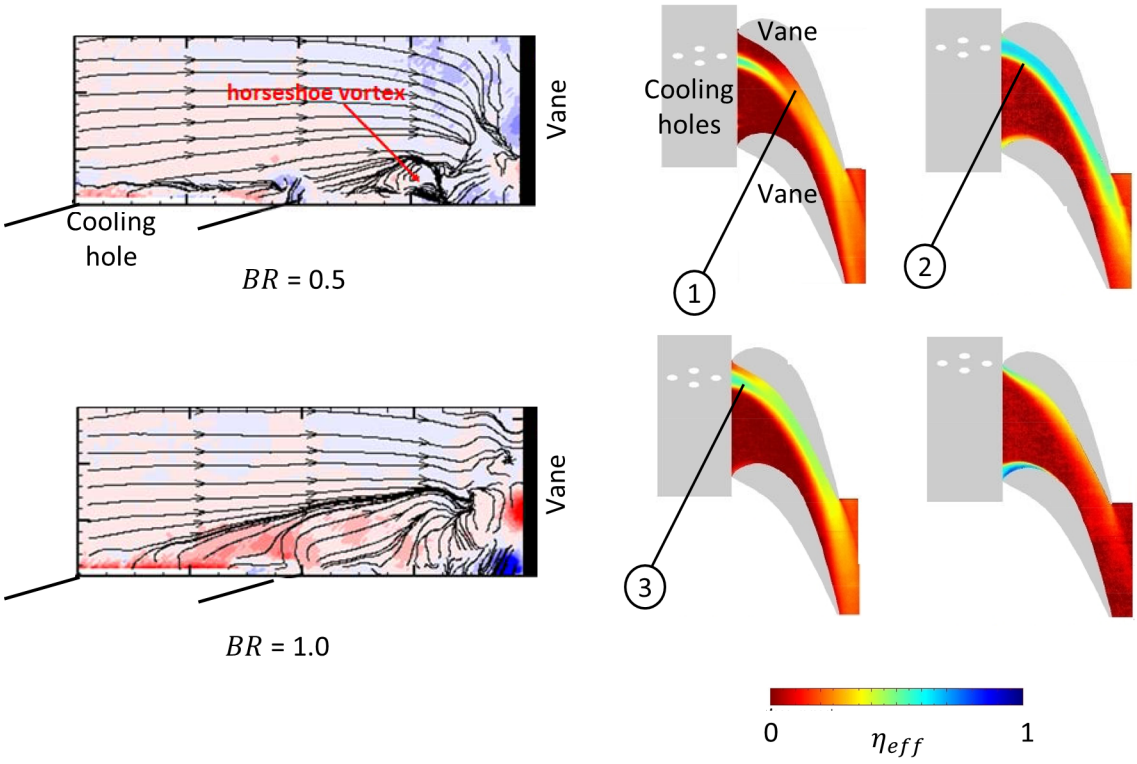
Oke et. al. (2000) performed traverse measurements in a cascade passage, with the endwalls cooled by a double-row of film cooling holes placed upstream of the vane. With increasing blowing ratio, the cooling jets can be seen to migrate further to the pressure side, overcoming the cross-passage secondary flows. Zhang and Jaiswal (2001) studied adiabatic effectiveness contours on a cascade endwall with slot/double row injection. Secondary flows decreased as blowing ratio is increased. However, it is difficult to draw firm conclusions from the study because of the absence of cooling holes at important upstream locations in the

facility. Barigozzi et. al. (2010) reported traverse measurements in a passage with an endwall cooled by multiple rows of film cooling holes. A decrease in passage vortex intensity and cross-passage flows was observed at high coolant blowing ratio.

In gas turbines, a gap is designed at the combustor-turbine interface to allow for thermal expansion. Coolant flow is purged from the gap to avoid hot gas ingestion. Seals, used to reduce leakage, result in coolant emerging at low blowing ratio. Kost and Nicklas (2001), Thole and Knost (2005) and Knost and Thole (2005) studied an endwall cooled by an upstream slot and a downstream cooling hole pattern. The slot approximates the combustor-turbine interface gap. Injection of slot coolant at low blowing ratio results in a thicker inlet boundary layer and aggravates secondary flows.

Takeishi et. al. (2013) studies a configuration with a single cooling hole upstream of a symmetric airfoil. The authors suggest that the downwash of the horseshoe vortex is suppressed by coolant momentum normal to the wall (see Figure 1-8 (a)). However, results from Kost and Nicklas (2001) show that coolant injection from a slot normal to the wall can aggravate secondary flows. The slot flow acts as an obstruction to the upstream endwall boundary layer. The low momentum slot flow thickens the boundary layer downstream of injection.

Benton et. al. (2005a) and Benton (2005b) demonstrated cooling of the PS endwall using holes positioned upstream. They describe the coolant being projected over the endwall boundary layer separation line, and reattaching downstream to cool the PS endwall. Figure 1-8 (b) shows η_{eff} results obtained by the authors using the ammonia-diazo technique. The pitchwise location of injection changes between the plots. In plot 1, coolant is injected far from the vane, but is diffused to the pressure side. This redistribution is probably caused by the passage vortex. However, no signs of endwall boundary layer separation are seen in the plots marked 2 and 3. Coolant jets do not appear impeded by secondary flows.



(a) Streamlines on vane stagnation plane (adapted from Takeishi, 2013)

(b) Endwall η_{eff} for different pitchwise injection locations (adapted from Benton et. al., 2005)

Figure 1-8: (a) Streamlines at vane stagnation plane (from Takeishi, 2013); (b) Endwall η_{eff} plots from Benton et. al. 2005

It is more likely that the streamwise momentum of the coolant energizes the boundary layer, and suppresses secondary flows. Thrift et. al. (2013) obtained endwall cooling effectiveness data and velocity vector data in the vane stagnation plane. They demonstrate that the injection of streamwise momentum by a slot can accelerate the boundary layer and suppress horseshoe vortex formation. This effect is observed at high slot momentum flux ratio and low slot inclination.

Further evidence for this mechanism of secondary flow suppression is given in Section 3.1.3.

1.10 Contribution of this study

In this study, experiments are presented that show that vane secondary flows can be suppressed by coolant injection. This will add to the growing body of evidence on the subject. CFD studies provide insight into this interaction. The knowledge gained has been used to propose design rules for endwall cooling systems. A CFD optimization method has been developed and has been used to design improved endwall cooling systems. This method has been applied to improve endwall cooling in an engine HP NGV.

2 EXPERIMENTAL AND COMPUTATIONAL METHODS

CFD methods are increasingly being used to predict flows in engines and to design flow path components. While CFD methods have improved considerably, accurate turbulence modelling remains an unsolved problem. Experimental validation of CFD results is still considered essential.

This study will use a combined experimental and CFD approach. Experimental results are used to validate CFD predictions. The CFD methods will then be used to explore new designs.

2.1 Super Scale Platform Cooling Facility (SSPCF)

The Super Scale Platform Cooling Facility was developed to study endwall film cooling flows. A schematic of the facility is shown in Figure 2-1. The SSPCF is a large scale linear cascade, composed of 7 vanes. The vane geometry is a linear analogue of a commercial engine HP NGV. The endwalls of the central two passages are composed of removable cassettes. Coolant at room temperature is introduced through film cooling holes machined into these cassettes. A blower drives flow through the facility. Mainstream flow is heated by a mesh heater (described in Section 2.1.1) to provide a temperature difference between the mainstream and coolant flow. A combustor simulator positioned upstream of the vane section generates high inlet turbulence levels. SSPCF flow conditions are given in Table 2-1.

Vane geometry	Tangential chord length (at midspan)	227 mm
	Axial chord length (at midspan)	110 mm
	Inlet, Outlet angle	0^o, 74^o
	Pitch/tangential chord	1.0
	Inlet span/tangential chord	1.2
	Outlet span/tangential chord	1.0
Dilution hole geometry	**Hub**	
	Diameters: row 1, row 2	40 mm, 64 mm
	Hole spacing	224 mm
	Casing	
	Diameter: row 1, row 2	48 mm, 71 mm
	Hole spacing	224 mm
Cooling hole geometry	**Casing (RODN):**	
	Number of rows	2
	Diameter	8 mm
	Hole inclination to endwall	40^o
	Hole pitch/diameter	2.0
	Row axial spacing/diameter	2.8
	Hole length/diameter	3.8
	Hub (RIDN):	
	Number of rows	2
	Diameter	5.6 mm
	Hole inclination to endwall	40°
	Hole pitch/diameter	3.6
	Row axial spacing/diameter	3.8
	Hole length/diameter	6.5
Tunnel flow conditions	Vane inlet and outlet velocity	4 and 40 m/s
	Re (based on outlet velocity and chord length)	7.5×10^5
	Freestream temperature	313 K
	Coolant temperature	293 K

Table 2-1: SSPCF flow conditions

The individual components of the facility are now described.

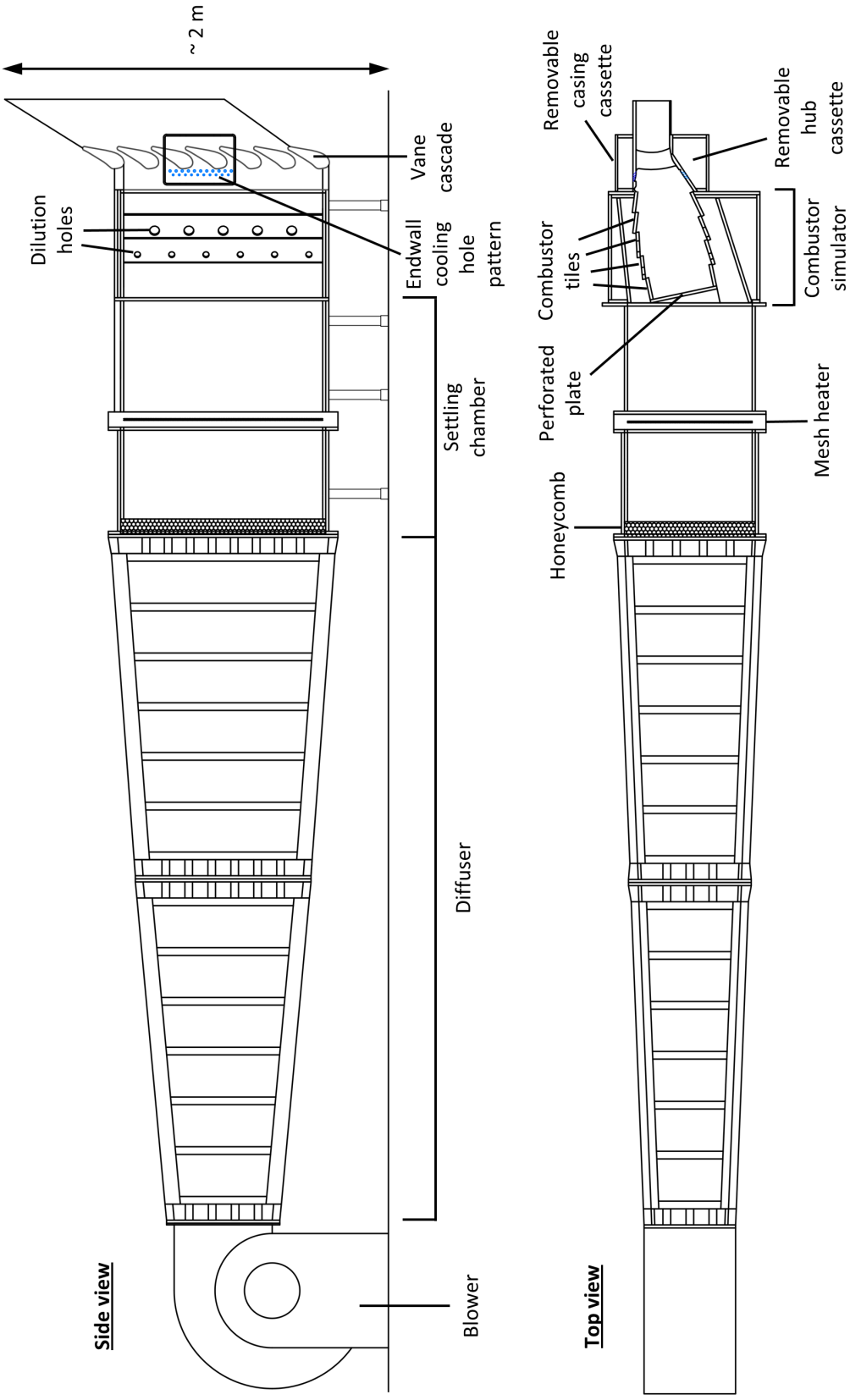


Figure 2-1: SSPCF schematic

2.1.1 Flow conditioning

A mesh heater was used to heat the mainstream flow. The mesh heater is a screen composed of interwoven conducting wires. Electric current is passed through the mesh resulting in resistive heating. The power output was 60 kW, corresponding to a 20 K temperature rise.

It is important to ensure uniform flow through the mesh heater, as variations will result in a distorted temperature profile. Rules proposed for low speed wind tunnel design by Mehta and Bradshaw (1979) were used to design components. The diffuser cone angle was set to 10^{o} to avoid flow separation. A honeycomb of cell length-to-diameter 7 was used to reduce swirl. The mesh heater is at a distance of 120 honeycomb cell diameters downstream. This distance was considered adequate to smooth flow disturbances introduced by the honeycomb.

Infrared images were obtained of the mesh heater in operation without the downstream sections attached (see Figure 2-2). Uniform radiometric values were observed on the mesh heater screen, except at locations of minor manufacturing defects. This confirmed well-conditioned flow through the mesh heater.

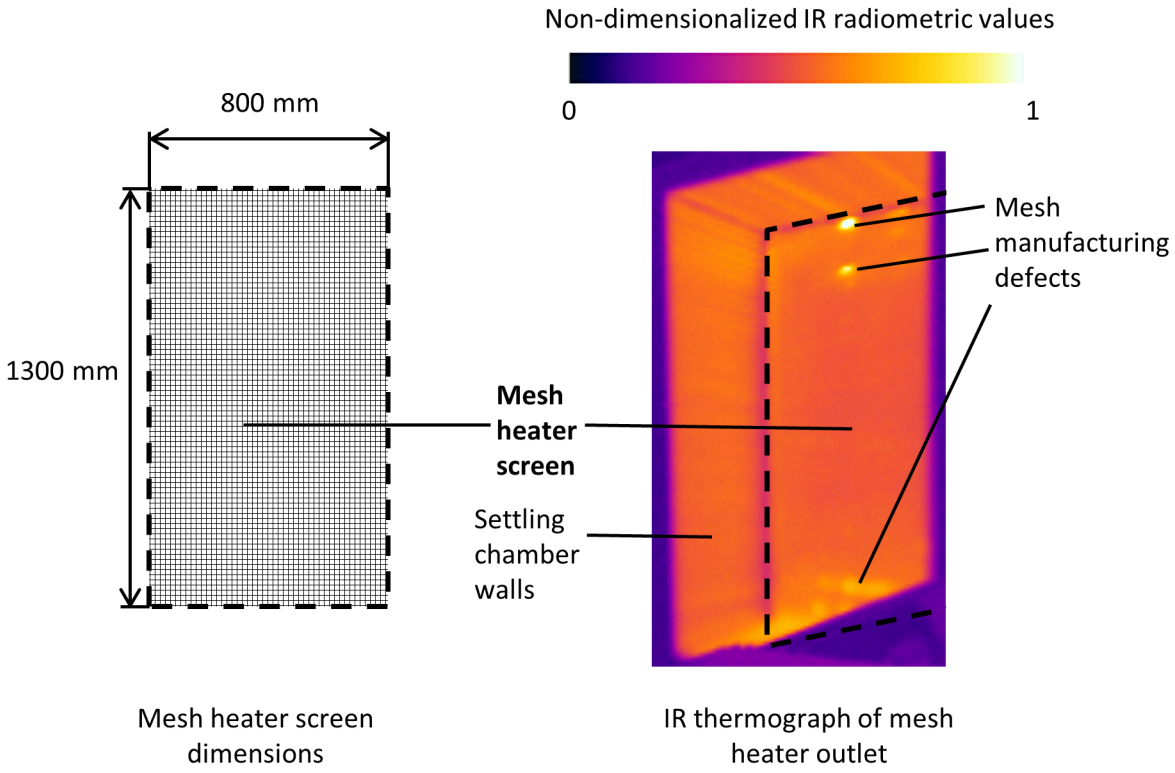


Figure 2-2: IR thermograph of mesh heater outlet

2.1.2 Instrumentation

Pressure transducers from Sensortechnics of 1000 Pa, 6900 Pa, 5 bar range were used. The pressure transducers provided an amplified analogue voltage signal, which was acquired by a National Instruments PCI-6033E 16 bit DAQ card. Signals were sampled at 1000 Hz and data averaged over 2 second windows. This reduces AC (50 Hz) pickup.

Temperature data was acquired by a National Instruments TC-2095 thermocouple rack and digitized by a PCI-6224 16 bit DAQ card. To minimize AC pickup, signals were sampled at 500 Hz and averaged over a 2 second window. Also, shielded, twisted-pair thermocouple extension cables were used.

Measurement uncertainties for pressure, temperature and derived quantities are given in Appendix A. All uncertainty estimates given in this work are based on a 95% confidence interval.

2.1.3 Vanes

The SSPCF vane geometry, shown in Figure 2-3 (b), is a linearized version of an engine representative HP NGV (Figure 2-3 (a)).

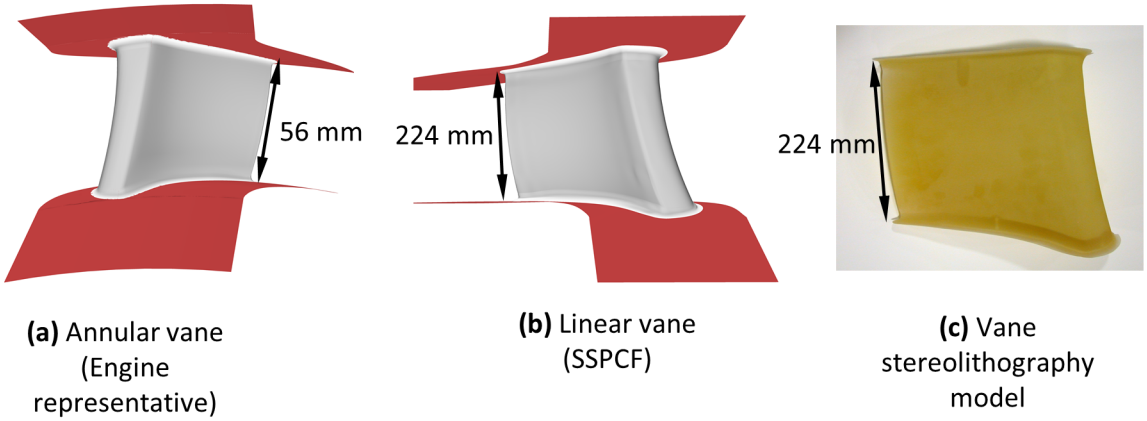


Figure 2-3: Engine and SSPCF vane geometries

The transformation of the annular engine representative vane geometry was done using the following procedure. Curves defining the wireframe were extracted and converted to a cloud of points. The points were transformed from cylindrical coordinates (X, R, θ) to linear coordinates (x, y, z) using the following expressions:

$$\begin{aligned} x &= X \\ y = R &= \sqrt{(X - X_0)^2 + (Y - Y_0)^2} \\ z &= R_{ms} \sin\theta, \end{aligned} \tag{2-1}$$

where R_{ms} is the radius at mid-span of the NGV, (X, Y, Z) is the Cartesian coordinate system describing the annular blade with (X_0, Y_0, Z_0) as the origin. θ was obtained using the expression:

$$\theta = \sin^{-1} \frac{Z}{\sqrt{(X - X_0)^2 + (Y - Y_0)^2}} \tag{2-2}$$

These expressions describe the unwrapping of the blade around the midspan radius from an annular to a linear configuration. A wireframe was constructed by interpolating NURBS curves through the transformed points. A surface was lofted through the wireframe

to obtain the linear vane geometry. The linear vane is larger than the engine NGV by a factor of 4.

The vane was fabricated by stereolithography in two pieces of 5 mm thickness. These were glued together to obtain the final model (Figure 2-3 (c)). An approximate stress analysis was performed using the formulae provided by Roark (1989). The two glued pieces were considered simply supported plates, with a maximum pressure difference of 1024 Pa ($= {}^{1}/_{2}\,\rho u_{out}{}^{2}$) acting across their faces. A deflection of 0.25% of vane chord length was predicted. The small deflection will not affect the vane aerodynamics significantly. Rubber gaskets were used in recesses at the top and bottom of the vane to prevent leakage (Figure 2-4 (a)).

Static pressures on the vane were obtained using surface pressure taps at 10%, 50%, 90% spanwise locations (Figure 2-4 (a)). The surface pressure tapping marked at the vane LE in Figure 2-4 (a) was used to measure vane stagnation pressure/dynamic pressure head (gauge pressure: P_{dyn}). Tests were repeated at a range of Re around the nominal operating condition (Re = 750,000) by varying the blower power. Static pressures were converted to C_P, defined as:

$$C_P = \frac{P - P_{dyn}}{P_{dyn}}, \tag{2-3}$$

The estimated uncertainty in C_P was 1% (see Appendix A). Little variation in vane pressure distribution is noted in the C_P plots of Figure 2-4 (b) (data points visually overlay). The vane pressure distribution is largely determined by the inviscid flow field, and is insensitive to Re in the range $4.9 \times 10^5 < \text{Re} < 10.0 \times 10^5$.

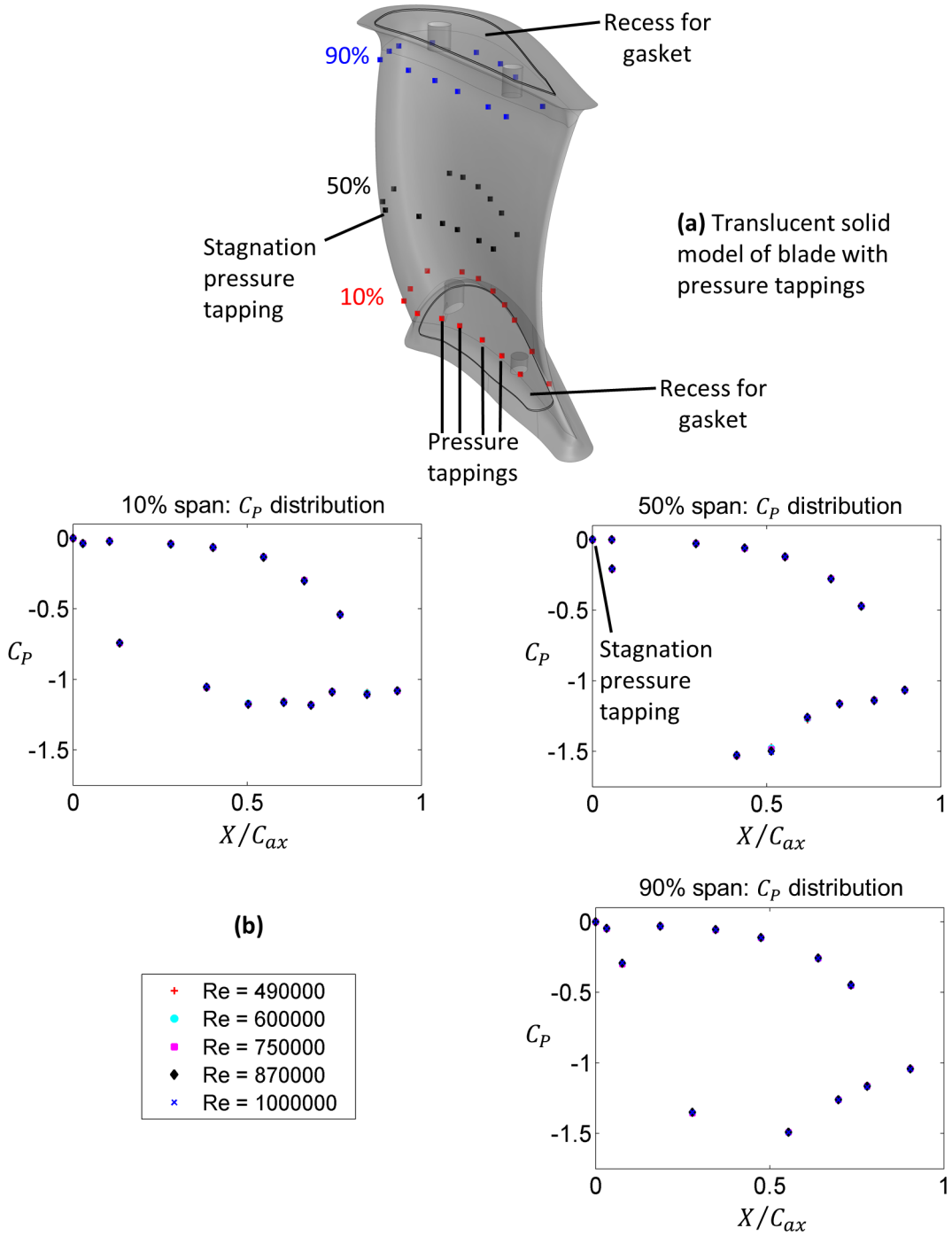


Figure 2-4: (a) Vane surface pressure tap locations; (b) C_P distribution

Neglecting total pressure losses in the vane passage, the dynamic head P_{dyn} provided an estimate for vane outlet velocity:

$$u_{out} = \sqrt{\frac{2P_{dyn}}{\rho}} \tag{2-4}$$

Low strength Rohacell foam was used to construct components of the combustor simulator. Loading across the combustor tiles, for example, increase with tunnel flow rate and thus blower power. The blower power was set to target u_{out} = 42 m/s. This ensured that stresses in these components were within safe limits. Also, at this setting, the static pressures measured in the facility were in the range of the 1000 Pa transducers.

Mainstream mass flow through a vane passage was estimated using the expression:

$$\dot{m}_{\infty} = \rho A_{th} u_{out}, \tag{2-5}$$

where A_{th} was the vane geometric throat area estimated at the plane marked in Figure 2-6. $\dot{m}_{\infty}$ was measured at 0.48 kg/s and the uncertainty in $\dot{m}_{\infty}$ was estimated at ±2.5% (see Appendix A).

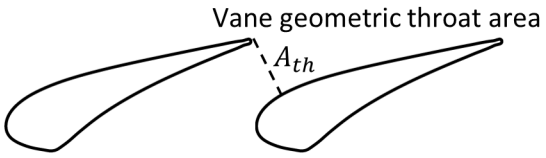


Figure 2-5: Vane geometric throat location

2.1.4 Combustor simulator

The importance of simulating the combustor in modelling turbine vane flows is being recognized in recent literature (see Section 1.8). In order to generate engine-representative turbulence conditions, a combustor simulator was used upstream of the vane cascade (Figure 2-1 and detail in Figure 2-6 (a)). The combustor simulator cross-section was representative of an RQL combustor. The combustor contraction was modelled, as was the tile geometry. These features are expected to influence the development of the boundary layer and the total pressure profile entering the vane section.

Dilution jets issue into the mainstream generating high Tu. Geometrical details of the casing and hub dilution holes, and their distances from the vane inlet plane are given in Figure 2-6 (b) and (c). Thole et. al. (1994) demonstrated the generation of mean turbulence

levels as high as 20% using jets in a cross-flow. Moss and Oldfield (1991) showed that the characteristics of turbulence are not affected by heat addition. Barringer et. al. (2002) measured turbulence profiles from a cold-flow combustor simulator. They measured engine representative turbulence levels (Tu = 15%) at the combustor outlet, and measured turbulence length scales on the order of the dilution jet diameter. A combustor simulator with cold flow can thus be used to generate engine-representative turbulence.

The dynamics of dilution jets is determined by the momentum flux ratio, I (Lefevbre, 1999). Appendix E explains the matching of parameters for the combustor simulator. The conditions were matched at the combustor outlet plane marked in Figure 2-6 (a). To match engine conditions, the target value of I is 11.9. Appendix E shows that the dilution jets in the combustor simulator need to issue with a velocity, u_j, of 15.8 m/s in order to match I. If conditions in the dilution plenum are assumed stagnant, $^1/_2\,\rho {u_j}^2$ is the pressure drop across the dilution holes. A perforated plate (Figure 2-6 (d)) was placed upstream of the combustor simulator to restrict flow and set this pressure drop.

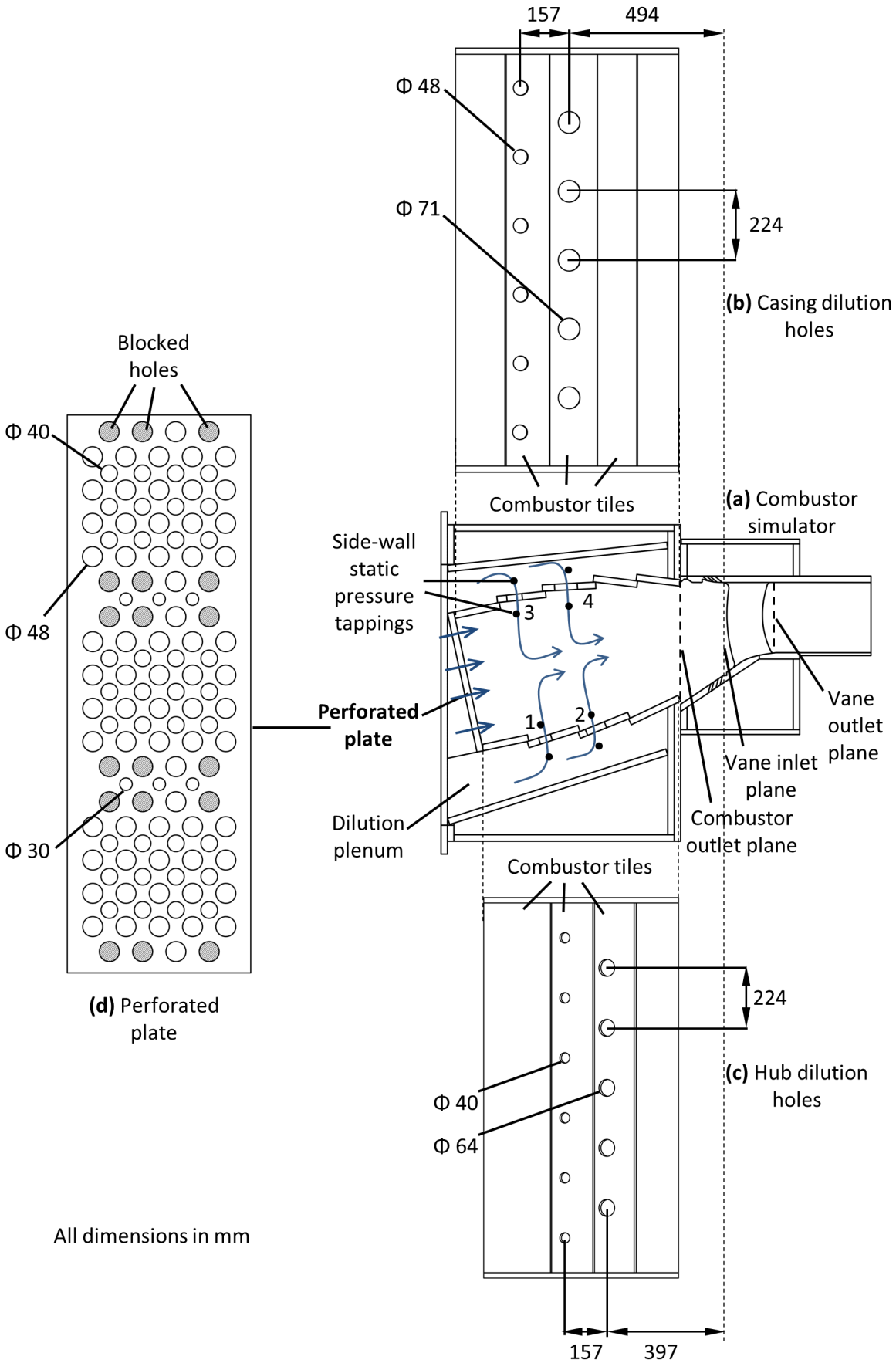


Figure 2-6: Combustor simulator schematic

The perforated plate design is now explained. The volume flow through the combustor simulator is given by:

$$\dot{V} = C_{D,mean} A_{open} u_j, \tag{2-6}$$

where A_{open} is the open area of all holes in the combustor simulator, $C_{D,mean}$ is the average discharge coefficient of the holes and u_j is the mean jet velocity through the holes. At design conditions, volume flow rate ($\dot{V}$) through the facility was measured at 2.64 m^3/s (see Section 2.1.3). Substituting values for u_j, $\dot{V}$ and assuming $C_{D,mean}$ = 0.7, A_{open} is estimated using Equation (2-6) as 0.239 m^2. The total open area of the dilution holes is 0.053 m^2. An initial estimate for the open area of the perforated plate is thus 0.186 m^2. The total area of the holes on the perforated plate (Figure 2-6 (b)) was set to this value. To match turbulence length scales, the hole sizes are in the same range as the dilution holes.

The static pressure difference across the combustor tiles was measured at surface tappings on the adjacent wall (shown in Figure 2-6 (a)). This provides an estimate for the pressure drop, ΔP, across the holes. An approximate value of dilution momentum flux ratio is estimated as:

$$I = \frac{\Delta P}{{}^1\!/_2\, \rho u_{c,out}^2} = \frac{\Delta P}{{}^1\!/_2\, \rho \left(\frac{A_{th}}{A_{c,out}} u_{out}\right)^2}, \tag{2-7}$$

where $u_{c,out}$ is the velocity at combustor outlet plane, marked in Figure 2-6 (a). $u_{c,out}$ has been estimated from the vane outlet velocity, u_{out}, using the continuity equation. I was estimated using measured values of ΔP and u_{out}, and iteratively adjusted by blocking holes in the perforated plate (see Figure 2-6 (c)), until the target was achieved. For the dilution hole rows marked 1 to 4 in Figure 2-6 (a), I was measured at design conditions as 10, 8.1, 10.1 and 9.5 respectively (uncertainty: ±0.6). While these values are lower than the target I (11.9 at vane outlet conditions), they were considered acceptable.

2.1.5 Test section

The SSPCF cascade was composed of 7 vanes (Figure 2-7 (a)). The endwalls were lined with low conductivity Rohacell material (thermal conductivity = 0.04 W/mK). The endwalls of the central two passages were composed of removable cassettes. New endwall cooling hole patterns can be investigated by replacing these cassettes. The casing endwall is flat, while the hub endwall has a contraction (Figure 2-7 (c)). The hub endwall also models a combustor-turbine interface step, although no leakage occurs at this location.

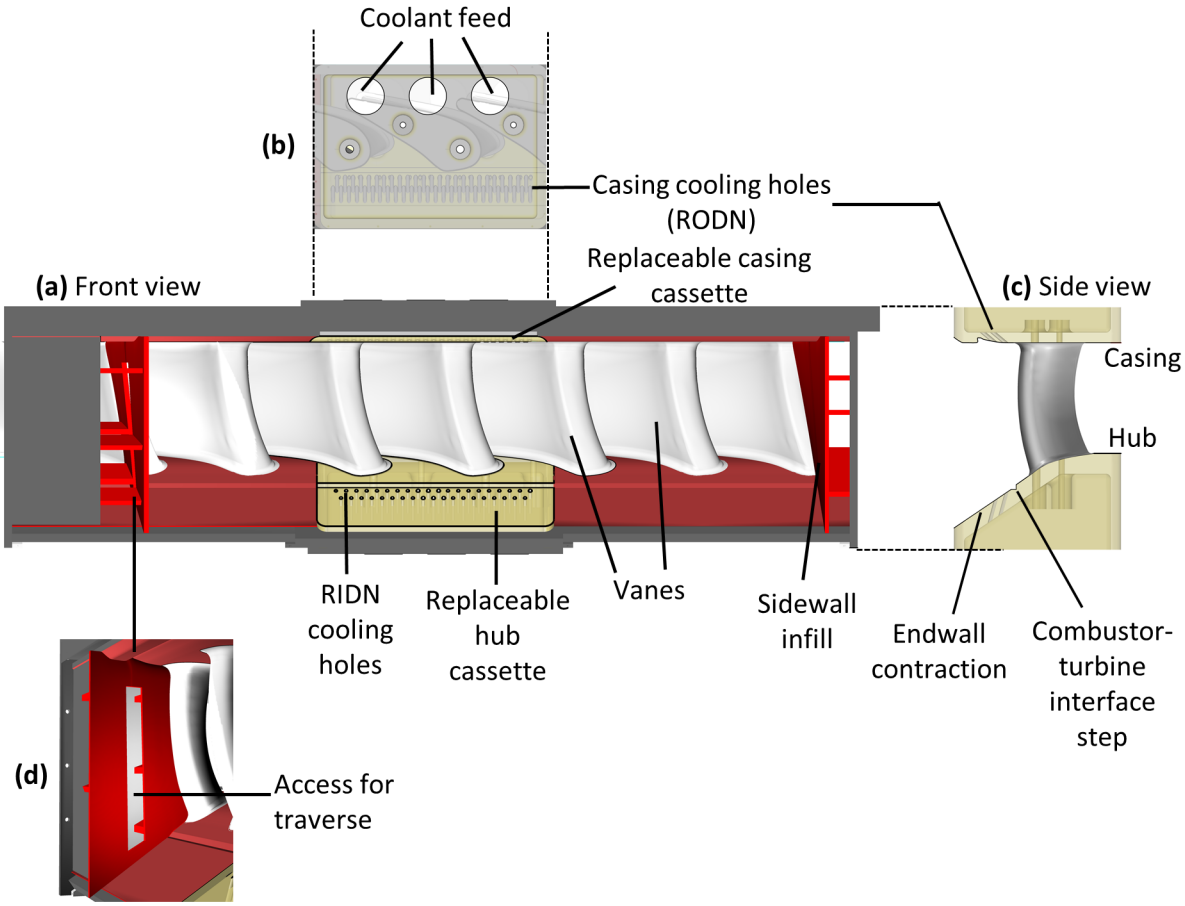


Figure 2-7: SSPCF test section

One of the cooling systems investigated in this study is the Rear-Inner Discharge Nozzle (RIDN)/Rear-Outer Discharge Nozzle (RODN) cooling system used in the engine. These are double-rows of cylindrical holes positioned upstream of the vanes, with the RIDN

cooling the hub endwall and the RODN cooling the casing endwall. Geometrical details of the RIDN/RODN cooling holes are given in Table 2-1 and shown in Figure 2-8.

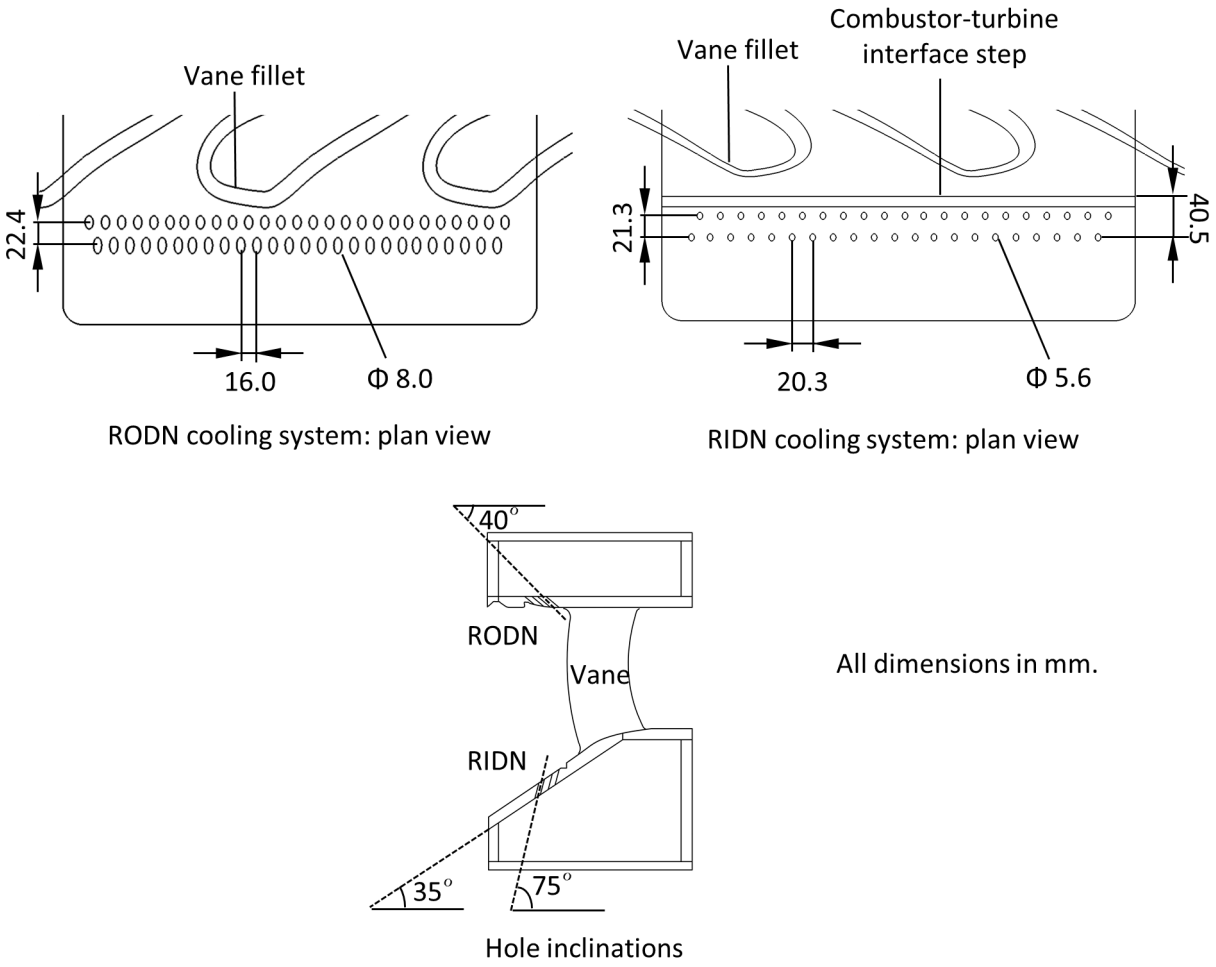


Figure 2-8: RIDN/RODN cooling system: geometrical details at SSPCF scale

At the cascade extremities, infill pieces effect a smooth transition from the flat sidewalls to the vanes. The top infill piece (Figure 2-7 (d)) includes a slot to allow access for a traversing probe.

2.1.6 Coolant feed

Coolant was fed to the rear of the cassettes through three large holes (Figure 2-7 (b)). The total area of the coolant feed holes is 4 times the total area of the RODN cooling holes. The dynamic head of the coolant feed is thus low. Flow in the coolant plenum is expected to be uniform.

Coolant flow was metered using a critical-flow venturi nozzle. Nozzle geometries were generated according to the ISO 9300 standard (Measurement of gas flows, 1990). Choking of the nozzle occurs for inlet total-to-outlet static pressure ratios greater than 1.9. If the nozzle is choked, mass flow rate through the nozzle is a function of inlet total pressure ($P_{0,in}$) and inlet total temperature ($T_{0,in}$):

$$\dot{m} = K \frac{P_{0,in}}{\sqrt{T_{0,in}}}, \tag{2-8}$$

where K is a constant dependent on nozzle throat area, Re and gas properties (ratio of specific heats, γ, and gas constant, R). Stereolithography models of venturi nozzles of throat diameters 5 mm, 7 mm, 9 mm (shown in Figure 2-9), 11 mm, 15 mm were obtained.

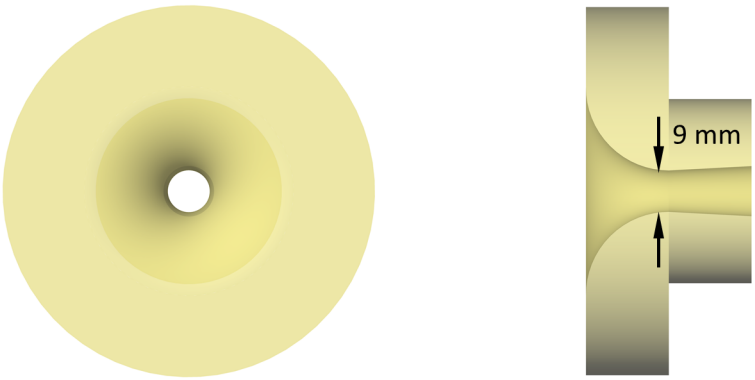


Figure 2-9: Critical-flow venturi nozzle (Throat diameter = 9 mm)

Coolant and tunnel flow rates, $\dot{m}_c$ and $\dot{m}_\infty$, are given as mass flow per two passages, as each endwall cassette cools two passage endwalls. $\dot{m}_\infty$ was measured as 1.09 kg/s at design condition. By using nozzles of different throat diameters and setting pressure upstream of the nozzle, different coolant-to-mainstream flow fractions ($\dot{m}_c/\dot{m}_\infty$) were achieved (Table 2-2). Uncertainty estimates are described in Appendix A.

Throat diameter	$P_{0,in}$ ($T_{0,in}$ = 293 K)	Coolant flow rate ($\dot{m}_\infty$ = 1.09 kg/s)
5 mm	2.4 bar	11 g/s ($\dot{m}_c/\dot{m}_\infty = 1\% \pm 0.02\%$)
7 mm	2.4 bar	22 g/s ($\dot{m}_c/\dot{m}_\infty = 2\% \pm 0.03\%$)
9 mm	2.2 bar	33 g/s ($\dot{m}_c/\dot{m}_\infty = 3\% \pm 0.05\%$)
11 mm	2.0 bar	44 g/s ($\dot{m}_c/\dot{m}_\infty = 4\% \pm 0.07\%$)
11 mm	2.5 bar	55 g/s ($\dot{m}_c/\dot{m}_\infty = 5\% \pm 0.08\%$)
15 mm	2.4 bar	99 g/s ($\dot{m}_c/\dot{m}_\infty = 9\% \pm 0.15\%$)

Table 2-2: Coolant mass flow metering

2.1.7 IR thermography

A FLIR A325 infrared camera was used to obtain temperature maps of the cooled endwall. The camera resolution was 320x240 pixels, with around 7 to 10 pixels resolving the length of a cooling hole diameter. The camera outputs radiometric data at each pixel as a number between 0 and 16384 (2^{14}).

The calibration procedure used to convert the raw radiometric values to temperature data is now described. Tunnel and coolant flow conditions were set at target values. The mesh heater was turned on and ramped in 4 steps, each with 45 seconds dwell (see Figure 2-10 (b)). Calibration thermocouples were sited in low thermal gradient regions of the endwall (marked in Figure 2-10 (a)). Raw radiometric values were averaged in a 3x3 pixel square adjacent to each thermocouple. The averages were plotted against the thermocouple measurement. Values at steady state (shaded bars in Figure 2-10 (b)) were used to obtain a calibration curve via linear fit (see Figure 2-10 (c)). Little variation was seen for calibration curves obtained from different thermocouples (see Figure 2-10 (d)). The mean slope and intercept was used as the calibration curve for the run.

IR radiometric images were captured at 30 frames per second. Video playback showed few signs of unsteady flow, except at very high coolant flow rates ($\dot{m}_c/\dot{m}_\infty$ > 12%).

Fifteen frames were averaged, and converted to a mean temperature map using the calibration curve.

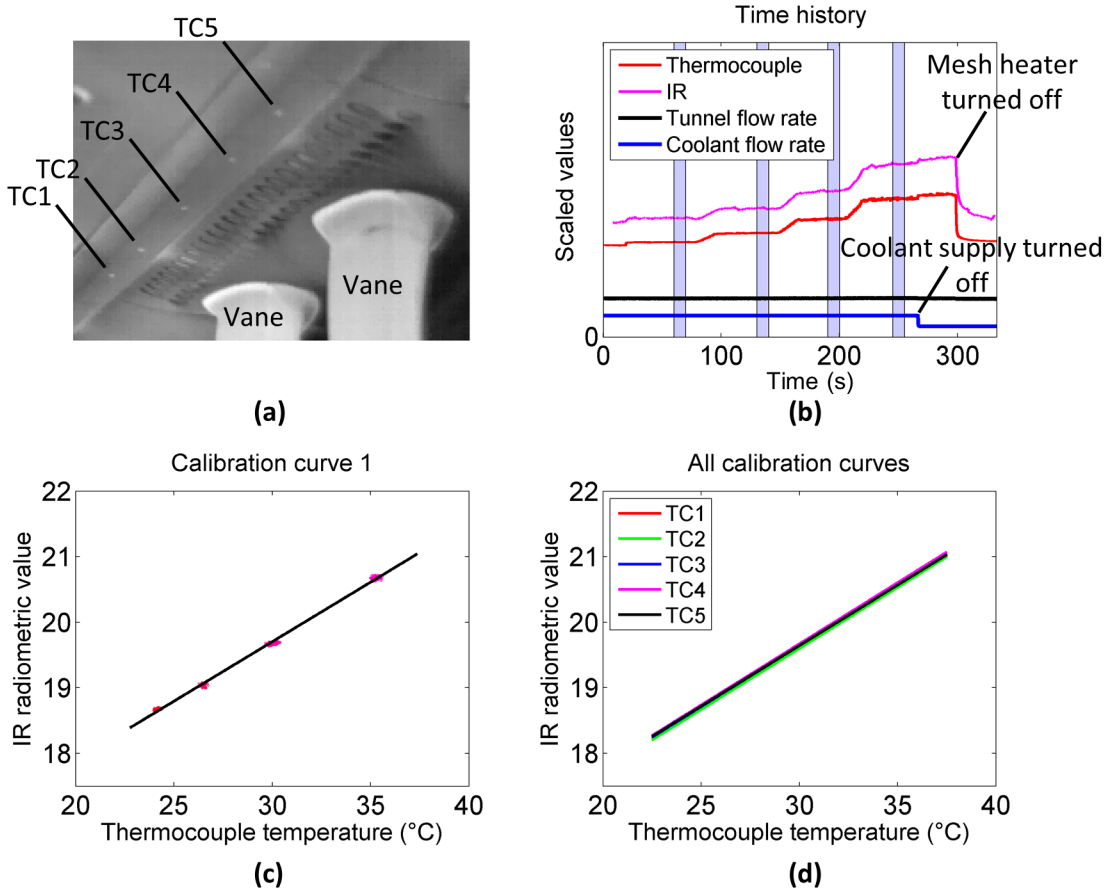


Figure 2-10: IR calibration procedure

Figure 2-10 (a) was obtained a few seconds after the mesh heater was switched off. The Rohacell endwalls have low conductivity, and thus respond rapidly to changes in mainstream temperature (Ireland et. al., 1999). The vanes and the glue securing the thermocouple remain at a high temperature and remain clearly visible in the IR map. This image was also used to identify the outline of the vane in η_{eff} maps.

The cameras were positioned using a solid model of the test facility. ZnS windows allowed optical access to the front of the cascade (see Figure 2-11 (a)), while cutouts on opposite endwalls were used to image the rear of the cascade (see Figure 2-11 (d)).

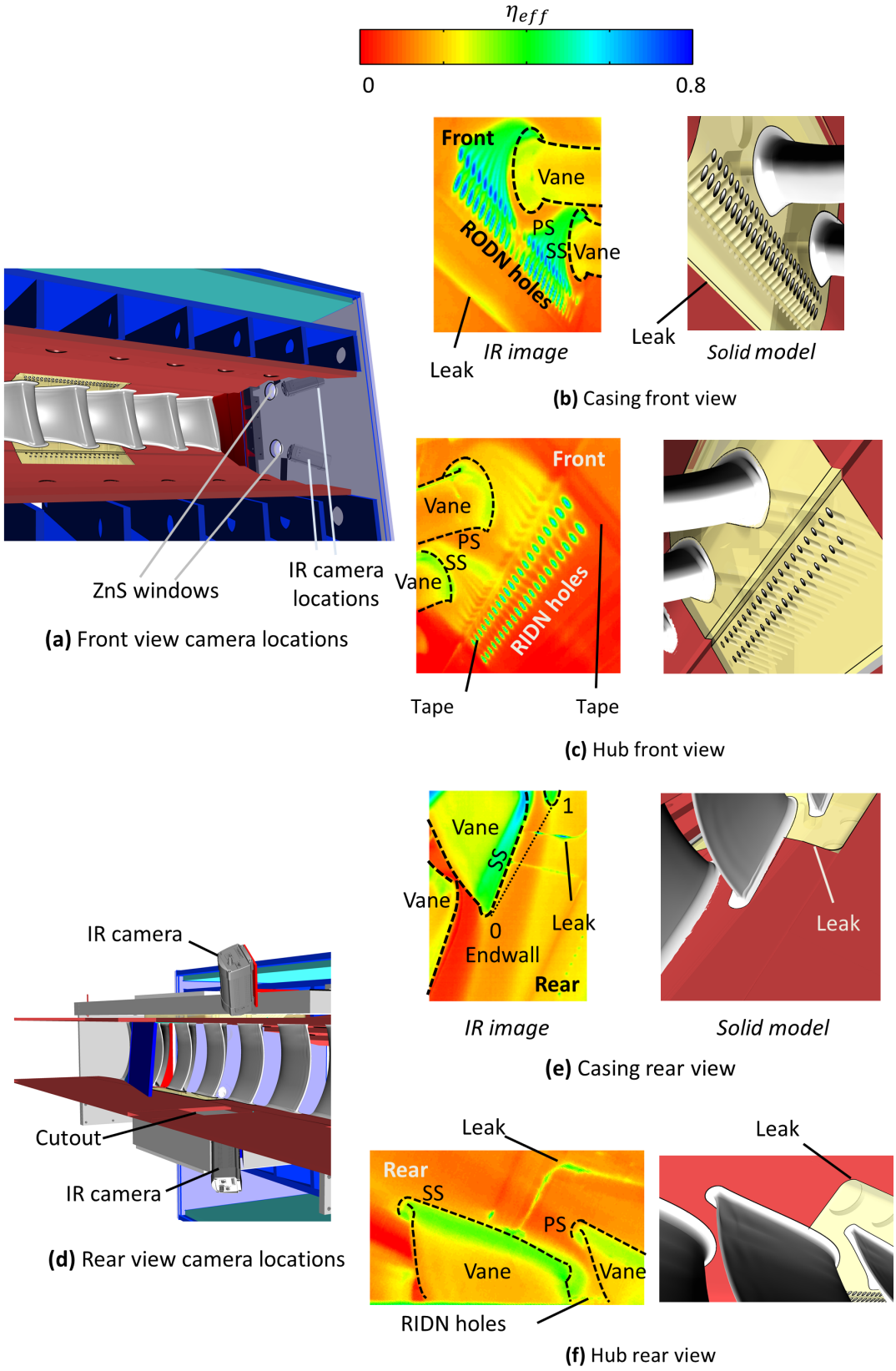


Figure 2-11: IR camera views

Temperature maps were converted to η_{eff} maps using measurements of the freestream and coolant temperatures. Lateral conduction on the Rohacell endwalls is expected to be small. The thermal conductivity of the vane material is much higher (0.176 W/mK). The adiabatic assumption is not valid on the vanes and η_{eff} data are unreliable. Sample IR maps of the front (Figure 2-11 (b) and (c)) and rear (Figure 2-11 (e) and (f)) of the cascade are shown alongside solid models. The location of the cooling holes, the outline of the vanes and the endwall PS/SS are marked

Machining tolerances result in gaps around the edges of the cassettes. Foam gaskets were used around the casing cassette to minimize leakage. However, minor leakage results in non-zero η_{eff} (Figure 2-11 (b)) in the casing front view, upstream of the cooling holes. The thermocouple and IR data plotted in Figure 2-10 (b) were obtained at endwall locations upstream of the cooling hole rows. However, after coolant is turned off, their values rise. This confirms the presence of coolant leaks upstream of the thermocouple locations. Minor leaks are also seen to occur at the rear edges of the casing cassette in Figure 2-11 (e).

Masking tape was used to seal the edges of the hub cassette (see Figure 2-11 (c)). The tape is flush with endwall and is of similar roughness to the foam material. The tape does not lie in the endwall passage and does not affect η_{eff} data in the region of interest. This was a better sealing solution; η_{eff} values observed upstream of the cooling holes on the hub endwall are approximately zero (see Figure 2-11 (c)).

Uncertainty in η_{eff} was estimated at ±0.04 (see Appendix A), giving an uncertainty of 6.7% at $\eta_{eff} = 0.6$.

2.1.8 Cascade periodicity

Cascade periodicity is improved by using tailboards. Figure 2-12 shows the rear of the cascade. The vanes at the extremities have tailboards that mate with the trailing edges. The tailboard angle can be set by rotation about the axes shown.

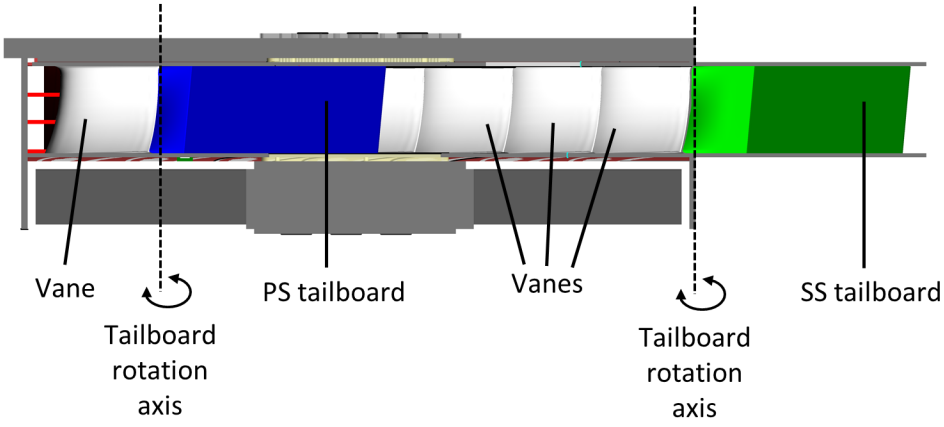


Figure 2-12: Test section viewed from vane outlet

CFD was used to select the optimum tailboard angle for periodicity. This work was done by Gibb (2011) as part of a final year MEng project. A summary is provided here.

Figure 2-13 (a) shows a CFD model of the cascade, with an enclosure to model the exhaust to atmosphere. Two models were constructed, one with tailboards and another without. Midspan cuts of the CFD meshes used for both cases are shown in Figure 2-13 (b) and (c). Contours of normalized velocity (u/u_{out}) on this plane are shown in Figure 2-13 (d), (e), (f). Periodicity was gauged by plots of C_P ($= 2(P - P_{out})/\rho u_{out}^2$) on a line downstream of the cascade at midspan location. The line is marked in Figure 2-13 (b) and (c), plots are shown in Figure 2-13 (g). Also, a plot from a single-passage CFD case with periodicity enforced as a boundary condition is shown as a benchmark. The tailboard angle, θ, is marked in Figure 2-13 (c).

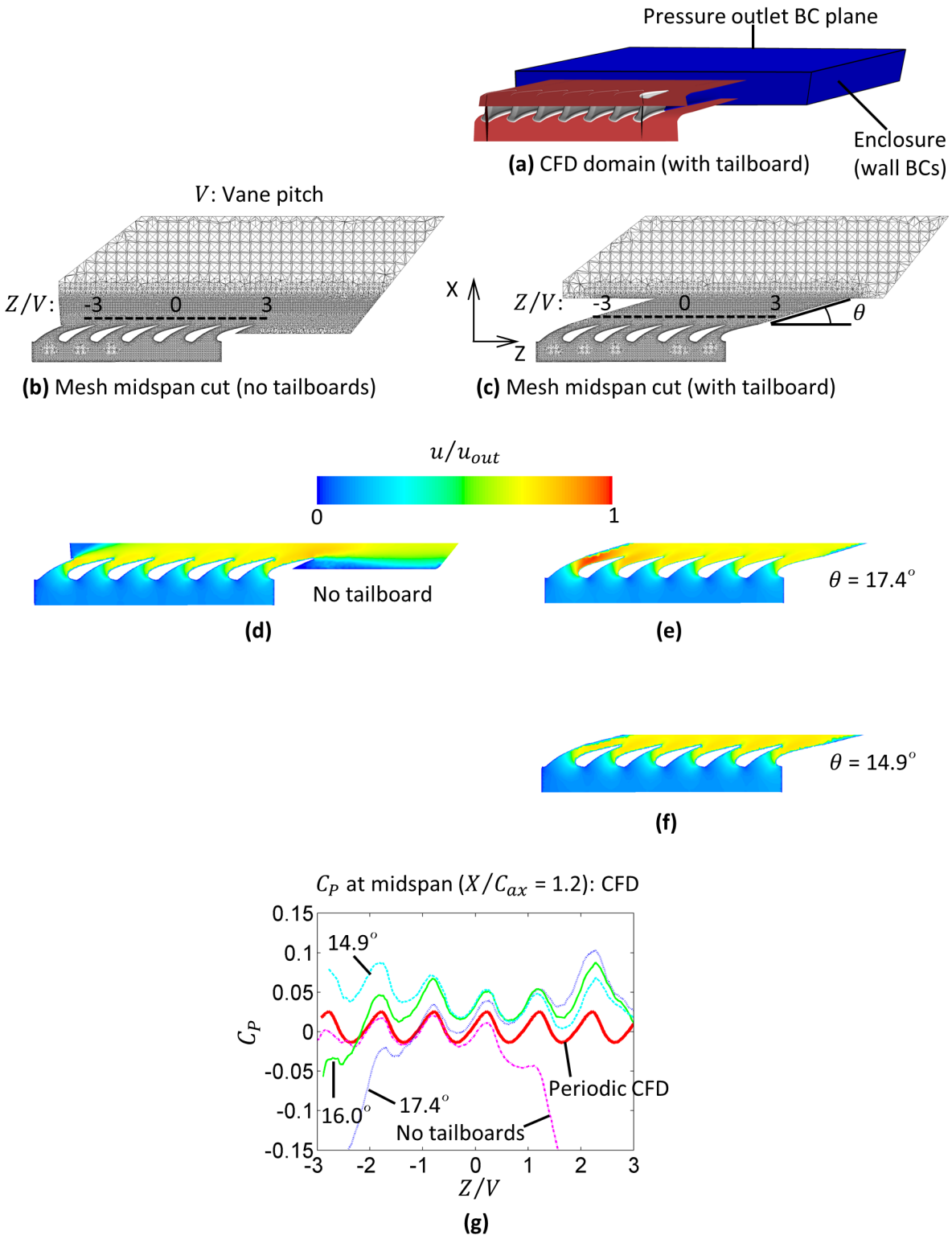


Figure 2-13: Tailboard angle setting

Flow acceleration occurs at the PS of the cascade in the no-tailboard case (Figure 2-13 (d)) disrupting periodicity from Z/V = 0 to 3 (Figure 2-13 (g)). At a high angle of 17.4°, high velocities are observed at the PS of the cascade (Figure 2-13 (e)). This is caused by

acceleration downstream of the passage between the tailboard and the mainstream. At a low tailboard angle of 14.9^o, the flow at the PS of the cascade is compressed leading to higher static pressures here (see Figure 2-13 (g)). The cascade averaged static pressure has also increased. The optimum angle for attainment of periodicity lies in between these two values. Gibb (2011) shows that a tailboard angle of 16.0^o provides minimum variation of downstream C_P. This was used as the tailboard angle setting in the SSPCF.

2.2 CFD models

The pressure based solver in Ansys FLUENT was used for computing flow solutions. Unstructured tetrahedral meshes were generated using ICEM-CFD.

Rhino was used for solid modelling operations. A script was written to automatically generate a film cooling CFD domain given a table with hole locations, inclinations, diameters, compound angles. Scripts were written to automate mesh read-in, solution and post-processing in FLUENT. This semi-automated CFD loop allowed the evaluation of a new cooling hole arrangement in under a day. This optimization loop is detailed in Appendix B.

The presence of high mesh densities near the periodic boundaries often resulted in the failure of the ICEM-CFD mesh generation algorithm. To resolve this problem, a six passage geometry was used (Figure 2-14). Mesh density is concentrated in the central two passages, with very coarse mesh in adjacent passages. Meshing was thus made error-free and was automated by scripting.

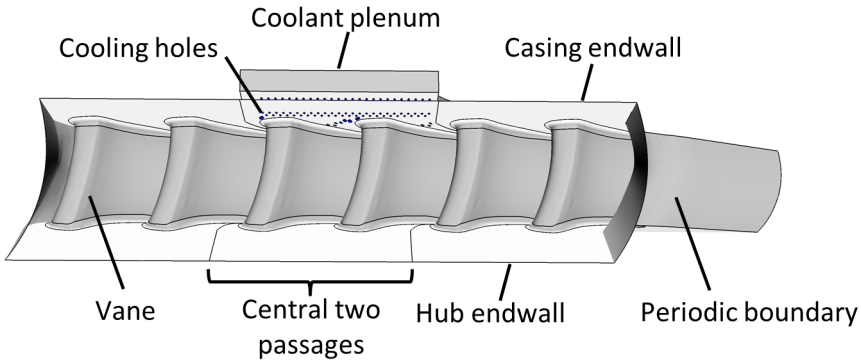


Figure 2-14: CFD model

The boundary conditions used for CFD simulations are shown in Table 2-3. Incompressible boundary conditions correspond to SSPCF operating conditions. For Chapters 3, 4, compressible simulations were run at engine representative maximum take-off thrust operating conditions, given in Table 2-3. Variations of specific heat capacity with temperature were ignored. A uniform total temperature inlet boundary condition was used.

	Incompressible conditions	**Compressible conditions**
Mainstream conditions	$P_{0,\infty}$ = 1024 Pa (gauge) P_{out} = 0 Pa (gauge) $T_{0,\infty}$ = 313 K Tu = 15%, l = 0.22V (V = vane pitch)	$P_{out}/P_{0,\infty}$ = 0.55 Tu = 15%, l = 0.22V (V = vane pitch)
Coolant conditions	$T_{0,c}$ = 293 K Specified coolant mass flux: $\dot{m}_c$. *Nominal values:* $\dot{m}_c/\dot{m}_\infty$ = 3% for hub (RIDN) $\dot{m}_c/\dot{m}_\infty$ = 6% for casing (RODN) Tu = 15%, l = 0.22V	$T_{0,c}/T_{0,\infty} = 2.33$ $P_{0,c}/P_{0,\infty}$ = 1.029 Tu = 15%, l = 0.22V
Wall boundary conditions	Adiabatic	Adiabatic

Table 2-3: CFD boundary conditions

Chapter 5 will describe the optimization of an engine endwall cooling system. In that chapter, a combustor representative temperature profile will be simulated. The boundary conditions used will be described in Chapter 5.

As described in Section 1.5, the quantity of interest is η_{eff} at the rear endwall. Harrison and Bogard (2008) compare experimental η_{eff} data with CFD predictions by RANS turbulence models. CFD solutions under-predict lateral spreading of the coolant, while over-predicting centreline values. While turbulence introduced by injection of coolant is anisotropic, the use of the Reynolds Stress model does not offer an improvement over two-equation eddy viscosity models. In all CFD simulations in this study, the vane outlet line was at least 30 hole diameters downstream of injection. Prediction of η_{eff} at this location is determined mainly by mixing of the coolant with the freestream. It is also important to accurately predict boundary layer separation at the horseshoe vortex lift-off line. The realizable k- ε model predicts mixing, shear layers and boundary layer separation accurately (Bradshaw, 1996) and was thus chosen for this study. The SST k- ω model deals with high y^+ values more robustly, and was used for the compressible simulations of Chapter 5.

To study mesh independence, CFD solutions were obtained on five tetrahedral meshes, labelled ‘Coarser’ (0.3 million cells), ‘Coarse’ (1.2 million cells), ’Intermediate’ (1.7 million cells), ’Fine’ (4.25 million cells), ’Finer’ (8.5 million cells). The cooled hub endwall was solved at incompressible conditions; the cooled casing endwall was solved at compressible conditions. The boundary conditions used are given in Table 2-3. Standard wall functions were used for wall treatment. η_{eff} was examined at lines on the casing/hub inlet and outlet. These are marked on the hub endwall in Figure 2-15 (a).

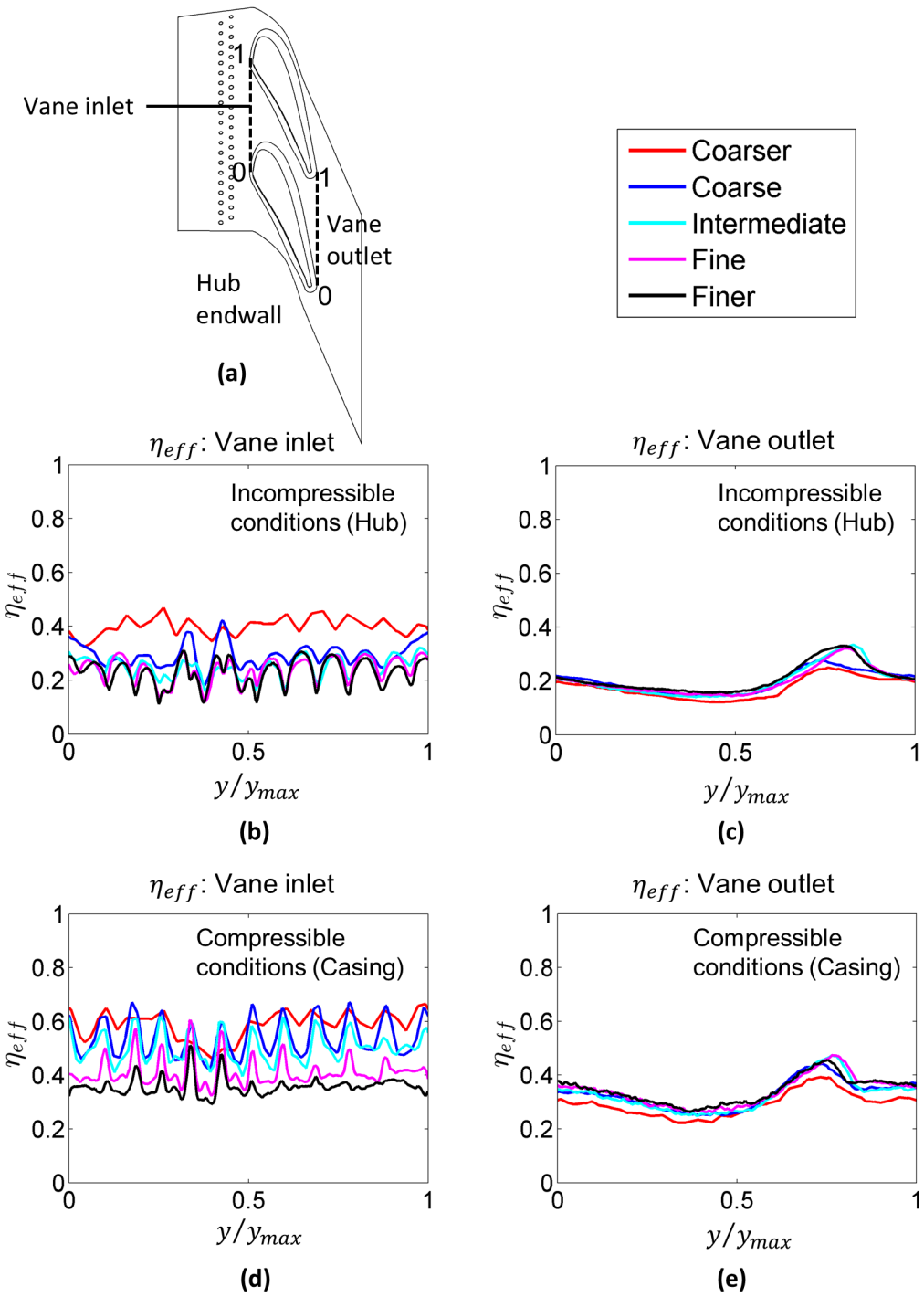


Figure 2-15: Mesh independence study

Figure 2-15 (b) shows η_{eff} at incompressible conditions on the hub inlet line. Increasing mesh size results in better prediction of coolant lift-off, resulting in lower values of η_{eff}. Increasing mesh size also results in lower numerical diffusivity and higher η_{eff} at the vane outlet line (Figure 2-15 (c)). However the changes are small, with a 6% difference in

mean η_{eff} between the 'Fine' and 'Finer' mesh results. Similar trends are observed in simulations at compressible conditions (Figure 2-15 (d) and (e)). The 'Finer' mesh (8.5 million cells) resolution offered the most accurate solution for the available computer resources. This mesh size was chosen for both incompressible and compressible simulations. The mesh resolution on the cooled endwall is shown in Figure 2-16.

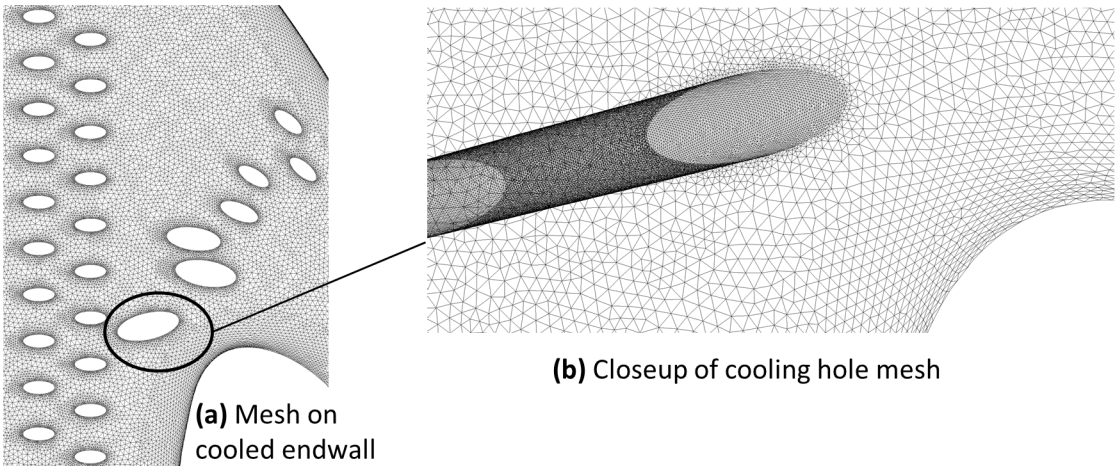


Figure 2-16: Endwall mesh resolution

For accurate use of standard wall functions, the first cell centroid needs to be placed such that $30 < y^+ < 300$. y^+ increases with local freestream velocity. Maximum y^+ values observed at the vane outlet were 50 for the incompressible case, and 400 for the compressible case. The y^+ value is not optimal in the compressible simulations. The boundary layer is better resolved before the throat where lower y^+ values were observed (minimum y^+ of 100). But limitations on computing power prohibited the use of finer meshes. Further, it is noted in Chapter 3 and 4 that important flow features introduced by coolant injection lie well above the boundary layer. The experimental validation described in Chapter 3 increases confidence in the CFD methods used.

2.3 Turbulence modelling theory

The realizable k-ε turbulence model used in these simulations is an eddy viscosity model (Bradshaw, 1996). The steady Reynolds Averaged momentum equation is shown below:

$$\frac{\partial}{\partial x_j}\left(\rho u_i u_j\right) = -\frac{\partial p}{\partial x_i} + \frac{\partial}{\partial x_j}\left[\mu\left(\frac{\partial u_i}{\partial x_j} + \frac{\partial u_j}{\partial x_i} - \frac{2}{3}\delta_{ij}\frac{\partial u_l}{\partial x_l}\right)\right] + \frac{\partial}{\partial x_j}\left(-\rho\langle u_i' u_j'\rangle\right) \tag{2-9}$$

The Boussinesq hypothesis is used to model the Reynolds stress terms, $-\rho\langle u_i' u_j'\rangle$. The closure equation is shown below:

$$-\rho\langle u_i' u_j'\rangle = \mu_T\left(\frac{\partial u_i}{\partial x_j} + \frac{\partial u_j}{\partial x_i} - \frac{2}{3}\delta_{ij}\frac{\partial u_l}{\partial x_l}\right) \tag{2-10}$$

μ_T is the turbulent eddy viscosity. It can be seen that turbulence modelled in this manner is isotropic. i.e. $\rho\langle {u_1'}^2\rangle = \rho\langle {u_2'}^2\rangle = \rho\langle {u_3'}^2\rangle$. While this is an approximation, this has been shown to provide reasonably accurate results for film cooling flow problems. (Harrison and Bogard, 2008).

The energy equation for steady, incompressible flow is modelled in FLUENT using the following equation (Ansys FLUENT theory guide, 2012):

$$\begin{gathered}\rho c_p \nabla T = \kappa_{eff}\nabla^2 T \\ \kappa_{eff} = \left(\kappa + \left(\frac{c_p \mu_T}{\mathrm{Pr}_t}\right)\right),\end{gathered} \tag{2-11}$$

where κ is the molecular thermal conductivity, and κ_{eff} is the effective thermal conductivity. The turbulent contribution to thermal conductivity is given by the term $\left(\frac{c_p \mu_T}{Pr_t}\right)$: a model constant, the turbulent Prandtl number (Pr_t) is used to relate this term to the eddy viscosity (μ_T).

The k- ε family of turbulence models solves equations for turbulent kinetic energy, k, and turbulence dissipation rate, ε. k and ε are expressed as:

$$k = \frac{1}{2}\langle u_i' u_i' \rangle$$
$$\varepsilon = \nu \langle \left(\frac{\partial u_i'}{\partial x_j} + \frac{\partial u_j'}{\partial x_i} \right)^2 \rangle \quad (2\text{-}12)$$

k is the turbulent kinetic energy per unit mass (units: m^2/s^2), and ε is the rate of dissipation of kinetic energy (units: m^2/s^3). Dimensional analysis is used to correlate μ_T with k and ε:

$$\mu_T = \rho C_\mu \frac{k^2}{\varepsilon}, \quad (2\text{-}13)$$

where C_μ is an empirical constant.

Turbulence intensity (Tu) and length scale (l) are specified as boundary conditions at the inlets of the domain. These are converted to values of k and ε using the following expressions:

$$k = \frac{3}{2}\left(u_{avg}.Tu\right)^2$$
$$\varepsilon = C_\mu^{3/4} \frac{k^{3/2}}{l}, \quad (2\text{-}14)$$

where u_{avg} is the mean flow velocity.

The effect of turbulence quantities on endwall cooling is described in Section 3.1.5. Turbulence determines the mixing of cooling jet momentum and thermal energy with the freestream. Accurate modelling of turbulence is thus important for film cooling prediction.

3 PHYSICS OF ENDWALL FLOWS

Secondary flow features have been recognized as significant in the near-wall flow. Models based on these features have informed the design of endwall cooling systems. The validity of these models and their limits of applicability will be examined in this chapter.

3.1 Planar Cascade Study

To study the influence of different variables on near-wall flows, CFD simulations were performed on a simple vane cascade geometry. An engine NGV mid-span section (Figure 3-1 (a)) was linearized and extruded to form the vane geometry. The CFD domain used is shown in Figure 3-1 (b). The endwalls are flat; contraction is not modelled. A six-passage geometry, described in Section 2.2, was used to simplify mesh generation in ICEM-CFD. A double-row of film cooling holes is located on the top endwall of the central two passages. The inclination angle of the holes is 40° and their length to diameter ratio is 2.85. Coolant is fed through a plenum to the double-row of film cooling holes. These are located only upstream of the central two passages of the top endwall.

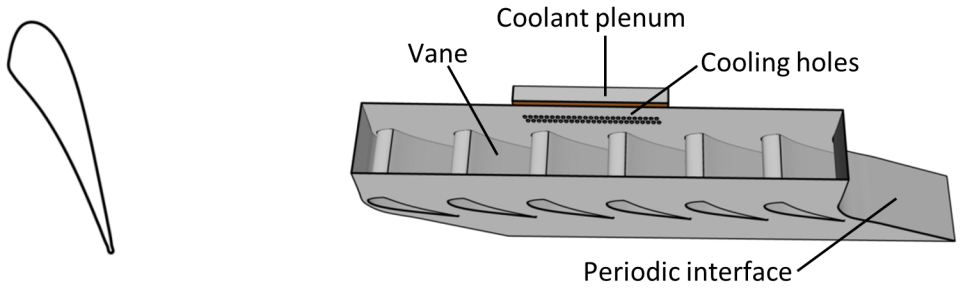


Figure 3-1: Planar cascade geometry: (a) Vane cross-section; (b) CFD domain

A tetrahedral mesh with 6 million elements was generated. The incompressible pressure-based solver in FLUENT was used to obtain CFD solutions. The k-ε turbulence model was used with wall functions. Maximum y^+ values of 40 were calculated on the endwall. A total pressure inlet boundary condition (BC) was specified at the inlet of the

cascade, and a constant mass flow rate BC was specified at the inlet of the coolant plenum. A constant static pressure outlet BC was used. The incompressible flow boundary conditions used are given in Table 2-3. The effect of varying flow parameters at these boundaries is studied in the following sections.

Experimental and CFD results are presented in terms of adiabatic effectiveness, defined as:

$$\eta_{eff} = \frac{T_\infty - T_{aw}}{T_\infty - T_c}, \tag{3-1}$$

where T_∞ is the freestream temperature, T_c is the coolant temperature, T_{aw} is the adiabatic wall temperature.

3.1.1 Low coolant flow rate

The coolant-to-mainstream mass flux ratio ($\dot{m}_c/\dot{m}_\infty$) was set to 1%. Adiabatic effectiveness contours on the cooled endwall are shown in Figure 3-2.

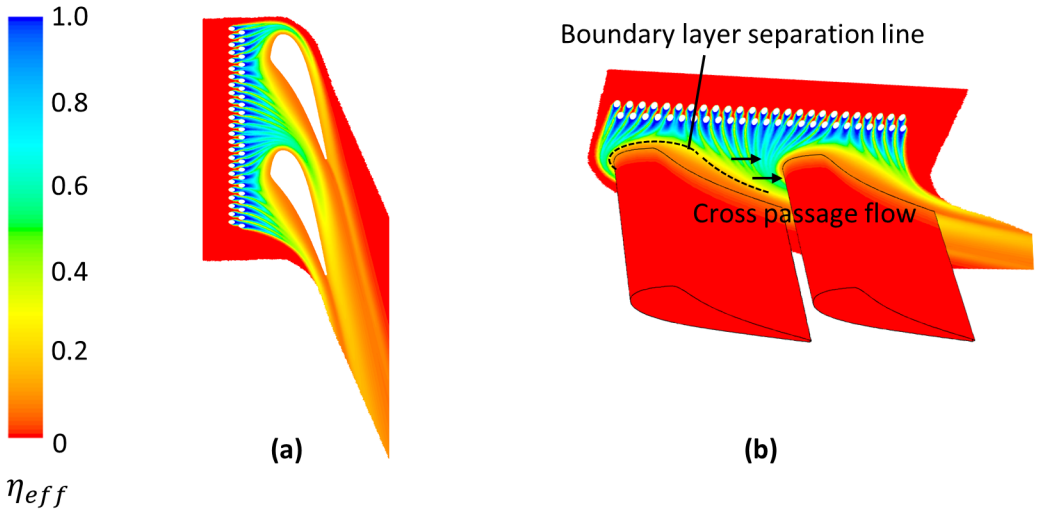


Figure 3-2: η_{eff} contours (CFD) for $\dot{m}_c/\dot{m}_\infty = 1\%$: (a) Plan view; (b) Isometric view

At these low coolant mass flux ratios, the near-wall flow is described well by the classical secondary flow models of Section 1.6. The coolant acts a marker for the near-wall flow. The endwall boundary layer can be seen separating upstream of the vanes in Figure 3-2

(b). The low momentum near-wall flow is driven from the PS endwall to the SS endwall. The coolant is unable to reach the vane PS. The cross-passage flow leaves a large portion of the rear endwall PS uncooled (Figure 3-2 (a)).

Surface streamlines coloured by η_{eff} are shown in Figure 3-3. The horseshoe vortex recirculation bubble is visible. The boundary layer separation line is marked by the warm uncooled ring around the vane. The swirl of the oilflow streamlines in this separated region is mild compared to secondary flow models in literature. It is worth noting that the authors (Langston, 1977, Sharma and Butler, 1987, Wang and Olson, 1997) state that their models show vortices with exaggerated spin for clarity.

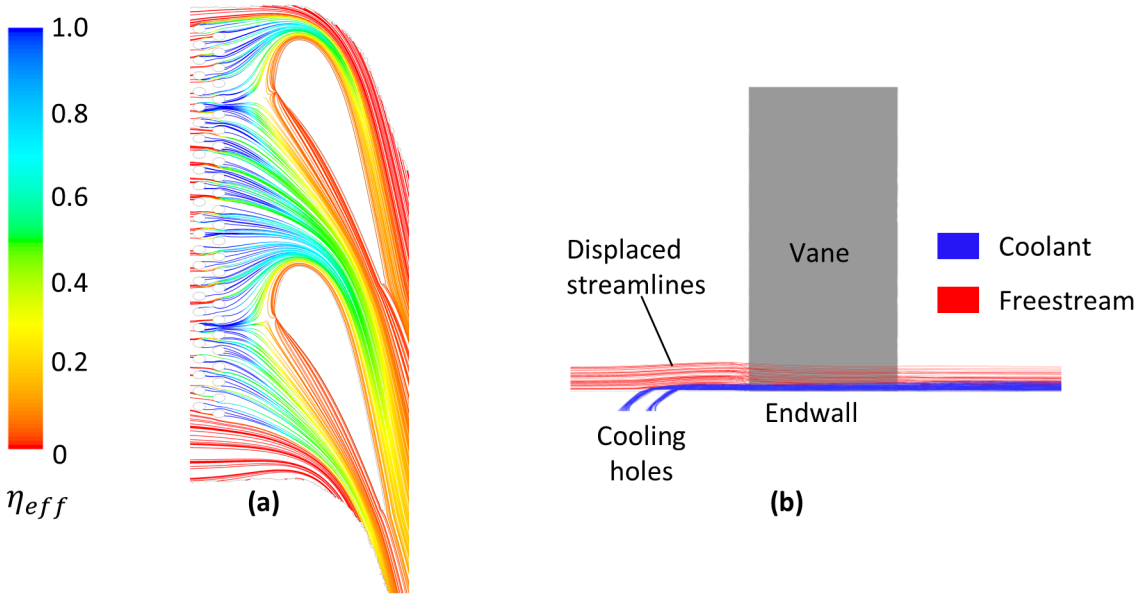


Figure 3-3: (a) Surface streamlines coloured by η_{eff}; (b) Freestream and coolant streamlines

At these low coolant flow rates, coolant trajectories are influenced significantly by the pressure field of the vane. Figure 3-3 (a) shows coolant emerging from holes with considerable deviation from the axial direction. Figure 3-3 (b) shows streamlines in the near-wall region. Coolant displaces mainstream flow from the endwall. As will be discussed in

Section 3.1.3, the low momentum of this coolant film gives rise to classical secondary flow features.

3.1.2 Effect of inlet boundary layer

The effect of an inlet boundary layer is now considered. A 1/7th power law velocity profile was used to model the boundary layer. This is given by the following equation:

$$\frac{U}{U_\infty} = \left(\frac{z}{\delta}\right)^{1/7}, \tag{3-2}$$

where δ is the boundary layer thickness, set to $0.2\,S$. A constant inlet velocity profile was used as the inlet boundary condition for a comparison test case. These profiles are shown in Figure 3-4 (a). Turbulence intensity and length scale were kept constant at 15% and $0.22\,V$ for both cases. While turbulence quantities do vary in the boundary layer, it was decided to isolate the effect of velocity variation in this study. It is expected that the resulting total pressure variation will have the greatest impact on secondary flow formation.

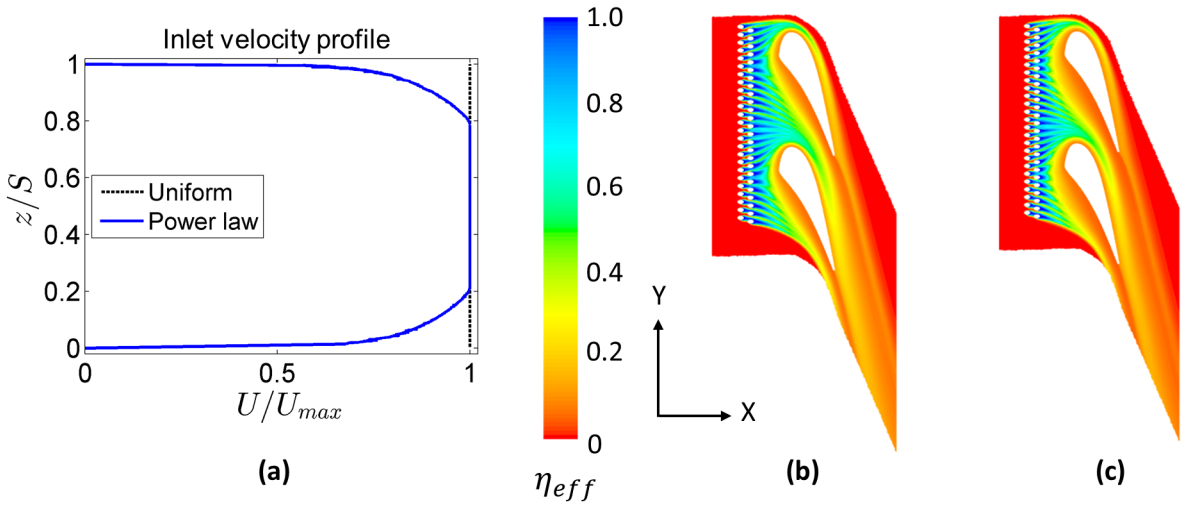


Figure 3-4: (a) 1/7th power law velocity profile; η_{eff} contours with: (b) Constant inlet velocity; (c) Power-law velocity profile

Figure 3-4 (b) shows endwall η_{eff} contours for the constant inlet velocity case. Figure 3-4 (c) shows contours for the power-law inlet velocity profile case. The boundary layer

separation line has advanced upstream in the simulation with a velocity profile. The thicker boundary layer is more susceptible to the adverse pressure gradient imposed by the vane. Separation occurs earlier on the endwall, resulting in the larger uncooled region on the PS of the passage.

3.1.3 Mitigation of secondary flows at higher coolant flow rates

CFD solutions were obtained with $\dot{m}_c/\dot{m}_\infty$ set to 2%, 3%, 6%. A uniform total pressure BC was used at the inlet. η_{eff} contours on the cooled endwall are shown in Figure 3-5.

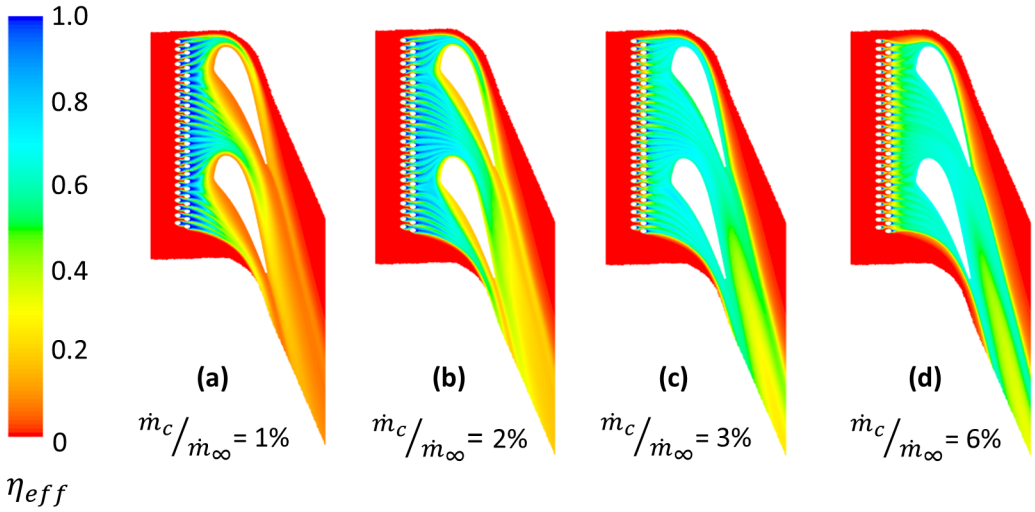


Figure 3-5: Effect of coolant injection on secondary flows

The near-wall flow is modified considerably by the injection of coolant. At low coolant flow rates, $\dot{m}_c/\dot{m}_\infty$ = 1% and 2% (Figure 3-5 (a) and (b)), a clear boundary layer separation line is observed. Cross-flows drive coolant from the endwall PS to the SS. However at a moderate coolant flow rate, $\dot{m}_c/\dot{m}_\infty$ = 3% (Figure 3-5 (c)), no boundary layer separation is observed. Coolant is able to reach the vane PS and the entire endwall is cooled.

As described in Section 1.6, secondary flows are driven by the vane inlet total pressure gradient. Figure 3-6 shows plots of pitchwise-averaged total pressure profiles on a

plane 2.5 hole diameters downstream of the last cooling hole row. A non-dimensional variable, $\hat{P} = (P_0 - P_{out})/(P_{0,in} - P_{out})$, is used to present the profiles. $\hat{P} > 1$ implies a surplus of total pressure, and thus momentum; $\hat{P} < 1$ implies a deficit.

The near-wall flow for the low coolant flow rate cases ($\dot{m}_c/\dot{m}_\infty$ = 1%, 2%) has a deficit in momentum. This results in separation of the boundary layer and the classical secondary flow pattern.

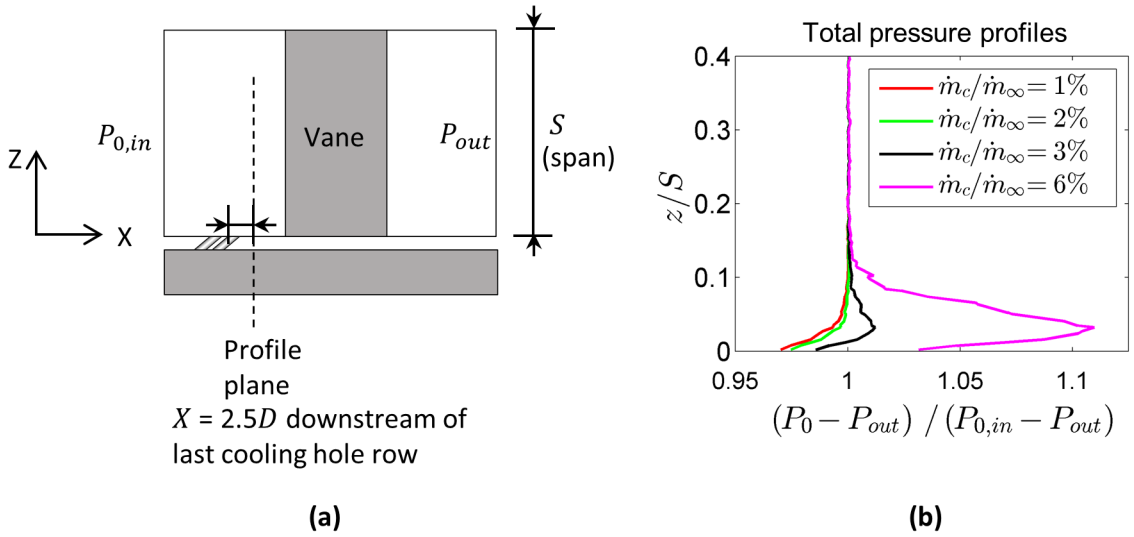
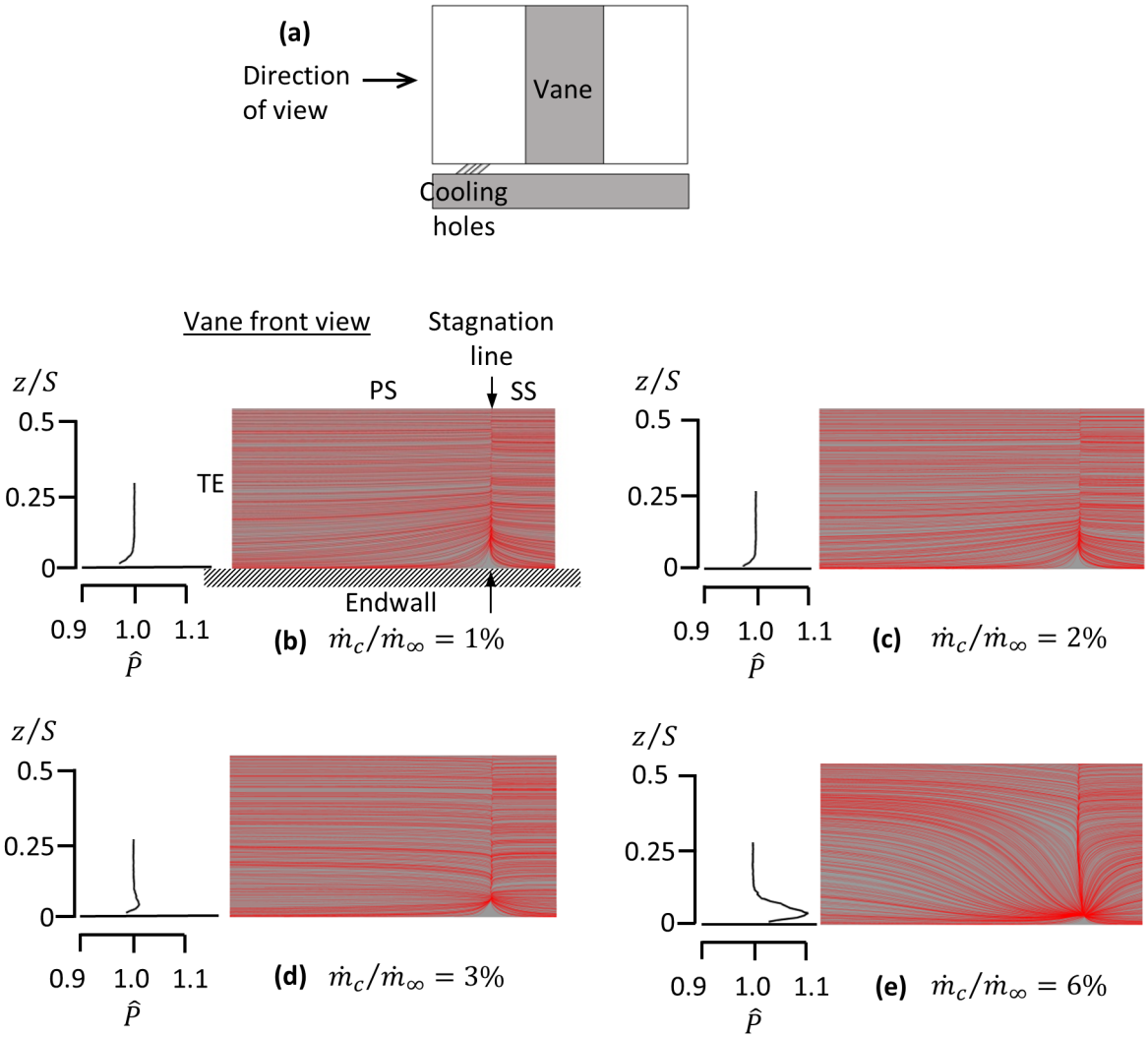


Figure 3-6: Total pressure profile: (a) Averaging plane location; (b) Pitchwise averaged total pressure profiles

However at higher coolant flow rate ($\dot{m}_c/\dot{m}_\infty$ = 3%, 6%) a surplus of P_0 is observed. Boundary layer separation does not occur at these high coolant flow rate cases (Figure 3-5 (c) and (d)); the near-wall flow is able to overcome the adverse pressure gradient imposed by the vane. The radial equilibrium equation (Equation (1-7), Section 1.6) requires that the near-wall flow migrates from SS to PS: the direction of cross-passage flow is reversed. In Figure 3-5 (c) and (d), coolant is driven towards the endwall PS and emerges as a cool streak at the PS TE.

Oilflow streamlines on the vane surface are shown in Figure 3-7. The vane is viewed from upstream (see Figure 3-7 (a)). The location of the stagnation line is shown by the oilflow pattern – this is marked in Figure 3-7 (b) along with the location of the vane TE and the endwall. The pitchwise average of non-dimensional total pressure, $\hat{P} = (P_0 - P_{out})/(P_{0,in} - P_{out})$, was plotted in Figure 3-6 (b). It is shown next to the oilflow diagrams.



$$\hat{P} = (P_0 - P_{out})/(P_{0,in} - P_{out})$$

Figure 3-7: Oilflow streamlines on vane surface

The vane inlet dynamic pressure is converted to static pressure at the stagnation line. The resulting pressure gradient drives vortex flows. Figure 3-7 (b) and (c) show oilflow patterns at low coolant flow rates ($\dot{m}_c/\dot{m}_\infty$ = 1%, 2%). Downwash resulting from the classical horseshoe vortex is visible on either side of the stagnation line near the endwall. The $\hat{P}$ plot for these conditions shows decreasing total pressure towards the endwall. This results in downwash. At higher coolant flow rates, coolant injection results in increased near-wall total pressure. For $\dot{m}_c/\dot{m}_\infty$ = 3% (Figure 3-7 (d)), a peak in total pressure is observed at z/S = 0.03, with $\hat{P}$ > 1. Upwash and downwash are noted on either side of the peak. At a higher coolant mass flow rate ($\dot{m}_c/\dot{m}_\infty$ = 6%, Figure 3-7 (e)), these flow structures are more prominent. A peak in $\hat{P}$ is observed at z/S = 0.03, with strong upwash and downwash on either side.

Coolant streamlines are shown in Figure 3-8. At low coolant mass flux ratio ($\dot{m}_c/\dot{m}_\infty$ = 1%, Figure 3-8 (a)), the vane pressure field stops the coolant streamlines from reaching the vane PS. As coolant mass flux ratios increases ($\dot{m}_c/\dot{m}_\infty$ = 2% and 3%, Figure 3-8 (b) and (c)), the coolant streamlines have sufficient momentum to reach the vane PS. At high coolant mass flux ratio ($\dot{m}_c/\dot{m}_\infty$ = 6%, Figure 3-8 (d)), coolant streamlines jet to the vane. They are driven away from the endwall and into the freestream (Figure 3-8 (d)). This results in inefficient cooling of the endwall.

Higher blowing ratio is observed at the leading-row of cooling holes. This will be described in Section 3.3.2. This results in coolant jets lifting off downstream of the leading-row of holes (Figure 3-8 (e)). Coolant jets emerging from the trailing-row are attached to the endwall (Figure 3-8 (f)). However, upwash on the vane directs coolant streamlines away from the endwall. Due to lift-off, the streamlines from the leading-row meet the vane at a

greater spanwise distance from the endwall. This drives them further up the vane than coolant from the trailing-row (compare Figure 3-8 (e) with (f)).

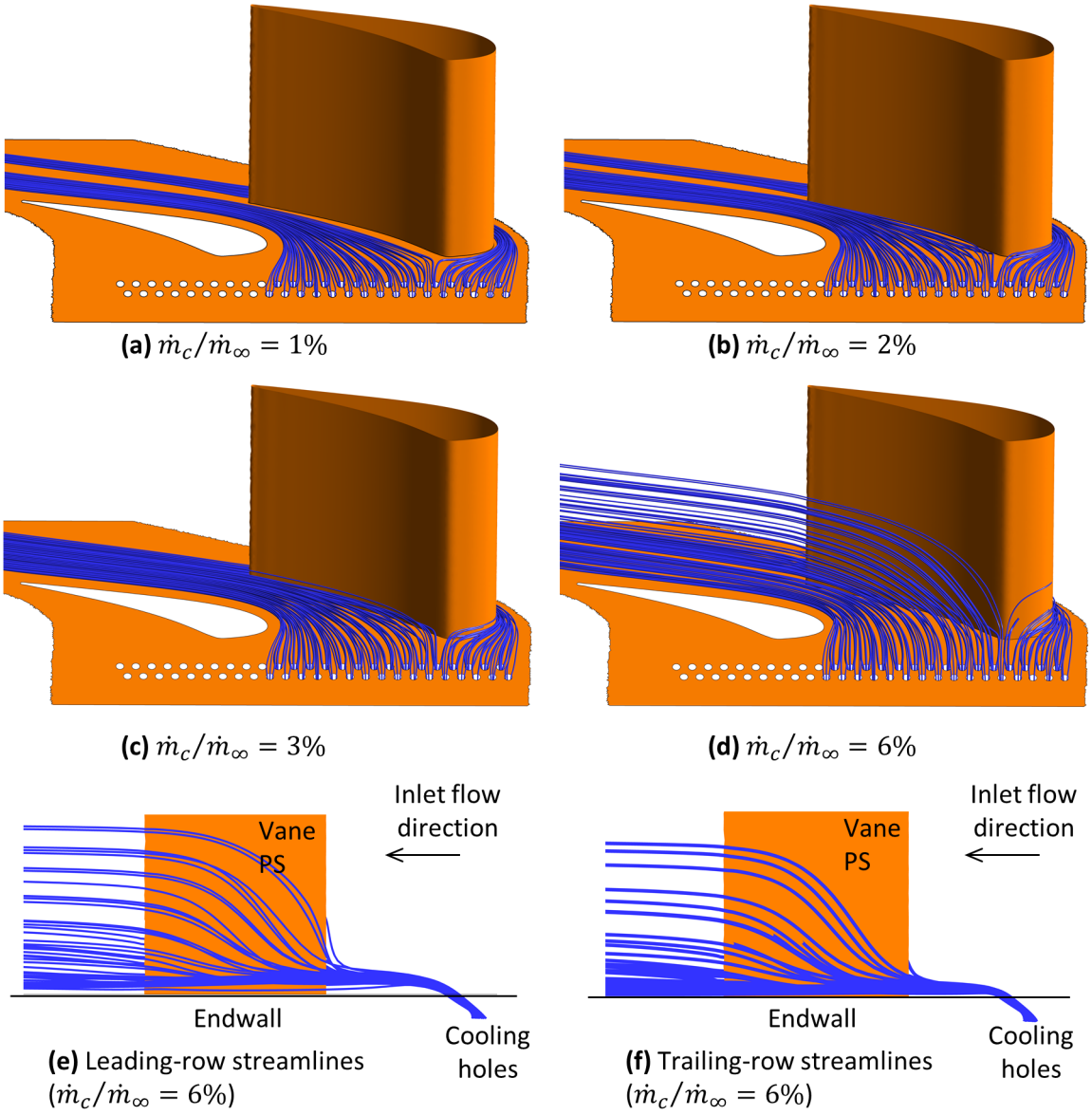


Figure 3-8: Coolant streamlines

3.1.4 Effect of hole inclination angle

The effect of hole inclination is now considered. Manufacturing constraints limit minimum hole inclination to around 25°. In this section, the performance of holes at this lower inclination is contrasted with the baseline system (40° inclination). Wall thickness was

kept constant. Hole length-to-diameter ratios thus increase from 2.85 for the high inclination holes, to 4.4 for the low inclination holes.

η_{eff} contours for $\dot{m}_c/\dot{m}_\infty$ = 2% are shown in Figure 3-9. A separation line is observed on the PS endwall for both the baseline inclination (Figure 3-9 (a)) and the low inclination case (Figure 3-9 (b)). However the separation line is shifted closer to the vane when coolant is injected at low inclination. This is shown in Figure 3-9 (c), which compares η_{eff} on a line $C_{ax}/4$ length downstream of the vane LE. The coolant is seen to reach further towards $y/y_{max} = 1$, leaving a smaller uncooled region on the PS endwall. Also, lower mixing with the freestream results in higher mean η_{eff} for the low inclination case.

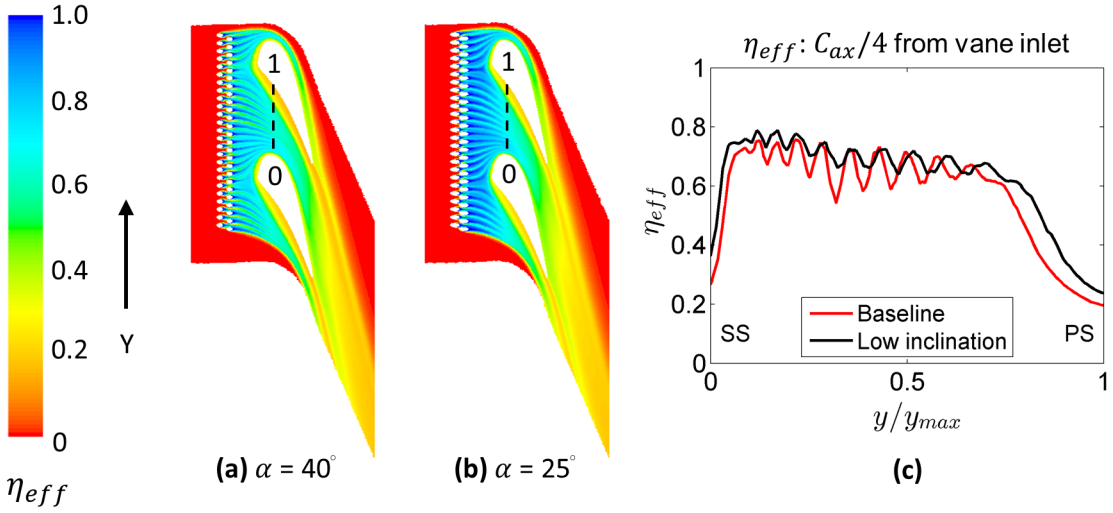


Figure 3-9: Effect of hole inclination ($\dot{m}_c/\dot{m}_\infty$ = 2%)

Higher streamwise momentum is injected into the boundary layer when coolant is injected at lower inclination. Figure 3-10 shows plots of pitchwise averaged vane inlet profiles, obtained on a plane downstream of the cooling holes (refer to Figure 3-6 (a) for location of plane). While little difference is observed in the profiles at a low coolant mass flow rate ($\dot{m}_c/\dot{m}_\infty$ = 1%, Figure 3-10 (a)), the low inclination holes are seen to provide a greater boost to near-wall total pressure at $\dot{m}_c/\dot{m}_\infty$ = 2%, 3% (Figure 3-10 (b), (c)). The endwall boundary layer has greater momentum, and is better able to resist the adverse

pressure gradient imposed by the vanes. Thus, at low to moderate coolant mass flux ratios, injecting coolant at a lower angle is advantageous if boundary layer separation is to be suppressed.

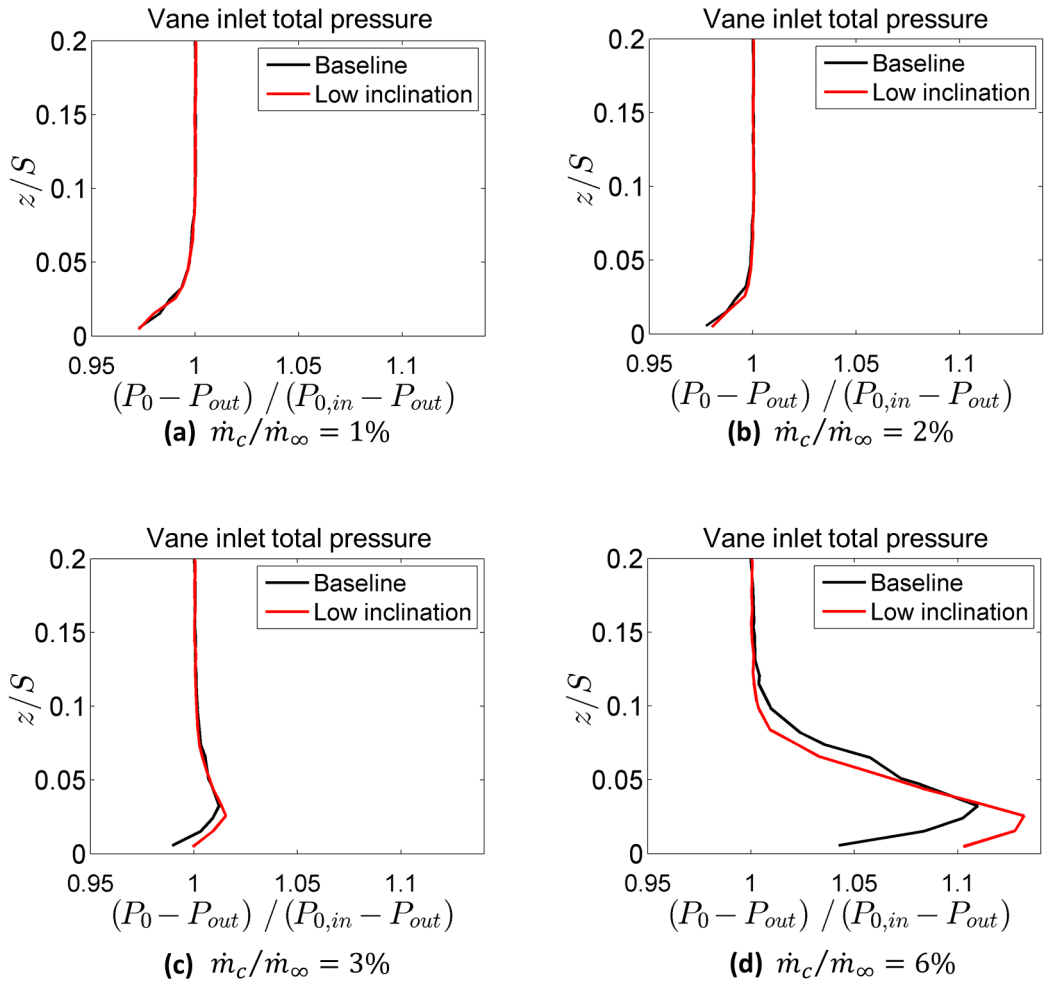


Figure 3-10: Effect of hole inclination: pitchwise averaged $\hat{P}$ plots

At $\dot{m}_c/\dot{m}_\infty = 6\%$, the low inclination holes provide the boundary layer with much more momentum than the baseline case (Figure 3-10 (d)). In Section 3.1.3 it was noted that a surplus in the $\hat{P}$ profile results in upwash on the vane, which drives coolant away from the endwall. While comparisons of η_{eff} on the endwall (later shown in Figure 3-11 (d), (e), (f)) do not show decreased η_{eff} at low inclination, coolant upwash results in inefficient endwall cooling and is undesirable.

Figure 3-11 shows η_{eff} contours at these high coolant flow rates for the baseline and low inclination case. Comparing Figure 3-11 (a) with (b), and Figure 3-11 (d) with (e), it is clear that the leading endwall is cooled better in the low hole inclination case. Figure 3-11 (c) and (f) show comparisons of η_{eff} distribution on the vane outlet line marked on the contour maps. The mean value of η_{eff} is shown with coloured squares. While the mean value of η_{eff} has not changed significantly, the coolant is redistributed further towards the SS and PS extremities in the low inclination case.

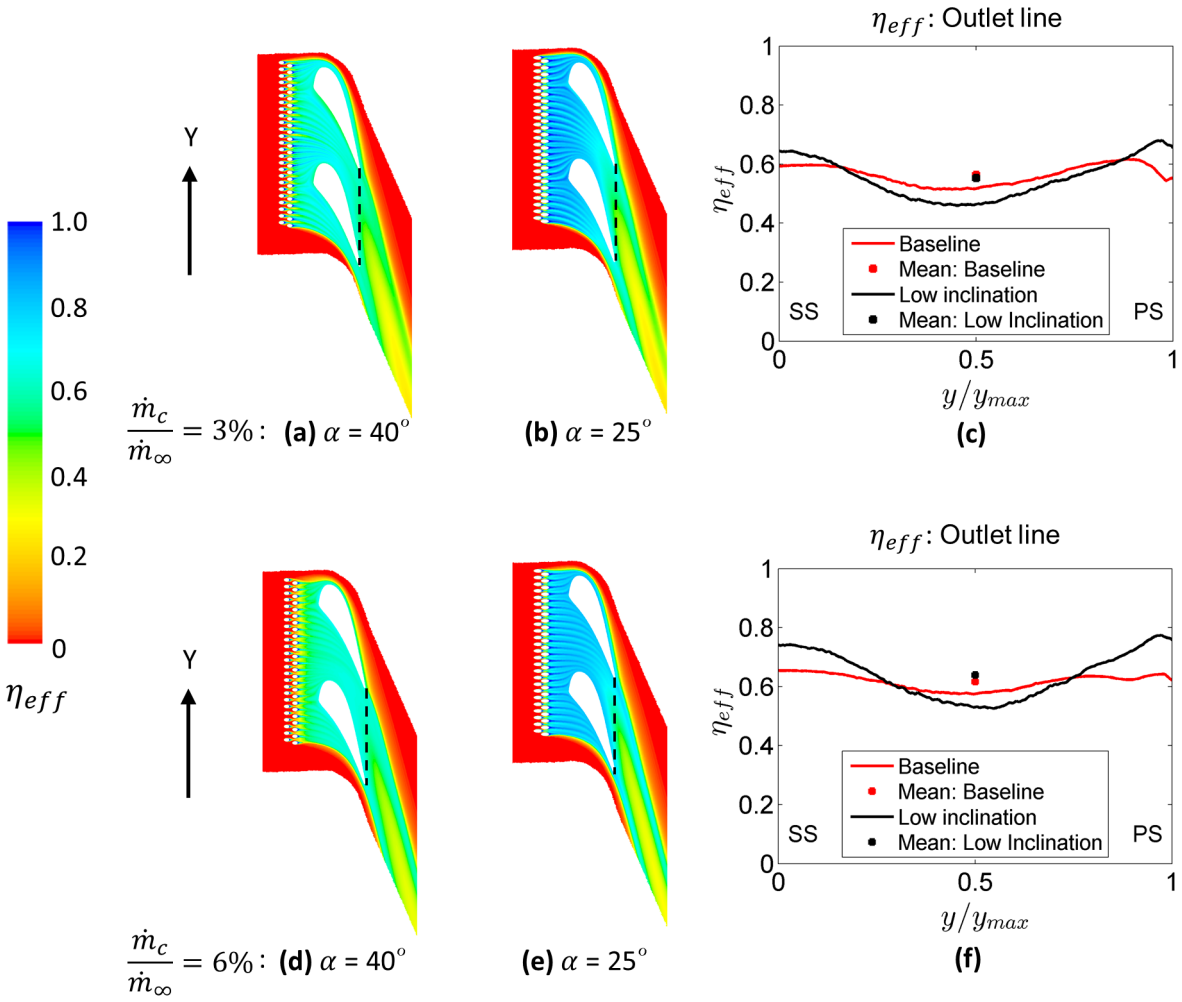


Figure 3-11: Effect of hole inclination (m_c/m_∞ = 3%, 6%)

This redistribution is explained with the oilflow plots of Figure 3-12 and Figure 3-13. As shown in Section 3.1.3, the vane inlet total pressure profile drives upwash and downwash

on either side of the peak $\hat{P}$ location. Figure 3-10 (c) and (d) compared inlet total pressure profiles for the baseline and low hole inclination cases. The peak $\hat{P}$ location is closer to the endwall for the low inclination cases. This results in a smaller region of downwash on the vane for the low inclination case (see Figure 3-12 (b) for $\dot{m}_c/\dot{m}_\infty$ = 3%, and Figure 3-13 (b) for $\dot{m}_c/\dot{m}_\infty$ = 6%) than the corresponding high inclination cases (Figure 3-12 (a) for $\dot{m}_c/\dot{m}_\infty$ = 3%, and Figure 3-13 (a) for $\dot{m}_c/\dot{m}_\infty$ = 6%). This results in more coolant at the PS and SS corners of the endwall. In contrast, at baseline hole inclination, coolant is driven away from the PS and SS corner by the downwash (see Figure 3-12 (c)). Indeed, at low hole inclination and high coolant mass flux ratio ($\dot{m}_c/\dot{m}_\infty$ = 6%), the near-wall flow possesses sufficient momentum to approach the vane in a nearly axial direction (Figure 3-13 (c)).

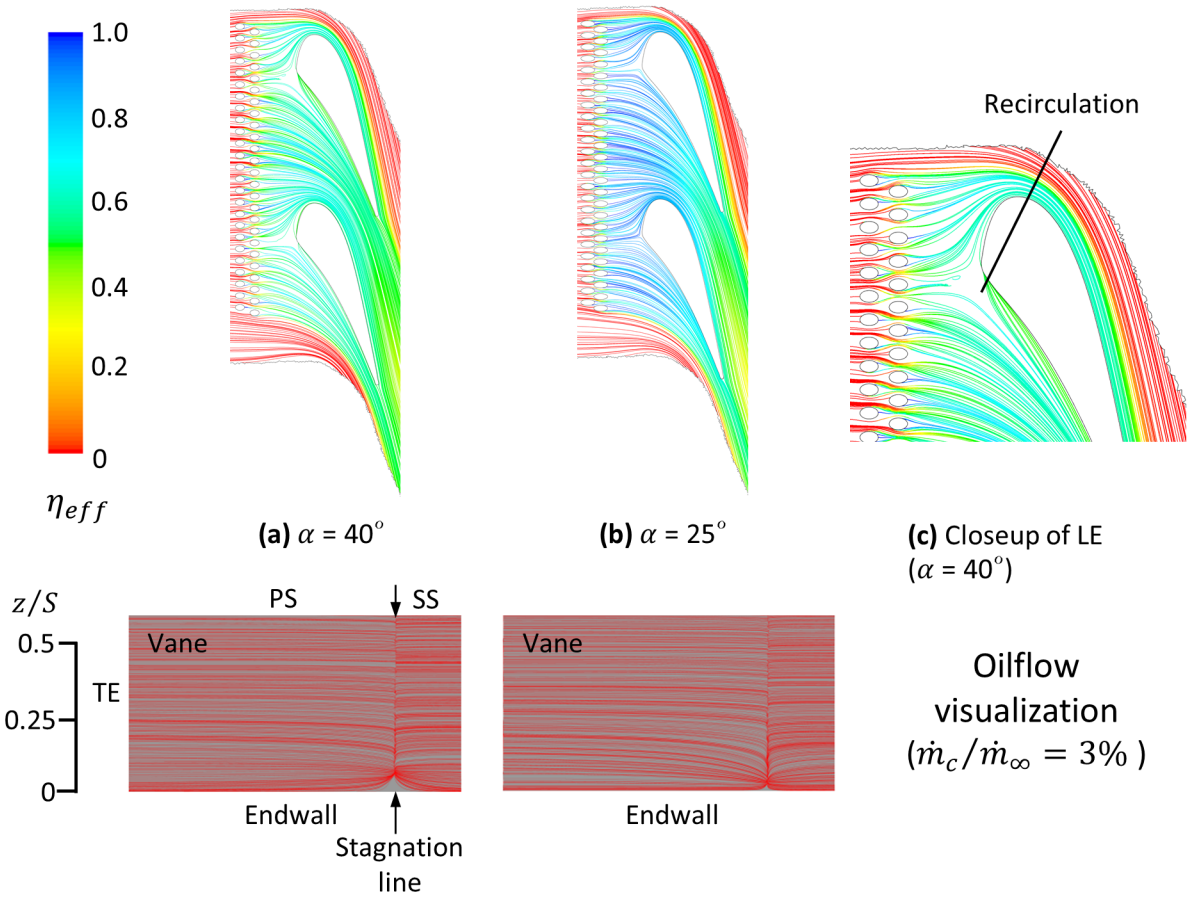


Figure 3-12: Oilflow visualization: $\dot{m}_c/\dot{m}_\infty$ = 3%

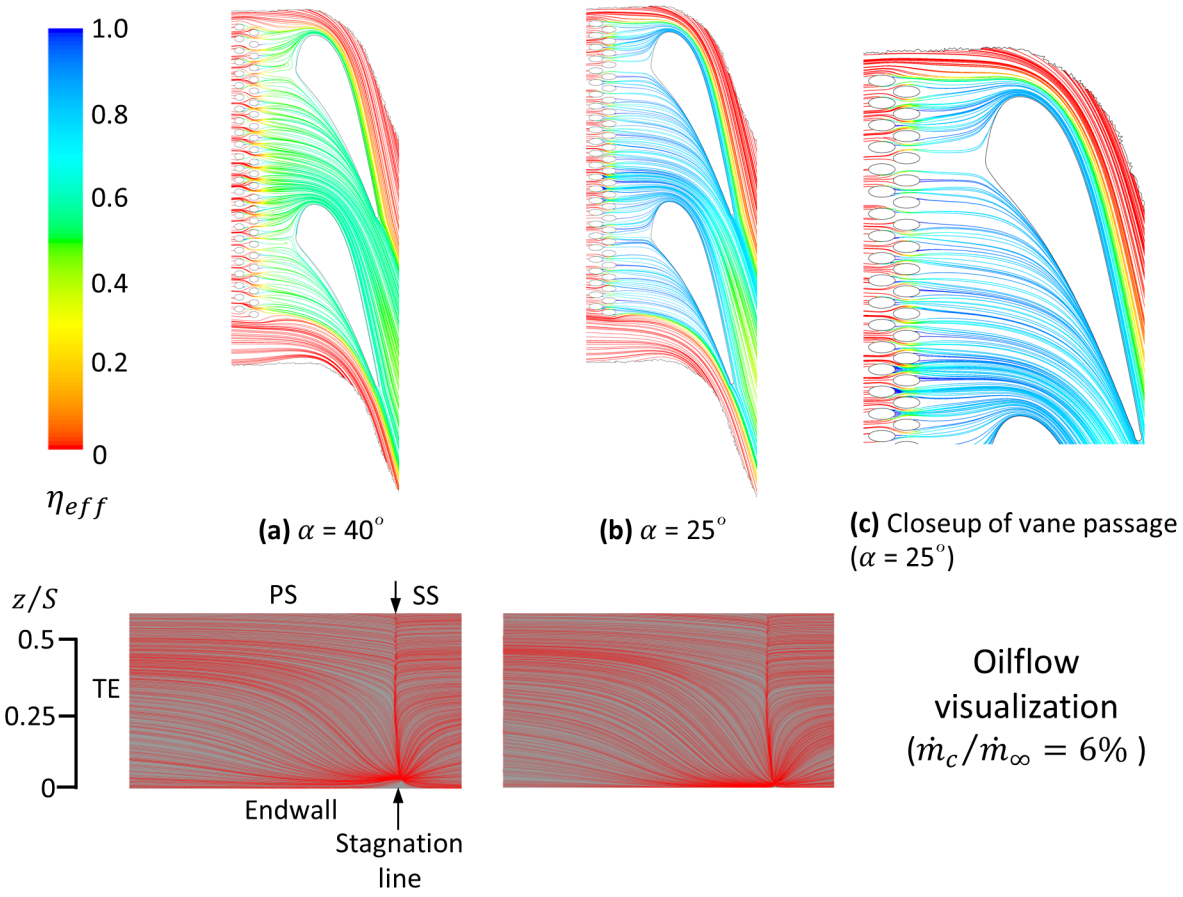


Figure 3-13: Oilflow visualization: $\dot{m}_c/\dot{m}_\infty$ = 6%

As will be explained in Chapter 5, the alignment of the combustor hot spot leaves the endwall downstream of the vane TE at a higher temperature. The redistribution of the coolant towards the vane-endwall junction at low hole inclination can be exploited to cool this region better. Also, it has been noted in Figure 3-11 (c) and (f) that the mean η_{eff} value at the rear of the passage is not changed significantly by reducing hole inclination. However, considerable improvement is noted in the front of the passage. An improved cooling strategy would involve injecting coolant at low inclination angle to suppress secondary flows and cool the front endwall better. Additional cooling holes can be placed further downstream to cool the rear endwall. This strategy will be studied in Chapter 4.

3.1.5 Effect of inlet turbulence level

Vigorous mixing of dilution jets leads to high turbulence intensities at the outlet of an RQL combustor (Cha et. al., 2012). Measurements by Barringer et. al., 2002, show that the turbulence length scale is on the order of the dilution jet diameter. Engine representative values of turbulence intensity (Tu = 15%) and turbulence length scale ($l = 0.22V$) were used in the baseline planar cascade simulations.

The realizable k-ε turbulence model was described in Section 2.3. The effect of turbulence is modelled through eddy viscosity, μ_T, which is obtained by solving field equations for turbulence kinetic energy (k) and turbulence dissipation rate (ε).

Figure 3-14 compares CFD predictions of endwall η_{eff} at the baseline (Tu = 15%) and a low freestream turbulence intensity level (Tu = 3%). At higher freestream turbulence intensity, Equations (2-13) and (2-14) predict greater eddy viscosity (μ_T). This results in higher effective thermal conductivity, κ_{eff} (Equation (2-11)). Higher κ_{eff} increases mixing in the thermal field.

Cooling effectiveness decays earlier on the passage in the high Tu cases (Figure 3-14 (a) for $\dot{m}_c/\dot{m}_\infty$ = 1%, and Figure 3-14 (c) for $\dot{m}_c/\dot{m}_\infty$ = 3%) than the corresponding low Tu cases (Figure 3-14 (b) for $\dot{m}_c/\dot{m}_\infty$ = 1%, and Figure 3-14 (d) for $\dot{m}_c/\dot{m}_\infty$ = 3%). This is caused by increased mixing with the mainstream. Figure 3-14 (a) and (b) compare η_{eff} on the endwalls for $\dot{m}_c/\dot{m}_\infty$ = 1%. A clear boundary layer separation line is visible on the η_{eff} contours in the low Tu case (Figure 3-14 (b)). Enhanced mixing in the high Tu case (Figure 3-14 (a)) diffuses cooling effectiveness into the PS endwall. Many early linear cascade studies of film cooling have been conducted with low inlet turbulence intensities (Graziani et. al., 1980, Friedrichs et. al., 1999). The presence of a marked separation line on endwall η_{eff} contour plots is attributable to low freestream Tu. Coolant lift-off is marked by a trough in

η_{eff} downstream of the cooling holes in Figure 3-14 (d). This trough is not observed in the high Tu case (Figure 3-14 (c)) – greater mixing diffuses cooling effectiveness to the endwalls.

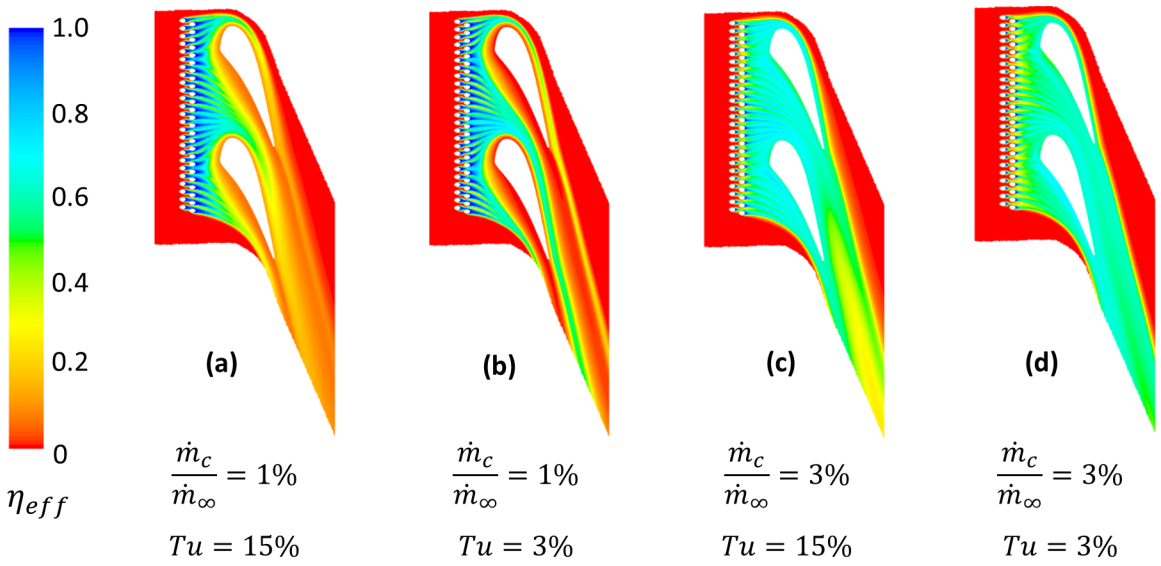
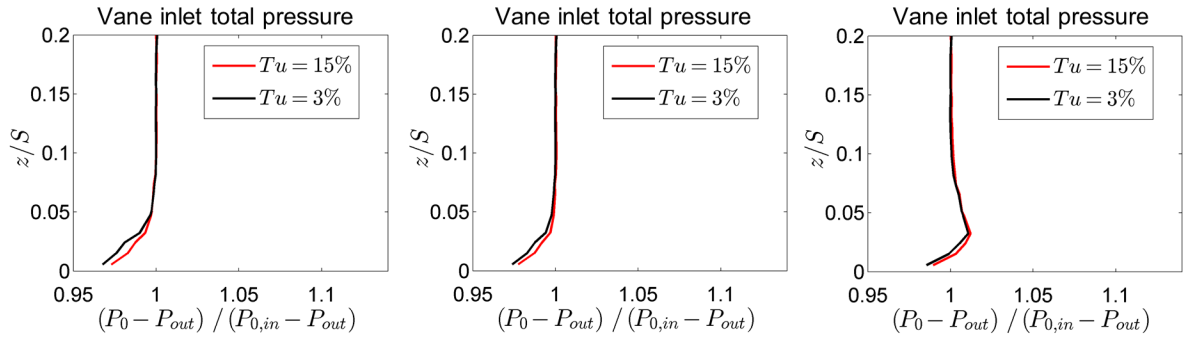


Figure 3-14: Effect of turbulence intensity: η_{eff} contours

Figure 3-15 compares vane inlet profiles at high and low Tu for different coolant mass flow rates. Higher values of $\hat{P}$ are observed in the near-wall region for the high turbulence cases (Tu = 15%). This is caused by greater transport of momentum. As observed in Section 3.1.2, a greater deficit in near-wall total pressure leads to earlier separation of the endwall boundary layer. This is likely another cause for the large separated zones observed in low-turbulence linear-cascade tests. Recent measurements by Thole et. al. (2002), Narzary et. al. (2009) confirm that the horseshoe vortex is formed closer to the vane at high turbulence levels.



(a) $\dot{m}_c/\dot{m}_\infty = 1\%$ **(b)** $\dot{m}_c/\dot{m}_\infty = 2\%$ **(c)** $\dot{m}_c/\dot{m}_\infty = 3\%$

Figure 3-15: Effect of turbulence intensity: vane inlet total pressure profiles

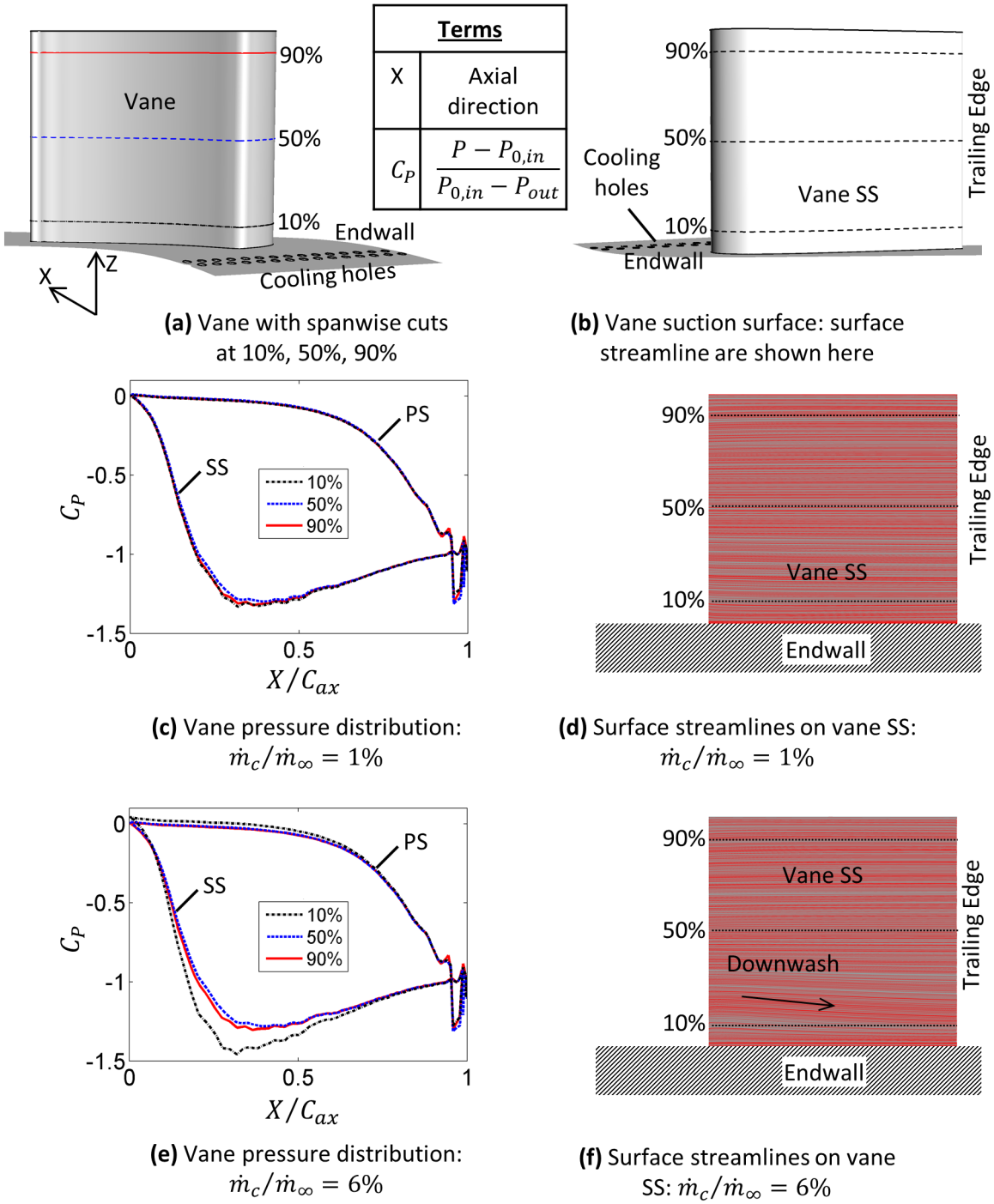
3.1.6 Effect of coolant injection on vane pressure field

Coolant injection changes the velocity of the near-wall fluid. This alters vane secondary flows. In section 3.1.3, coolant injection was seen to drive spanwise flows on the vane (see Figure 3-7). The spanwise flow was driven by gradients in the inlet total pressure field. This effect is now examined.

Figure 3-16 (a) shows a solid model of the vane with cuts marked at 10%, 50%, 90% span. Surface streamlines were plotted on the vane suction surface, shown in Figure 3-16 (b). Plots of C_P on the vane are shown in Figure 3-16 (c) for $\dot{m}_c/\dot{m}_\infty$ = 1%. Little difference is noted between the C_P distribution at 10%, 50% and 90% span. As expected, the surface streamlines shown on the vane SS (Figure 3-16 (d)) show little spanwise migration.

However at a higher coolant injection rate, $\dot{m}_c/\dot{m}_\infty$ = 6%, the near-wall C_P distribution (10% span) is significantly altered (see Figure 3-16 (e)). The total pressure of the near-wall flow has increased, resulting in higher C_P on the PS. A lower pressure is required to turn the higher velocity flow around the suction surface shoulder. This results in lower C_P on the SS. The pressure gradient from 50% to 90% span drives downwash on the vane SS (see Figure 3-16 (f)). The surplus near-wall momentum eventually mixes out with the freestream.

The C_P curves for 10%, 50%, 90% span thus collapse at the rear of the vane (X/C_{ax} > 0.7 in Figure 3-16 (e)).



(a) Vane with spanwise cuts at 10%, 50%, 90%

(b) Vane suction surface: surface streamline are shown here

(c) Vane pressure distribution: $\dot{m}_c/\dot{m}_\infty = 1\%$

(d) Surface streamlines on vane SS: $\dot{m}_c/\dot{m}_\infty = 1\%$

(e) Vane pressure distribution: $\dot{m}_c/\dot{m}_\infty = 6\%$

(f) Surface streamlines on vane SS: $\dot{m}_c/\dot{m}_\infty = 6\%$

Figure 3-16: Effect of coolant injection on vane pressure field

Figure 3-17 contrasts C_P at 10% span for coolant injection at baseline (40°) vs. low inclination (25°) angle ($\dot{m}_c/\dot{m}_\infty$ = 6%). The effects on C_P persist further downstream in the

low inclination case. Greater streamwise momentum is imparted when injecting coolant at low inclination (see Figure 3-10 (d)). Also, coolant momentum mixes less rapidly with the freestream.

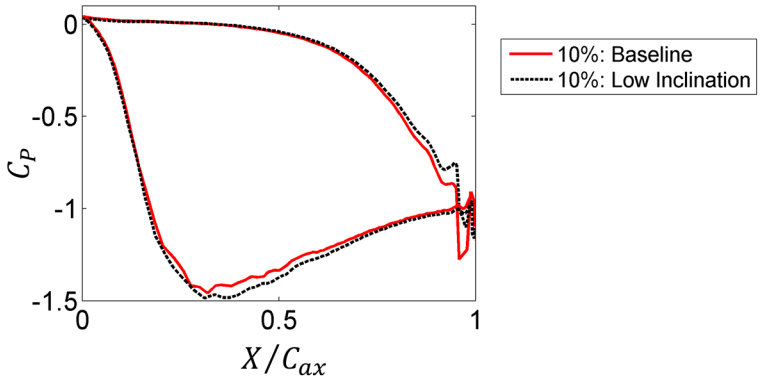


Figure 3-17: Vane pressure field at 10% span: Baseline vs. Low inclination ($\dot{m}_c/\dot{m}_\infty$ = 6%)

3.2 Experimental validation

3.2.1 Planar cascade vs. SSPCF cascade geometry

Several studies in literature use the planar cascade geometry of Section 3.1-3.1.5, to study endwall cooling flows. This geometry lends itself to simpler experimentation and offers valuable insight into near-wall flow. However, several engine realistic features are not captured in experiments using flat-endwall cascades.

The Superscale Platform Cooling Facility (SSPCF), described in Section 2.1, was used to obtain experimental η_{eff} maps on cooled endwalls. Figure 3-18 shows a solid model of the test section of the facility. The SSPCF cascade was a linear analogue of an engine representative NGV section. The vane geometry retained the 3D features of the engine representative NGV, including fillets at the endwall junction. The endwall profile was accurately reproduced. The outer platform (casing) in Figure 3-18 was flat; the inner platform (hub) had a contraction. Steps that resulted from engine realistic features, such as the combustor-turbine interface, have been modelled. These engine realistic features are expected

to play a significant role in determining boundary layer development. Also, the RODN cooling holes are closer to the vane than in the planar cascade CFD geometry. Local static pressure variation resulting from the vane potential field will be more significant than in the planar cascade case. This potential field effect will be examined in Section 3.3.2.

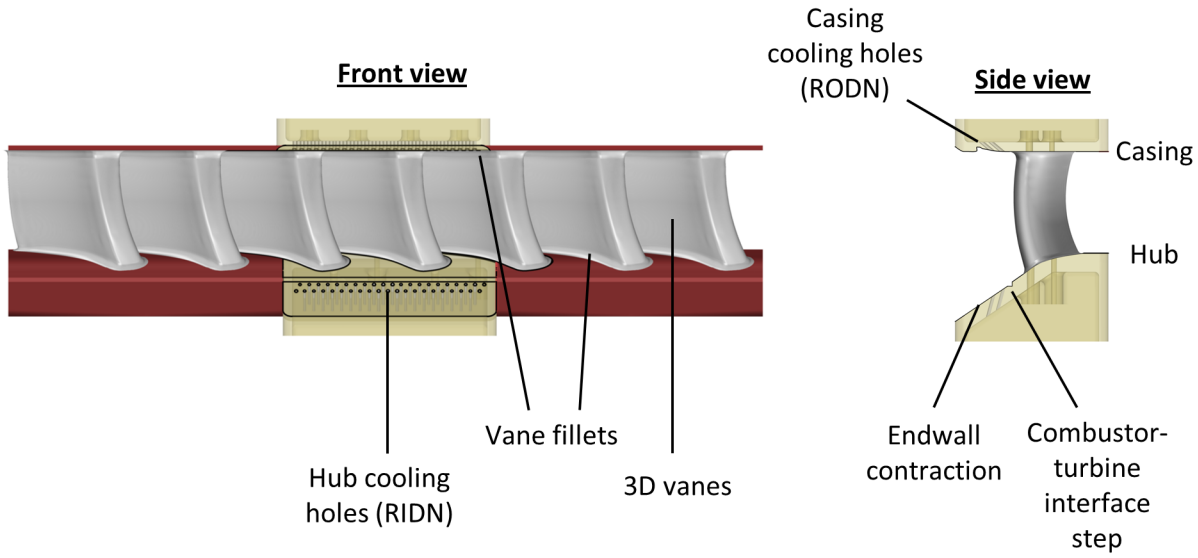


Figure 3-18: Solid model of SSPCF cascade and cooling system

A combustor simulator (see Section 2.1.4) was used upstream of the NGVs to generate representative inlet turbulence conditions. The cooling system studied in the SSPCF is a double row of film cooling holes called the RIDN/RODN. Figure 3-18 shows the location of the cooling holes – only the central two passages of the cascade are cooled. Details of the RIDN/RODN film cooling hole diameters, combustor simulator geometry, tunnel flow conditions are provided in Table 2-1 of Section 2.1.

3.2.2 Casing: CFD and experimental validation

IR thermographs of the casing are obtained at different coolant flow conditions using the procedure described in Section 2.1.7. The CFD results were obtained using the model described in Section 2.2.

Figure 3-19 shows sample η_{eff} maps obtained using experiment and CFD. IR thermographs were obtained of the front of the cascade (a) and the rear (b). The vanes are marked with dashed lines, and the location of the RODN film cooling holes is shown. In both the CFD and experimental η_{eff} maps, complete rows of RODN holes are only present upstream of the central passage. Thus, only data obtained from this passage will be considered. The suction side (SS) of the central passage is marked in Figure 3-19 (b). The passage PS lies outside the image. The CFD η_{eff} map, (c), is shown in plan view. Again, only data from the central passage will be considered.

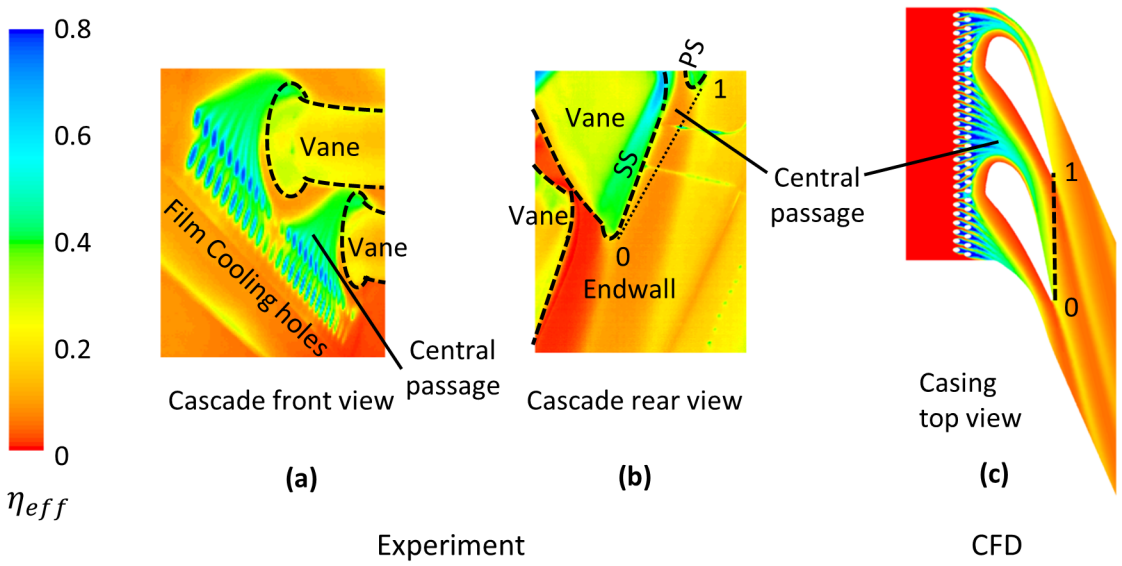


Figure 3-19: Experimentally measured η_{eff} on casing: (a) Cascade front view, (b) Cascade rear view; (c) CFD η_{eff} map on casing

Figure 3-20 (a) shows a CFD η_{eff} map obtained at low mass flux ratio ($\dot{m}_c/\dot{m}_\infty$ = 1%). Experimentally measured η_{eff} maps are shown in Figure 3-20 (d) and (e). The behaviour of the near-wall flow is visualized using the surface streamlines of Figure 3-20 (c). At this low mass flux ratio, the flow structure agrees with the classical picture. The coolant acts as a marker for the near-wall flow. The coolant separates upstream of the vanes, leaving an uncooled patch on the endwall PS (CFD, Figure 3-20 (a), Experiment, (d)). The coolant is driven towards the SS endwall by the cross-passage flow and climbs the trailing

vane SS (Figure 3-20 (e)). The surface streamline plot (Figure 3-20 (c)) shows that flow swirl is mild. This was noted in Section 3.1.1: secondary flow models in literature (Langston, 1977, Sharma and Butler, 1987, Wang and Olson, 1997) depict vortex systems with exaggerated spin.

The flow patterns are similar to the CFD results of the planar cascade at $\dot{m}_c/\dot{m}_\infty$ = 1% (Section 3.1.1). These patterns are caused by the classical secondary flow mechanisms described in Section 1.6. The low momentum near-wall flow is unable to overcome the adverse pressure gradient imposed by the vane. This results in flow separation. The mechanism driving the cross-flow is also classical: the cross-passage pressure gradient influences the near-wall flow more strongly because of its low momentum, driving it further towards the endwall SS. The effect of these mechanisms is to leave large sections of the critical trailing endwall uncooled (CFD: Figure 3-20 (a), experiment: (e)).

The casing cooling hole rows are closer to the vane in the SSPCF than in the planar cascade (compare Figure 3-20 (a) with Figure 3-2 (a)). The vane potential field thus has a greater influence. The cooling holes upstream of the vane PS are starved because of higher local static pressure (Figure 3-20 (d)).

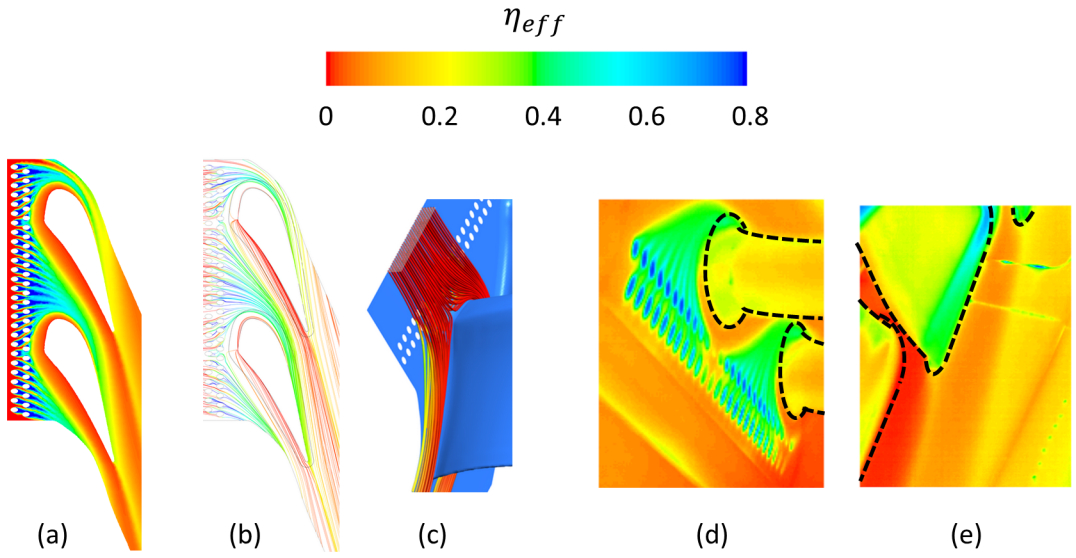


Figure 3-20: $\dot{m}_c/\dot{m}_\infty$ = 1%: (a) CFD predicted η_{eff}; (b) Oilflow streamlines (CFD) coloured by η_{eff}; (c) LE flow structure; Experimentally measured η_{eff} on: (d) Leading endwall, (e) Trailing endwall

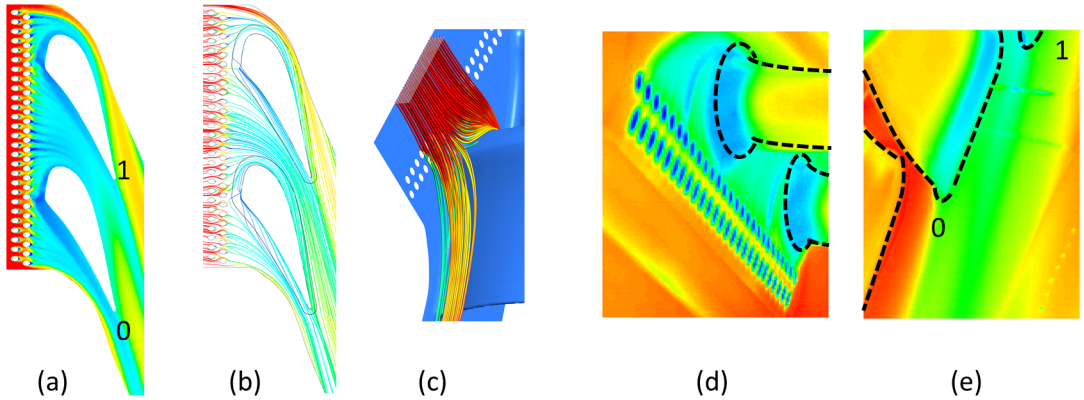


Figure 3-21: $\dot{m}_c/\dot{m}_\infty$ = 4%: (a) CFD predicted η_{eff}; (b) Oilflow streamlines (CFD) coloured by η_{eff}; (c) LE flow structure; Experimentally measured η_{eff} on: (d) Leading endwall, (e) Trailing endwall

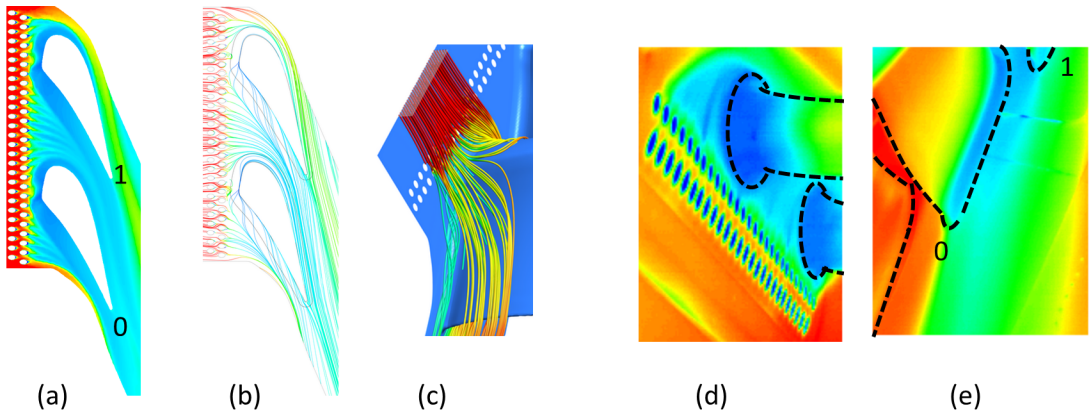


Figure 3-22: $\dot{m}_c/\dot{m}_\infty$ = 9%: (a) CFD predicted η_{eff}; (b) Oilflow streamlines (CFD) coloured by η_{eff}; (c) LE flow structure; Experimentally measured η_{eff} on: (d) Leading endwall, (e) Trailing endwall

Figure 3-21 shows results at $\dot{m}_c/\dot{m}_\infty$ = 4%. This is an engine representative coolant mass flux ratio. The flow-structure has changed significantly at this higher flow rate. The boundary layer does not separate upstream of the vane. The entire endwall is cooled, including the endwall PS (CFD: Figure 3-21 (a), experiment: (d), (e)). The oilflow streamlines of Figure 3-21 (b) show that the cross-flow direction is reversed. Coolant is driven towards the endwall PS and emerges as a cool streak at the vane TE (CFD: Figure 3-21 (a), experiment: (e)).

Figure 3-23 shows profiles of pitchwise-averaged normalized total pressure ($\hat{P}$) at the vane inlet plane. These are similar to the profiles shown in Figure 3-6 for the planar cascade case. The averaging plane is shown in Figure 3-23 (a). z/S = 0 corresponds to the location of the casing. It can be seen that higher coolant mass flux ratios result in greater momentum of the near-wall flow. As discussed in Section 3.1.3, this momentum allows the near-wall flow to overcome the adverse pressure gradient of the vane and avoid flow separation. The reversal of cross-flow direction at high coolant mass flux ratios was also seen in the planar cascade case (Section 3.1.3). As predicted by Equation (1-7) (Section 1.6), the surplus momentum drives near-wall flow towards the PS.

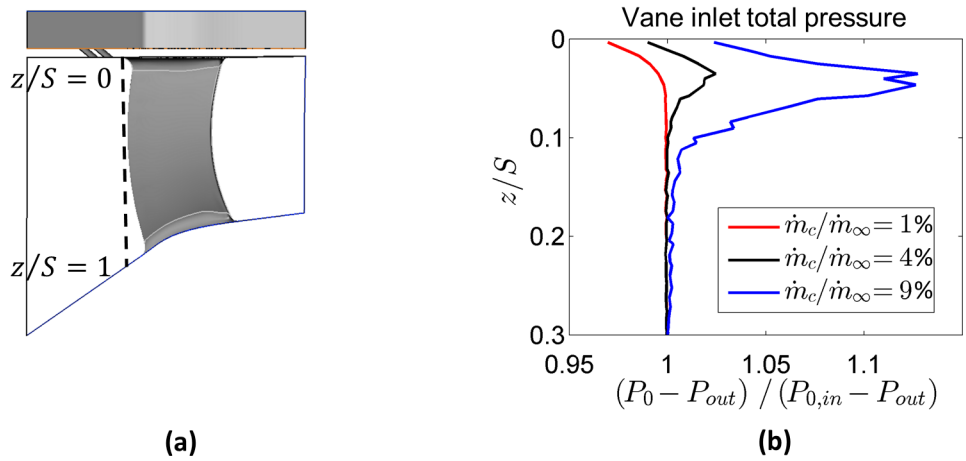
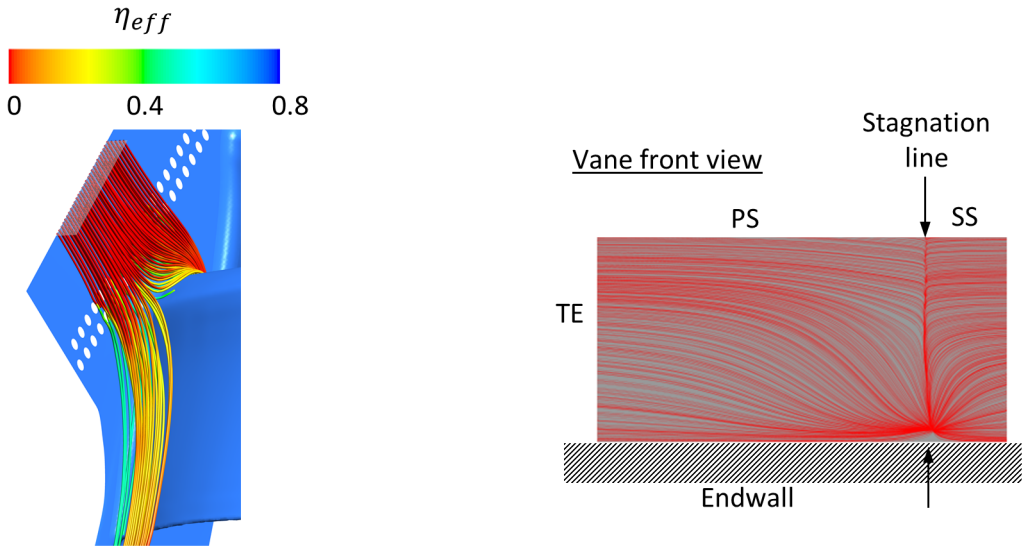


Figure 3-23: (a) Location of vane inlet plane; (b) $\hat{P}$ profiles at vane inlet plane

Inlet dynamic head is converted to static pressure on the vane stagnation line. Gradients in the static pressure field drive vortex flows. The streamline plot of Figure 3-24 (a) shows near-wall flow branching into upwash and downwash, driven by these pressure gradients. Similar secondary flows were observed at high mass flux ratios on the planar cascade oilflow streamlines (Figure 3-7 (e), repeated in Figure 3-24 (b)).



(a) Near-wall streamlines coloured by η_{eff} SSPCF: $\dot{m}_c/\dot{m}_\infty = 4\%$

(b) Surface streamlines on vane Planar cascade: $\dot{m}_c/\dot{m}_\infty = 6\%$

Figure 3-24: Upwash and downwash on vane: (a) Near-wall streamlines in SSPCF, $\dot{m}_c/\dot{m}_\infty$ = 4%; (b) Surface streamlines on planar cascade vane, $\dot{m}_c/\dot{m}_\infty$ = 6%

While coolant is attached to the wall downstream of the film cooling holes in the $\dot{m}_c/\dot{m}_\infty$ = 1% case (CFD, Figure 3-25 (a) and Experiment, (b)), this is not the case at $\dot{m}_c/\dot{m}_\infty$ = 4%. Films from the leading row are clearly lifted-off in both CFD (Figure 3-25 (a)) and experimentally measured (Figure 3-25 (b)) η_{eff} maps. The trough in η_{eff} downstream of the trailing row marks lift-off and reattachment of coolant from these holes. This was also observed in the planar cascade case ($\dot{m}_c/\dot{m}_\infty$ = 6%, Figure 3-5 (d)).

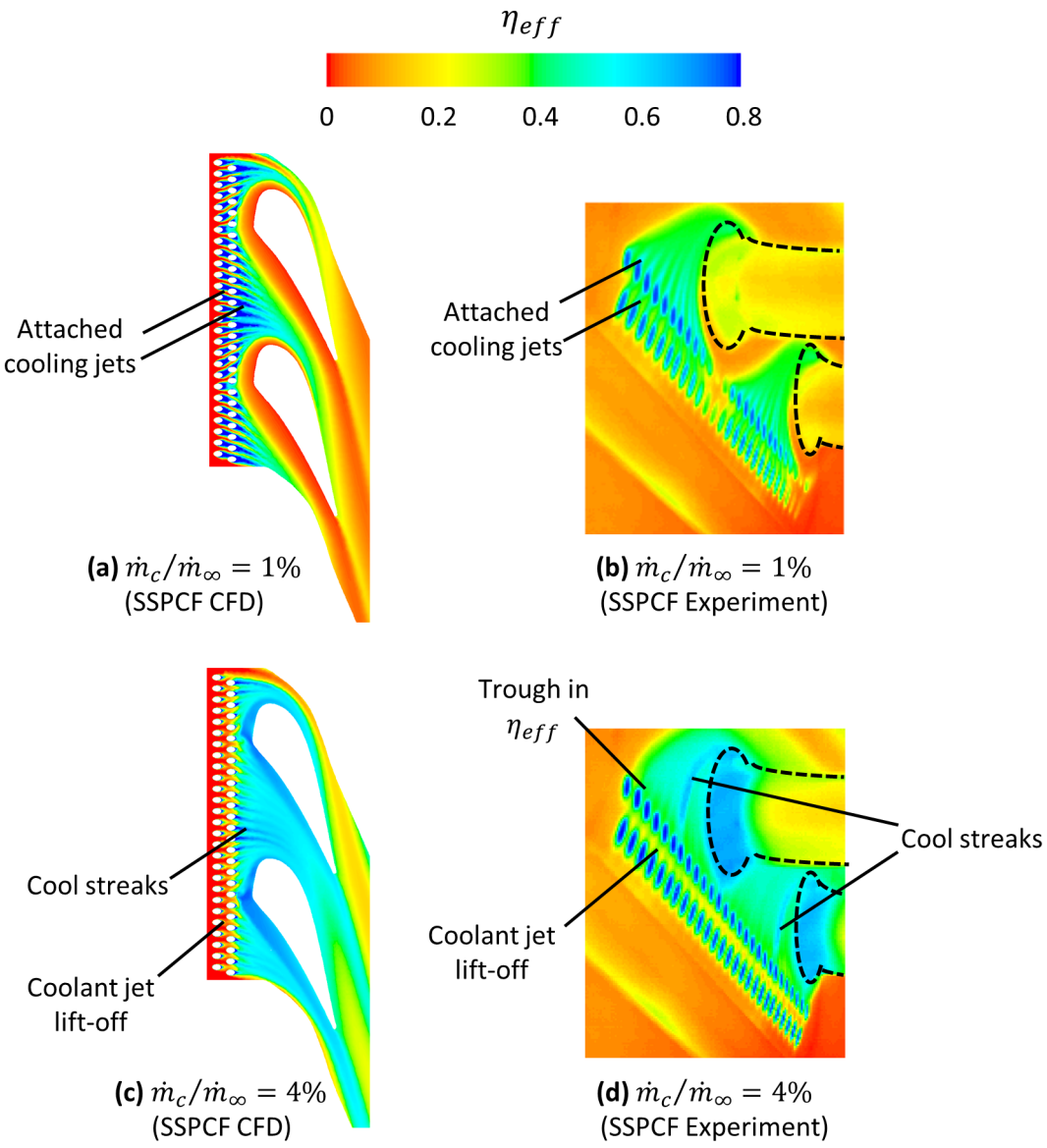


Figure 3-25: η_{eff} data for $\dot{m}_c/\dot{m}_\infty$ = 1%: (a) CFD predicted, (b) Experimentally measured; η_{eff} data for $\dot{m}_c/\dot{m}_\infty$ = 4%: (a) CFD predicted, (b) Experimentally measured

Cool streaks appear to issue from holes upstream of the vane SS (CFD, Figure 3-25 (c) and Experiment, (d)). This is a result of lower static pressure on this region of the endwall. Cooling holes in this region issue coolant at a lower blowing ratio, because of lower freestream static pressure. Coolant jets do not lift-off, resulting in higher local η_{eff}. This is described in more detail in Section 3.3.2.

Figure 3-26 shows CFD results at $\dot{m}_c/\dot{m}_\infty$ = 9%. This is a higher mass flux ratio than would be acceptable in engine design. Oilflow streamlines (Figure 3-26 (b)) show the coolant

wash back onto the endwall from the vanes. A cooled ring is observed around the vane where this recirculation occurs (see Figure 3-26 (a)). This recirculation pattern drives coolant away from the vane-endwall junction; this effect is particularly prominent on the PS endwall junction and drives a cross-flow from PS to SS.

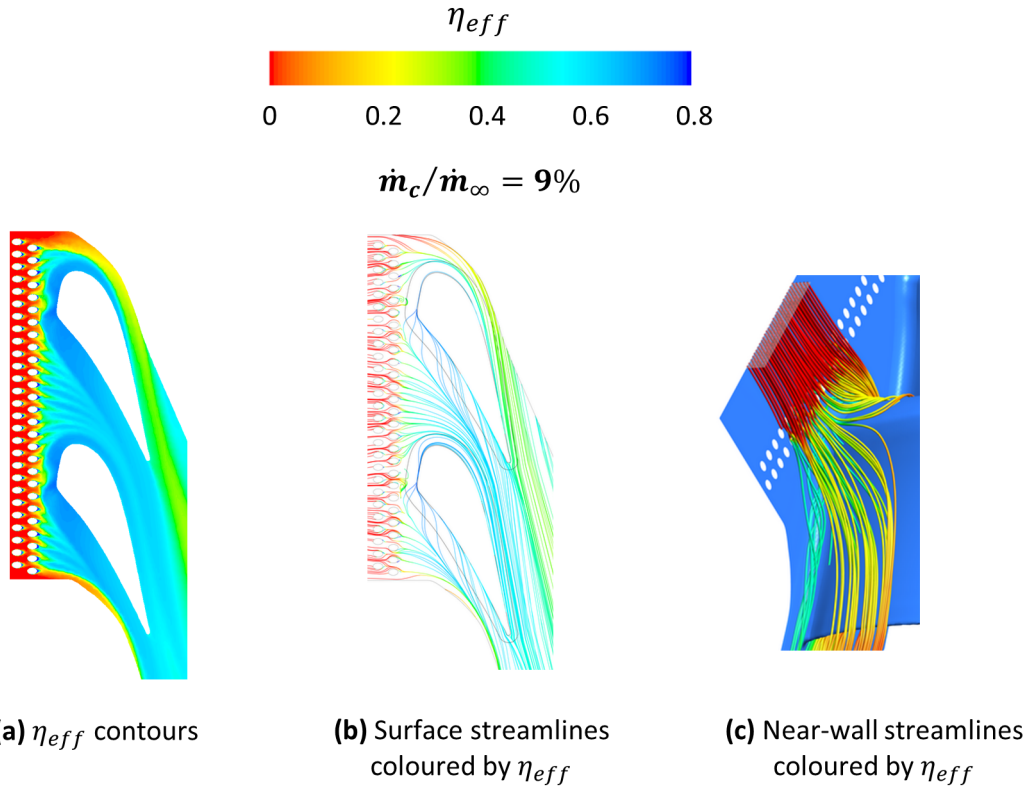
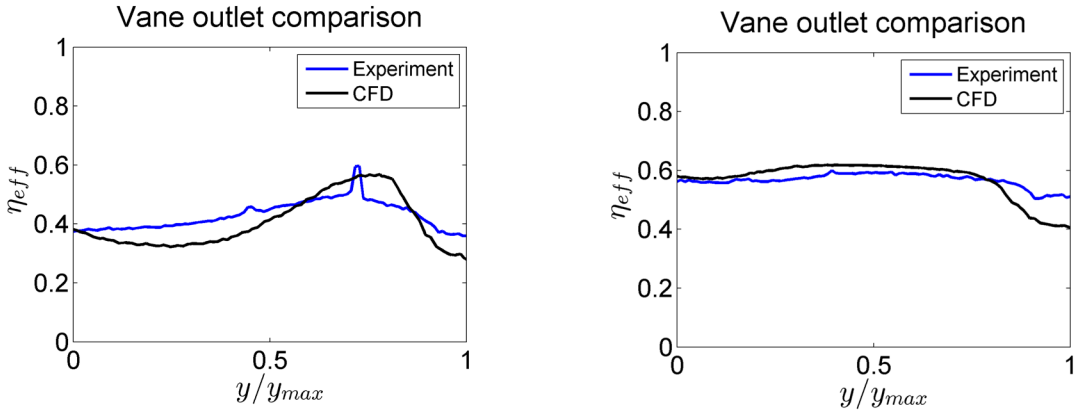


Figure 3-26: CFD predictions for $\dot{m}_c/\dot{m}_\infty$ = 9%

The $\hat{P}$ profile at $\dot{m}_c/\dot{m}_\infty$ = 9% shows a significant peak in the near-wall region (see Figure 3-23 (b)). This drives a near-wall vortex structure, which can be seen on the PS fillet in Figure 3-26 (c)). This recirculation pattern is observed at $\dot{m}_c/\dot{m}_\infty$ = 4% as well (Figure 3-21 (b), (c)), but is weaker. The gradient in inlet $\hat{P}$ also drives upwash; near-wall streamlines are driven further up the vane as a result (Figure 3-26 (c)). This upwash is similar to that observed on the planar cascade (Figure 3-8, Section 3.1.3).

Experimentally measured and CFD predicted η_{eff} are compared on the vane outlet line marked in Figure 3-19 (b) and (c); the η_{eff} maps of Figure 3-21, Figure 3-22 (a) and (e)

also have the endpoint of these lines marked as '0' and '1'. This comparison is shown in Figure 3-27 for $\dot{m}_c/\dot{m}_\infty$ = 4%, (a) and 9%, (b). The uncertainty in experimental η_{eff} was estimated as ±0.04 (see Appendix A). The peak in experimental η_{eff} data at y/y_{max} = 0.7 ($\dot{m}_c/\dot{m}_\infty$ = 4%, Figure 3-27 (a)) is caused by a leak at the cassette edge. The agreement in the mean level of η_{eff} is good, but greater pitchwise variation is observed in the CFD result. CFD under-predicts lateral spreading of coolant. This has been reported in literature (Harrison and Bogard, 2008).



(a) $\dot{m}_c/\dot{m}_\infty = 4\%$ **(b)** $\dot{m}_c/\dot{m}_\infty = 9\%$

Figure 3-27: Comparison of η_{eff} at vane outlet line

3.2.3 Hub: results and discussion

Figure 3-28 shows IR thermographs obtained of the hub endwall, cooled by the RIDN double-row cooling system. A schematic is shown in Figure 3-28 (a). The vane outline and RIDN holes are marked in Figure 3-28 (d); the location of the endwall PS and SS are also shown.

The hub endwall differs from the casing in the use of a contraction. Also modelled is the combustor-turbine interface step. There is no leakage flow through the step. These features are expected to influence the development of the endwall boundary layer.

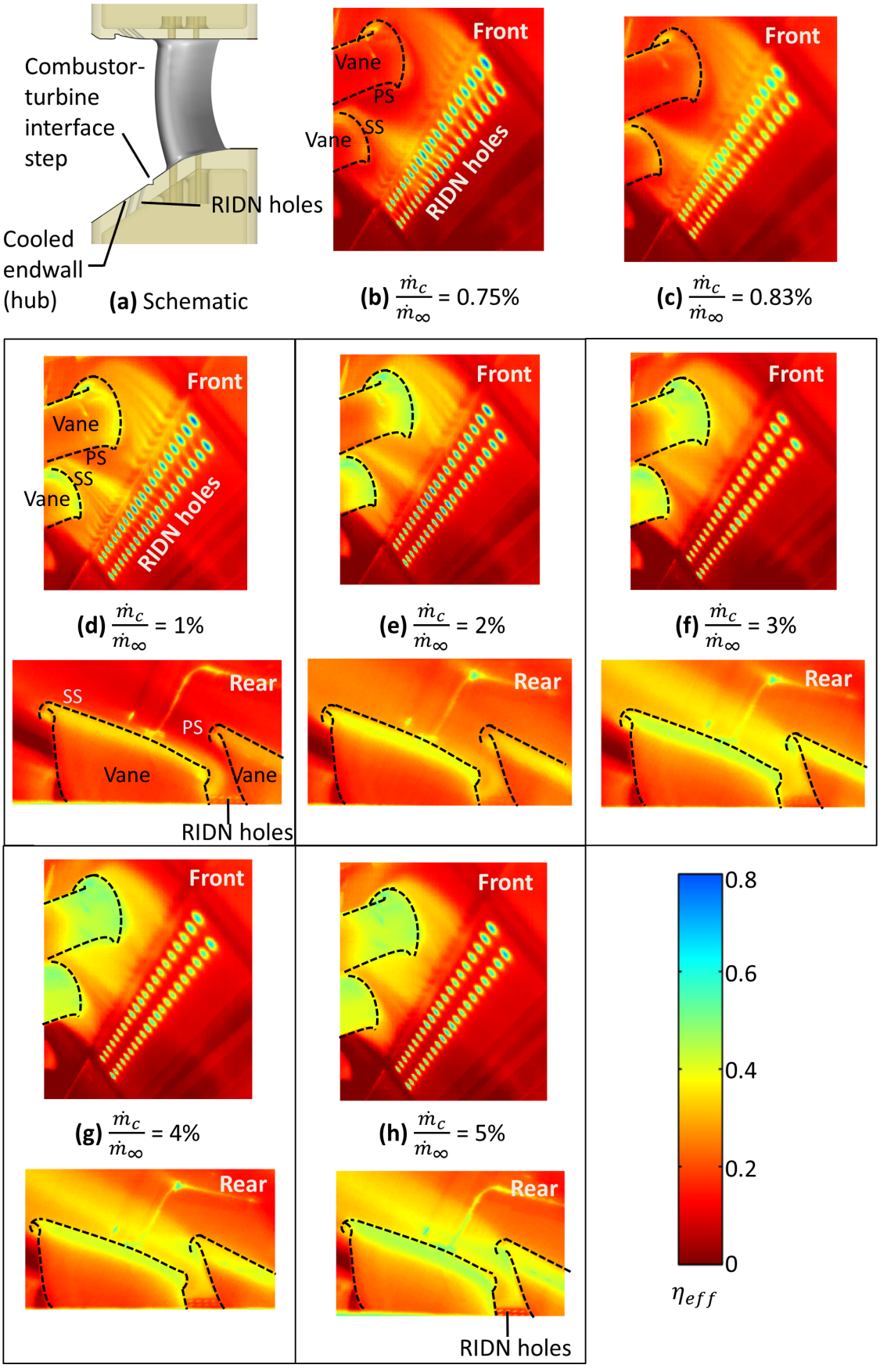


Figure 3-28: Experimentally measured η_{eff} maps on the hub endwall

Figure 3-28 (b), (c) shows η_{eff} contours on the endwall for $\dot{m}_c/\dot{m}_\infty$ = 0.75% and 0.83%. Coolant at this low mass flux ratio is attached to the endwall. Distinct coolant jets can be seen to issue from each hole. These are seen to climb the combustor-turbine interface step. The effect of the vane potential field can be observed up to the leading row of cooling holes: a pitchwise component of velocity is imparted to the coolant flow, directing it to either side of the vane. Unlike the RODN low coolant mass flux ratio case (Figure 3-25 (b)), the cooling holes upstream of the vane PS are not starved. The RIDN holes are farther from the vane than the RODN holes (see Figure 3-28 (a)). The vane potential field thus has a weaker influence.

The boundary layer separates upstream of the vane, leaving an uncooled ring on the endwall PS. Coolant entering the passage is driven towards the vane SS. This is caused by classical secondary flow mechanisms, and has been observed at low coolant flux ratios in the planar cascade CFD results (Figure 3-2) and in the casing η_{eff} maps (Figure 3-20). As concluded in Section 3.1.1 and Section 3.2.2, injection of low momentum coolant flow thickens the boundary layer, causing these flow patterns.

As coolant flow is increased, the separated zone diminishes. The separated zone is considerably smaller at $\dot{m}_c/\dot{m}_\infty$ = 1% (Figure 3-28 (d)) and has disappeared at $\dot{m}_c/\dot{m}_\infty$ = 2%, (e). Examining the rear endwall in (d) and (e), it can be seen that the coolant heads further towards the vane PS. At a higher mass flux ratio, $\dot{m}_c/\dot{m}_\infty$ = 3% (Figure 3-28 (f)), coolant is driven towards the PS endwall and emerges at the trailing edge as a cool streak. This continues to be the case at higher mass flux ratios $\dot{m}_c/\dot{m}_\infty$ = 4%, 5% (Figure 3-28 (g), (h)).

Coolant jets can be seen attached to the endwall up to $\dot{m}_c/\dot{m}_\infty$= 1%. At $\dot{m}_c/\dot{m}_\infty$= 2% and above (Figure 3-28 (e) to (h)), jets from both rows of cooling holes have lifted off. Reattachment is mostly seen to occur downstream of the interface step.

3.3 Further observations

3.3.1 Effect of combustor simulator

The effect of the combustor simulator on endwall flow structure was studied. The perforated plate was removed and dilution jets were blocked (Figure 3-29 (b)) and η_{eff} measurements were compared.

Little difference in near-wall flow structure can be discerned from the η_{eff} maps in the cases with and without dilution flow (Figure 3-29 (d), (f), (h) vs. (c), (e), (g)). This observation was made in measurements made by Barringer et. al. (2002). They study the effect of dilution jets on the vane inlet total pressure profile. They show that dilution jets injected at high momentum flux ratio increase the total pressure of the combustor core flow. They have less influence on the near-wall total pressure profile. The near-wall flow structure was thus not influenced significantly by dilution flow.

Dilution jets increase turbulence levels in the freestream. Higher turbulence levels result in boundary layers with higher momentum, which result in weaker secondary flows (Thole et. al., 2002, Narzary et. al., 2009). At low mass flux ratios, this is expected to delay boundary layer separation on the endwall, and decrease cross-passage flows. However, this effect is not observed in the η_{eff} maps of Figure 3-29 (c) and (d). It is unclear if the differences between the two η_{eff} maps are caused by real physical effects or experimental uncertainty in coolant mass flux ratio.

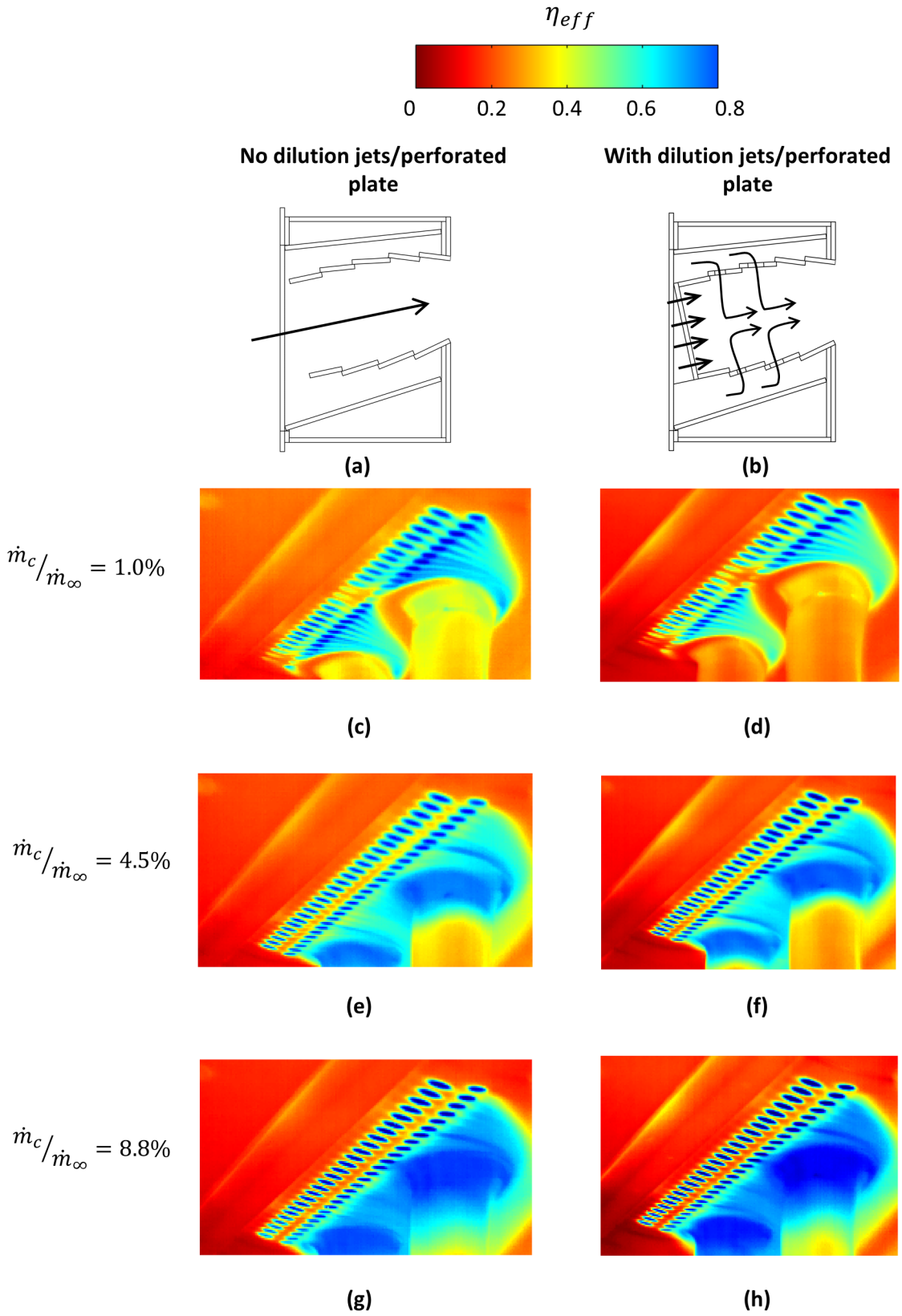


Figure 3-29: Effect of combustor simulator

Mayhew et. al., 2003 showed that cooling effectiveness from lifted-off film-cooling jets is diffused to the wall at high turbulence levels. This leads to higher endwall η_{eff}. Evidence of this is noted downstream of the trailing row of cooling holes in Figure 3-29 (f). The higher turbulence level is also expected to lead to accelerated decay of cooling effectiveness. While η_{eff} on the rear endwall was not compared, higher η_{eff} is expected in the no-dilution flow (low-turbulence) case.

3.3.2 Effect of vane potential field

The influence of the vane extends upstream resulting in variation of static pressure on the leading endwall. The RODN cooling hole rows are in close proximity to the vane LE; their location is shown in Figure 3-30 (a).

Averages of cooling jet velocities, u, were obtained at hole inlet surfaces in the CFD domain, for the condition $\dot{m}_c/\dot{m}_\infty$ = 4%. These are plotted as a non-dimensional jet velocity, u/u_{in}, in Figure 3-30 (b). u_{in} is the cascade inlet velocity.

Static pressure on an uncooled endwall was obtained using a CFD simulation. The local value of freestream velocity, u_∞, is estimated from this value using the Bernoulli equation. Blowing ratio, u/u_∞, is plotted in Figure 3-30 (c).

Mean blowing ratio decreases from the leading row to the trailing row (Figure 3-30 (c)). U/U_{in} and U/U_∞ show stronger variation on the trailing row because of its proximity to the vane. Cooling holes in y/P = 0.2 to 0.6 are upstream of the vane SS. The low static pressure in this region results in high coolant jet velocities (Figure 3-30 (b)). However, high local freestream velocities (U_∞) result in low blowing ratios (Figure 3-30 (c)). The cooling jets from holes upstream of the vane SS are thus attached, and have the appearance of cool streaks. This was observed in the experimental images and CFD contour plots of Section

3.2.2 (Figure 3-25 (c) and (d)). The cooling holes with low BR at the trailing row are marked in Figure 3-30 (a). Coolant streamlines from these holes are plotted in Figure 3-30 (d). The coolant jets are attached to the endwall. Reduced lift-off of coolant jets upstream of the vane SS was confirmed in the traverse measurements of Oke et. al. (2002).

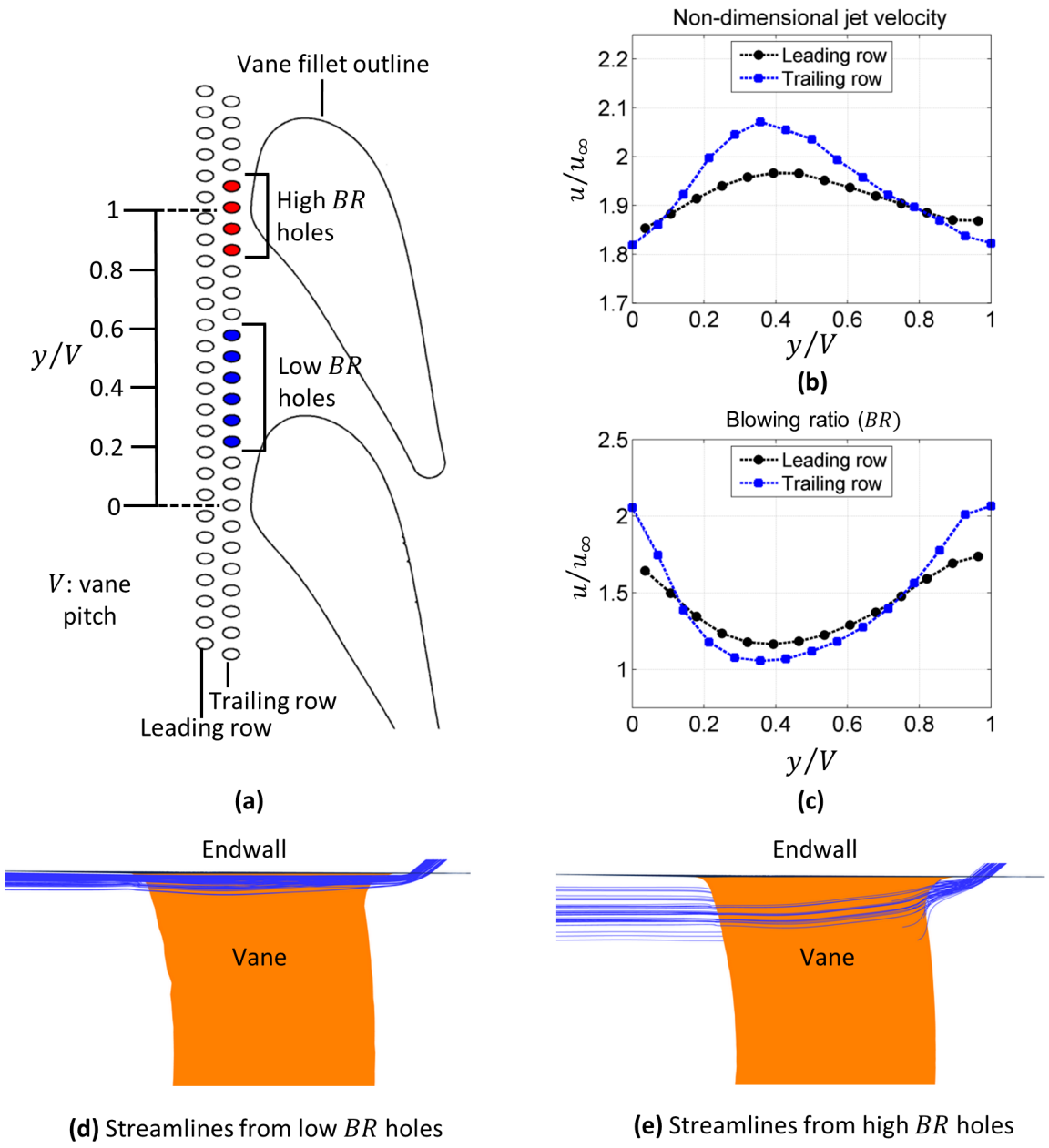


Figure 3-30: Effect of vane potential field for $\dot{m}_c/\dot{m}_\infty$ = 4%

Cooling holes in y/P = 0 to 0.2, and y/P = 0.8 to 1.0 are upstream of the PS of the vane (Figure 3-30 (b)). The higher local static pressure on the endwall in this region reduces

cooling jet velocities. This is close to the stagnation region of the vane; high blowing ratios are a result of low freestream velocities. Cooling holes with high BR at the trailing row are marked in Figure 3-30 (a). The coolant streamlines from these holes (Figure 3-30 (e)) lift off and are driven further away from the endwall by upwash on the vane. The trailing endwall is protected by turbulent thermal diffusion from these streamlines. However, coolant injection into the freestream at high BR increases mixing and is undesirable. Reducing hole inclination to avoid coolant lift-off is considered in Section 4.3.2.

3.3.3 Effect of low coolant mass flux ratio

Coolant injected at low mass flux ratio ($\dot{m}_c/\dot{m}_\infty$) introduces low momentum fluid into the near wall region. This low momentum injection aggravates secondary flows. This is illustrated in Figure 3-31. Surface streamlines (CFD) are shown on the casing for two cases: a cascade with no cooling holes (Figure 3-31 (b)), and a cascade with cooling holes, injecting at a low mass flow rate, $\dot{m}_c/\dot{m}_\infty$= 1% ((Figure 3-31 (c)). The streamlines in the no cooling case (Figure 3-31 (b)) are well behaved and show no evidence of secondary flows. The streamlines in the latter case separate upstream of the vane and are driven from the PS to SS by a cross-flow (Figure 3-31 (c)). Spanwise plots of $\hat{P}$ (Figure 3-31 (a)) show that the near-wall fluid in the cooled case has low momentum. This results in the appearance of secondary flow features.

The gap at the combustor-turbine interface leaks flow at a low blowing ratio. Several studies of this cooling configuration report increased secondary flows (Kost and Nicklas, 2001, Thole and Knost, 2005, Knost and Thole, 2005). Discrete cooling holes blowing at high BR can be used to boost near-wall momentum and reduce this effect.

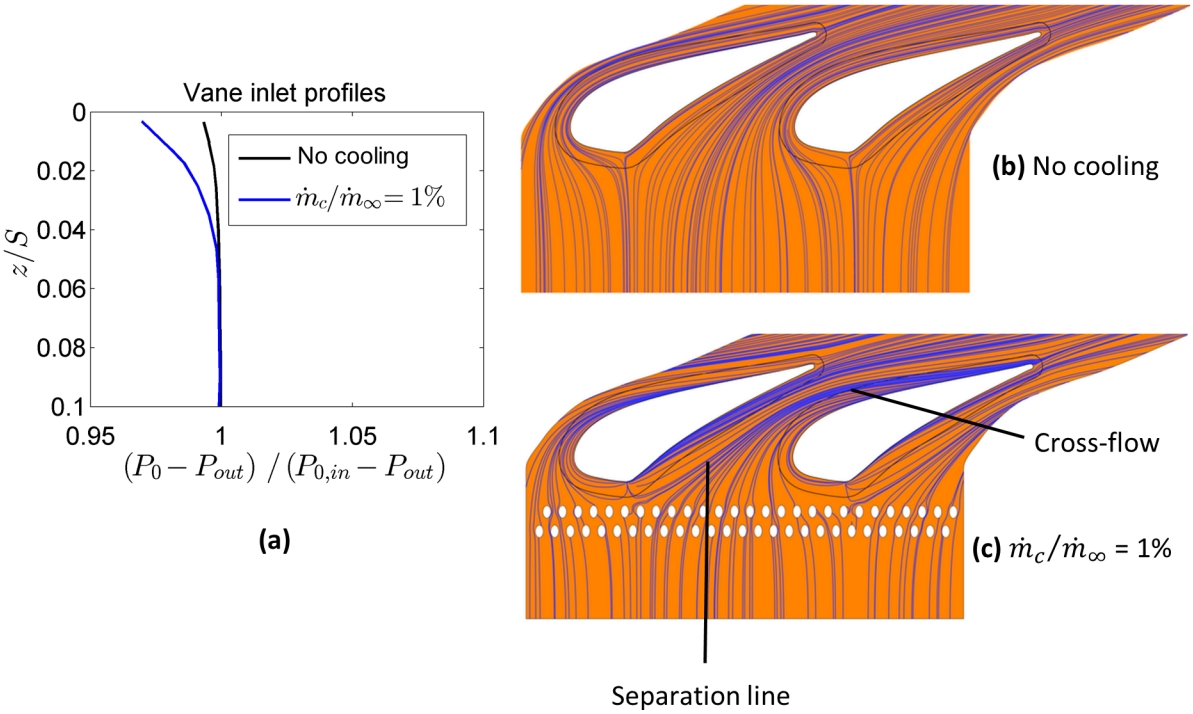


Figure 3-31: Effect of coolant injection at low mass flux ratio

3.3.4 Effect of endwall contraction

Figure 3-32 shows $\hat{P}$ profiles at the vane inlet plane for a cascade with no cooling flow. The endwall contraction accelerates the flow at the hub resulting in a thinner boundary layer with less momentum deficit. This was also shown in the traverse measurements of Barigozzi et. al. (2010).

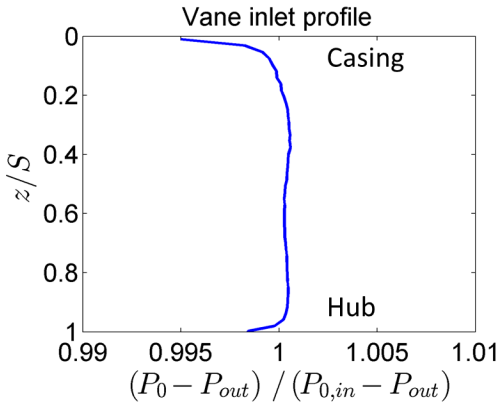


Figure 3-32: Effect of contouring: total pressure profile

3.3.5 Effect of reducing cooling hole diameters

The effect of adjusting cooling hole diameters on the vane inlet total pressure profile is shown in Figure 3-33 (a). Coolant is injected at $\dot{m}_c/\dot{m}_\infty$ = 4% in the RODN baseline case through holes of diameter D. This results in a considerable surplus in near-wall $\hat{P}$; this has been observed to eliminate flow separation and reverse the direction of cross-flow (see surface streamlines in Figure 3-33 (b)).

$\hat{P}$ profiles are plotted for a simulation retaining the same coolant total pressure, $P_{0,c}$, but with cooling holes of diameter $D/4$ (called the 'reduced diameter' case). The resulting coolant flux ratio was $\dot{m}_c/\dot{m}_\infty$ = 0.16%. A surplus in $\hat{P}$ is no longer observed. This is a result of reduced coolant flow rate: the near-wall flow is not energized to the same extent by higher momentum coolant flow. The vane inlet $\hat{P}$ profile for this case is similar to that for a cascade with no cooling holes. Since secondary flows are driven by the vane inlet total pressure profile (Hawthorne, 1951, Hermanson and Thole, 2000b) the near-wall flow structure can be expected to be similar for the two cases. Indeed, the surface streamlines for the no cooling case (Figure 3-31 (b)) and the reduced diameter case (Figure 3-33 (c)) are similar.

The $\hat{P}$ profile for the case with baseline hole diameters (D) and $\dot{m}_c/\dot{m}_\infty$ = 1% was shown in Figure 3-31 (a); it is shown in Figure 3-33 (a) for comparison. The large deficit in near-wall $\hat{P}$ resulted in boundary layer separation and PS-SS cross-flows. The deficit in near-wall $\hat{P}$ for the reduced diameter case is not as large. The injection of coolant momentum is just adequate to suppress boundary layer separation and PS-SS cross-passage flows. Thus, by examining the $\hat{P}$ plot, cooling holes can be sized to reduce secondary flows.

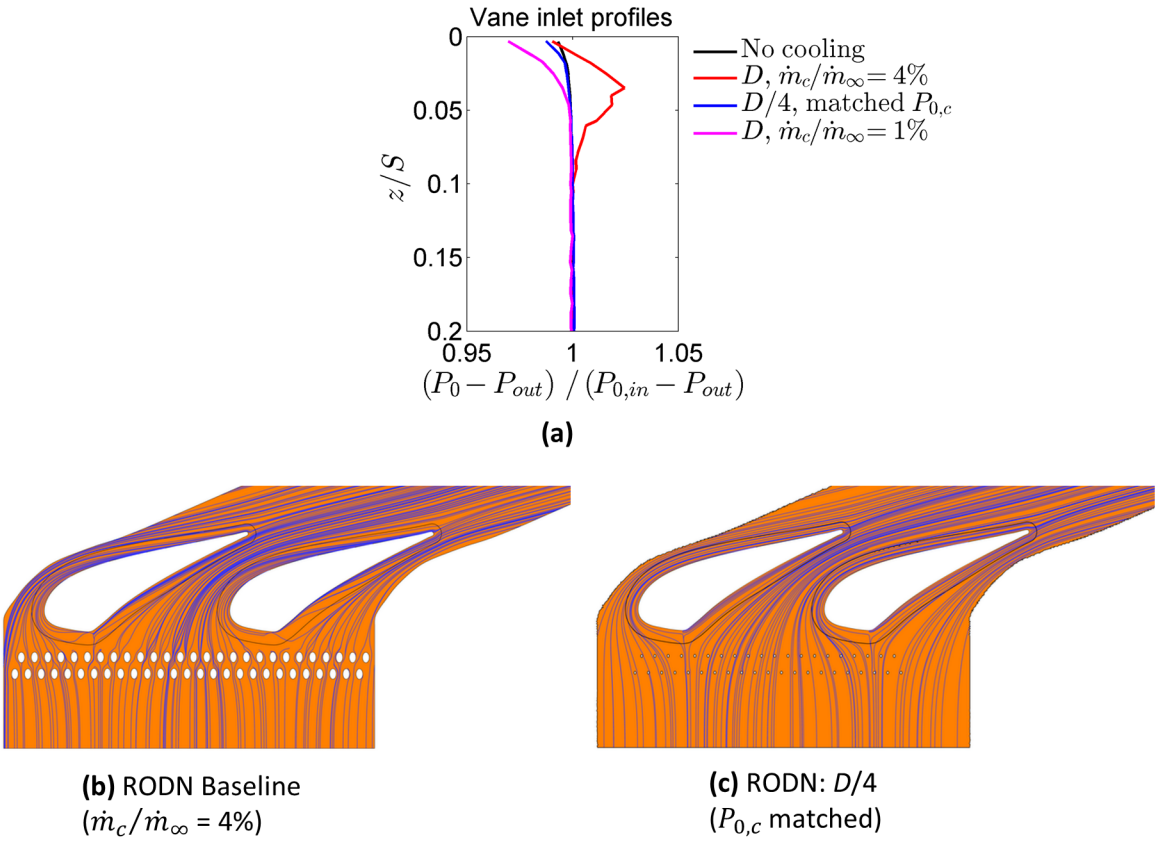


Figure 3-33: Effect of reducing diameters: (a) Total pressure profiles; Oilflow streamlines for: (b) RODN baseline, $\dot{m}_c/\dot{m}_\infty$ = 4%; (c) RODN: $D/4$ ($P_{0,c}$ matched)

It must be noted that the surplus in near-wall momentum caused by coolant injection will decay due to wall shear and mixing with the freestream. This could give rise to cross-passage flows further downstream in the passage. In this section, the cooling hole diameters were reduced by a large factor (4) for demonstration. In sizing cooling hole rows for mitigation of secondary flows, the near-wall total pressure profile needs to be examined not only at the vane inlet plane but also at planes further downstream in the passage.

3.4 Conclusions

The following conclusions were obtained from this study:

- Endwall secondary flows can be suppressed by injection of high momentum coolant upstream of the vane.

- Cooling holes can be sized by studying their effect on the near-wall $\hat{P}$ profile: a mild surplus of $\hat{P}$ will suppress endwall boundary layer separation, and is thus beneficial. A large surplus is detrimental: this results in upwash that drives coolant away from the endwall.

3.5 Engine conditions vs. SSPCF conditions

Certain engine conditions were not modelled in the SSPCF. The SSPCF cascade is a linear analogue of an engine NGV section; experimental data has been acquired at incompressible conditions. The engine operates at compressible conditions, with Re one order of magnitude higher than the SSPCF. High turbulence levels have been modelled in the SSPCF using a combustor simulator. However, the temperature profile at the engine combustor outlet is not uniform; this effect is not modelled in the SSPCF. The temperature difference between the coolant and the freestream results in a density ratio, ρ_c/ρ_∞, of around 2 in the engine. ρ_c/ρ_∞ in the SSPCF is around 1. The differences in flow behaviour at these two conditions are now examined.

CFD models of the linearized engine vane used in the SSPCF, and the annular engine vane are shown in Figure 3-34 (a) and (b). CFD solutions were obtained on each model at wind tunnel and engine flow conditions (see Table 2-3). Mesh independence studies were performed; finer meshes were used for the compressible solutions. The linear/incompressible model used a tetrahedral mesh of 0.7 million cells. The annular/compressible model used a 4 million cell tetrahedral mesh. This model included film cooling holes with blocked inlets; the effect of these holes on vane aerodynamics was assumed to be small.

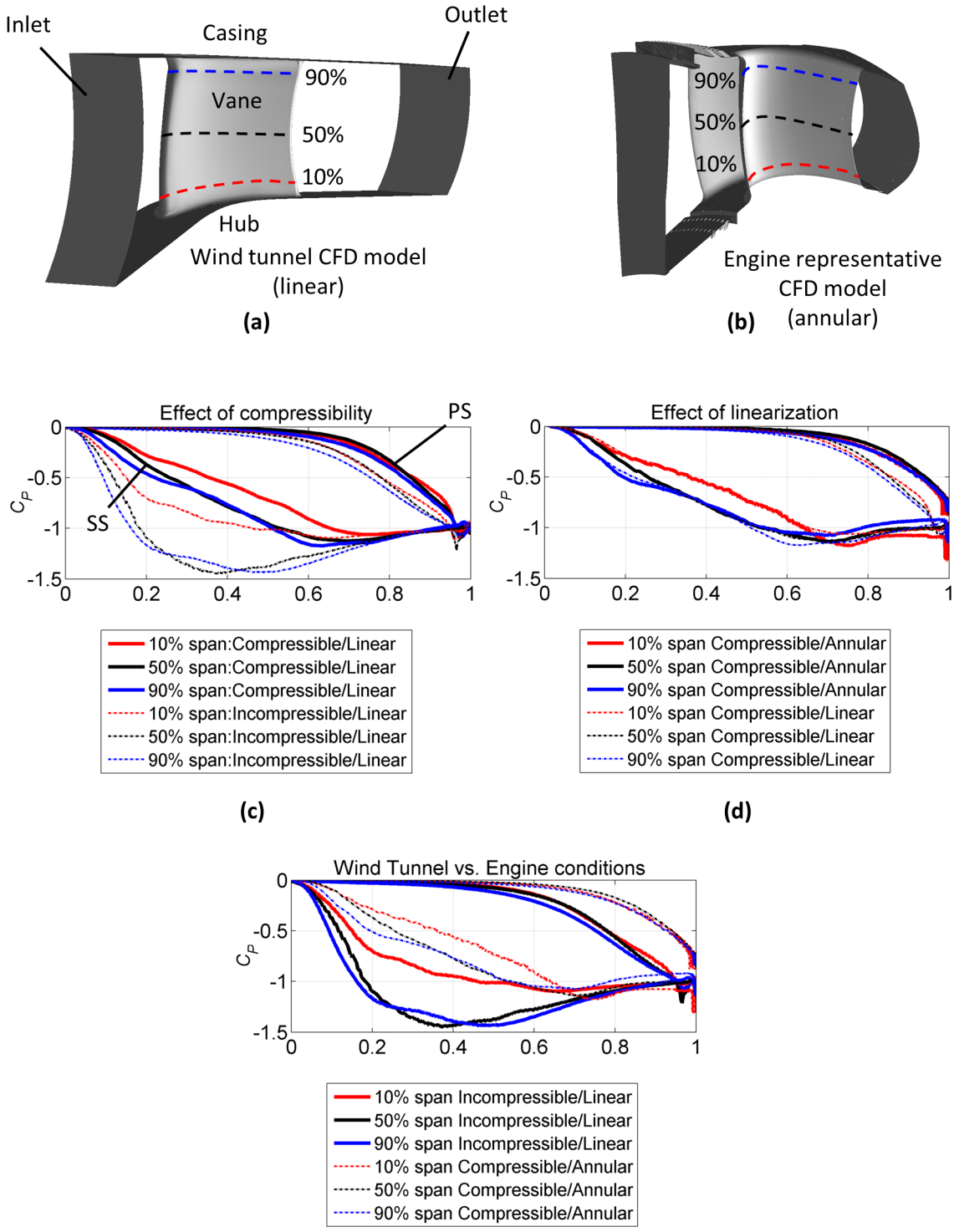


Figure 3-34: Mismatches in C_P at engine realistic conditions

Pressure coefficient (C_P) distributions were obtained on the 10%, 50%, 90% span vane cross-sections shown. C_P is defined as:

$$C_P = \frac{P - P_{0,in}}{P_{0,in} - P_{out}}, \tag{3-3}$$

where P is the vane surface static pressure, $P_{0,in}$ is the inlet total pressure, P_{out} is the outlet static pressure. C_P defined by Equation (3-3) is approximately 0 at the stagnation point and -1 at the TE.

Figure 3-34 (c) compares incompressible and compressible C_P distributions on the linear vane geometry (shown in Figure 3-34 (a)). The SS and PS segments of the 50% span C_P plot (compressible/linear condition) are marked. On the PS, C_P remains roughly constant at a value of 0 from the stagnation point to around x/C_{ax} = 0.6. A gradual acceleration reduces C_P to the outlet value of -1 at the vane TE. On the SS, the flow experiences acceleration up to x/C_{ax} = 0.75. This is followed by mild diffusion up to the TE. While SS vane distributions are similar at 50%, 90% span, higher C_P is observed at 10% span. The hub endwall contraction results in more gradual acceleration and reduces loading.

The compressible C_P distribution is rear-loaded. The position of minimum C_P is further downstream on the SS than in the incompressible case. Also acceleration begins further downstream on the PS.

Hermanson and Thole (2000a) perform CFD studies to compare secondary flows in a vane passage with incompressible (outlet M = 0.09) and compressible (outlet M = 0.85) flow. They show that secondary flows are determined by the vane inlet total pressure profile. For the same inlet boundary layer thickness, secondary flows evolve in a similar manner up to the location of the trailing edge shock. For constant Mach number inlet conditions, secondary flows are much smaller in both compressible and incompressible cases, resulting only from boundary layer growth at the leading part of the domain. However, the thinner boundary layer in the higher M case results in lower secondary flows.

C_P distributions at compressible conditions are compared for the linear and annular geometry in Figure 3-34 (d). While differences are noted at the trailing PS, the procedure used to linearize the vanes (see Section 2.1.3) has not altered the aerodynamics significantly.

SSPCF results are also mismatched in Reynolds number: the engine operates at an Re of 6.6 × 10^6, while the SSPCF experiments are conducted at an Re of 7.5 × 10^5. C_P is determined by inviscid aerodynamics and is not expected to change significantly with Re. This was shown by the measurements described in Section 2.1.3. Thinner boundary layers are expected at engine conditions because of higher Re. This is expected to reduce the severity of secondary flows.

Figure 3-34 (e) compares C_P distributions at SSPCF and engine conditions. This shows the cumulated effects of compressibility, linearization and Re mismatch. Considerable differences in vane loading are noted. The near-wall and mainstream flow will be driven to different parts of the passage at SSPCF and engine conditions.

Coolant flow conditions are mismatched because of different density ratios (engine $\rho_c/\rho_\infty = 2.33$, SSPCF $\rho_c/\rho_\infty \approx 1$). Non-dimensional variables describing film coolant flow were described in Section 1.3. These include density ratio ($DR = \rho_c/\rho_\infty$), blowing ratio ($BR = \rho_c U_c/\rho_\infty U_\infty$), momentum flux ratio ($I = \rho_c U_c^2/\rho_\infty U_\infty^2$). These variables are related by the equation:

$$I = \frac{BR^2}{DR}, \tag{3-4}$$

Figure 3-21 presented experimental data at engine representative mass flux ratios ($\dot{m}_c/\dot{m}_\infty$ = 4%). Matching $\dot{m}_c/\dot{m}_\infty$ resulted in matched BR. An estimate for momentum flux ratio in the engine case is provided in Appendix E. From Equation (3-4), momentum flux ratio in the SSPCF case is 2.33 (Engine DR) times the engine case. It was noted in Section

3.1.3 that injection of coolant momentum into the boundary layer suppresses secondary flows. Far more momentum is injected into the boundary layer at SSPCF conditions. To simulate the suppression of secondary flows, momentum flux ratio is the important variable to be matched. This is supported by evidence in literature. Narzary et. al. (2009) study the effect of coolant injection from an upstream slot at different density ratios. With blowing ratio kept fixed, the horseshoe vortex is seen to form closer to the vane as density ratio is decreased. A CO_2 coolant injection system was developed as part of this study. This is described in Appendix C. This system can be used in future study to better match coolant flow conditions in the SSPCF to the engine.

The effect of combustor temperature profile on secondary flows is studied by Hermanson and Thole (2000b). Considering uniform inlet velocity and an inlet temperature profile with a peak at midspan, higher total pressure is observed at the endwall. This results in secondary flow vortices with a sense of rotation inverted from the classical horseshoe vortex. However, in an engine-representative flow with an inlet boundary layer and a non-uniform inlet temperature profile, the boundary layer velocity variation contributes significantly more to inlet total pressure variation. CFD studies that use an engine representative temperature profile will be presented in Chapter 5.

3.6 Usefulness of conclusions in engine design

The SSPCF was used to validate CFD predictions of endwall cooling flows. Very good agreement was obtained between CFD predictions and SSPCF experimental data (Section 3.2). Due to the mismatches in flow conditions described in the last section, data from the SSPCF cannot be directly used in engine design. However, the validated CFD methods can be used to predict flows at engine conditions. Also, the conclusions obtained

from this study, listed in Section 3.4, are relevant in engine design. In Chapter 4, the insight gained is applied to optimize endwall cooling systems using these validated CFD methods.

4 OPTIMIZATION OF ENDWALL FILM COOLING SYSTEMS

The interaction of endwall coolant with secondary flows was studied in Chapter 3. The conclusions obtained will be used to design improved endwall cooling systems. These conclusions are listed below:

- The vane inlet total pressure profile determines secondary flows: deficit in near-wall P_0 results in endwall boundary-layer separation upstream of the vane and PS-SS cross-passage flows (Section 3.1.3).
- Injection of high-momentum coolant energizes the boundary layer: a surplus in near-wall P_0 can result. This surplus can suppress boundary-layer separation and can reverse the direction of cross-passage flows.
- The surplus in the near-wall P_0 profile results in coolant upwash: this can result in coolant being driven away from the endwall.
- The vane potential field results in significant variation in blowing ratios of upstream holes (Section 3.3.2).

4.1 Optimization goals

The optimum endwall film cooling system will deliver a target adiabatic cooling effectiveness, η_{eff}, while using minimum coolant flow and incurring minimum aerodynamic loss.

Adiabatic cooling effectiveness is defined in this chapter as:

$$\eta_{eff} = \frac{T_{0,\infty} - T_{aw}}{T_{0,\infty} - T_{0,c}} \tag{4-1}$$

The driving temperature in compressible flow is the local recovery temperature (T_r) and not the total temperature ($T_{0,\infty}$). The difference between the two quantities is small. This

was described in Section 1.3. This definition of η_{eff} is chosen since it makes analysis using the passive scalar tracking method simpler.

4.2 Passive-scalar tracking method

4.2.1 Theory

The passive-scalar tracking method was devised to examine contribution of individual cooling holes to η_{eff}. This is done by studying the concentration of a passive scalar released at the inlet of a cooling hole.

CFD solutions for the momentum and continuity equations are first obtained. The steady-state transport of the scalar through the domain is modelled by the advection equation. The expression for scalar concentration, $\phi_i(x, y, z)$, is shown below.

$$\frac{\partial(\rho u_j \emptyset_i)}{\partial x_j} = \Gamma \frac{\partial^2 \emptyset_i}{\partial x_j \partial x_j} \tag{4-2}$$

Here Γ is the scalar diffusivity and u_j is the velocity vector. The steady-state energy equation is given below:

$$\frac{\partial(\rho u_j c_p T)}{\partial x_j} = \left(k + \left(\frac{c_p \mu_T}{Pr_t}\right)\right) \frac{\partial^2 (c_p T)}{\partial x_j \partial x_j} \tag{4-3}$$

The quantity $\left(k + \left(\frac{c_p \mu_T}{Pr_t}\right)\right)$ is the effective turbulent thermal diffusivity, k_{eff}. If scalar diffusivity is set to effective turbulent thermal diffusivity, i.e. $\Gamma = k_{eff}$, then the passive-scalar will reproduce the behavior of the thermal field.

The following boundary condition is set at the inlet to cooling hole *i*:

$$\begin{aligned} \phi_j &= 1, \text{ for } j = i \\ \phi_j &= 0, \text{ for } j \neq i \end{aligned} \tag{4-4}$$

The boundary condition $\phi_i = 0$ is set at the freestream inlet, for all i. A control volume analysis is now used to relate passive-scalar concentration, ϕ_i, to coolant concentration (Figure 4-1).

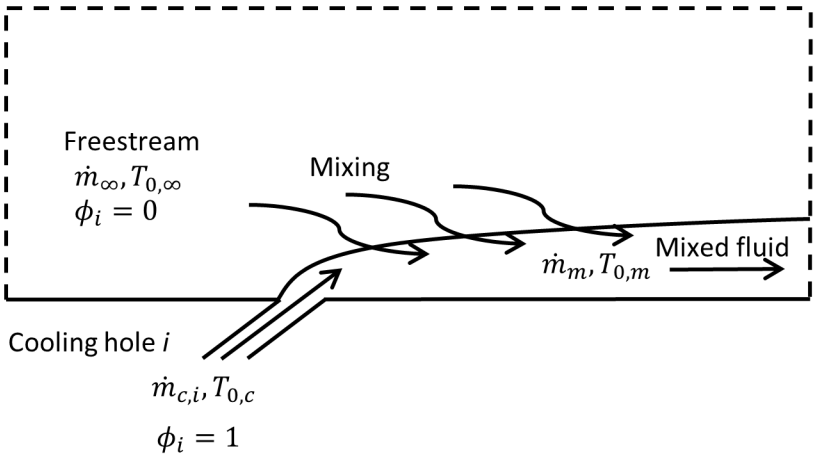


Figure 4-1: Control volume analysis for scalar concentration

Scalar concentration in the mixed condition is given by:

$$\emptyset_i = \frac{\dot{m}_{c,i} \times \phi_i]_{c,i} + \dot{m}_\infty \times \phi_i]_\infty}{\Sigma_i \dot{m}_{c,i} + \dot{m}_\infty} = \frac{\dot{m}_{c,i}}{\dot{m}_m}, \tag{4-5}$$

since the concentration of scalar i from cooling hole i, $\phi_i]_{c,i} = 1$, and the concentration of scalar i in the freestream, $\phi_i]_\infty = 0$.

The scalar concentration, $\emptyset_i$, is the contribution to coolant mass fraction from hole i. If the scalar concentrations were summed over all cooling holes, the net coolant mass fraction is obtained:

$$\sum_i \emptyset_i = \frac{\dot{m}_c}{\dot{m}_m} \tag{4-6}$$

The continuity and energy equations are:

$$\dot{m}_m = \dot{m}_c + \dot{m}_\infty \tag{4-7}$$

$$\dot{m}_m c_{p_m} T_{0,m} = \dot{m}_\infty c_{p_\infty} T_{0,\infty} + \dot{m}_c c_{p_c} T_{0,c} \tag{4-8}$$

For $c_p \neq f(T)$, i.e. $c_{p_m} = c_{p_\infty} = c_{p_c}$, dividing Equation (4-8) by $\dot{m}_m$, eliminating $\dot{m}_\infty$ using Equation (4-7) and substituting $\sum \phi_i$ from equation (4-6), the following expression is obtained:

$$T_{0,m} = T_{0,\infty} - \left(\sum_i \emptyset_i\right)(T_{0,\infty} - T_{0,c}) \tag{4-9}$$

In compressible flow, the adiabatic wall temperature, T_{aw}, is the local recovery temperature, T_r. This can be estimated from $T_{0,m}$ using the equation:

$$T_{aw} = T_r = T_{0,m} - (1 - r)\frac{u_\infty^2}{2c_p}, \tag{4-10}$$

where $r = \mathrm{Pr}^{1/3}$ is the recovery factor in turbulent flows.

The difference between T_r and $T_{0,m}$ is ignored to simplify analysis. Setting T_{aw} = $T_{0,m}$ in Equation (4-9), and substituting the definition of η_{eff} provided in Equation (4-1), the following expression is obtained:

$$\eta_{eff} = \Sigma\emptyset_i = \frac{T_{0,\infty} - T_{aw}}{T_{0,\infty} - T_{0,c}} \tag{4-11}$$

The sum of scalar concentration, $\Sigma\emptyset_i$, is thus a proxy for cooling effectiveness, η_{eff}. In particular, the contribution of an individual hole to η_{eff} is given by $\emptyset_i$, the concentration of the scalar associated with the hole.

The variation of specific heat with temperature was neglected in this formulation. In a gas turbine engine, c_p varies by about 10% over the range of temperatures between coolant and mainstream. An improved derivation accounting for this variation is provided in Appendix D.

The effect of varying hole diameters is now considered. For small changes in D_i, coolant flow rate, $\dot{m}_{c,i}$, varies as:

$$\dot{m}_{c,i} = f\left(\frac{P_{0,c}}{P_{\infty,i}}, {D_i}^2\right), \tag{4-12}$$

where $P_{\infty,i}$ is the hole outlet static pressure and D_i is the hole diameter. With the hole outlet point fixed, $P_{0,c}/P_{\infty,i}$ remains unchanged. Coolant flow rate ($\dot{m}_{c,i}$) thus scales with ${D_i}^2$. In Equation (4-5), $\emptyset_i$ is proportional to $\dot{m}_{c,i}$. Thus the cooling effectiveness contribution can be scaled for small changes in hole diameter using the following equation:

$$\phi_{i,new}(x,y,z) = \frac{{D_{i,new}}^2}{{D_i}^2}\phi_i(x,y,z), \tag{4-13}$$

where the suffix 'new' corresponds to the new diameter hole. η_{eff} distributions can thus be estimated for cooling systems of different diameter distributions, but with holes at the same locations, using the superposition equation:

$$\eta_{eff,new} = \sum_i \phi_{i,new}(x,y,z) = \sum_i \frac{{D_{i,new}}^2}{{D_i}^2}\phi_i(x,y,z) \tag{4-14}$$

This offers a tool for optimization of film cooling systems.

4.2.2 Implementation in FLUENT and validation

The implementation of the passive-scalar tracking method in a CFD solver is shown in Figure 4-2. ANSYS FLUENT was chosen for this study. The method remains unchanged for similar CFD packages.

Surfaces were created at the hole inlets. Solutions for the continuity, momentum and energy equations were obtained on a CFD model with a coolant plenum (Figure 4-2 (a)). Flow profiles were outputted from the hole inlet boundary surfaces (Figure 4-2 (b)). These were values of P_0, T_0, k, ε, and unit vectors of velocity direction. The flow profiles were set as boundary conditions on a CFD model without a coolant plenum (Figure 4-2 (c)); CFD solutions were obtained. Postprocessing lines on the hub endwall are shown in Figure 4-2 (d).

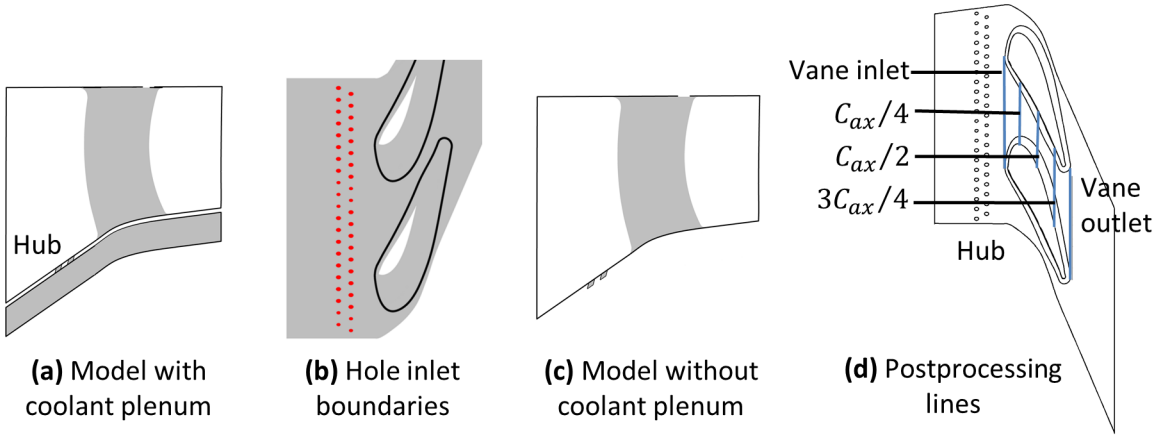


Figure 4-2: Passive-scalar tracking method implementation

Comparison of endwall η_{eff} for the CFD models with and without coolant plenums is shown in Figure 4-3 (a). The results agree closely. This shows that decoupling the plenum does not affect the flow solution.

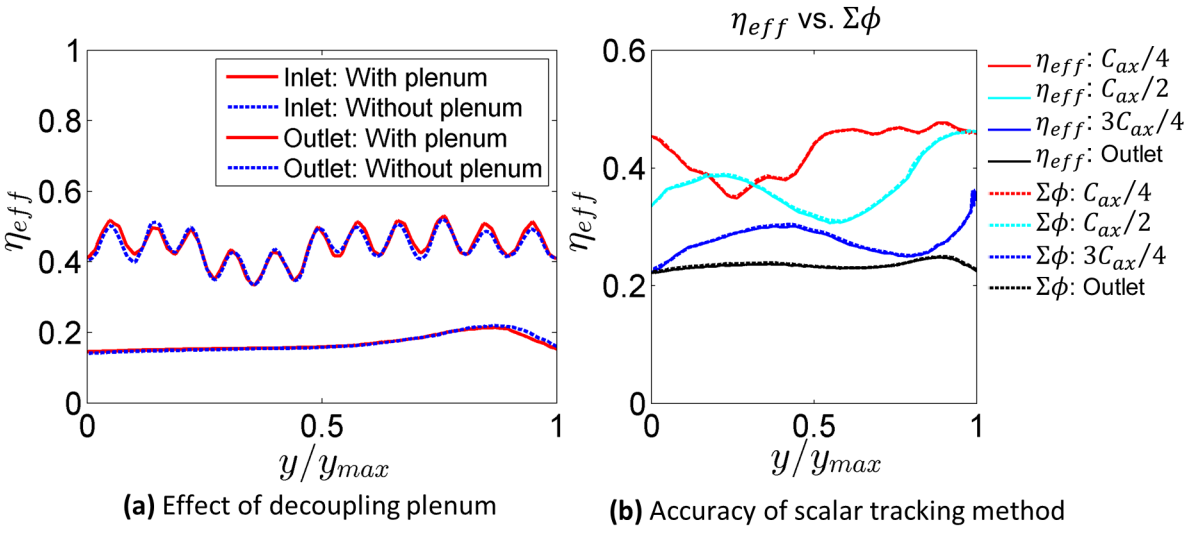


Figure 4-3: Passive-scalar tracking method: validation

Equations for scalar concentrations ϕ_1 to ϕ_N were setup using the FLUENT User Defined Scalar feature. N is the number of cooling holes. The following scalar boundary conditions were set at the inlet to hole i:

$$\phi_j = 1, \text{ for } j = i \tag{4-15}$$

$$\phi_j = 0, \text{ for } j \neq i$$

The boundary condition ϕ_i = 0, for all i, is set at the freestream inlet.

To have the scalar reproduce the behaviour of the temperature field, the value of scalar diffusivity, Γ, needs to be set to $\left(k + \left(\frac{c_p \mu_T}{Pr_t}\right)\right)$ (see Equation (4-2), (4-3)). This was done using a FLUENT User Defined Function.

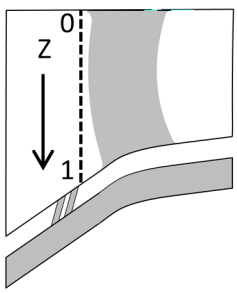
The field equations for ϕ_i (Equation (4-2)) were then solved. Equation (4-11) predicts the equality of η_{eff} and $\Sigma\phi_i$. This is confirmed in the plots in Figure 4-3 (b): the lines for η_{eff} and $\Sigma\phi_i$ agree extremely well. This demonstrates the accuracy of the passive-scalar tracking method.

4.3 Application to cooling system optimization

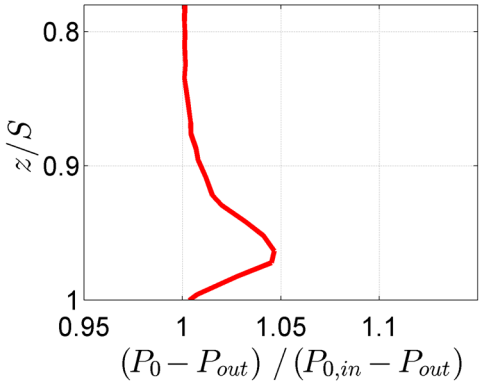
4.3.1 Compensating for cross-passage flow

Figure 4-4 (a) shows a CFD model of the cooled hub endwall in the SSPCF. A double row of cooling holes of uniform diameter are located upstream of the vane. This cooling system design is labelled Baseline1. Details of cooling hole geometry are given in Table 2-1. Flow solutions were obtained at incompressible conditions for an engine representative coolant mass flux ratio, $\dot{m}_c/\dot{m}_\infty$ = 3.0%.

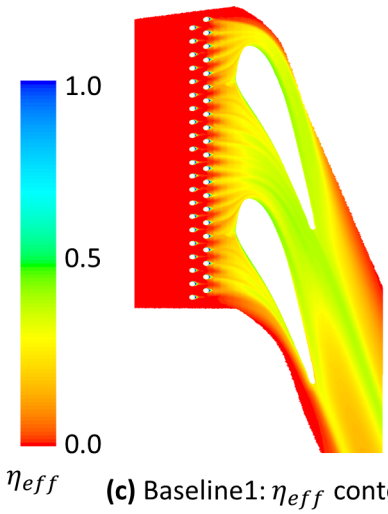
Figure 4-4 (c) shows η_{eff} contours on the hub endwall cooled by the Baseline1 design. The η_{eff} distribution at the trailing endwall is non-uniform, with the coolant emerging as a streak at the PS TE. Coolant injection at high blowing ratio results in surplus near-wall P_0 (Figure 4-4 (b)), which drives this coolant migration. The passive-scalar tracking method will now be used to target a uniform η_{eff} distribution at the vane outlet line.



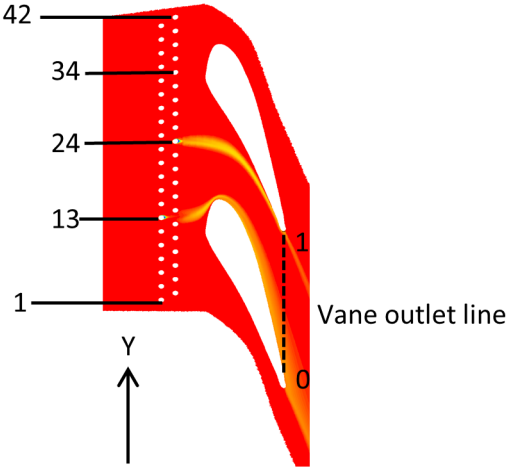
(a) CFD model: Baseline1



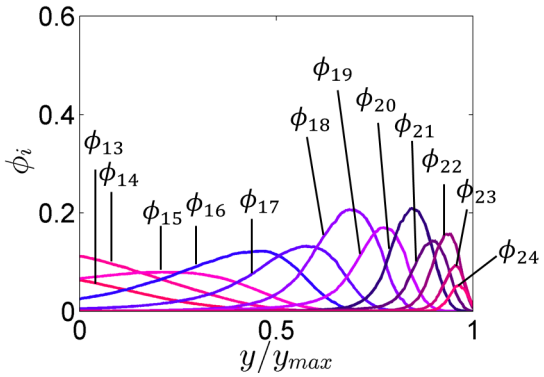
(b) Vane inlet total pressure profile



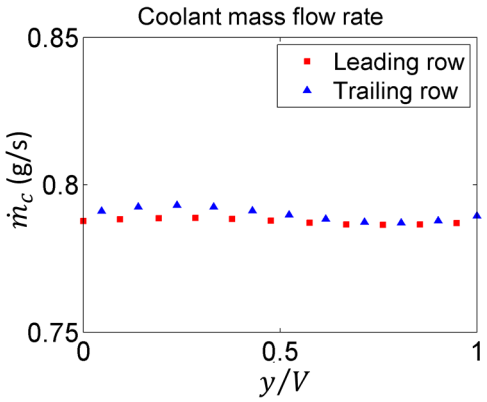
(c) Baseline1: η_{eff} contours



(d) Contours of ϕ_{13} and ϕ_{24}



(e) Plots of ϕ_i at vane outlet



(f) Cooling hole mass flow rate

Figure 4-4: Scalar tracking method applied to RIDN SSPCF model

The scalar concentration equations (Equation (4-2)) were solved for all 42 cooling holes in the domain. Scalar concentrations, ϕ_i, on the vane outlet line are plotted in Figure 4-4 (e). Holes marked 13 to 24 (see Figure 4-4 (d)) were identified as significant contributors

to cooling effectiveness. The contour plots for the scalar linked to hole 13 (ϕ_{13}) and hole 24 (ϕ_{24}) are shown in Figure 4-4 (d). They show coolant emerging from the SS TE and PS TE respectively. The vane outlet line, marked in Figure 4-4 (e), spans the region cooled by these holes. Holes 13 to 34 cover one pitch length. Upwash on the vane (described in Section 3.1.3) drives coolant from holes 24 to 34 away from the endwall and into the freestream. Holes 24 to 34 thus do not contribute to cooling at the vane outlet.

It can be seen from Figure 4-4 (e) that coolant from holes 17 to 24 reaches y/y_{max} = 0.5 to 1.0. Only coolant from holes 13 to 16 reaches y/y_{max} = 0 to 0.5. This is caused by the cross-passage flow driving coolant towards the PS endwall. This distribution of coolant is now improved by adjusting the diameters of holes 13 to 24.

The diameters of holes 1 to 42 (see Figure 4-4 (a)) are called D_i. D_{Base} is the uniform hole diameter of the Baseline1 cooling system. The diameters of holes 13 to 24 are called d_j (j = 1 to N, $N = 12$). A linear variation of diameters was prescribed for holes 13 to 24. The diameter of hole number j is expressed as:

$$d_j = d_a + \frac{j-1}{N-1}(d_b - d_a), \tag{4-16}$$

where d_a and d_b are hole diameters for j = 1 and $j = N$ respectively. The notation is summarized in Figure 4-5.

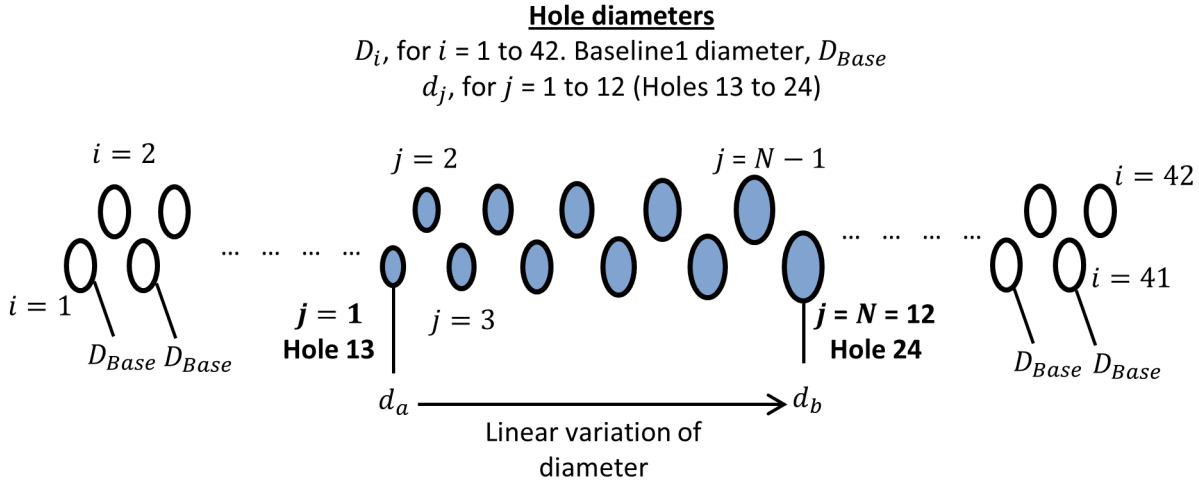


Figure 4-5: Hole diameter distribution

The mass flux through individual cooling holes is plotted in Figure 4-4 (f). Little variation is seen in cooling hole mass flow rate. Thus, for the Baseline1 design the total coolant flow for holes 1 to N can be expressed as:

$$\dot{m}_{original} = k\sum_{j=1}^{N} {D_{Base}}^2 = kN{D_{Base}}^2, \tag{4-17}$$

where k is a constant. For small changes in hole diameters, the coolant flow rate through holes 13 to 24 can be approximated as:

$$\begin{aligned}\dot{m}_{new} = k\sum_{j=1}^{N} {d_j}^2 \quad &= k\sum_{j=1}^{N}\left(d_a + \frac{(j-1)}{N-1}(d_b - d_a)\right)^2 \\ &= k\left(N{d_a}^2 + \frac{(d_b - d_a)^2}{(N-1)^2} \times \frac{N(N-1)(2N-1)}{6}\right. \\ &\qquad \left. + \frac{2}{(N-1)} d_a(d_b - d_a) \times \frac{N(N-1)}{2}\right)\end{aligned} \tag{4-18}$$

Coolant mass flow consumption is to remain unchanged. Setting $\dot{m}_{original} = \dot{m}_{new}$, the following expression was obtained:

$$N{d_a}^2 + \frac{(d_b - d_a)^2}{(N-1)}\frac{N(2N-1)}{6} + d_a(d_b - d_a)N = N{D_{Base}}^2 \tag{4-19}$$

Substituting values D_{Base} = 6.9 mm and N = 12 in Equation (4-19), an expression for d_b was obtained:

$$d_b{}^2 + 0.871 d_a d_b + \left(d_a{}^2 - 135.49\right) = 0 \tag{4-20}$$

Equation (4-20) is a quadratic expression for d_b in terms of d_a. This is solved as:

$$d_b = \sqrt{135.49 - 0.81 d_a{}^2} - 0.44 d_a \tag{4-21}$$

For a particular value of d_a, the constant coolant mass flow requirement constrains d_b to the value specified by Equation (4-21). The hole diameter distribution of Equation (4-16) is thus fully specified by a value of d_a. For small changes in diameter, $\eta_{eff,new}$ can be estimated using the superposition method of Equation (4-14). This is repeated below:

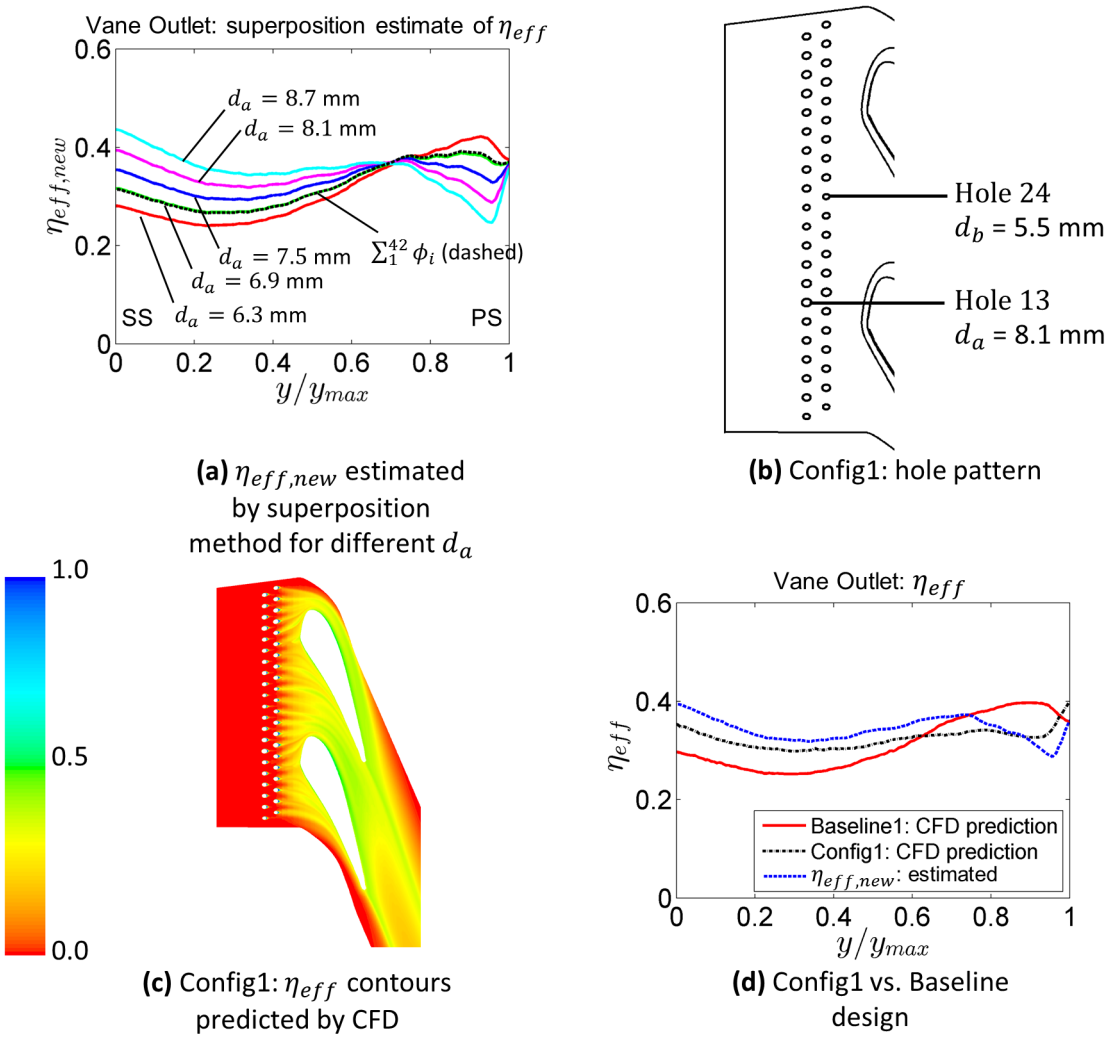
$$\eta_{eff,new} = \sum_{i=1}^{42} \frac{D_i{}^2}{D_{Base}{}^2} \phi_i \tag{4-22}$$

Since $D_i = D_{Base}$ for all holes besides i = 13 to 24, Equation (4-22) can be rewritten as:

$$\eta_{eff,new} = \sum_{i=1}^{42} \phi_i + \sum_{j=1}^{N} \left(\frac{d_j{}^2}{D_{Base}{}^2} - 1 \right) \phi_{j+12} \tag{4-23}$$

$\eta_{eff,new}$ at the vane outlet line (marked in Figure 4-4 (d)) is plotted for various values of d_a in Figure 4-6 (a). As required by Equation (4-23), the plots for $\sum_{i=1}^{42} \phi_i$ and $d_a = D_{Base}$ = 6.9 mm overlay. This corresponds to the Baseline1 design. As d_a increases, $\eta_{eff,new}$ increases at the vane outlet SS, and decreases at the vane outlet PS. The $\eta_{eff,new}$ distribution for d_a = 8.1 mm is considerably more uniform than the baseline design. The hole pattern for d_a = 8.1 mm, called Config1, is shown in Figure 4-6 (b). Only holes 13 to 24 have been

modified. Diameters decrease linearly from hole 13 (d_a = 8.1 mm) to hole 24 (d_b = 5.5 mm).



(a) $\eta_{eff,new}$ estimated by superposition method for different d_a

(b) Config1: hole pattern

(c) Config1: η_{eff} contours predicted by CFD

(d) Config1 vs. Baseline design

Figure 4-6: Optimization using scalar tracking method

A CFD model was solved for the Config1 hole pattern. Coolant flow rate was set to the Baseline1 condition ($\dot{m}_c/\dot{m}_\infty$ = 3%). η_{eff} distributions for the Baseline1 and Config1 designs are compared at the vane outlet in Figure 4-6 (d). The η_{eff} distribution is considerably more uniform for the Config1 design than the Baseline1 design.

CFD predicted η_{eff} contours for the Config1 design are shown in Figure 4-6 (c). Coolant migrates to the PS TE in the Baseline1 design (Figure 4-4 (c)). This tendency remains unchanged with the Config1 hole pattern. However, more coolant is introduced

upstream of the vane SS than the vane PS. This results in a more uniform η_{eff} distribution at the vane outlet.

For the Config1 design, the cooling effectiveness estimated using Equation (4-23), $\eta_{eff,new}$, is compared with the CFD result in Figure 4-6 (d). $\eta_{eff,new}$ over-estimates cooling effectiveness for y/y_{max} = 0 – 0.8 and under-estimates cooling effectiveness for y/y_{max} = 0.8 – 1. This is a result of two approximations: (i) assuming that hole mass flow rate, $\dot{m}_{c,i}$, scales with D^2 (Equation (4-12)); (ii) assuming that cooling effectiveness contribution, ϕ_i, scales with $\dot{m}_{c,i}$ (Equation (4-13)). Changing the hole diameter changes the discharge coefficient of the hole. It also changes the rate of mixing of coolant with the mainstream. The larger SS holes deliver lower η_{eff} in y/y_{max} = 0 – 0.8 than estimated. Similarly the smaller PS holes deliver higher η_{eff} in y/y_{max} = 0.8 – 1 than estimated. The large changes in hole diameters result in inaccurate estimation. The $\eta_{eff,new}$ estimate will be closer to CFD predictions if this process is iterated: if scalar concentration equations for the Config1 cooling holes are solved, and diameters readjusted by smaller values to target uniform outlet η_{eff}.

4.3.2 Improving cooling of the trailing endwall

The trailing endwall is difficult to cool: cooling films released upstream decay in effectiveness before they reach the rear endwall; injecting coolant locally results in high aerodynamic losses because of high freestream M. High M, thin boundary layers and enhanced mixing in the vane wake also result in high heat transfer rates in this region. The focus of this section is to improve η_{eff} values on the trailing endwall.

The scalar tracking method was applied to optimize the hub endwall film cooling system design, called Baseline2, shown in Figure 4-7 (a). This configuration is identical to

the Baseline1 design shown in Section 4.3.1 (Figure 4-4 (a)), but with hole length-to-diameter ratios matched with the engine RIDN system (L/D = 1.8 for Baseline2 vs. L/D = 6.5 for Baseline1). Also, the flow BCs were set to compressible, engine representative conditions (given in Table 2-3).

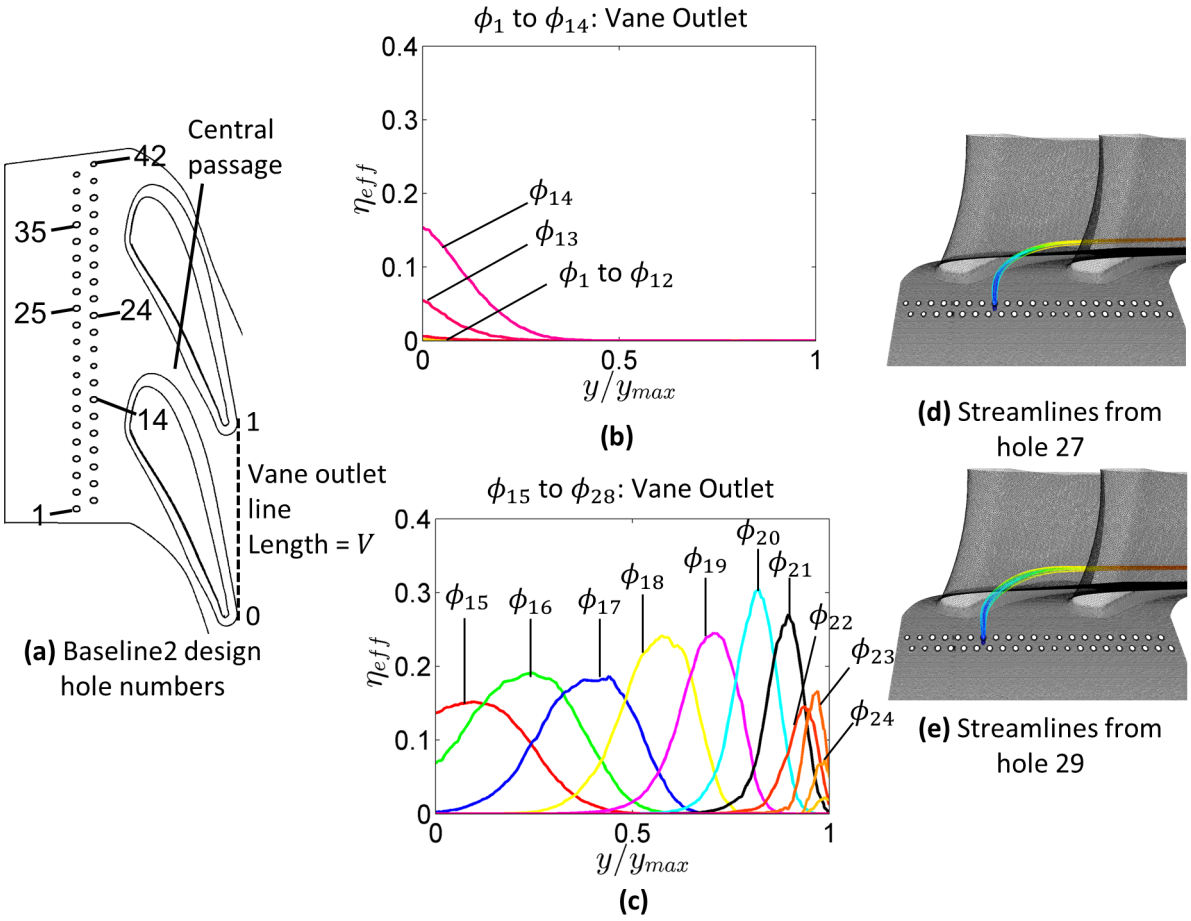


Figure 4-7: Hub cooling system optimization

Scalar concentration equations were solved for all 42 cooling holes in the domain (Figure 4-7 (a)), and reported at the vane outlet line of the central passage. Individual concentrations are plotted in Figure 4-7 (b), (c). Cooling holes are numbered from 1 to 42 in increasing order of pitch-wise coordinate. Cooling holes 14-24 show significant concentrations (ϕ_{14} to ϕ_{24}) at the vane outlet line: the holes are marked in Figure 4-7 (a).

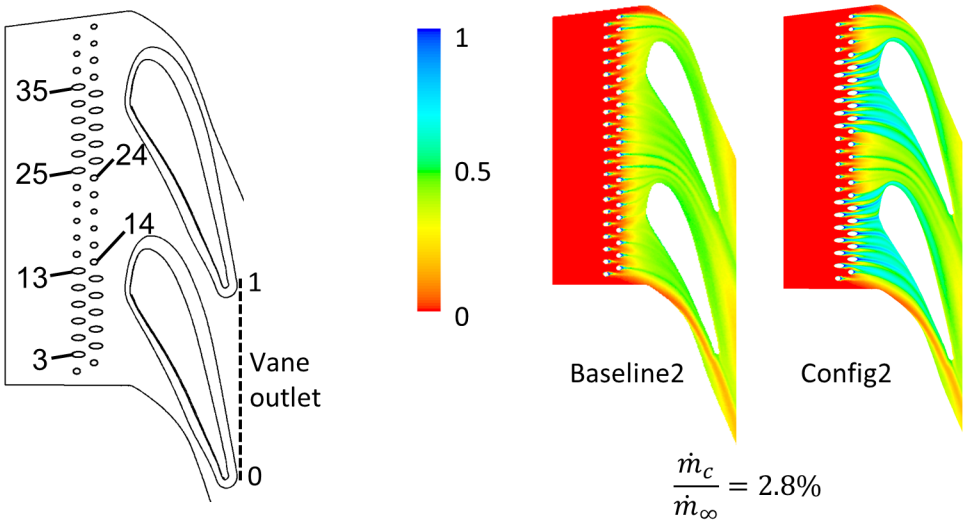
Each passage endwall is cooled by 22 film cooling holes. Considering holes 14-35, cooling holes 25 to 35 are located upstream of the central passage but do not show significant scalar concentration at the vane outlet. To understand why, coolant pathlines coloured by scalar concentration were plotted for the holes. Examples of such plots are given in Figure 4-7 (d), (e). Upwash on the vane (described in Section 3.1.3) drives the coolant issuing from these holes into the freestream, away from the endwall. The coolant mixes in the freestream and has zero or negligible impact on the downstream overall effectiveness.

In an attempt to reduce the upwash, the inclination angles were reduced by 20° for these holes (numbers 25-35). To maintain periodicity, the inclination angles of corresponding holes in the adjacent passage (numbers 3-13) were reduced as well. Cooling holes 14-24 were left unaltered. The outline of the modified design (Config2) is shown in Figure 4-8 (a).

η_{eff} contours obtained for this new cooling system design (Config2) are compared with the Baseline2 design in Figure 4-8 (b). The coolant mass flows for the Baseline2 and Config2 designs agreed to within 0.1%. The coolant to mainstream mass flow ratio was $\dot{m}_c/\dot{m}_\infty$ = 2.8%. Design Config2 has significantly better performance than the baseline design in the leading part of the passage. Reducing cooling hole inclination results in better attached jets.

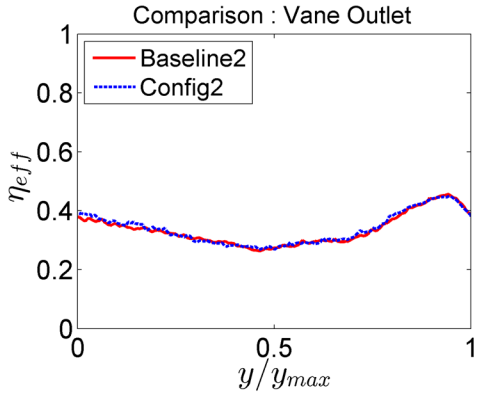
The η_{eff} distribution is essentially unchanged at vane outlet, as shown in Figure 4-8 (c). It was noted in Section 3.1.3 that upwash on the vane is driven by a surplus in vane inlet total pressure in the near-wall region. As shown in Figure 3-10 (Section 3.1.4), reducing hole inclination results in greater streamwise coolant momentum, which increases this surplus. The coolant from holes 25-35 is thus washed further up the vane than before, and has negligible impact on downstream η_{eff}. While reducing hole inclination reduces coolant lift-off, it increases upwash on the vanes. It was noted in Section 3.3.5 that reducing hole

diameters reduces the surplus in near-wall total pressure. This design modification will be studied in the next section (Section 4.3.3).



(a) Config2 hole numbers

(b) η_{eff} contours



(c) η_{eff} comparison: Baseline2 vs. Config2

Figure 4-8: Config2 design

To illustrate the improvements that can be achieved with relatively simple design changes, a partially optimized design is now considered in which some cooling holes are placed in the NGV passage.

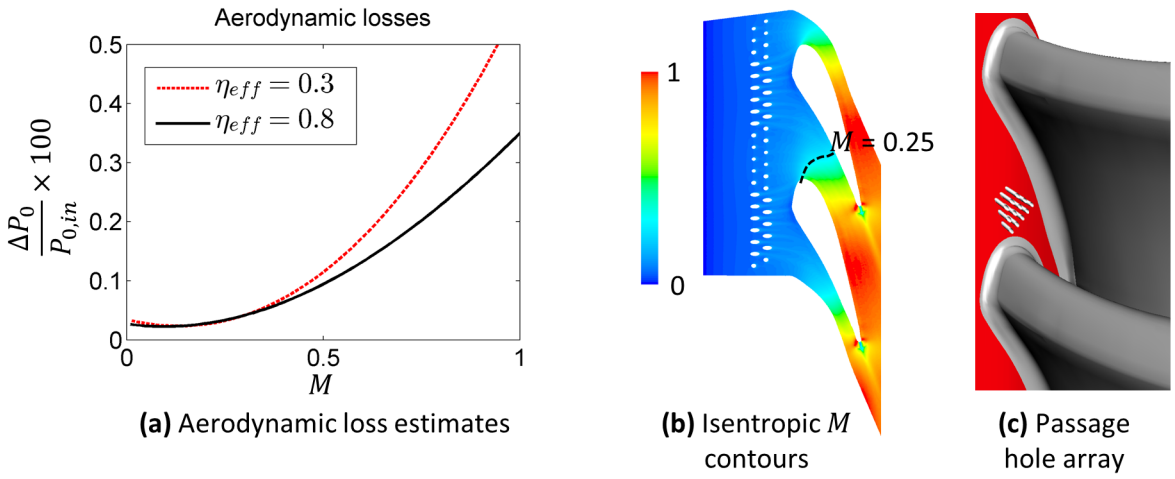
The aerodynamic loss model of Kollen and Koschel (1985) was used to quantify the aerodynamic cost of coolant injection into the freestream. The model expresses total pressure loss as a function of *M* at the point of injection, and an estimated value of η_{eff}. A lower η_{eff}

value results when coolant has mixed to a greater degree with the freestream. This results in greater aerodynamic loss. The expression for non-dimensionalized total pressure loss is given below.

$$\frac{\Delta P_0}{P_{0.in}} = \frac{\left(\dot{m}_c P_{0,c} + \dot{m}_\infty P_{0,\infty}\right) - P_{0,out}\left(\dot{m}_c + \dot{m}_\infty\right)}{\left(\dot{m}_c P_{0,c} + \dot{m}_\infty P_{0,\infty}\right)}, \tag{4-24}$$

Here $P_{0.in}$ is the mass averaged total pressure of the coolant and the freestream flow. $P_{0,out}$ is the mass-averaged total pressure at the mixed plane calculated using the Kollen and Koschel model (1985); the mixed stream in the near-wall region has a different total pressure from the unperturbed freestream, accounting for total pressure losses.

$\Delta P_0/P_{0.in}$ is plotted in Figure 4-9 (a) for two different values of η_{eff}, for an injected coolant mass flow fraction, $\dot{m}_c/\dot{m}_\infty$ = 1.0%. Aerodynamic loss is very low for $M < 0.25$, allowing cooling holes to be included in this region with minimal aerodynamic penalty. The near wall Mach number contours are shown in Figure 4-9 (b), showing the region available for passage cooling at low cost.



(a) Aerodynamic loss estimates

(b) Isentropic M contours

(c) Passage hole array

Figure 4-9: Passage hole placement for minimal aerodynamic loss

An array of passage cooling holes, shown in Figure 4-9 (c), was embedded upstream of the M = 0.25 contour on the hub endwall. The coolant mass flow rates at these locations

were estimated by using the local static pressure. To offset the mass flow rate, holes 25-35 and 3-13 (the holes of reduced inclination angle discussed with reference to Figure 4-8 (a)) were reduced in diameter. It was noted that coolant from these holes is driven away from the endwall by upwash. Reducing their diameters will reduce surplus near-wall total pressure, and will weaken this tendency. The resulting cooling system design is labelled Config3.

The η_{eff} contours of Config3 are shown in Figure 4-10 (a). The overall coolant mass flux ratio was unchanged ($\dot{m}_c/\dot{m}_\infty$ = 2.8%): the coolant flux ratio of the front hole rows is $\dot{m}_c/\dot{m}_\infty$ = 2.1% and the passage hole array is $\dot{m}_c/\dot{m}_\infty$ = 0.7%.

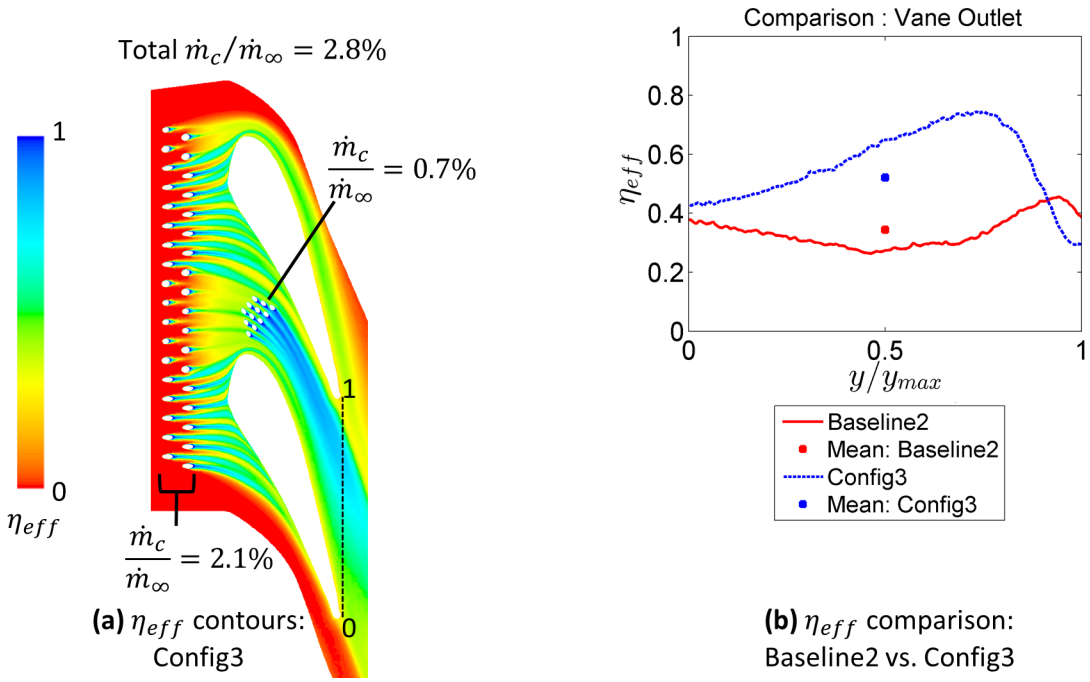


Figure 4-10: Config3 design

Figure 4-10 (b) shows a comparison of the η_{eff} distributions of the Baseline2 and Config3 designs at the vane outlet. All cooling holes are located far from the vane outlet line (minimum distance of 25 hole diameters). Heat transfer augmentation (h_f/h_0) at this location caused by coolant injection is thus likely to be minimal (see Section 1.3). The mean η_{eff} at the vane outlet line has increased by 51%. The cooling of the rear endwall has been improved

considerably, with minimal increase in aerodynamic penalty and little change in coolant consumption.

4.3.3 Reducing coolant consumption

The cooling system for the casing endwall is now considered. Optimization was performed at incompressible, SSPCF representative conditions (see Table 2-3). η_{eff} contours (CFD) on the casing endwall are shown in Figure 4-11 (a). The cooling system (called Baseline3) consists of a double row of cooling holes of diameter, $D_{baseline}$ = 8 mm. Complete details of this cooling system are given in Table 2-1. A large amount of coolant ($\dot{m}_c/\dot{m}_\infty$ = 6%) is injected through these holes, upstream of the vane passage. The injection of momentum at this location is beneficial: it suppresses endwall boundary layer separation and improves endwall cooling. However, the leading endwall is overcooled. As described in Section 4.3.2, it is more important to cool the trailing endwall. The cooling system is now redesigned to reduce coolant consumption while maintaining similar levels of cooling effectiveness at the trailing endwall.

To reduce coolant consumption, hole diameters were set to $0.5D_{baseline}$. It was seen in Section 3.1.4 that lower hole inclinations suppress endwall boundary layer separation better. This is because of greater streamwise momentum injected into the boundary layer. Also, because coolant lift-off is reduced, lower hole inclinations result in improved η_{eff} downstream. The hole inclination was thus reduced from the baseline value of 40^o, to 25^o, a typical manufacturing limit.

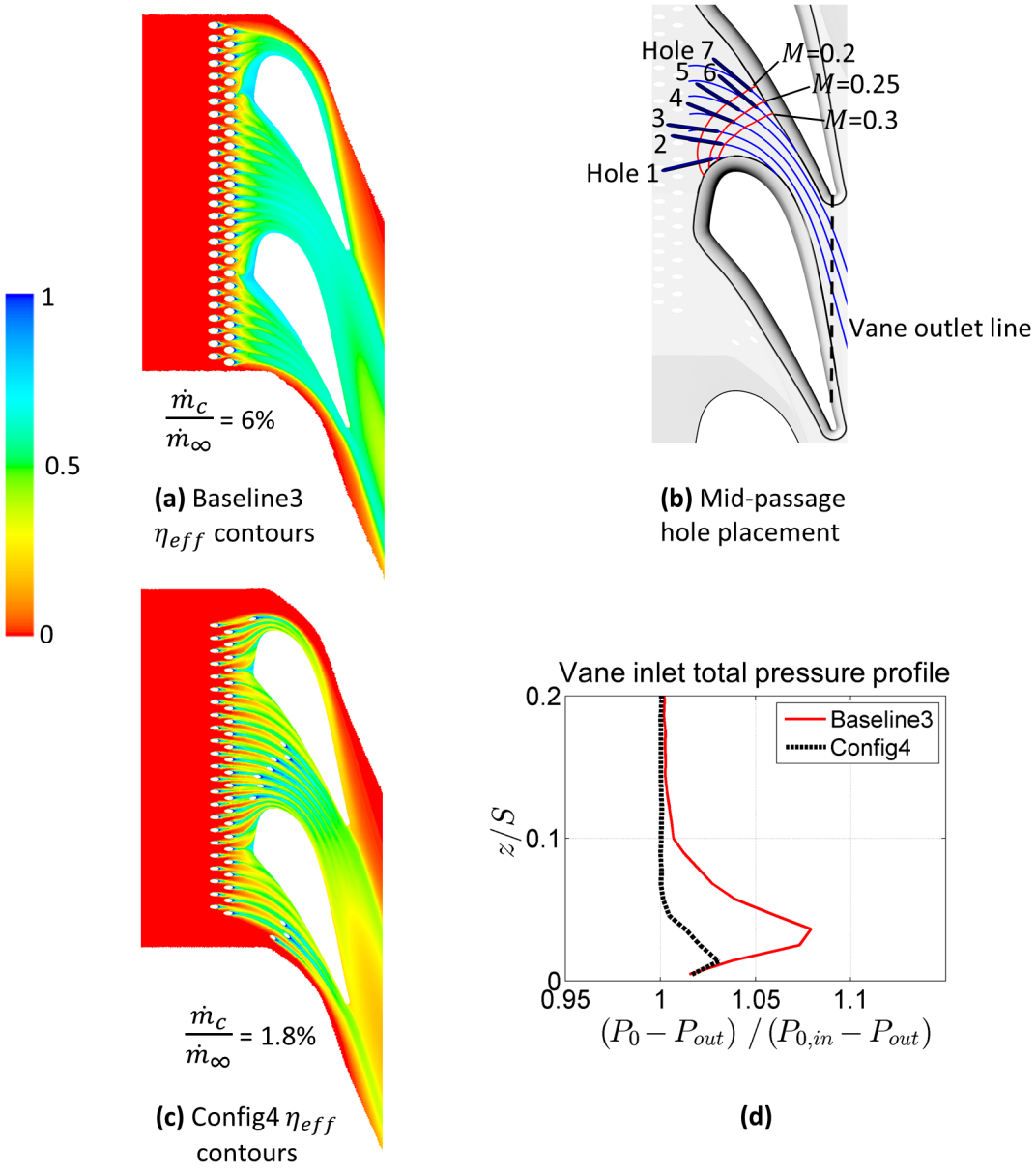


Figure 4-11: Optimization procedure: Config4 design

A CFD simulation of this new cooling hole pattern was run with the same coolant total pressure, $P_{0,c}$. Surface streamlines were obtained. These are shown in Figure 4-11 (b). New cooling holes, numbered 1-7, were placed mid-passage. These were aligned with the local surface streamline direction. Holes 1-3 direct coolant towards the SS endwall, while holes 5-7 direct coolant towards the PS endwall. Hole diameters were set to a constant value, $D_{platform} = 0.4D_{baseline}$. Hole inclinations were set to 25°.

These simulations were performed at incompressible conditions. However, to demonstrate a procedure for optimization, contours of isentropic Mach number were obtained from a compressible CFD simulation. All cooling holes were placed upstream of the M = 0.3 contour (Figure 4-11 (b)). This would result in minimal aerodynamic loss at engine condition.

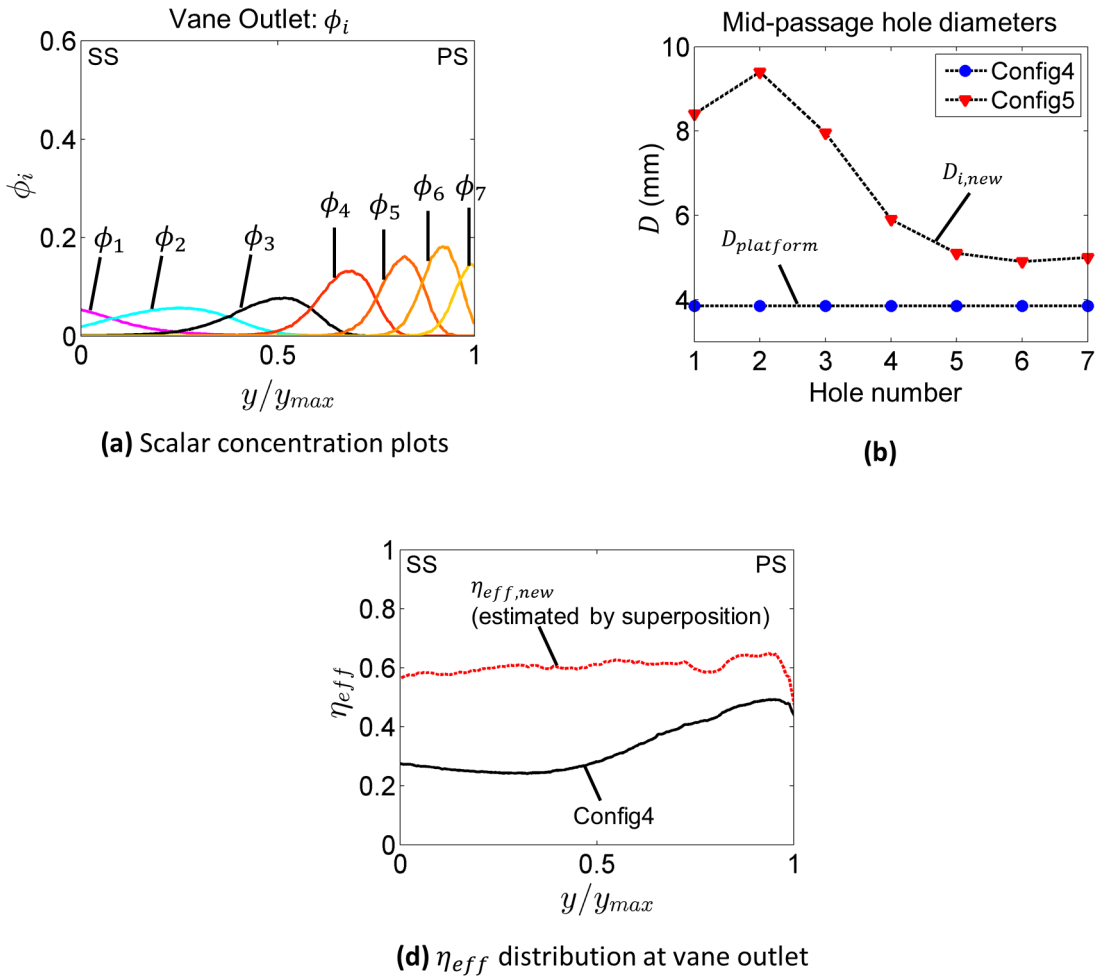
The new cooling system design is labelled Config4. A CFD simulation was run with the same coolant total pressure, $P_{0,c}$. η_{eff} contours for Config4 are shown in Figure 4-11 (c). Endwall boundary layer separation does not occur upstream of the vane. The vane inlet $\hat{P}$ profile for the Baseline3 and Config4 design are shown in Figure 4-11 (d). While reducing cooling hole diameters has decreased the near-wall total pressure peak, it retains a surplus over the freestream. This is able to suppress boundary layer separation, and drive passage cross-flows in the SS to PS direction. The reduction in near-wall total pressure will also reduce upwash on the vanes, and will keep coolant films near the endwall. The coolant consumption has decreased to $\dot{m}_c/\dot{m}_\infty$ = 1.8% from 6%. However cooling effectiveness at the trailing endwall has also decreased. The diameter of the mid-passage holes will now be adjusted to improve η_{eff} at the vane outlet line.

Following the procedure described in Section 4.2.2, scalar concentration equations were solved for the mid-passage holes. Scalar concentrations ϕ_1 to ϕ_7 correspond to holes 1 to 7 (marked in Figure 4-11 (b)). Plots of ϕ_1 to ϕ_7 at the vane outlet line are shown in Figure 4-12 (a).

Equation (4-14) was used to estimate $\eta_{eff,new}$ for new hole diameter distributions ($D_{i,new}$), given ϕ_1 to ϕ_7. Total coolant mass flow rate was estimated using the expression:

$$\dot{m}_{c,new} = \dot{m}_{Config4} + \sum_{i=1}^{7} \left(\frac{{D_{i,new}}^2}{D_{platform}^2} - 1 \right) \dot{m}_{c,i}, \tag{4-25}$$

where $\dot{m}_{Config4}$ was the coolant consumption of the Config4 design and $\dot{m}_{c,i}$ was the coolant flow rate through the mid-passage holes of Config4.



(a) Scalar concentration plots

(b)

(d) η_{eff} distribution at vane outlet

Figure 4-12: Optimization of Config4 design using scalar tracking method

A uniform value of $\eta_{eff} = 0.6$ was targeted at the vane outlet line (marked in Figure 4-11 (b)) with a coolant flux constraint, $\dot{m}_c/\dot{m}_\infty$ = 3.0%. To achieve these goals, the diameters of holes 1-7 were adjusted by trial-and-error, until the optimized values shown in Figure 4-12 (b) were obtained. $\eta_{eff,new}$ estimated by Equation (4-14) for this optimized design is shown in Figure 4-12 (c). The total coolant mass flux ratio (mid-passage and upstream holes) estimated using Equation (4-25) was $\dot{m}_c/\dot{m}_\infty$ = 2.9%.

A CFD simulation was run with this new distribution of mid-passage hole diameters. The design, called Config5, is shown in Figure 4-13 (a). Flow boundary conditions, including coolant total pressure ($P_{0,c}$), were not changed. The endwall η_{eff} contours for Config5 are shown in Figure 4-13 (b). The CFD predicted coolant mass flux ratio for the Config5 design was $\dot{m}_c/\dot{m}_\infty$ = 3.0%, closely matching the value estimated by Equation (4-25), $\dot{m}_c/\dot{m}_\infty$ = 2.9%.

The η_{eff} distributions for the Baseline3 and Config5 designs are compared at the vane outlet in Figure 4-13 (c). While coolant consumption for the Config5 design has decreased by 50% from the Baseline3 design, the mean η_{eff} at vane outlet is only 5% lower. The Config5 design has thus achieved the optimization goal of reducing coolant consumption while maintaining similar levels of cooling effectiveness on the trailing endwall.

Figure 4-13 (c) also compares $\eta_{eff,new}$ estimated by Equation (4-14), with the CFD prediction (marked Config5). The mismatch is small despite the large adjustments in diameter. The target η_{eff} of 0.6 can be achieved with greater accuracy if this process is iterated: if scalar concentration equations for the mid-passage holes of Config5 are solved, and diameters are readjusted by smaller values.

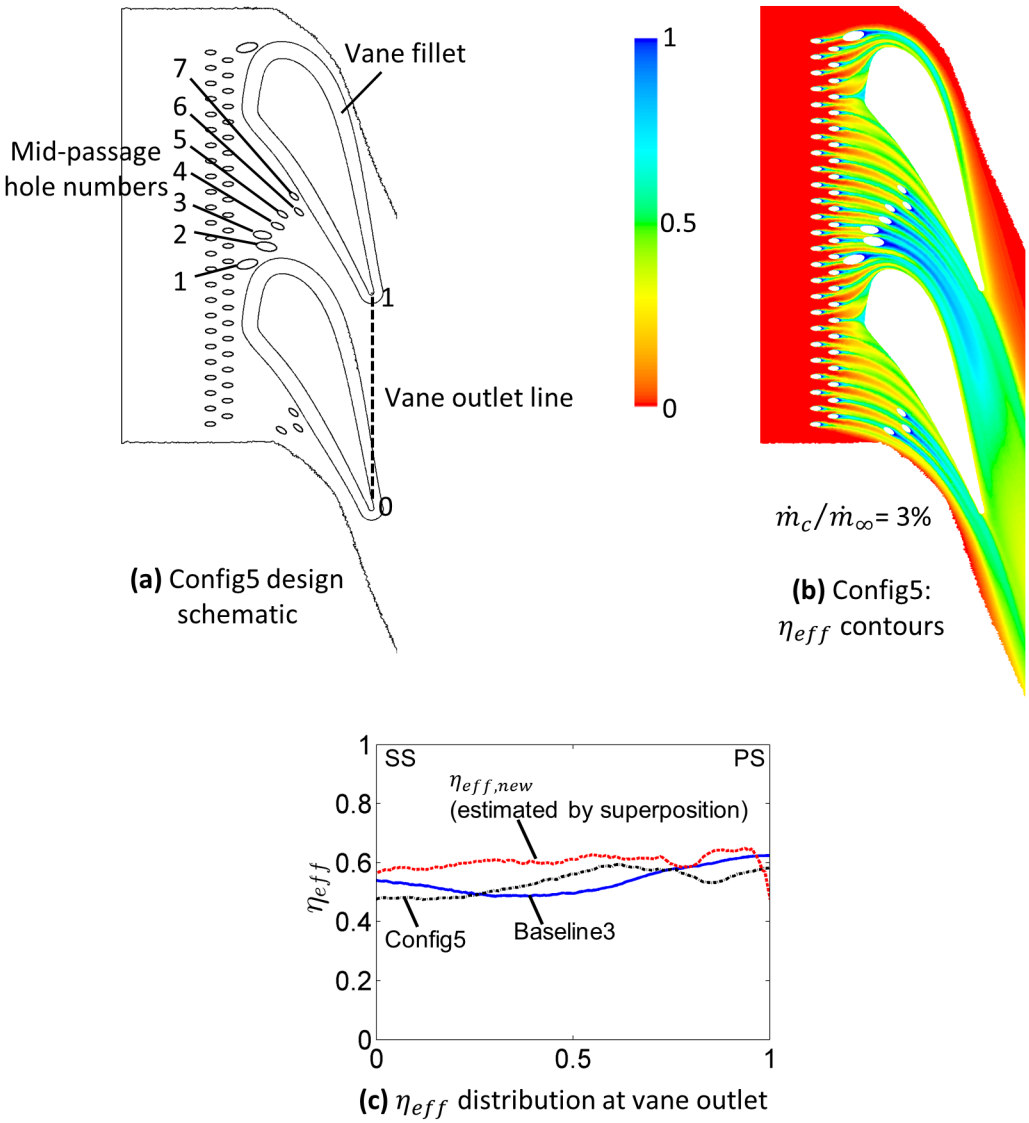
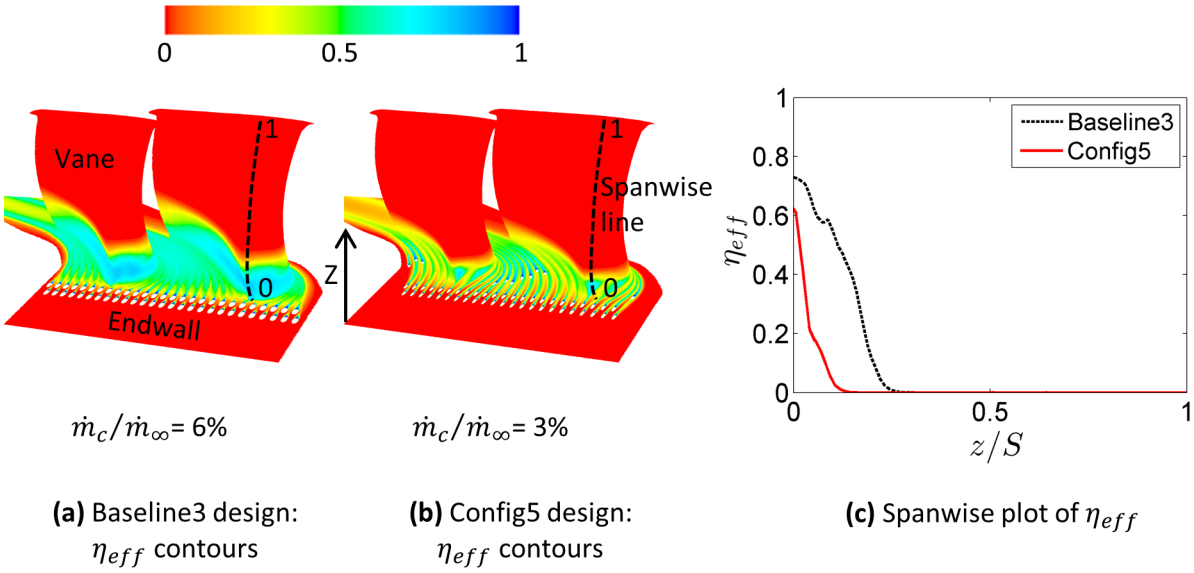


Figure 4-13: Config5 design

η_{eff} contours on the vane for the Baseline3 and Config5 design are shown in Figure 4-14 (a) and (b). The η_{eff} distributions on a spanwise line are compared in Figure 4-14 (c). Coolant is driven up the vane surface and away from the endwall in the Baseline3 design. The vane inlet $\hat{P}$ profiles for the Baseline3 and Config4 design were shown in Figure 4-11 (d). Since the upstream cooling hole rows have not been modified, the $\hat{P}$ profiles for the Config4 and Config5 designs are approximately the same. Coolant injection leads to surplus total pressure in the near-wall region. As described in Section 3.1.3, this drives upwash on the vane surface. The peak in $\hat{P}$ is closer to the endwall in the Config5 design than the Baseline3

design because of lower hole inclination. The near-wall $\hat{P}$ values are also smaller because of lower coolant flow rate. This results in reduced upwash and more efficient cooling of the endwall.



(a) Baseline3 design: η_{eff} contours

(b) Config5 design: η_{eff} contours

(c) Spanwise plot of η_{eff}

Figure 4-14: Coolant upwash on vane

Injecting high momentum coolant through the endwall upstream of the vane energizes the boundary layer. Secondary flows are suppressed and endwall cooling is improved. However, using large coolant mass flows at this location drives upwash, resulting in inefficient cooling of the endwall.

4.4 Summary

Table 4-1 provides a summary of the optimization studies in this chapter.

Design goal	Design name	Description
Compensating for cross-passage flow (hub endwall, SSPCF representative conditions)	Baseline1	Uniform diameter, double-row of cooling holes.
	Config1	*Design change*: cooling hole diameter distribution changed; no new cooling holes added.
Result: Config1 has more uniform η_{eff} distribution at vane outlet line than Baseline1.		
Improving cooling of the trailing endwall (hub endwall, engine representative conditions)	Baseline2	Uniform diameter, double row of cooling holes.
	Config2	*Design change*: hole inclinations reduced on certain holes to prevent cooling jet lift-off.
	Config3	*Design change*: additional array of cooling holes in low M region.
Result: Config3 has 51% improved mean η_{eff} at vane outlet line than Baseline2.		
Reducing coolant consumption (casing endwall, SSPCF representative conditions)	Baseline3	Uniform diameter, double row of cooling holes
	Config4	*Design change*: hole inclinations and diameters reduced; mid-passage cooling holes added.
	Config5	*Design change*: diameters of mid-passage holes adjusted to target mean vane outlet η_{eff} = 0.6, with $\dot{m}_c/\dot{m}_\infty$ = 3.0%.
Result: Coolant consumption is decreased from $\dot{m}_c/\dot{m}_\infty$ = 6.0% (Baseline3) to $\dot{m}_c/\dot{m}_\infty$ = 3.0% (Config5) while maintaining similar levels of cooling effectiveness at vane outlet line (mean η_{eff} = 0.5).		

Table 4-1: Summary of optimization studies

5 OPTIMIZATION OF AN ENGINE HP NGV ENDWALL COOLING SYSTEM

The design methods and principles demonstrated in Chapter 4 were applied to optimize the endwall cooling system of an engine HP NPV. The semi-automated CFD loop described in Appendix B allowed completion of this task in 6 weeks.

The HP NGV section is composed of 20 vane pairs. A solid model of the NGV vane pair is shown in Figure 5-1 (a). The vane pairs are mated using a feather seal at the location shown. The passage enclosed by the vanes is referred to as the closed passage. The adjacent passages are labelled open passages. The leading and trailing vane are marked in Figure 5-1 (a).

The endwalls are cooled using a double-row of staggered cylindrical cooling holes called the RODN (casing) and RIDN (hub).

A CFD domain was constructed using the vane pair solid model. To automate meshing in ICEM-CFD, this used a six passage configuration (Figure 5-1 (b)) similar to the one described in Section 2.2. Cooling holes are located only on the endwall of the central vane pair. Unstructured tetrahedral meshes were obtained. Around 10 million cells of the total mesh count (10.5 million) were concentrated in the central passages. The SST k-ω turbulence model was used. Maximum y^+ values of 200 were observed on the endwall. The y^+ values are within recommended limits for the SST k-ω wall-treatment. While the meshes used were relatively coarse, they were considered adequate for a design study.

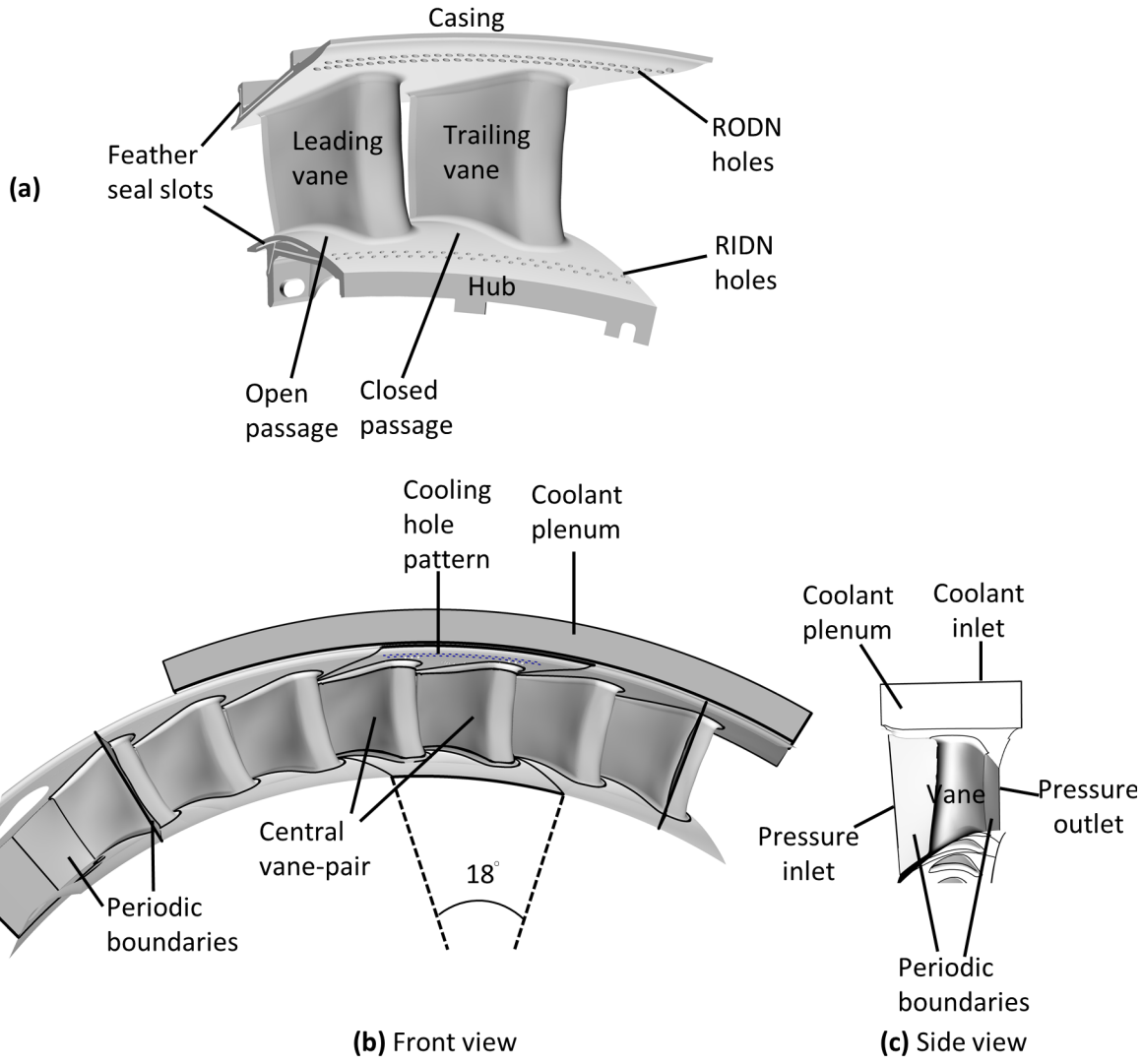


Figure 5-1: (a) Vane pair solid model; CFD model: (b) Front view, (c) Side view

Geometrical data and flow boundary conditions used are listed in Table 5-1. Combustor outlet profiles provided by Rolls-Royce were used as boundary conditions for total temperature and turbulence quantities. Adiabatic boundary conditions were set on all walls. The turbulence boundary conditions, shown in Figure 5-2, are circumferentially uniform. The variation caused by dilution jets is ignored.

Vane geometry:	Radius at midspan	375 mm
	Axial chord length at midspan (C_{ax})	29.3 mm
	Inlet span/axial chord length	2.2
	Outlet span/axial chord length	1.8
	Angular pitch	9^o
Cooling hole geometry:	**Casing (RODN):**	
	Hole diameter	1.8 mm
	Hole inclination to endwall	40°
	Hole pitch/diameter	2.2
	Hole length/diameter	1.7
	Number of rows	2
	Row spacing/diameter	2.9
	Hub (RIDN):	
	Hole diameter	1.5 mm
	Hole inclination to endwall	40°
	Hole pitch/diameter	2.8
	Hole length/diameter	1.9
	Number of rows	2
	Row axial spacing/diameter	2.2
Flow boundary conditions (set at pressure inlet/outlet, coolant inlet shown in Figure 5-1 (b), (c))	Inlet turbulent kinetic energy (k) and dissipation rate (ε)	Profile, see Figure 5-2
	Inlet total temperature	Profile, see Figure 5-3
	$P_{0,in}/P_{out}$	1.81
	$P_{0,c}/P_{0,in}$	1.029

Table 5-1: Engine geometry and flow boundary conditions

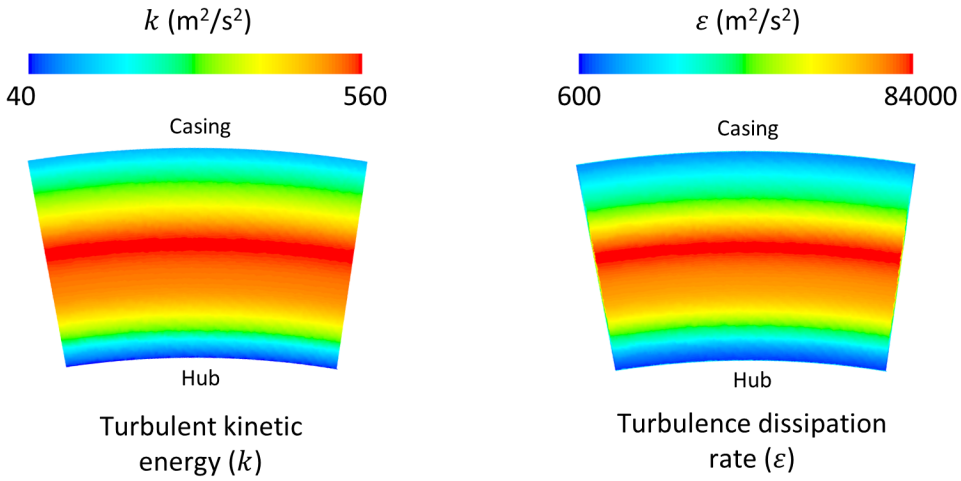


Figure 5-2: Inlet turbulence profiles

In this chapter, as in Chapter 3 and 4, cooling system optimization will target reduction in total temperature of the fluid on the adiabatic walls. The adiabatic wall temperature can be estimated from total temperature using Equation (4-10) (Section 4.2.1).

5.1 Uncooled NGV

A CFD simulation was run on a model with no film cooling holes. The flow boundary conditions in Table 5-1 were used. Total temperatures are expressed as a non-dimensional variable, ψ, defined as:

$$\psi = \frac{T_0 - T_{0,min}\big]_{inlet}}{T_{0,max}\big]_{inlet} - T_{0,min}\big]_{inlet}}, \tag{5-1}$$

The non-dimensional total temperature profile specified at the NGV inlet is shown in Figure 5-3 (a). The vane angular pitch is 9^{o}. One fuel nozzle is positioned upstream of each vane pair. The periodic angle of the combustor temperature profile is thus 18^{o}.

The contours of total temperature on the vane pair surfaces are shown in Figure 5-3 (b). The combustor hot spot (Figure 5-3 (a)) is aligned with the leading vane. This vane is thus at a higher temperature.

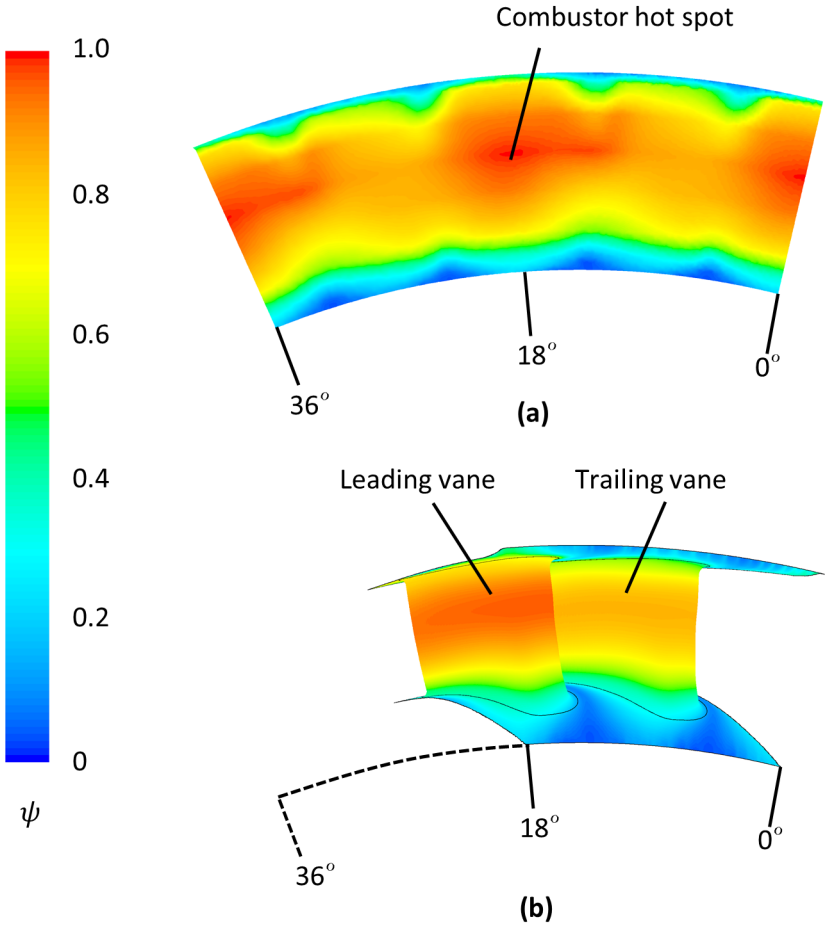


Figure 5-3: (a) Inlet ψ profile; (b) Contours of ψ on vane pair

The temperatures on the uncooled casing and hub endwall are shown in Figure 5-4 (a) and (b). The average non-dimensional temperature on the casing is $\Delta\psi = 0.16$ higher than the hub. Endwall temperatures on the open passage are particularly high because of the combustor hot spot upstream. The combustor hot spot also results in a hot patch downstream of the leading vane TE. A similar hot patch is observed downstream of the trailing vane TE, but this is less intense.

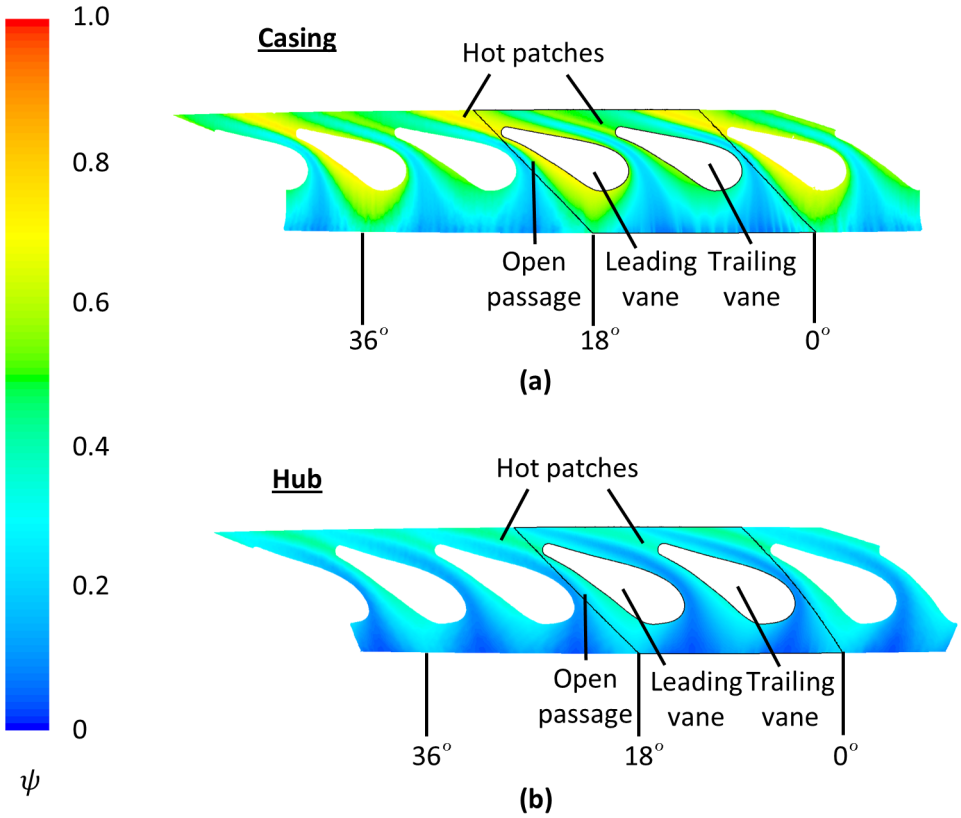


Figure 5-4: Contours of ψ on: (a) Uncooled casing endwall; (b) Uncooled hub endwall

5.2 Baseline RIDN/RODN cooling system

CFD simulations were run with the baseline RIDN/RODN cooling system. The coolant mass flux ratios ($\dot{m}_c/\dot{m}_\infty$) for the baseline RODN and RIDN systems are 4.75% and 2.5%. Adiabatic wall total temperatures on the casing and hub open passages are shown in Figure 5-5 (a) and (b). Note the use of different colour maps – the casing is at a higher temperature than the hub. The open passage is exposed to the combustor hot spot. Hot patches are observed downstream of the leading vane TE. The RIDN/RODN cooling system is unable to effectively cool this area. Also, heat transfer rates at the vane wake are high due to increased turbulent mixing. Optimization will thus focus on reducing temperatures in this critical region.

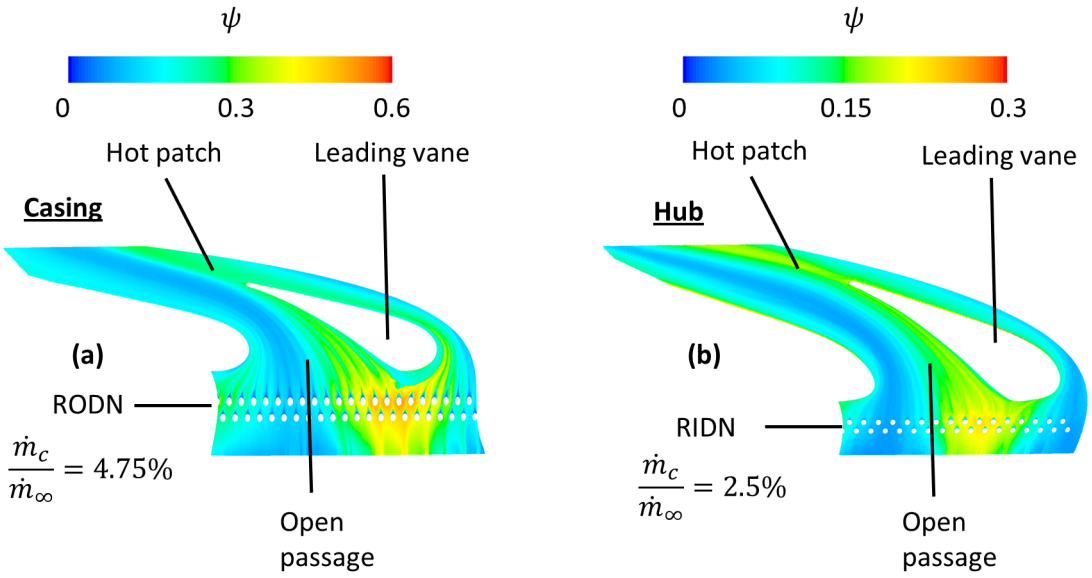


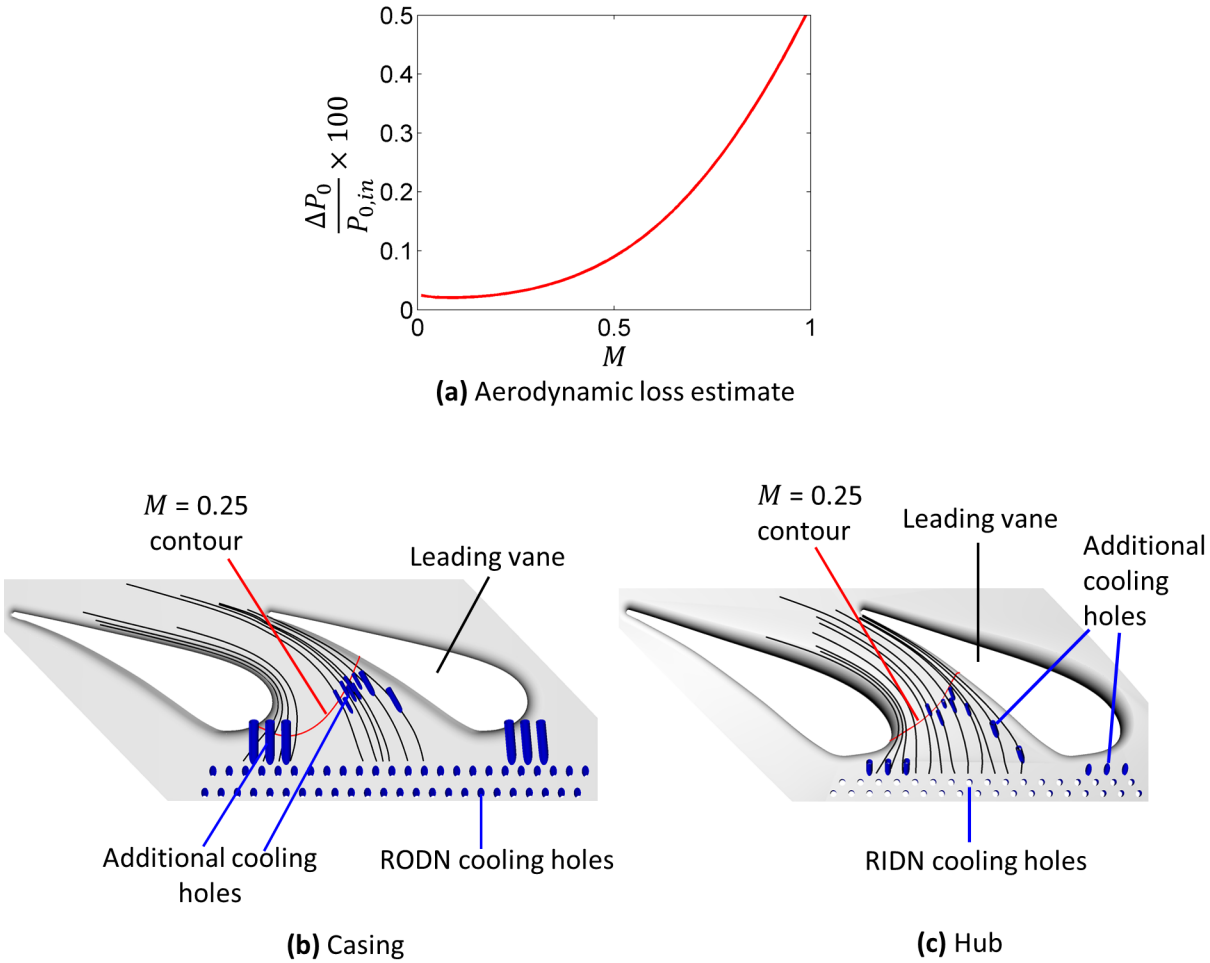
Figure 5-5: Contours of ψ with baseline cooling system: (a) Casing; (b) Hub

5.3 Design of optimized cooling system

The design principles of Chapter 4 are now applied to improve the baseline cooling system.

Figure 5-6 (a) shows aerodynamic losses estimated using the Kollen and Koschel (1985) model for $\dot{m}_c/\dot{m}_\infty$ = 1%, hole inclination of 25^o, with coolant mixing to η_{aw} = 0.3. This loss model was described in Section 4.3.2. Losses are low for injection below M = 0.25.

Surface streamlines were obtained from the CFD simulation performed for the baseline cooling system. These are shown on the casing and hub in Figure 5-6 (b) and (c). Surface streamlines were used as a guide for locating cooling holes on the endwall. Hole blowing ratio decreases downstream in the passage. Coolant released at low blowing ratios will approximately trace the trajectory of the surface streamline.



(a) Aerodynamic loss estimate

(b) Casing

(c) Hub

Figure 5-6: Placing cooling holes on the endwall: design principles

As discussed in Section 5.2, improved cooling of the endwall downstream of the leading vane TE is desired. Additional cooling holes were placed on surface streamlines directed towards the PS and SS TE (see Figure 5-6 (b) and (c)). The RIDN/RODN cooling holes were left unchanged. Cooling effectiveness decays with distance downstream. Placing holes closer to the TE is thus beneficial. To minimize aerodynamic loss, all holes were placed upstream of the M = 0.25 contour. To simplify manufacturing, hole compound angles were set to a constant value, equal to the average angle of the surface streamlines at the injection locations.

The casing open passage is first considered. A CFD simulation was run with the optimized cooling hole pattern using the boundary conditions given in Table 5-1. Contours of

ψ on the endwall are shown in Figure 5-7 (b). Contours of T_0 obtained with the baseline (RODN) cooling system are shown in Figure 5-7 (a) for comparison. The additional cooling holes of the optimized design eliminate the hot patch at the TE of the leading vane. ψ is compared on a line marked at the vane outlet (see Figure 5-7 (a), (b)). The comparison is shown in Figure 5-7 (c). Peak and mean non-dimensional total temperatures have been reduced by $\Delta\psi = 0.1$ and 0.05. The coolant mass flux ratio ($\dot{m}_c/\dot{m}_\infty$) has increased, from 4.75% for the baseline system, to 6.25% for the optimized system. While the vane outlet line spans a vane pitch angle (9^o), the ψ plots are aperiodic because the vane inlet temperature profile has a periodicity of two vane passages (18^o, see Figure 5-3 (a)).

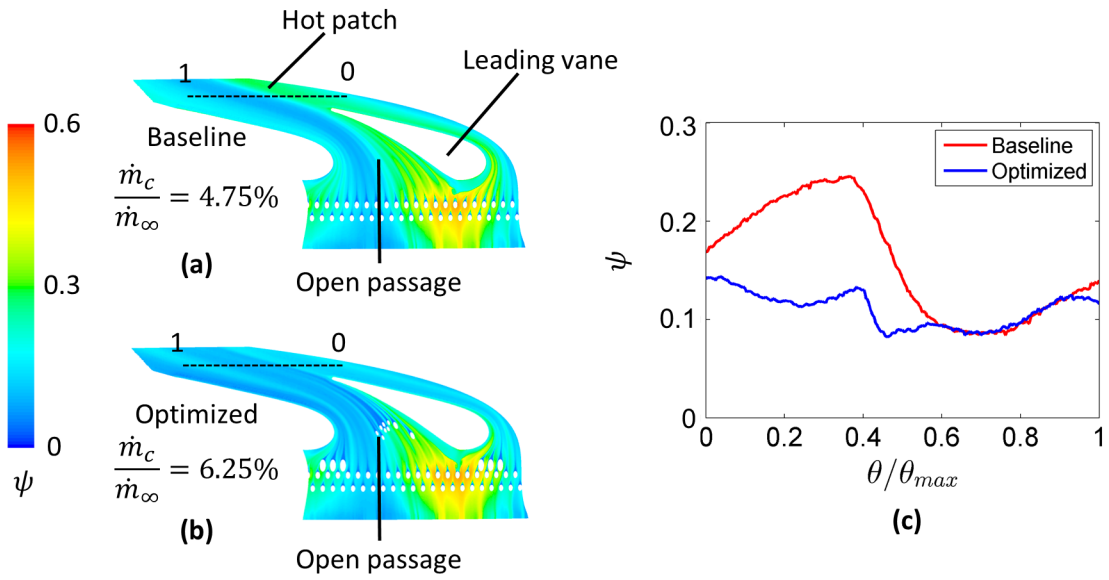


Figure 5-7: Contours of ψ on casing (open passage) with: (a) Baseline (RODN) cooling system, (b) Optimized cooling system; (c) Comparison of ψ at vane outlet line

A CFD simulation was run with the optimized cooling hole pattern on the open passage hub. Contours of ψ on the endwall are shown for the baseline cooling system (Figure 5-8 (a)) and the optimized cooling system (Figure 5-8 (b)). The optimized cooling system eliminates the hot patch at the leading vane TE. Temperatures are compared on a line at the vane outlet in Figure 5-8 (c). Peak non-dimensional total temperature is reduced by $\Delta\psi$ =

0.06 and the mean is reduced by $\Delta\psi$ = 0.03. The coolant mass flux ratio ($\dot{m}_c/\dot{m}_\infty$) has increased, from 2.5% for the baseline system, to 3.2% for the optimized system.

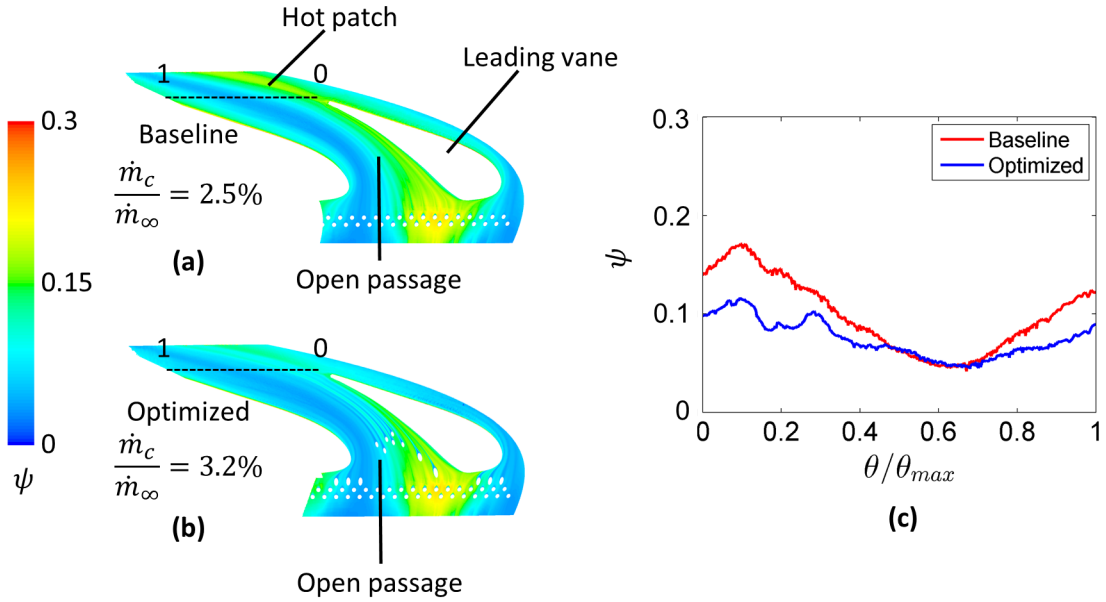


Figure 5-8: Contours of ψ on hub (open passage) with: (a) Baseline (RIDN) cooling system, (b) Optimized cooling system; (c) Comparison of ψ at vane outlet line

The temperature profile at the vane outlet determines temperatures in the downstream rotor. Figure 5-9 shows circumferentially averaged temperatures at the vane outlet. The optimized design delivers temperature reductions of $\Delta\psi$ = 0.05 at the casing (Figure 5-9 (a)) and $\Delta\psi$ = 0.025 at the hub (Figure 5-9 (b)). This will reduce temperatures on the rotor endwalls.

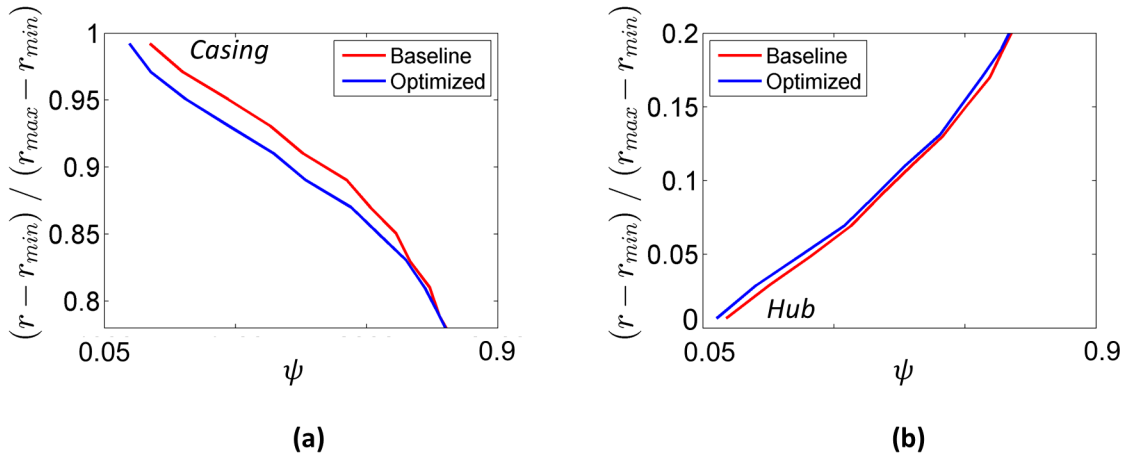


Figure 5-9: Circumferentially averaged temperatures at the vane outlet

Endwall cooling of the critical open passage has been considered thus far. Figure 5-10 (a) shows contours of ψ on the closed passage endwall, cooled by the baseline RODN system. While a hot patch is seen downstream of the trailing vane TE, temperatures are less critical and additional cooling is not required. However, the optimized cooling system can be used to eliminate this hot patch as well (see Figure 5-10 (b)).

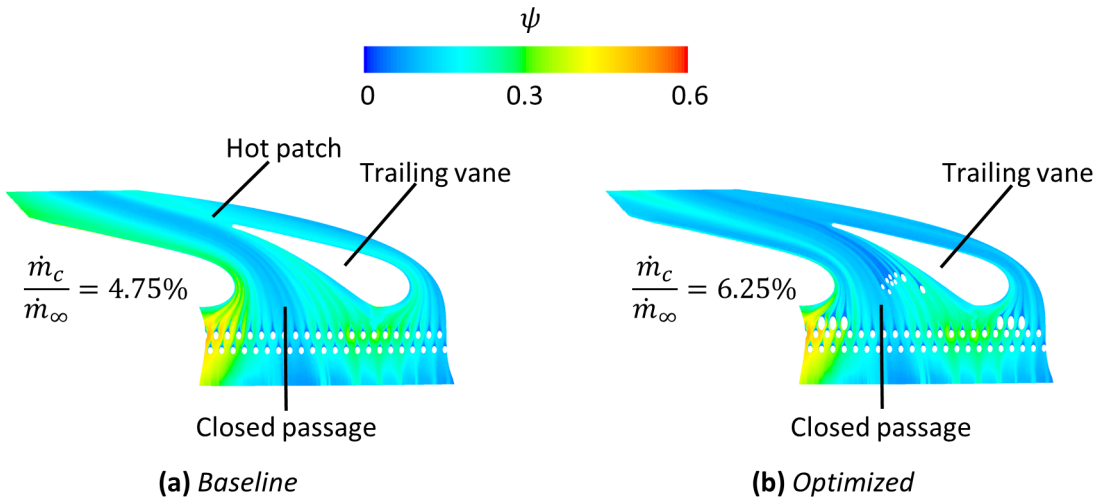


Figure 5-10: Cooling of the closed passage casing

The optimized system consumes more coolant than the baseline system. In order to decrease coolant consumption to baseline values ($\dot{m}_c/\dot{m}_\infty$ = 4.75% and 2.5% for the casing and hub cooling systems), the diameters of the RIDN/RODN cooling holes were reduced. The additional mid-passage cooling holes were left unaltered. Mass flow through the

RIDN/RODN cooling holes was assumed proportional to D^2, where D was the hole diameter. This approximation was explained in Section 4.2.1. Coolant mass flow through the additional mid-passage holes was obtained from the CFD simulations as $\dot{m}_c/\dot{m}_\infty$ = 1.5% for the casing and $\dot{m}_c/\dot{m}_\infty$ = 0.7% for the hub. In order to offset this additional flow, RODN and RIDN hole diameters were decreased by 17% and 11.5%. The coolant mass flux ratio ($\dot{m}_c/\dot{m}_\infty$) of the new "reduced-flow" design was 4.75% for the casing and 2.65% for the hub. The reduced-flow design consumes approximately the same coolant flow as the baseline design.

Contours of ψ on the casing cooled by the reduced-flow design are shown in Figure 5-11 (a). The temperatures on the vane outlet line are compared in Figure 5-11 (c). Endwall temperatures are higher with the reduced-flow design than the optimized design. This is a result of reducing RIDN/RODN diameters. However the reduced-flow design retains a significant advantage over the baseline design: a $\Delta\psi$ = 0.05 reduction in peak temperature and $\Delta\psi$ = 0.025 reduction in mean temperature are observed.

ψ contours for the reduced-flow hub design is shown in Figure 5-11 (b). The reduced-flow design delivers a $\Delta\psi$ = 0.04 reduction in peak temperature and a $\Delta\psi$ = 0.015 reduction in mean temperature over the baseline.

Aerodynamic losses were estimated for the cooling systems (hub and casing) using the Kollen and Koschel (1985) method. Coolant mass flow rates through individual holes and freestream Mach numbers at the points of injection were obtained from CFD simulations. The normalized total pressure losses caused by coolant injection, $\Delta P_0/P_{0,in}$, was estimated as 0.18% for the baseline design, 0.25% for the optimized design, 0.19% for the reduced-flow design.

The reduced-flow design thus improves endwall cooling while using approximately the same coolant flow as the baseline design and incurring little extra aerodynamic penalty.

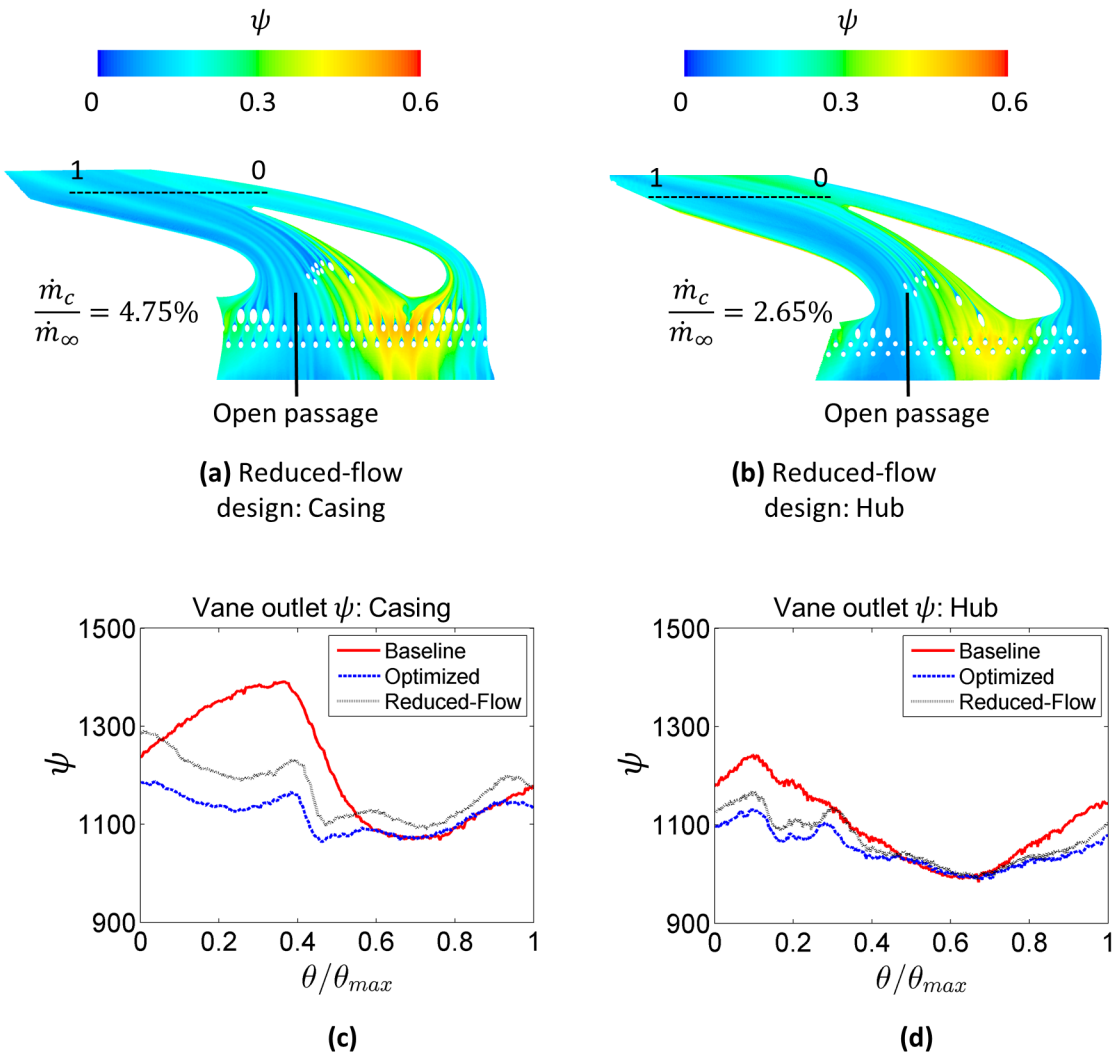


Figure 5-11: Reduced-flow design: ψ contours on (a) casing, (b) hub; comparison on ψ on vane outlet line on (c) casing, (d) hub

5.4 Robustness to combustor outlet profile

The combustor outlet temperature profile is difficult to determine and subject to considerable uncertainty. A simple study was conducted to verify the robustness of the optimized designs to variation in combustor output. CFD simulations were run with the combustor ψ profile (shown in Figure 5-3 (a)) clocked by $+2^{o}$ and -2^{o} (pitch angle = 9^{o}).

A clocking angle of +2° is first considered. Figure 5-12 (a) and (b) show ψ contours on the endwall for the baseline and optimized designs. Figure 5-12 (c) compares temperatures on the vane outlet line. The optimized design performs better than the baseline design with

these boundary conditions, delivering a mean temperature reduction of $\Delta\psi$ = 0.05. Similar results are shown in Figure 5-12 (d), (e), (f) for a clocking angle of -2°. The optimized system continues to perform better than the baseline design, reducing mean temperature at the vane outlet line by $\Delta\psi$ = 0.027.

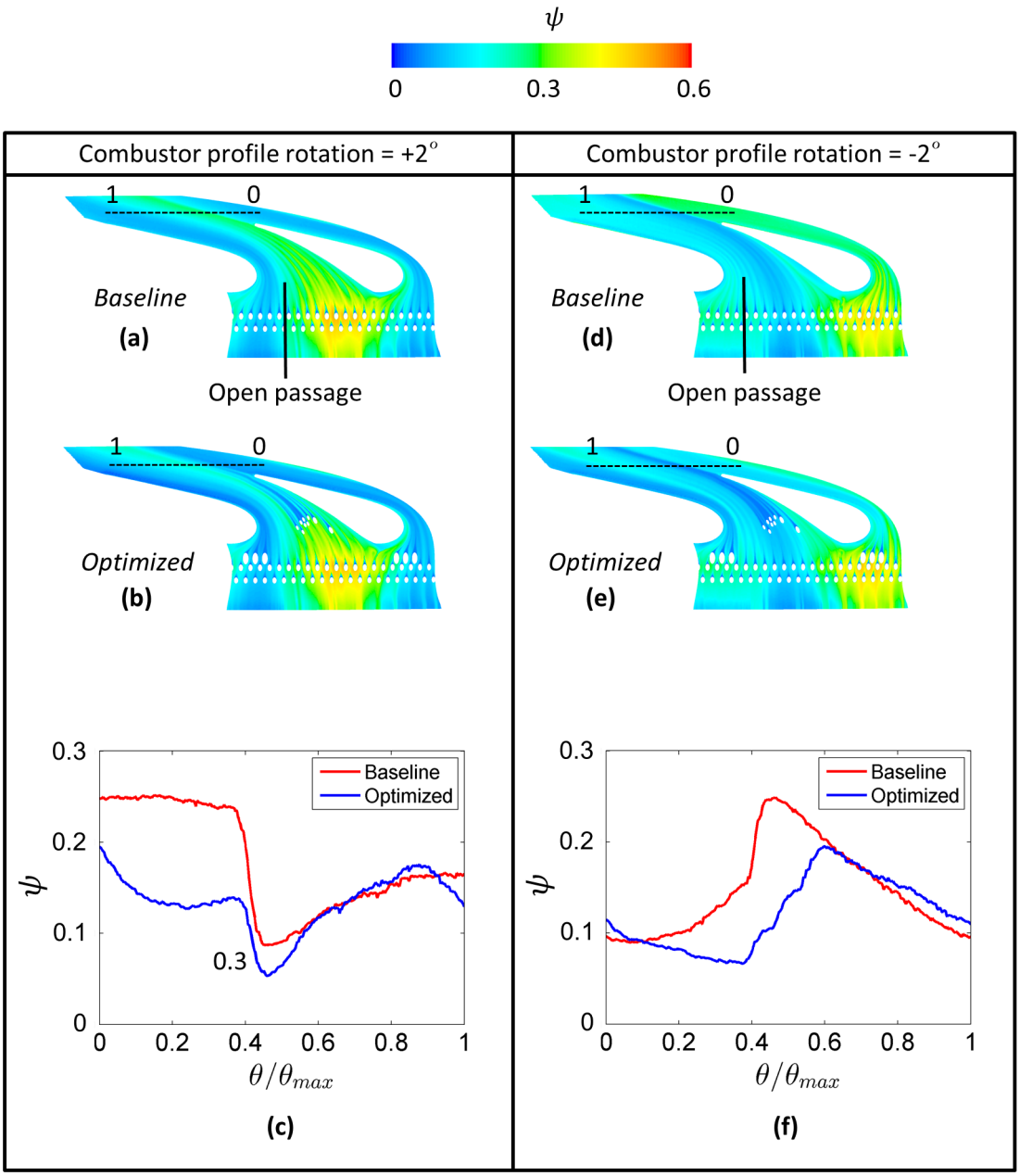


Figure 5-12: Effect of clocking combustor outlet profile

5.5 Summary

The insight gained from this study has been applied to optimize endwall cooling systems in an engine under development. Considerable reductions in endwall temperatures are predicted.

6 CONCLUSIONS

Conclusions from this work are now presented. These are progressed in four sections.

6.1 Interaction of endwall coolant with vane secondary flows

The design of engine endwall cooling systems has been informed by classical secondary flow models. These secondary flow models show that endwall boundary layer separation and cross-passage flows make it difficult to film-cool endwalls. Experimental and CFD studies in this work show that coolant injection in the endwall upstream of the vane can be used to suppress secondary flows. Secondary flows are determined by the vane inlet total pressure profile. The viscous deficit in near-wall total pressure causes classical secondary flow structures. Injection of high momentum coolant through the endwall decreases this deficit.

A small surplus in near-wall total pressure provides the boundary layer with sufficient momentum to overcome the adverse pressure gradient imposed the vanes. Boundary layer separation on the endwall is eliminated, and the entire endwall can be cooled. A large surplus in near-wall total pressure introduces new secondary flow patterns. The direction of cross-passage flow is reversed. The spanwise gradient in total pressure caused by coolant injection drives new vortex structures. Of particular detriment is upwash on the vanes, which drives coolant flow away from the endwalls. Upstream cooling holes can be optimally sized by studying the vane inlet total pressure profile in the near-wall region. Greater momentum is provided by larger diameter holes.

Also studied was the effect of engine-representative turbulence levels on vane secondary flows. CFD studies show that endwall boundary layers have greater momentum in flows with high freestream turbulence. Secondary flows are weaker as a result.

6.2 Validation of CFD results with experiment

CFD predictions were validated by experimental measurements in the SSPCF. Good agreement was obtained, which increased confidence in the use of CFD to predict and optimize endwall film-cooling systems.

6.3 Improved design philosophy and methods for endwall film cooling systems

The insight obtained from the CFD and experimental studies was used to propose an improved design philosophy for endwall film cooling systems. Coolant is injected in the endwall upstream of the vanes to reduce the viscous deficit in near-wall total pressure. Secondary flows are thus reduced, allowing for improved cooling of the leading endwall. The critical trailing endwall is cooled by holes placed further downstream, in low Mach number regions of the endwall.

A passive scalar tracking method was devised that allowed the isolation of cooling effectiveness contribution from individual holes. This was shown to be an accurate and effective tool for optimizing endwall cooling systems using CFD.

A cooling system designed according to this philosophy, using the passive scalar tracking method, delivered similar cooling effectiveness on the rear endwall for half the coolant supply.

6.4 Application to engine development program

The results of this research have been transferred to an engine development program. Optimized endwall film cooling systems have been delivered for an engine HP NGV. These systems perform considerably better than the baseline.

7 SUGGESTIONS FOR FURTHER RESEARCH

7.1.1 Experimental studies

- Traverse studies are recommended in the SSPCF, to measure total pressure, temperature and turbulence quantities at the vane inlet and outlet plane. The vane inlet flow profiles determine secondary flows. These profiles are influenced by the upstream combustor simulator. Accurate boundary conditions can be specified in CFD simulations if these measurements are made. If coolant is injected upstream of the vane, the rate of mixing of coolant momentum and enthalpy with the freestream can be studied by comparing the vane inlet and outlet profiles. Accurate prediction of mixing is important for CFD simulation; these measurements can be used to validate CFD predictions. Temperature measurements at the outlet plane can also be used to validate CFD predictions of coolant upwash on the vanes.
- Experimental η_{eff} data was obtained on the hub endwall (Section 3.2.3), but was not compared with CFD predictions. Such comparisons can provide useful validation of CFD. They can also provide insight into the effect of endwall contraction on secondary flows and coolant injection.
- A CO_2 coolant injection system was developed during this project. This is described in Appendix C. This system will allow the density ratio to be matched better, allowing a more realistic match of coolant flow conditions with the engine. The data acquired can be used for CFD validation.
- The optimized designs presented in Section 4.3 can be tested in the SSPCF and results can be compared with CFD predictions. The accuracy of CFD in predicting improvements in η_{eff} can thus be validated.
- Future engines will use a lean combustor architecture, with considerable swirl at the vane inlet plane. The SSPCF combustor simulator can be modified to include a central swirler,

to model a prescribed swirl profile. Swirl changes the direction of flow in the near-wall region. Endwall cooling systems can be redesigned in CFD for the measured swirl profile. Design changes anticipated are alignment of RIDN/RODN and mid-passage cooling holes with the local flow direction. This will increase momentum imparted to the near-wall flow and will decrease mixing of coolant with the freestream. The modified designs can be validated by experiments in the SSPCF.

7.1.2 CFD studies

- Coolant flow injected through holes with a converging cross-section (Figure 7-1) will experience lower total pressure losses. For the same coolant mass flow, such holes will impart greater momentum to the near-wall flow than cylindrical holes. These converging holes can be used in the endwall upstream of the vane to suppress secondary flows. The use of these hole geometries can be studied using CFD and improvements, if any, can be validated by experiments in the SSPCF.

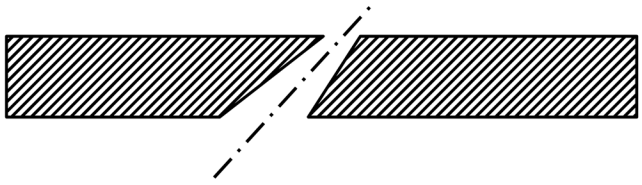


Figure 7-1: Converging hole geometry

- The effect of leakage from the combustor-turbine interface gap was not considered. It was noted in Section 3.3.3 that low momentum leakage flow from this gap will aggravate secondary flows. However, this can be overcome by high momentum coolant injection through discrete holes. This combined slot/discrete hole configuration can be studied in CFD. Cooling holes can be sized to decrease the near-wall deficit in total pressure caused by low-momentum slot coolant. The results can be validated by experiments in the SSPCF.

- Uniform diameter RIDN/RODN hole rows were used in this study. Further optimization is possible if coolant can be injected only where necessary to suppress secondary flows: the pitchwise variation of near-wall total pressure needs more attention. While RIDN/RODN hole diameters and inclinations were adjusted in the optimized designs presented, no attention was paid to other geometric variables. Reducing hole spacing (pitch-to-diameter, row spacing) will improve downstream cooling effectiveness.
- In Section 4.3.3 and 5.3, mid-passage holes were aligned with surface streamlines and placed in low M regions. Placing holes further downstream results in greater aerodynamic loss, but improves η_{eff} at the critical trailing endwall. The passive scalar tracking method can be used to study decay of η_{eff} with streamwise distance from the injection location. The hole location on the surface streamline can then be optimized. Also, the principles used to optimize double-row cooling systems can be applied to these mid-passage holes.
- The injection of coolant increases fluid momentum in the near-wall region. However, wall shear and mixing with the freestream will decrease this surplus momentum. PS to SS cross-passage flows may re-emerge in the trailing endwall. While this study focused on the vane inlet total pressure profile, the study of near-wall total pressure at downstream locations of the passage is recommended. CFD predictions of the rate of decay of coolant momentum can be validated by traverse measurements at the vane inlet and outlet plane in the SSPCF.

REFERENCES

Abernethy, R. B., Thompson, J. W., 1973, "Handbook: Uncertainty in Gas Turbine Measurements", AEDC Technical Report 73-5

Ammari, H. D., Hay, N., Lampard, D., 1990, "The Effect of Density Ratio on the Heat Transfer Coefficient From a Film-Cooled Flat Plate", J. of Turbomachinery

ANSYS FLUENT theory guide, 2012, Release 14.5, ANSYS Inc.

Barringer, M. D., Richard, O. T., Walter, J. P., Stitzel, S. M., Thole, K. A., 2002, "Flow Field Simulations of a Gas Turbine Combustor", J. of Turbomachinery

Bender, W. R., 2006, "Lean Pre-Mixed Combustion" In "The Gas Turbine Handbook", US Department of Energy, NETL

Benton, R., Rabe, G., Schiffer, H.-P., Berg, P., 2005a, "Ballistic Cooling of Turbine Nozzle Guide Vane Platform", Int. Symp. on Air Breathing Engines

Benton, 2005b, "Platform cooling arrangement for the nozzle guide vane stator of a gas turbine", US Patent 7637716 B2

Biesinger, T. E., Gregory-Smith, D.G., 1993, "Reduction in Secondary Flows and Losses in a Turbine Cascade by Upstream Boundary Layer Blowing", ASME Paper No. 93-GT-114

Biollo, R., Benini, E., 2013, "Recent advances in transonic axial compressor aerodynamics", Prog. in Aerospace Sciences

Bogard, D. G., Thole, K. A., 2006, "Gas Turbine Film Cooling", J. of Propulsion and Power

Boletis, E., 1985, "Effects of Tip Endwall Contouring on the Three-Dimensional Flow Field in an Annular Turbine Nozzle Guide Vane: Part 1 – Experimental Investigation", J. of Engg. For Gas Turbines and Power

Bradshaw, P., 1996, "Turbulence Modeling with Application to Turbomachinery", Prog. Aerospace Sci.

Bunker, R. S., 2001, "A Review of Turbine Blade Tip Heat Transfer", Annals of the New York Academy of Sciences

Cha, C. M., Ireland, P. T., Denman, P. A., Savarianandam, V., 2012, "Turbulence levels are high at the combustor-turbine interface", ASME Paper No. GT2012-69130

Chyu, M. K., 2001, "Heat Transfer near Turbine Nozzle Endwall", Annals of the New York Academy of Sciences

Colban, W. F., Thole, K. A., Zess, G., 2003a, "Combustor Turbine Interface Studies – Part 1: Endwall Effectiveness Measurements", J. of Turbomachinery

Colban, W. F., Thole, K. A., Zess, G., 2003b, "Combustor Turbine Interface Studies – Part 2: Flow and Thermal Field Measurements", J. of Turbomachinery

Denton, J. D., 1993, "Loss mechanisms in turbomachines", 1993, J. of Turbomachinery

Devenport, W. J., Simpson, R. L., Dewitz, M. B., Agarwal N. K., 1992, "Effects of a Leading-Edge Fillet on the Flow Past an Appendage-Body Junction", AIAA Journal

Friedrichs, S., Hodson, H. P., Dawes, W. N., 1997a, "Aerodynamic Aspects of Endwall Film-Cooling", J. of Turbomachinery

Friedrichs, S., 1997b, "Endwall Film Cooling in Axial Flow Turbines", PhD Thesis, University of Cambridge

Friedrichs, S., Hodson, H. P., Dawes, W.N., 1999, "The design of an improved endwall film cooling configuration", J. of Turbomachinery

Gibb, G. H., 2011, "Platform Cooling Investigations", Fourth year project report, University of Oxford

Goldstein, R. J., 1971, "Film Cooling", Advanced Heat Transfer

Granser, D., Schulenberg, T., 1990, "Prediction and Measurement of Film Cooling Effectiveness for a First-Stage Turbine Vane Shroud", ASME Paper No. 90-GT-95

Graziani, R. A., Blair, M. F., Taylor, J. R., Mayle, R. E., 1980, "An Experimental Study of Endwall and Airfoil Surface Heat Transfer in a Large Scale Turbine Blade Cascade", J. of Engineering for Power

Haas, W., Rodi, W., Schönung, B., 1991, "The Influence of Density Difference Between Hot and Coolant Gas on Film Cooling by a Row of Holes: Predictions and Experiments", ASME Paper No. 91-GT-255

Han, J. C., Dutta, S., Ekkad, S., 2013, "Gas turbine heat transfer and cooling technology", Boca Raton, FL: CRC Press, Taylor and Francis Group

Harrison, K. L., Bogard, D. G., 2008, "Comparison of RANS Turbulence Models for Prediction of Film Cooling Performance", ASME Paper No. GT2008-51423

Hawthorne, W. R., 1951, "Secondary Circulation in Fluid Flow", Proc. of the Royal Soc. of London, Series A: Mathematical and Physical Sciences

Hermanson, K. S., Thole, K. A., 2000a, "Effect of mach number on secondary flow characteristics", Int. J. of Turbo and Jet engines

Hermanson, K. S., Thole, K. A., 2000b, "Effect of inlet conditions on endwall secondary flow", Int. J. of Turbo and Jet engines

Hill, P. G., Peterson, C. R., 1992, "Mechanics and Thermodynamics of Propulsion", 2nd Edition, Reading, Mass: Addison-Wesley Publishing Co.

Ireland, P. T., Neely, A. J., Gillespie, D. R. H., Robertson, A. J., 1999, "Turbulent heat transfer measurements using liquid crystals", Int. J. of Heat and Fluid Flow

Jones, T. V., 1991, "Definition of Heat Transfer Coefficients in the Turbine Situation", Proc. of the Inst. of Mech. Engineers Turbomachinery: latest developments in a changing scene

Knezevici, D. C., Sjolander, S. A., Praisner, T. J., Allen-Bradley, E., Grover, E. A., 2010, "Measurements of Secondary Losses in a Turbine Cascade with the Implementation of Nonaxisymmetric Endwall Contouring", J. of Turbomachinery

Knost, D.G., Thole, K.A, 2005, “Adiabatic Effectiveness Measurements of Endwall Film-Cooling for a First-Stage Vane”, J. of Turbomachinery

Kollen, O., Koschel, W., 1985, “Effect of Film Cooling on the Aerodynamic Performance of a Turbine Cascade,” AGARD CP 390

Kost, F., Nicklas, M., 2001, “Film-Cooled Turbine Endwall in a Transonic Flow Field : Part 1 – Aerodynamic measurements”, J. of Turbomachinery

Lakshminarayana, B., 1996, “Fluid Dynamics and Heat Transfer of Turbomachinery”, John Wiley & Sons

Langston, L. S., Nice, M. L., and Hooper, R. M., 1977, "Three-Dimensional Flow Within a Turbine Cascade Passage", ASME J. of Engineering for Power

Langston, L.S., 1980, "Crossflows in a Turbine Cascade Passage", J. of Engineering for Power

Langston, L. S., 2001, “Secondary Flows in Axial Turbines – A Review”, Annals of the New York Academy of Sciences

Lefebvre, A.H., 1999, “Gas Turbine Combustion”, 2nd Edition, Philadelphia: Taylor & Francis

Lynch, S. P., Thole, K. A., Kohli, A., Lehane, C., 2011, “Computational Predictions of Heat Transfer and Film-Cooling for a Turbine Blade with Nonaxisymmetric Endwall Contouring”, J. of Turbomachinery

“Measurement of gas flows by means of critical flow Venturi nozzles”, 1990, ISO 9300, Geneva, Switzerland: ISO

Mehta, R. D., Bradshaw, P., 1979, “Design rules for small low speed wind tunnels”, Aeronautical Journal of the RAeS

Moss, R. W., Oldfield, M. L. G., 1991, “Measurements of Hot Combustor Turbulence Spectra”, ASME Paper No. 91-GT-351

Narzary, D. P., Liu, K. C., Han, J. C., 2009, “Influence of Coolant Density on Turbine Blade Platform Film-Cooling”, ASME Paper No. GT2009-59342

Nicklas, M., 2001, “Film-Cooled Turbine Endwall in a Transonic Flow Field: Part II – Heat Transfer and Film Cooling Effectiveness”, J. of Turbomachinery

"Nitrogen Oxides (NOx), Why and How They are Controlled", 1999, Technical Bulletin EPA

Oke, R. A., Simon, T. W., Burd, S. W., Vahlberg, R., 2000, "Measurements in a turbine cascade over a contoured endwall: discrete hole injection of bleed flow", ASME Paper No. 2000-GT-214

Praisner, T. J., Allen-Bradley, E., Grover, E. A, Knezevici, D. C., Sjolander, S. A., 2007, “Application of Non-Axisymmetric Endwall Contouring to Conventional and High-Lift Turbine Airfoils”, ASME Paper No. GT2007-27579

Roach, P.E., 1987, “The generation of nearly isotropic turbulence by means of grids”, Int. J. of Heat and Fluid Flow

Roark, R. J., 1989, “Roark’s formulas for stress and strain”, McGraw-Hill

Schlichting, H., Gersten, K., 2000, “Boundary layer theory”, 8th Edition, Springer

Saumweber, C., Schulz, A., Wittig, S., 2003, “Free-Stream Turbulence Effects on Film Cooling with Shaped Holes”, J. of Turbomachinery

Saumweber, C., Schulz, A., 2004, “Interaction of Film Cooling Rows: Effects of Hole Geometry and Row Spacing on the Cooling Performance Downstream of the Second Row of Holes”, J. of Turbomachinery

Sharma, O. P., and Butler, T. L., 1987, “Predictions of Endwall Losses and Secondary Flows in Axial Flow Turbine Cascades”, J. of Turbomachinery

Simon, T. W., Piggush, J. D., 2006, “Turbine Endwall Aerodynamics and Heat Transfer”, J. of Propulsion and Power

Simpson, R. L., 2001, “Junction Flows”, Annu. Rev. Fluid Mech

Sieverding, C. H., Wilputte, Ph., 1981, “Influence of Mach Number and Endwall Cooling on Secondary Flows in a Straight Nozzle Cascade”, J. of Engineering for Power

Sieverding, C. H., and Van den Bosche, P., 1983, “The Use of Coloured Smoke to Visualize Secondary Flows in a Turbine Cascade,” J. of Fluid Mechanics

Sieverding, C. H., 1985, “Recent Progress in the Understanding of Basic Aspects of Secondary Flows in Turbine Blade Passages”, J. of Engg. For Gas Turbines and Power

Suo, M., 1984, "Turbine Cooling" In Oates, G.C., (Ed.) "Aerothermodynamics of Aircraft Engine Components", New York, N.Y. : American Institute of Aeronautics and Astronautics

Takeishi, K., Oda, Y., Seguchi, J., Kozono, S., 2013, “Effect of endwall film cooling upstream of an airfoil/endwall junction to suppress the formation of horseshoe vortex in a symmetric airfoil”, ASME Paper No. GT2013-95385

The jet engine, 1996, 5th ed., Derby: Rolls Royce

Thole, K.A., Bogard, D. G., Whan-Tong, J. L., 1994, “Generating high freestream turbulence levels”, Experiments in Fluids

Thole, K. A., Radomsky, R. W., Kang, M. B., Kohli, A., 2002, "Elevated freestream turbulence effects on heat transfer for a gas turbine vane", Int. J. of Heat and Fluid Flow

Thole, K. A., Knost, D. G., 2005, "Heat transfer and film-cooling for the endwall of a first stage turbine vane", Int. J. of Heat and Mass Transfer

Thrift, A. A., Thole, K. A., Hada, S., 2011, "Effects of an Axisymmetric Contoured Endwall on a Nozzle Guide Vane: Adiabatic Effectiveness Measurements", J. of Turbomachinery

Thrift, A., Thole, K., Hada, S., 2013, "Impact of the Combustor-Turbine Interface Slot Orientation on the Durability of a Nozzle Guide Vane Endwall", J. of Turbomachinery

Wang, H. P., Olson, S. J., Goldstein, R. J., Eckert, E. R. G., 1997, "Flow Visualization in a Linear Turbine Cascade of High Performance Turbine Blades", J. of Turbomachinery

Zess, G. A., Thole, K. A., 2002, "Computational Design and Experimental Evaluation of Using a Leading Edge Fillet on a Gas Turbine Vane", J. of Turbomachiner**y**

Zhang, L. J., Jaiswal, R. S., 2001, "Turbine Nozzle Endwall Film Cooling Study Using Pressure-Sensitive Paint", J. of Turbomachinery

Appendix

A. Measurement uncertainty estimates

The partial derivative method described by Abernethy and Thompson (1973) was used to estimate measurement uncertainty. All uncertainties are specified for 95% confidence intervals.

Pressure measurement uncertainty

The Sensortechnics pressure transducers provided an amplified analogue voltage signal between 0.5 V (zero input) and 4.5 V (full scale input). A PCI-6033E 16 bit DAQ card from National Instruments was used to digitize voltage signals from the pressure transducers. Signals were sampled at 1000 Hz and data were averaged over 2 second windows. This reduced the effect of AC pickup. The DAQ voltage measurement accuracy was 1.6 μV. This resulted in a negligible 4×10^{-5}% uncertainty over the 4 V voltage output range of the pressure transducers. The DAQ card represents voltages from -5 V to 5 V as a 16 bit number. This uncertainty caused by digitization is $10/2^{16} = 1.5\times10^{-4}$ V. This is a negligible 3.75×10^{-3} % of pressure transducer voltage output. The voltage output of the transducers is proportional to the power supply voltage (5 V). A DC power supply unit of very low line regulation (0.05%) was used to minimize variation in power supply voltage. The uncertainties accrued by supply voltage fluctuation, data acquisition and digitization are negligible and are not considered.

Full span uncertainties were specified for the 1000 Pa, 6900 Pa, 5 bar, atmospheric (1100 mbar) pressure transducers by the manufacturer as 0.5% (5 Pa), 1% (69 Pa), 0.5% (2500 Pa), 1% (1100 Pa).

Purpose of uncertainty estimate

Experimental measurements of η_{eff} were compared with CFD predictions for a particular $\dot{m}_c/\dot{m}_\infty$. Experimentally measured vane stagnation pressure, P_{dyn}, freestream temperature, T_∞, and coolant mass flow rate, $\dot{m}_c$, were specified as boundary conditions in the CFD simulations. The experimental uncertainties in $\dot{m}_c/\dot{m}_\infty$ and η_{eff} are now estimated.

Uncertainty in coolant mass flow rate ($\dot{m}_c$)

The coolant mass flow ($\dot{m}_c$) was metered using a critical flow venturi nozzle. Nozzle geometries were generated according to the ISO 9300 standard (Measurement of gas flows, 1990). Mass flow rate through the nozzle is given by the following expression.

$$\dot{m}_c = \frac{A_* C_* P_0 C_d}{\sqrt{(R/M)T_0}}, \tag{A-1}$$

The quantities in the Equation (A-1) are as follows: A_* is the geometric throat area, C_* is $\sqrt{\gamma}\left(\frac{2}{\gamma+1}\right)^{(\gamma+1)/2(\gamma-1)}$, where γ is the ratio of specific heats, P_0 is the inlet total pressure, C_d is the discharge coefficient, R is the universal gas constant, M is the molecular weight of air. The uncertainty in coolant mass flow rate ($\Delta\dot{m}_c$) is given as:

$$\Delta\dot{m}_c = \sqrt{\left(\frac{\partial\dot{m}_c}{\partial A_*}\Delta A_*\right)^2 + \left(\frac{\partial\dot{m}_c}{\partial P_0}\Delta P_0\right)^2 + \left(\frac{\partial\dot{m}_c}{\partial T_0}\Delta T_0\right)^2}, \tag{A-2}$$

The partial derivatives are:

$$\frac{\partial\dot{m}_c}{\partial A_*} = \frac{C_* P_0 C_d}{\sqrt{(R/M)T_0}}, \frac{\partial\dot{m}_c}{\partial P_0} = \frac{A_* C_* C_d}{\sqrt{(R/M)T_0}}, \frac{\partial\dot{m}_c}{\partial T_0} = \frac{A_* C_* P_0 C_d}{2\sqrt{(R/M)T_0^3}}, \tag{A-3}$$

The uncertainty in throat area (percentage), $\Delta A_{*\%}$, is estimated as $\Delta A_{*\%} = 2\Delta D_{\%}$, where D is the throat diameter. The throat diameter was measured with vernier callipers of 0.05 mm accuracy. Three thermocouples were used to measure coolant temperature. An

uncertainty of 1.58 K is assumed for this measurement. Two pressure transducers of 5 bar range were used to measure P_0, resulting in an uncertainty of $2500/\sqrt{2}$ = 1768 Pa.

For the 4% mass flux ratio case ($\dot{m}_c$ = 44 g/s), nominal values were P_0 = 2 bar, C_d = 0.988, T_0 = 293 K, R = 8.314 J/mol.K, M = 2.9×10^{-2} kg/mol, D = 11 mm. The uncertainty, $\Delta\dot{m}_c$, is estimated from Equation (A-2) as 0.8 g/s (1.8%).

Uncertainty in passage mass flow rate ($\dot{m}_\infty$)

Mass flow rate through a vane passage was estimated from outlet velocity (u_{out}) using the expression:

$$\dot{m}_\infty = \rho_\infty A_{th} u_{out} = A_{th}\sqrt{2\rho_\infty P_{dyn}} = A_{th}\sqrt{2\frac{P_{atm}}{RT_\infty}P_{dyn}}, \quad \text{(A-4)}$$

where A_{th} is the vane geometric throat area, P_{atm} is the atmospheric pressure, T_{out} is the outlet temperature, P_{dyn} is the dynamic head.

$$\Delta\dot{m}_\infty = \sqrt{\left(\frac{\partial\dot{m}_\infty}{\partial P_{atm}}\Delta P_{atm}\right)^2 + \left(\frac{\partial\dot{m}_\infty}{\partial T_{out}}\Delta T_{out}\right)^2 + \left(\frac{\partial\dot{m}_\infty}{\partial P_{dyn}}\Delta P_{dyn}\right)^2}, \quad \text{(A-5)}$$

ΔT_{out} was measured with six thermocouples. ΔP_{atm}, the uncertainty in the atmospheric pressure transducer, is 1100 Pa; P_{dyn} was measured with two 6900 Pa transducers. The uncertainty in throat area (A_{th}) does not affect the coolant mass flux ratio ($\dot{m}_c/\dot{m}_\infty$) and is thus not included. Computing partial derivatives and substituting in Equation (A-5), the uncertainty in $\dot{m}_\infty$ is estimated to be 2.5%.

Uncertainty in coolant mass flux ratio ($\dot{m}_c/\dot{m}_\infty$)

Using the partial derivative method, the following expression was obtained for the uncertainty in $\dot{m}_c/\dot{m}_\infty$:

$$\Delta\left(\frac{\dot{m}_c}{\dot{m}_\infty}\right) = \frac{1}{\dot{m}_c}\sqrt{\left(\frac{\dot{m}_c}{\dot{m}_\infty}\Delta\dot{m}_c\right)^2 + \left(\left(\frac{\dot{m}_c}{\dot{m}_\infty}\right)^2 \Delta\dot{m}_\infty\right)^2}, \tag{A-6}$$

The uncertainty for $\dot{m}_c/\dot{m}_\infty$ ranges from 0.02% (absolute) for $\dot{m}_c/\dot{m}_\infty$ = 1% to 0.15% (absolute) for $\dot{m}_c/\dot{m}_\infty$ = 9%.

Uncertainty in η_{eff}

η_{eff} is given by the expression below.

$$\eta_{eff} = \frac{T_\infty - T_w}{T_\infty - T_c} = \frac{A}{B}, \tag{A-7}$$

The uncertainty $\Delta\eta_{eff}$ is expressed as:

$$\Delta\eta_{eff} = \sqrt{\left(\frac{\partial\eta_{eff}}{\partial A}\Delta A\right)^2 + \left(\frac{\partial\eta_{eff}}{\partial B}\Delta B\right)^2}, \tag{A-8}$$

where,

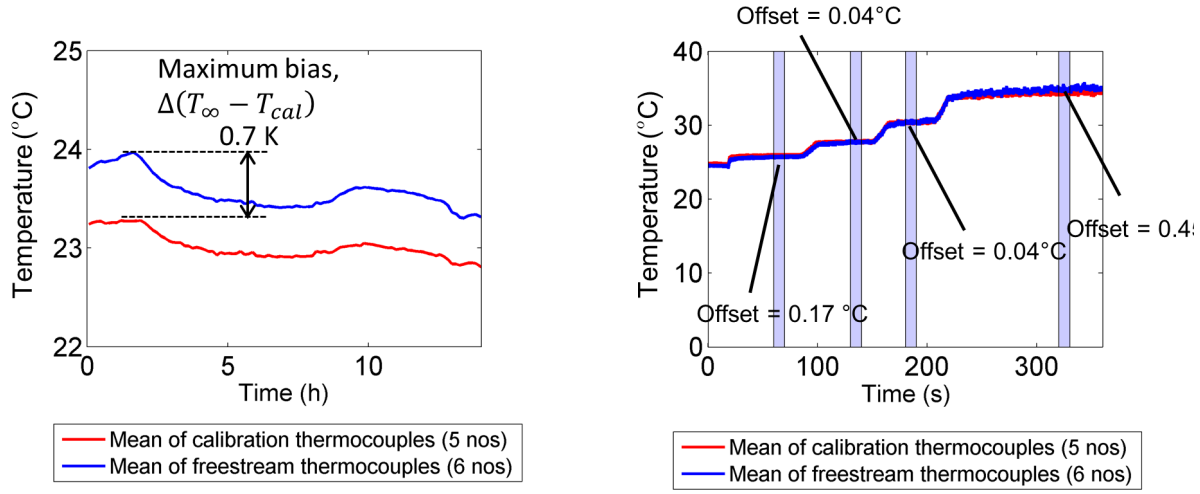
$$\frac{\partial\eta_{eff}}{\partial B} = \frac{-A}{B^2}, \frac{\partial\eta_{eff}}{\partial A} = \frac{1}{B},$$
$$\Delta\eta_{eff} = \frac{1}{B}\sqrt{\Delta A^2 + \frac{A^2}{B^2}\Delta B^2} \tag{A-9}$$

T_∞ and T_c were measured using six and three thermocouples, with thermocouples fabricated from the same roll of wire. T_{cal}, the mean temperature of the calibration thermocouples was estimated from five thermocouples from a different roll of wire. Temperature samples were obtained at 500 hz and averaged over a two second interval. The precision uncertainty of the thermocouple measurement is small because of the large number of samples averaged (1000 nos.).

ΔA is comprised of the offset between T_∞ and T_w, which is caused by two sources of uncertainty: (1) the mean bias between the thermocouples measuring the freestream

temperature and the calibration thermocouples $\Delta(T_\infty - T_{cal})$; (2) the uncertainty in the linear fit. ΔT_{fit}. These quantities are now estimated.

The thermocouple bias, $\Delta(T_\infty - T_{cal})$, was estimated by comparing measurements obtained over a 15 hour period (see Figure A-1 (a)). The maximum bias observed was 0.7 K. This value was confirmed by running the SSPCF through a range of temperatures by increasing the mesh heater output (see Figure A-1 (b)). The mean offset value was observed to be less than 0.7 K at different temperature values. Hence 0.7 K was used as an estimate for $\Delta(T_\infty - T_{cal})$.



(a) Thermocouple bias estimate: $\Delta(T_\infty - T_{cal})$

(b) Thermocouple bias measured at different temperatures

Figure A-1: Thermocouple bias estimate

Infrared radiometric data was converted to T_w using an in-situ calibration procedure (see Section 2.1.7). Five calibration curves (see Figure A-2 (a)) were obtained by plotting radiometric vs. thermocouple data obtained at five locations in isothermal regions of the endwall. These are of the form

$$T_{fit,j} = a_j + b_j I, \tag{A-10}$$

where a_j and b_j are the slope and intercept of the calibration curve j (j = 1 to 5), I is the radiometric intensity. The mean calibration curve was obtained by averaging the five calibration curves:

$$T_{fit} = \bar{a} + \bar{b}I \tag{A-11}$$

The uncertainty in slope, $\Delta\bar{a}$, and uncertainty in intercept, $\Delta\bar{b}$, were estimated as

$$\Delta\bar{a} = \frac{1}{5}\sqrt{\sum_{j=1}^{5}\Delta a_j^2}, \qquad \Delta\bar{b} = \frac{1}{5}\sqrt{\sum_{j=1}^{5}\Delta b_j^2} \tag{A-12}$$

where Δa_j, Δb_j are the uncertainties in the slope and intercepts of each calibration curve.

The uncertainty in linear fit, ΔT_{fit}, is expressed as:

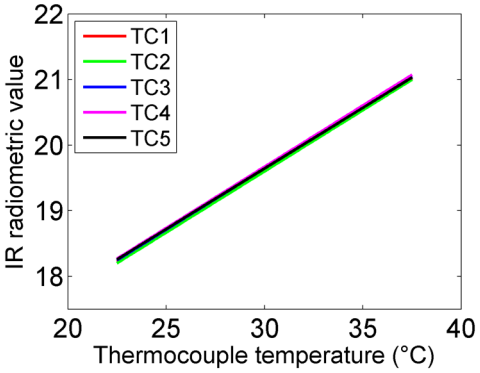
$$\Delta T_{fit} = \sqrt{\left(\frac{\partial T_{fit}}{\partial \bar{a}}\Delta\bar{a}\right)^2 + \left(\frac{\partial T_{fit}}{\partial \bar{b}}\Delta\bar{b}\right)^2 + \left(\frac{\partial T_{fit}}{\partial I}\Delta I\right)^2} = \sqrt{(\Delta\bar{a})^2 + \left(I\Delta\bar{b}\right)^2}, \tag{A-13}$$

The IR camera uncertainty, ΔI, is absorbed into the calibration. The uncertainty caused by the linear fit, ΔT_{fit}, was estimated as 0.35 K.

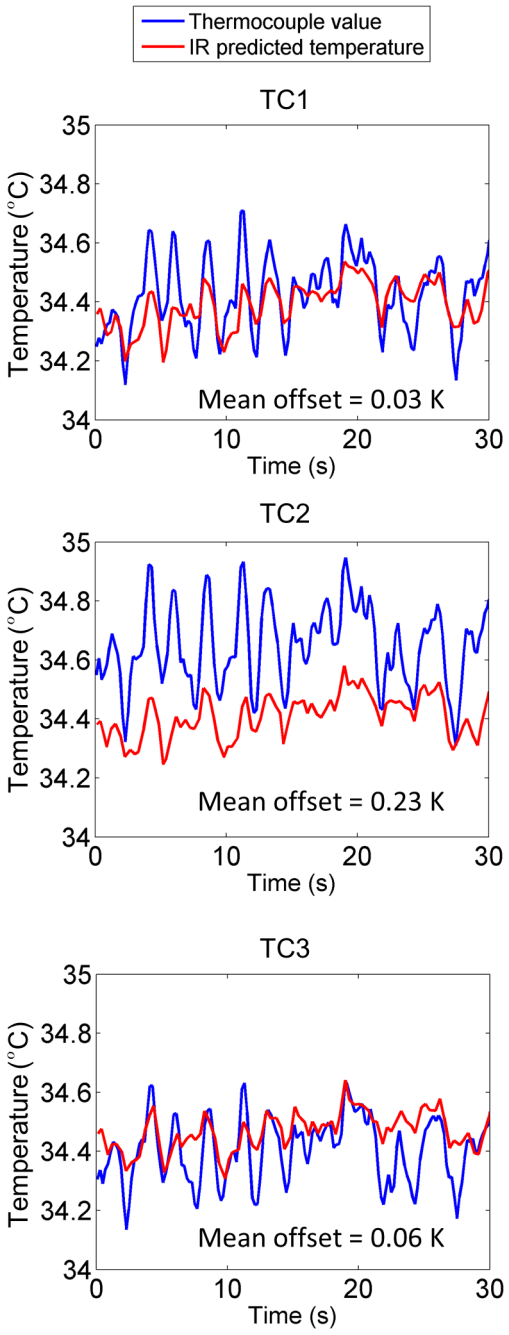
Temperature was predicted from the IR images using Equation (A-11). This temperature was averaged over 3×3 pixel squares positioned next to the calibration thermocouples. This IR predicted temperature is compared with thermocouple values in Figure A-2 (b) for three different calibration thermocouples. The mean offset in all cases is below the estimated ΔT_{fit} of 0.35 K.

The uncertainty $\Delta A = \Delta(T_\infty - T_w)$ is estimated by combining the uncertainties caused by linear fit and thermocouple bias:

$$\Delta A = \sqrt{\left(\Delta T_{fit}\right)^2 + \Delta(T_\infty - T_{cal})^2} = \sqrt{(0.35)^2 + (0.7)^2} = 0.78 \text{ K} \quad \text{(A-14)}$$



(a) IR calibration curves



(b) Thermocouple values vs. temperature predicted by IR camera

Figure A-2: IR calibration curves and uncertainties caused by curve fit

The thermocouple bias, $\Delta(T_\infty - T_c)$, was estimated by placing the thermocouples in an insulated box constructed from Rohacell and recording temperatures for a long duration. An initial settling period of 30 hours was allowed to establish isothermal conditions. Temperature measurements are shown in Figure A-3. The maximum value of the bias, $\Delta B = \Delta(T_\infty - T_c)$, observed in these measurements, was 0.3 K.

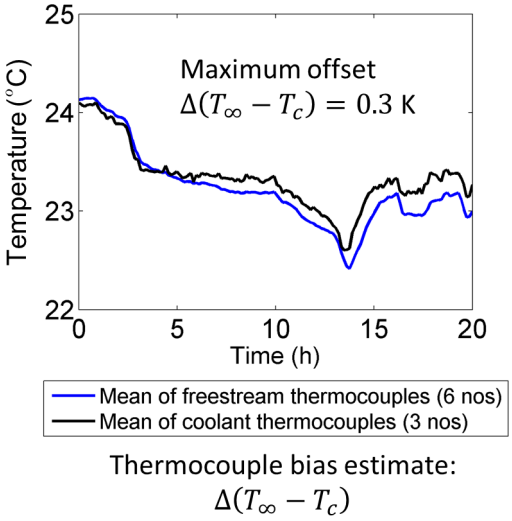


Figure A-3: Thermocouple bias estimate $\Delta(T_\infty - T_c)$

Substituting values for ΔA (0.78 K), ΔB (0.3 K), B (~ 20 K), A (~ 12 K for η_{eff} = 0.6) in Equation 1, $\Delta\eta_{eff}$ = ±0.04 at η_{eff} = 0.6.

Dilution momentum flux ratio uncertainty

Dilution momentum flux ratio (I) is defined as:

$$I = \frac{\frac{1}{2}\rho_j u_j^2}{\frac{1}{2}\rho_c u_{c,out}^2}, \tag{A-15}$$

where u_j is the dilution jet velocity and u_c is the freestream velocity at the combustor outlet plane (see Figure A-4). I can be rewritten as:

$$I = \frac{1}{K} \times \frac{P_{dil}}{P_{dyn}}, \tag{A-16}$$

where $P_{dil} = \frac{1}{2}\rho_j u_j^2$ is the pressure drop measured across the dilution holes and P_{dyn} is the dynamic head measured at the stagnation point of the vane. $u_{c,out}$ has been estimated as $(A_{th}/A_{c,out})u_{out}$, where u_{out} is the vane outlet velocity, A_{th} is the vane throat area and A_c is the combustor outlet area. K is defined as $(A_{th}/A_{c,out})^2$.

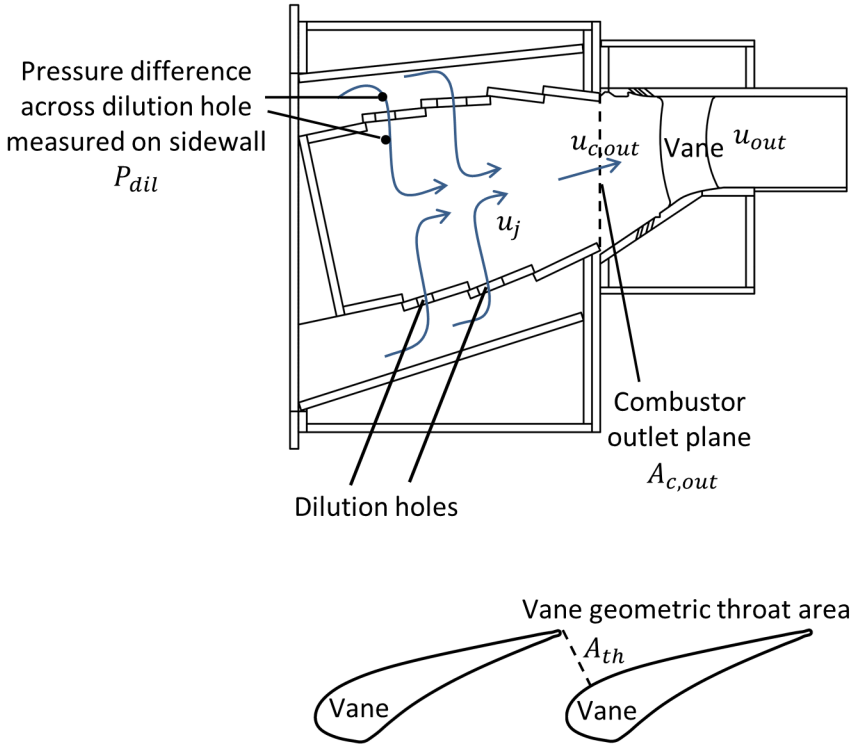


Figure A-4: Definitions of terms P_{dil}, A_{th}, u_{out}, u_j, $u_{c,out}$

The uncertainty, ΔI, is estimated as:

$$\Delta I = \sqrt{\left(\frac{\partial I}{\partial P_{dil}}\Delta P_{dil}\right)^2 + \left(\frac{\partial I}{\partial P_{dyn}}\Delta P_{dyn}\right)^2}, \tag{A-17}$$

$$\frac{\partial I}{\partial P_{dil}} = \frac{1}{K P_{dyn}}, \frac{\partial I}{\partial P_{dyn}} = \frac{J}{P_{dyn}}$$

P_{dil} was measured using one transducer of 1000 Pa range. P_{dyn} was measured using two transducers of 6900 Pa range. Substituting values in Equation (A-17), the uncertainty ΔI is expressed as:

$$\Delta I = \sqrt{0.1707 + 0.0024(I^2)}, \tag{A-18}$$

For the typical value of $I \approx 10$ measured, ΔI = 0.64 (6.4%). The high value of uncertainty is because of the choice of 6900 Pa range transducers to measure vane dynamic head ($\sim$ 1024 Pa). The tunnel was originally designed for operation at higher dynamic head, but tests were run at lower values to reduce mechanical stresses.

Uncertainty in vane pressure coefficient (C_P)

The vane pressure coefficient C_P is defined as:

$$C_P = \frac{P - P_{dyn}}{P_{dyn}}, \tag{A-19}$$

where P is the static pressure measured on the blade surface.

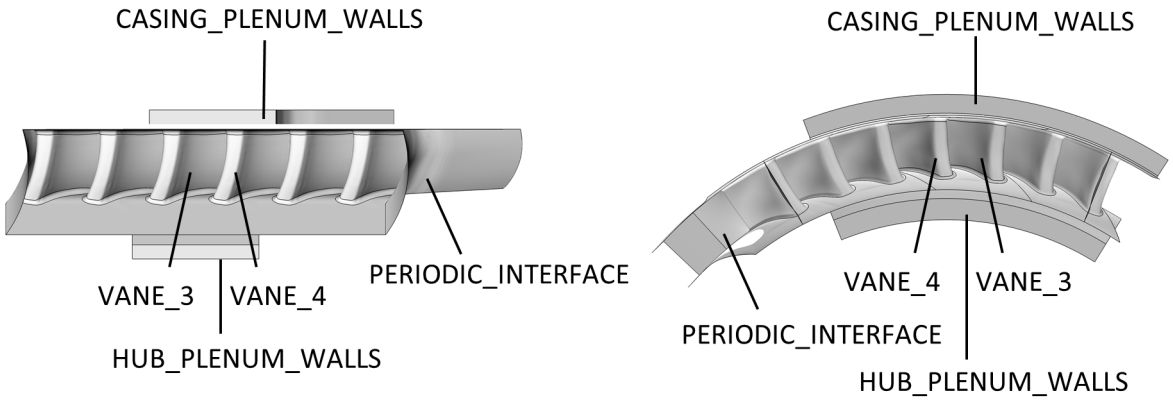
$$\Delta C_P = \sqrt{\left(\frac{\partial C_P}{\partial P}\Delta P\right)^2 + \left(\frac{\partial C_P}{\partial P_{dyn}}\Delta P_{dyn}\right)^2} = \sqrt{\left(\frac{1}{P_{dyn}}\Delta P\right)^2 + \left(\frac{P}{P_{dyn}^2}\Delta P_{dyn}\right)^2} \tag{A-20}$$

1000 Pa transducers were used to measure P_{dyn} and P. For $C_P = 0.5$, ΔC_P is estimated at 1%.

B. CFD optimization loop

Solid modelling, meshing, CFD case setup, solution and postprocessing were automated by scripting. CFD solutions of new endwall film cooling systems could be obtained very quickly using these scripts. Rhino was used for solid modelling, ICEM-CFD for meshing, FLUENT for CFD solution and postprocessing, and Matlab for plotting of results.

Figure B-1 shows template geometries created for SSPCF (a) and engine (b) film cooling simulation. All surfaces and curves have been created, with the exception of cooling holes. The surfaces have been assigned to layers with the names marked in Figure B-1: VANE_3, VANE_4 etc. The Rhino layer names were used as labels for boundary conditions in ICEM-CFD and FLUENT. Using identical layer names for all CFD geometries allows automation by scripting.



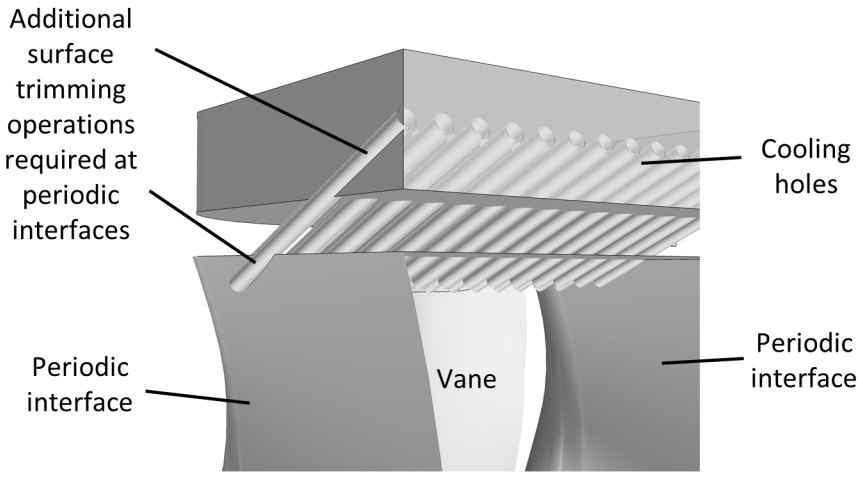
(a) SSPCF CFD template with some BC labels marked

(b) Trent XWB-97K CFD template with some BC labels marked

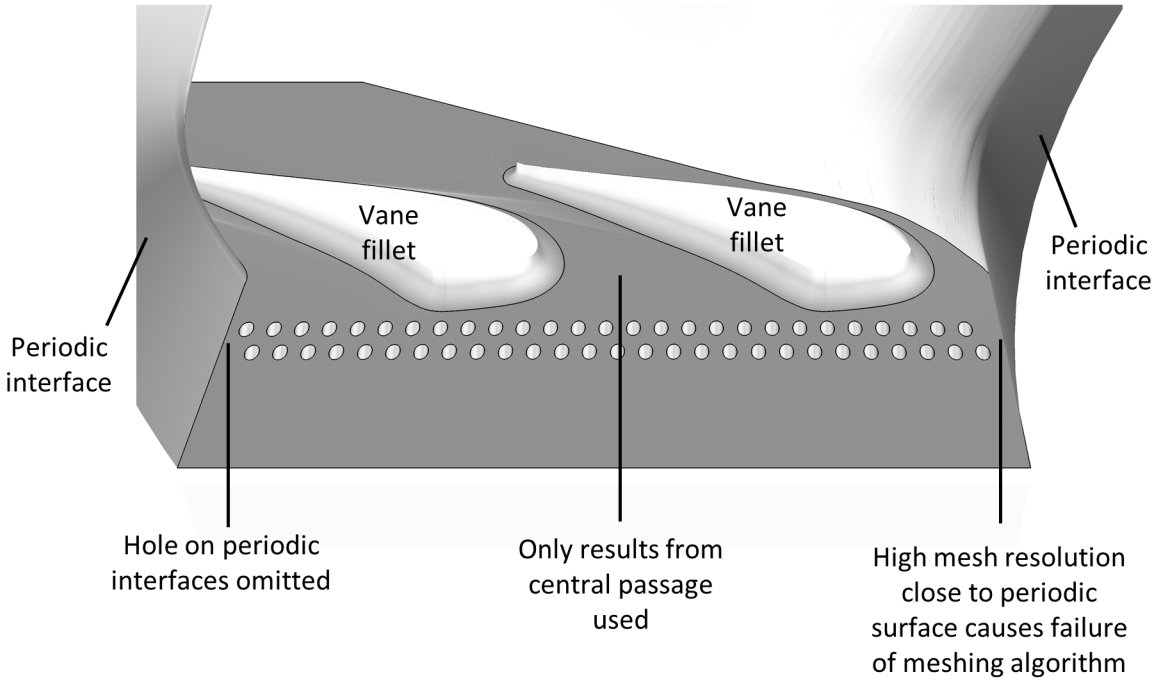
Figure B-1: SSPCF and engine CFD template domains

Six vane passages were used, with cooling holes on the central two endwalls. This configuration simplifies automation considerably. A single passage CFD geometry requires hole surfaces at the periodic interfaces to be trimmed and requires additional surfaces to be created (see Figure B-2 (a)). A two passage geometry eliminates this complication – cooling

holes can be omitted on the periodic interfaces, and simulation results from the central passage can be used (see Figure B-2 (b)).



(a) Single passage CFD domain



(b) Two passage CFD domain

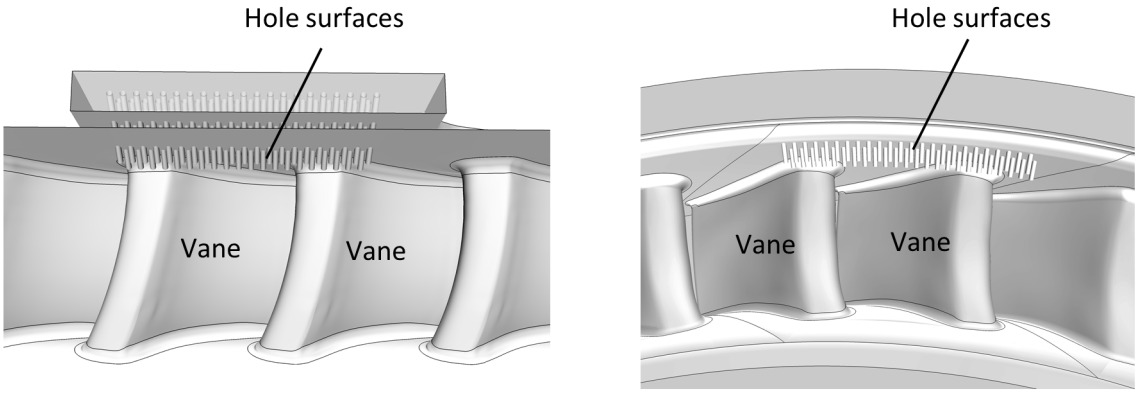
Figure B-2: Meshing automation problems using single passage and two passage CFD domains

Meshing in ICEM-CFD often failed at the periodic interfaces, if small mesh length scales were specified on adjoining endwalls. This problem was solved by using a six-passage domain with mesh density concentrated on the central two passages (around VANE_3 and

VANE_4). Large mesh length scales were specified on the peripheral passages – the increase in mesh count from a two-passage to a six-passage domain was less than 10%.

Cooling hole geometries were specified in a CSV (comma separated value) spreadsheet file, editable in Microsoft Excel. These details were diameter, inclination, compound angle, pitchwise and axial position for each hole in a passage.

The Rhino Visual Basic scripting tool was used to automate solid modelling operations. The hole geometry spreadsheet was read by a script and hole surfaces were created across the central two passages in the CFD template. The untrimmed hole geometries are shown in the SSPCF CFD template in Figure B-3 (a), and in the engine CFD template in Figure B-3 (b).



(a) Untrimmed hole geometries generated for SSPCF CFD domain

(b) Untrimmed hole surfaces generated for Trent XWB-97K CFD domain

Figure B-3: Untrimmed film cooling hole geometries

These hole surfaces were trimmed and patch surfaces were created at the hole inlet planes (see Figure B-4). These patch surfaces were used for assigning boundary conditions for passive-scalar tracking simulations (see Section 4.2.2). The patch surfaces were assigned layer names in order of pitchwise coordinate. The problem of mesh leakage through the edges of trimmed surfaces was solved by using surfaces of high resolution (see wireframe in Figure

B-4). While these surfaces required additional memory and slowed geometry operations, errors in ICEM-CFD meshing were eliminated.

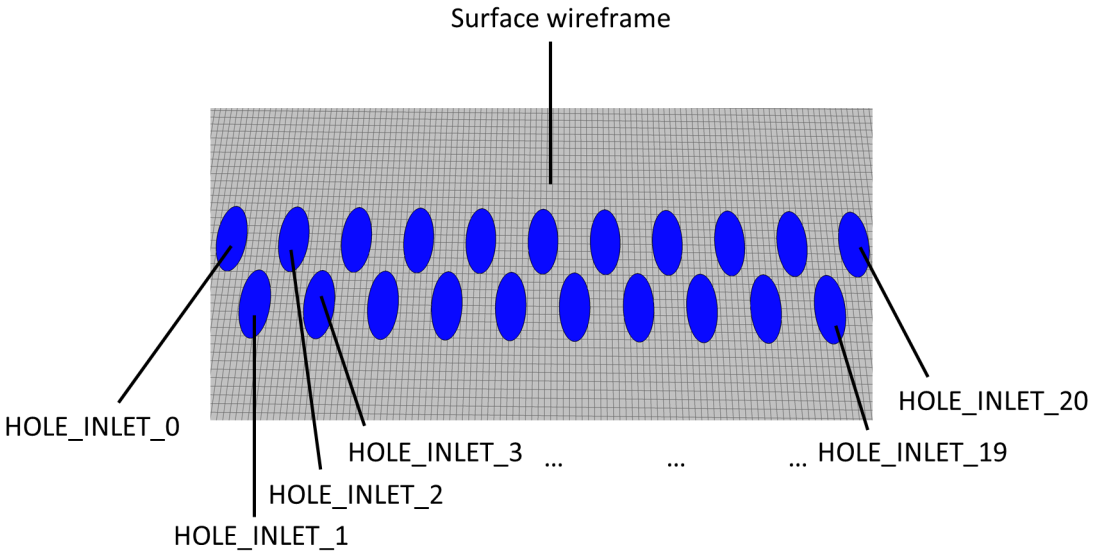


Figure B-4: Hole inlet patch surfaces

The final CFD geometry was exported to ICEM-CFD. Mesh dimension and boundary condition set up was automated using a macro. A tetrahedral mesh was generated and outputted in FLUENT format.

Case setup and solution was automated using the FLUENT Scheme programming language. Residuals, mass flux and temperature monitors were inspected to confirm solution convergence. A FLUENT script was then run to create post-processing surfaces and output data to text files. These text files were used by a Matlab script to plot results and compare with results from other cases.

C. CO_2 coolant injection system

The governing non-dimensional groups for film cooling were described in Section 1.3. These are the density ratio (DR), velocity ratio (VR), blowing ratio (BR), momentum flux ratio (I) and specific heat ratio (κ):

$$DR = \frac{\rho_c}{\rho_\infty}, VR = \frac{u_c}{u_\infty}, BR = \frac{\rho_c u_c}{\rho_\infty u_\infty}, I = \frac{\rho_c u_c^2}{\rho_\infty u_\infty^2}, \kappa = \frac{c_{p_c}}{c_{p_\infty}} \tag{C-1}$$

BR and I can be expressed as:

$$\begin{aligned} BR &= DR \times VR \\ I &= DR \times VR^2 \end{aligned} \tag{C-2}$$

The temperature ratio of the coolant to the freestream, $T_c/T_\infty \approx 2$, results in $DR \approx 2$ in a gas turbine. This large ratio in temperature is difficult to obtain in a laboratory setting. DR is matched by using a coolant gas with a different density than the freestream.

To demonstrate the effect of density ratio mismatch, an experiment is considered where I is matched to the engine condition. i.e. $I_{exp} = I_{engine}$, where subscripts *exp* and *engine* describe experimental and engine conditions. Using Equation (D-2) the following expression is obtained:

$$VR_{engine} = \sqrt{\frac{DR_{exp}}{DR_{engine}}} \times VR_{exp} \tag{C-3}$$

The mismatch in the blowing ratio is expressed as BR_{exp}/BR_{engine}.

$$\frac{BR_{exp}}{BR_{engine}} = \frac{DR_{exp} \times VR_{exp}}{DR_{engine} \times VR_{engine}} = \sqrt{\frac{DR_{exp}}{DR_{engine}}} \tag{C-4}$$

The mismatch, BR_{exp}/BR_{engine}, is larger when air is used as the coolant gas in the experiment ($DR_{exp} \approx 1$), than when a gas of higher density ($DR_{exp} > 1$) is used.

A CO_2 coolant injection system was developed for use in the SSPCF. The density ratio of CO_2 to air at the same temperature is 1.51. This allows better matching of BR and I. The specific heat ratio, κ, using CO_2 as coolant is 0.8, while this ratio is 0.9 in the engine. The schematic of the system is shown in Figure C-1.

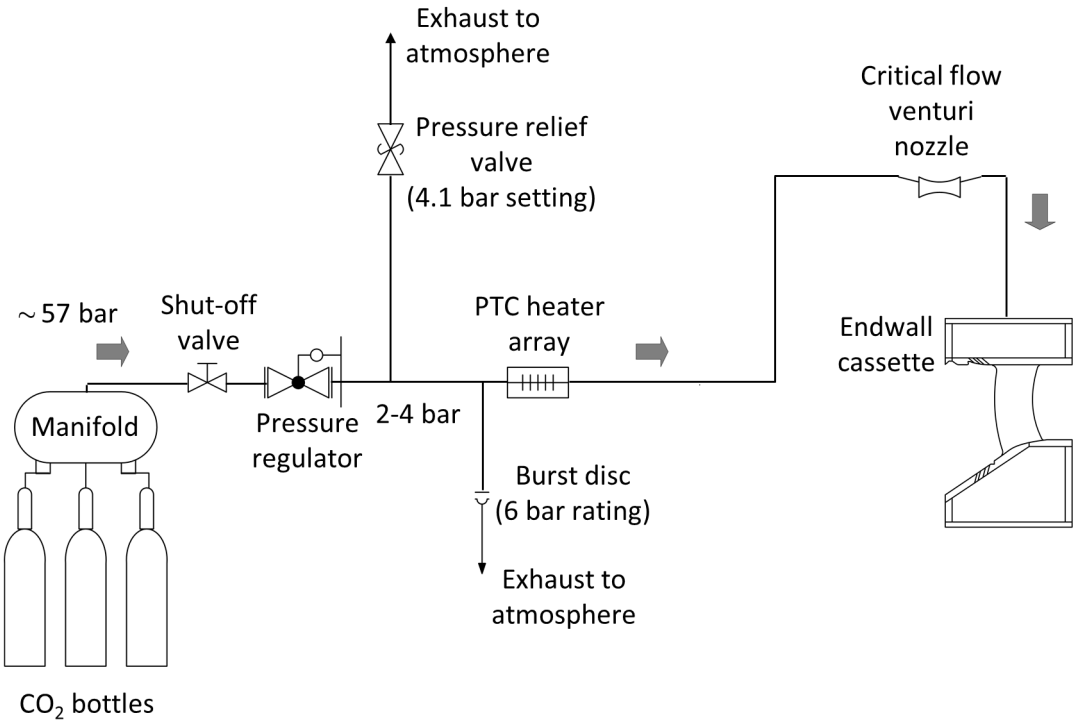


Figure C-1: CO_2 coolant injection system schematic

CO_2 is sourced from a bank of bottles. It is in liquid form at around 57 bar. It is expanded through a pressure regulator to a set pressure between 2 and 4 bar. The gas temperature drops by around 55 K because of the Joule Thomson effect. The gas is reheated by 35 K using an array of PTC (Positive Temperature Coefficient) heaters of 6 kW total output. This flow is metered using the critical flow venturi nozzle (described in Section 2.1.6) and fed to the endwall cassette. The CO_2 mass flow rate can be adjusted by changing the pressure upstream of the venturi nozzle using the pressure regulator. A pressure relief valve and burst disc ensure that pressure in the system is kept within safe limits.

D. Passive scalar tracking method: correction for specific heat variation

Specific heat (c_p) varies with temperature. This variation is now accounted for in the passive-scalar tracking method. Figure D-1 shows a control volume drawn around a cooling hole.

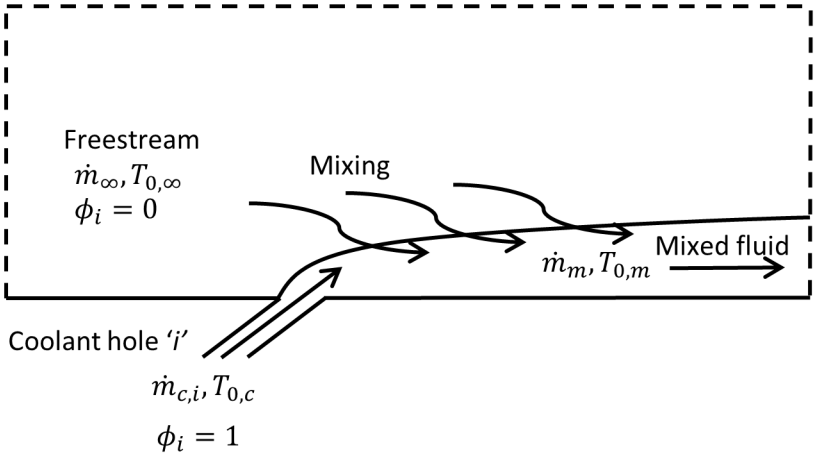


Figure D-1: Control volume analysis for scalar concentration

The continuity and energy equation were applied to the control volume. Note that $\dot{m}_c = \sum_i \dot{m}_{c,i}$.

$$\dot{m}_m = \dot{m}_\infty + \dot{m}_c \tag{D-1}$$

$$\dot{m}_m c_{p_m} T_{0,m} = \dot{m}_\infty c_{p_\infty} T_{0,\infty} + \dot{m}_c c_{p_c} T_{0,c} \tag{D-2}$$

Dividing Equation (D-2) by $\dot{m}_m c_{p_\infty}$, eliminating $\dot{m}_\infty$ using Equation (D-1), and setting $\Sigma\emptyset = \dot{m}_c/\dot{m}_m$, the following equation was obtained:

$$\frac{c_{p_m}}{c_{p_\infty}} T_{0,m} = (1 - \Sigma\phi) T_{0,\infty} + \Sigma\phi \frac{c_{p_c}}{c_{p_\infty}} T_{0,c} \tag{D-3}$$

Assuming a linear variation of c_p with temperature and setting $\kappa = c_{p_c}/c_{p_\infty}$ (constant), an expression for c_{p_m}/c_{p_∞} can be obtained. This is summarized below:

$\boldsymbol{T}$	$\boldsymbol{c_p}/\boldsymbol{c_{p_\infty}}$
$T_{0,\infty}$	1
$T_{0,c}$	$\kappa = {c_{p_c}}/{c_{p_\infty}}$
$T_{0,m}$	$\frac{c_{p_m}}{c_{p_\infty}} = 1 - (1-\kappa)\frac{T_{0,\infty} - T_{0,m}}{T_{0,\infty} - T_{0,c}}$

The expression for c_{p_m}/c_{p_∞} is substituted in Equation (D-3) to obtain:

$$\left(1 - (1-\kappa)\frac{T_{0,\infty} - T_{0,m}}{T_{0,\infty} - T_{0,c}}\right) T_{0,m} = (1 - \Sigma\phi) T_{0,\infty} + (\Sigma\phi)\kappa T_{0,c} \qquad \text{(D-4)}$$

This is a quadratic expression for $T_{0,m}$, which can be solved for given values of $T_{0,\infty}$, $T_{0,c}$, κ and scalar concentration sum $\Sigma\phi$. The cooled wall temperature can thus be estimated, since $T_{aw} \approx T_{0,m}$.

For a typical gas turbine, $\kappa = c_{p_c}/c_{p_\infty} = 0.9$ for $T_c \sim 900$ K and $T_\infty \sim 1800$ K. Substituting κ = 0.9, $\Sigma\phi$ = 0.6 in Equation (D-4), $T_{0,m}$ is estimated as 1282 K. $T_{0,m}$ estimated with κ = 1 (specific heat invariant with temperature) is 1260 K: the temperature is under-estimated by 22 K.

E. Combustor momentum flux ratio matching

The momentum flux ratio of the combustor dilution jets is now estimated. Stations 3 and 4 refer to compressor outlet and combustor outlet conditions respectively. All calculations are performed for conditions at the combustor outlet plane (marked in Figure E-1 for the SSPCF).

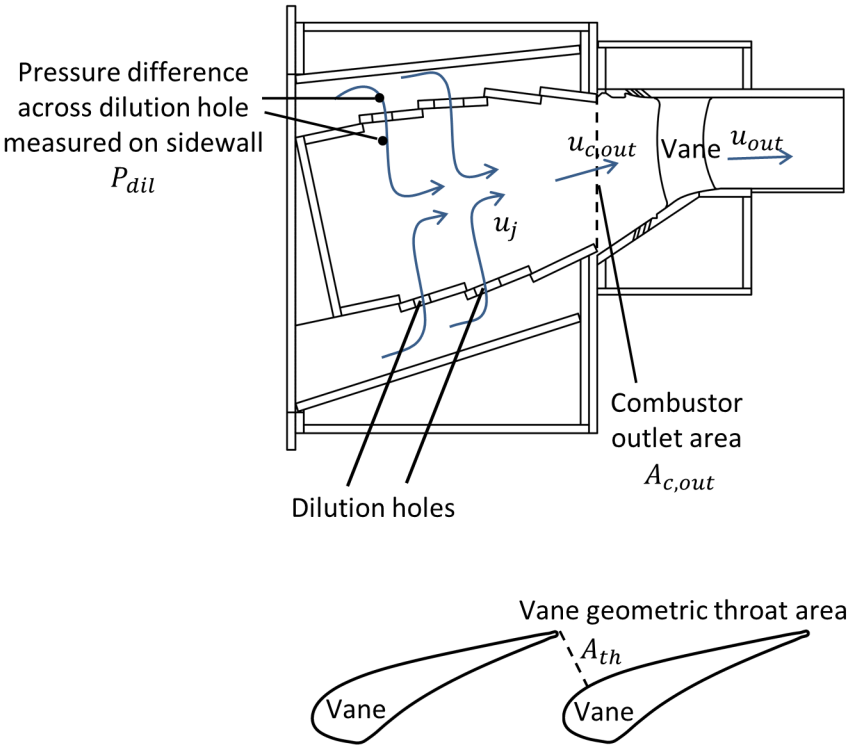


Figure E-1: Definitions of terms P_{dil}, A_{th}, u_{out}, u_j, $u_{c,out}$

Engine conditions

Mass flow rate through NGV throat (single passage) is given by the expression:

$$\dot{m} = \rho u A = \frac{P_{04}}{RT_{04}} M A_{th} \sqrt{\gamma R T_{04}}, \tag{E-1}$$

where the suffix 4 describes conditions at the combustor outlet plane. For engine conditions, $\dot{m}$ is estimated at 1.74 kg/s.

The Mach number at the combustor outlet plane (M_c) can be estimated given $\dot{m}$, using the expression below:

$$\dot{m} = \frac{P_{04}\sqrt{\gamma}M_c A_c}{\sqrt{RT_{04}}} \quad \text{(E-2)}$$

M_c is estimated at 0.055.

Total-to-static pressure ratio at this Mach number (M_c = 0.055) is P_4/P_{04} = 0.9979. The total pressure ratio caused by combustion, P_{03}/P_{04}, is specified as 1.023, where the suffix 3 describes conditions at the compressor outlet. Thus pressure drop across the dilution holes is given by:

$$P_{03} - P_4 = (1.023 - 0.9979)P_{04} = 0.0251P_{04} \quad \text{(E-3)}$$

Dilution jet momentum flux ratio, I, is now estimated as:

$$I = \frac{\frac{1}{2}\rho_j u_j^2}{\frac{1}{2}\rho_c u_c^2} = \frac{P_{03} - P_4}{P_{04} - P_4} = \frac{0.0251}{0.0021} = 11.9, \quad \text{(E-4)}$$

where u_j is the velocity of the dilution jet and u_c is the freestream velocity in the combustor.

SSPCF conditions

At design condition, the vane outlet velocity (u_{out}) for the SSPCF is 42 m/s. Using the continuity equation, the velocity at the combustor outlet (u_c) is estimated:

$$u_c = \frac{A_{th}}{A_c} u_{out}, \quad \text{(E-5)}$$

where A_{th} is the vane throat area and A_c is the combustor outlet area (see Figure E-1). Substituting values for u_{out} = 42 m/s and A_{th}/A_c = 0.11, u_c is estimated as 4.6 m/s.

In order to match momentum flux ratio, I, the jet velocity (u_j) needs to be:

$$u_j = \sqrt{I}u_c, \quad \text{(E-6)}$$

Substituting values for I and u_c, u_j is estimated as 15.8 m/s. The jet dynamic head, $^1/_2\,\rho u_j^2$, is 154 Pa.

RIDN/RODN momentum flux ratio estimate

At the RIDN/RODN injection location, the mainstream gas-path flow area $A_{RIDN/RODN}$ = 3.85 × 10^{-3} m^2. $M_{RIDN/RODN}$ is estimated using Equation (E-2) as 0.086. P_4/P_{04} at this Mach number is 0.9948.

$$P_{03} - P_4 = (1.023 - 0.9948)P_{04} = 0.0282P_{04} \quad \text{(E-7)}$$

The mean RIDN/RODN momentum flux ratio, I, is now estimated as:

$$I_{RIDN/RODN} = \frac{\frac{1}{2}\rho u_j^2}{\frac{1}{2}\rho u_c^2} = \frac{P_{03} - P_4}{P_{04} - P_4} = \frac{0.0282}{0.0052} = 5.42, \quad \text{(E-8)}$$